Benedikt Lübbers

AlGaN-based pH-Sensors

Impedance Characterisation, Optimisation and Application for Foetal Blood Sampling

AlGaN-based pH-Sensors

Impedance Characterisation, Optimisation and Application for Foetal Blood Sampling

Benedikt Lübbers

Universitätsverlag Ilmenau
2013

Impressum

Bibliografische Information der Deutschen Nationalbibliothek
Die Deutsche Nationalbibliothek verzeichnet diese Publikation in der Deutschen Nationalbibliografie; detaillierte bibliografische Angaben sind im Internet über http://dnb.d-nb.de abrufbar.

Diese Arbeit hat der Fakultät für Elektrotechnik und Informationstechnik der Technischen Universität Ilmenau als Dissertation vorgelegen.

Tag der Einreichung:	7. April 2011
1. Gutachter:	Univ.-Prof. Dr. rer. nat. habil. Andreas Schober (Technische Universität Ilmenau)
2. Gutachter:	Univ.-Prof. Dr.-Ing. habil. Hannes Töpfer (Technische Universität Ilmenau)
3. Gutachter:	PD Dr.-Ing. habil. Volker Cimalla (Fraunhofer-Institut für Angewandte Festkörperphysik Freiburg)
Tag der Verteidigung:	22. Juni 2012

Technische Universität Ilmenau/Universitätsbibliothek
Universitätsverlag Ilmenau
Postfach 10 05 65
98684 Ilmenau
www.tu-ilmenau.de/universitaetsverlag

Herstellung und Auslieferung
Verlagshaus Monsenstein und Vannerdat OHG
Am Hawerkamp 31
48155 Münster
www.mv-verlag.de

ISBN 978-3-86360-055-6 (Druckausgabe)
URN urn:nbn:de:gbv:ilm1-2012000298

Titelfoto: photocase.com | AlexFlint

We do not know what we measure when we measure pH, but we do know that it is very important.[1]

(Malcom Dole, 1941)

No more; - where
ignorance is bliss,
'Tis folly to be wise.

(Thomas Gray, 1742)

Danksagung

An dieser Stelle möchte ich mich bei allen bedanken, die zur Entstehung dieser Arbeit beigetragen und mich auf vielfältige Art und Weise unterstützt haben.

Allen voran möchte ich mich bei Prof. Oliver Ambacher bedanken, der mich als Doktorand im Fachgebiet Nanotechnologie aufgenommen hat und mir interessante und herausfordernde Aufgaben im Rahmen der Projekte "Pikofluidik" und "GaNano" übertrug. Besonderer Dank gilt auch Dr. Andreas Schober, der meine Betreuung später übernommen hat und mich in der Nachwuchsforschergruppe Mikrofluidik und Biosensorik und dem daraus entstandenen Fachgebiet Nano-Biosystemtechnik aufnahm.

Ein ganz herzlicher Dank geht an meine Mitdoktoranden und Leidensgenossen, die immer Leben in den Alltag am ZMN brachten. Dabei insbesondere Katja Tonisch für das stets offene Ohr und die guten Diskussionen, Florentina Will für die überschwängliche Begeisterung, Katharina Lilienthal für das Mitschreiben und -leiden, Mary Donahue für die Feinheiten der englischen Sprache, Manuel Hofer für die Feinheiten der österreichischen Sprache und Esskultur und Gabriel Kittler für den Staffelstab bei der Sensorentwicklung.

Danke an Volker Cimalla und Jörg Pezoldt für kritisch-konstruktive Gespräche und Meinungen. Mein Dank geht an Thomas Stauden und Michael Fischer für die praktische Laborunterstützung, an Gernot Ecke

für die AES-Messungen und an Dietmar Schäfer für die Erfüllung von Sonderwünschen bei Messaufbauten.

Für die tatkräftige Unterstützung bei der Herstellung der Sensoren danke ich besonders Ilona Marquardt, Karin Friedel, Birgitt Hartmann und Manuela Breiter.

Aus der Nachwuchsforschergruppe und dem Fachgebiet Nano-Biosystemtechnik danke ich Jörg Hampl und Frank Weise für konstruktive Ratschläge und ihren Vorrat an Dichtungen, Schläuchen und Adaptern, Mario Kittler für die programmier- und messtechnische Unterstützung, Uta Fernekorn, Sukhdeep Singh und Michael Gebinoga für die Erweiterung meines chemisch-biologischen Horizonts, Irina Cimalla für die Entwicklung der Passivierung und ganz besonders auch Maren Klett für die Herstellung von so mancher Pufferlösung und die vielen kleinen Tipps für den Laboralltag.

Im Rahmen des MBU-Projektes bedanke ich mich bei Dr. Lydia Seyfarth von der Uniklinik Jena, Peter Kaschlik von der LUCAS GmbH Jena und Dr. Jens Zosel vom KSI Meinsberg für die gute Zusammenarbeit.

Auch bei allen nicht namentlich genannten Mitarbeitern des ZMNs, die mich in der ein oder anderen Weise unterstützt haben, möchte ich mich bedanken. Nicht nur die gläsernen Büros im ZMN und der tolle Ausblick haben dazu beigetragen, dass ich die Arbeitsatmosphäre immer als besonders offen und freundlich empfunden habe.

"Meinen" HiWis und Studenten danke ich dafür, dass sie mir so manche stupide Messaufgabe abgenommen haben. Insbesondere für die Unterstützung von Kristin Schmidt und Patrick Mai möchte ich mich hierbei bedanken.

Mary Donahue, Adam Williams(z)on und Sebastian Lübbers gilt ein besonderer Dank dafür, dass sie diese Arbeit Korrektur gelesen und mir geholfen haben sprachliche Klippen zu umschiffen.

Zu guter Letzt, und an allererster Stelle, geht mein Dank an meine Frau Melanie, die mir stets den Rücken freigehalten hat (damit ich den Kopf frei hatte) und an meine Kinder Melina und Florian, die mich in letzter Zeit viel entbehren mussten (damit der Papa sein Buch schreiben konnte) und mich trotzdem immer freudig begrüßten.

Zusammenfassung

Der pH-Wert ist ein wichtiger Parameter in nahezu allen biochemischen Reaktionen und damit auch für eine Vielzahl von Anwendungsfeldern in der Medizin, Chemie und Umweltüberwachung. Die herkömmliche Bestimmung des pH-Wertes basiert auf der potentiometrischen Messung mit einer Glaselektrode. Manche Anwendungsbereiche können mit der Glaselektrode allerdings nicht oder nur unzureichend erschlossen werden, insbesondere im Hinblick auf kleinste Probenvolumina. Zu diesen Anwendungen gehört die fetale Mikroblutuntersuchung (MBU), die zur Überwachung der Sauerstoffversorgung von Föten während der Geburt eingesetzt wird. Mit herkömmlichen Blutgasanalysatoren kommt es immer wieder zu Schwierigkeiten bei der Messung des pH-Wertes in den geringen Mengen fetalen Blutes (wenige 10 µl), da diese Systeme ein Probenvolumen von mindestens (35–40) µl benötigen. Durch den Einsatz von ionensensitiven Feldeffekttransistoren (ISFET) kann das benötigte Volumen wesentlich reduziert werden. Insbesondere ISFETs auf der Basis von Aluminium-Gallium-Nitrid (AlGaN) und Gallium-Nitrid (GaN) zeichnen sich neben der Miniaturisierbarkeit durch eine hervorragende Sensitivität und eine hohe chemische Stabilität aus. In der vorliegenden Arbeit wurden AlGaN-basierte pH-Sensoren im Hinblick auf die genaue und präzise Bestimmung des pH-Werts untersucht. Auf Basis dieser Sensoren wurde ein Mikro-Blut-pH Analysator

für Probenvolumina von 10 µl entwickelt und realisiert, der die Durchführung der MBU deutlich vereinfacht.

Für die grundlegende Charakterisierung der pH-Sensoren wurden impedanzspektroskopische Methoden auf vereinfachten AlGaN/GaN Metall-Isolator-Heterostrukturen (MIHS) und Elektrolyt-Isolator-Heterostrukturen (EIHS) angewandt. Auf Grundlage der durchgeführten Untersuchungen wurde sowohl ein komplettes als auch ein reduziertes Ersatzschaltbild der Heterostruktur hergeleitet. Für die verwendeten
Konstant-Phasen-Elemente konnte gezeigt werden, dass sie sich gut für die phänomenologische Beschreibung von Defektzuständen im Halbleiter eignen. Außerdem zeigten die Ergebnisse, dass das standardmäßig verwendete eindimensionale Model nicht anwendbar ist, da die AlGaN/GaN Heterostruktur eine zweidimensionale Verarmungscharakteristik ihres leitfähigen Kanals, des zweidimensionalen Elektronengases (2DEG), aufweist. Diese Verarmungscharakteristik hat einen ausgeprägten Einfluss sowohl auf die elektrischen als auch auf die sensorischen Eigenschaften des EIHS-Sensors.

Um genaue und wiederholbare pH-Messungen zu ermöglichen, wurden Drifteinflüsse und die Querempfindlichkeit charakterisiert sowie die pH-Sensitivität der Sensoren bestimmt. Dazu wurden Impedanz-Spannungs-Profile von EIHS Sensoren aufgenommen. Neben der lichtinduzierten Drift durch persistente Photoleitung, konnte auch eine langsame elektrochemische Korrosion des Sensors nachgewiesen werden. Für die Bestimmung der pH-Sensitivität wurden drei verschiedene Auswertungsmethoden evaluiert. Die Auswertung über den Wendepunkt des Kapazitäts-Spannungs-Profils erwies sich als besonders geeignet. Eine spezifische Querempfindlichkeit gegenüber der Ionenstärke konnte nicht nachgewiesen werden.

Für die Reduzierung der lichtinduzierten Drift wurde die kontinuierliche Beleuchtung des EIHS-Sensors untersucht. Es wurde festgestellt, dass violettes Licht ungeeignet ist, da es eine ausgeprägte photoelektrochemische Korrosion hervorruft. Durch die Charakterisierung des stark korrodierten EIHS Sensors konnten allerdings weitere Einblicke in die elektrischen und sensorischen Eigenschaften der AlGaN/GaN Heterostruktur gewonnen werden. Eine deutliche Verkürzung der lichtinduzierten Drift konnte für rotes Licht nachgewiesen werden, ohne das eine Verstärkung der Korrosion auftrat. Durch die Vergrößerung der Dicke der GaN-Deckschicht auf 10 nm und die Reduzierung des Aluminiumgehalts in der AlGaN Barriereschicht auf 20% konnte die Korrosionbeständigkeit der Sensoren erhöht werden. Dabei wurde ein direkter Zusammenhang zwischen der Versetzungdichte an der Sensoroberfläche und der Größe der Korrosionsdrift entdeckt. Die pH-Sensitivität wurde im Allgemeinen nicht durch die Optimierungschritte beeinflusst. Nur bei der Optimierung der Heterostruktur wurde eine verringerte Sensitivität der Flächenladungsträgerdichte im 2DEG beobachtet.

Die Messung des pH-Wertes mit AlGaN-EIHS und ISFET Sensoren zeigte, dass eine Genauigkeit von ± 0.03pH für verschiedenste wässrige Lösungen sowie für Nabelschnurblut erreicht werden kann. Es wurde festgestellt, dass kontrollierte Umgebungsbedingungen ein besonders wichtiges Kriterium für eine hohe Messgenauigkeit sind.

Die erzielten Ergebnisse flossen in die Entwicklung eines Mikro-Blut-pH Analysators ein. Dadurch konnte ein Funktionsmuster erfolgreich realisiert werden, das ein Probenvolumen von nur 10 µl benötigt. Anhand der statistischen Auswertung von Messreihen mit Nabelschnurblut wurde nachgewiesen, dass das Funktionsmuster die Genauigkeits- und Präzisionsanforderungen der Richtlinie der Bundesärtzekammer erfüllt.

Im Rahmen dieser Arbeit konnte erstmalig gezeigt werden, dass AlGaN-basierte pH-Sensoren für die genaue und präzise Bestimmung des pH-Wertes in komplexen biochemischen Flüssigkeiten wie z.B. Nabelschnurblut geeignet sind. Dadurch können spezielle medizintechnische Anwendungsfelder erschlossen werden, die mit herkömmlichen pH-Sensoren nur unzureichend abgedeckt werden.

Abstract

The pH-value is an important parameter for nearly all biochemical reactions and thereby also for a multitude of application fields such as medicine, chemistry or environmental monitoring. The common method for the determination of pH-value is potentiometric measurement with a glass electrode. However, in some application fields the glass electrode cannot be employed or it is subject to certain limitations, especially with regard to very small sample volumes. One of those applications is foetal blood sampling (FBS), which is used for the monitoring of foetal oxygen supply during birth. The measurement of pH-value with common blood gas analysers is frequently complicated by the very small amounts of foetal blood (a few 10 µl) obtained from FBS, as these systems require a minimum volume of (35–40) µl. With the use of ion-sensitive field-effect transistors (ISFETs) the required volume can be reduced significantly. In particular, ISFETs based on aluminium-gallium-nitride (AlGaN) and gallium-nitride (GaN) exhibit excellent sensitivity and a high chemical stability, in addition to the miniaturisation potential. In this work, AlGaN-based pH-sensors are investigated with regard to the accurate and precise determination of pH-value. Based on these sensors, a micro-blood-pH analyser was developed and realised for sample volumes of 10 µl, which significantly simplifies FBS.

For the fundamental characterisation of the pH-sensors, impedance spectroscopy methods were applied to simplified AlGaN/GaN metal-insulator-heterostructures (MIHS) and electrolyte-insulator-heterostructures (EIHS). Based on the investigations that were carried out, a full and a reduced equivalent circuit for the heterostructure could be derived. The employed constant phase elements were shown to be a suitable phenomenological model of trap states in the semiconductor. Additionally, it was found that the commonly employed one-dimensional model cannot be applied, as the AlGaN/GaN heterostructure exhibits a two-dimensional depletion characteristic of its conducting channel, the two-dimensional electron gas (2DEG). This depletion characteristic has a pronounced impact on the electrical and sensory properties of the EIHS sensor.

In order to render accurate and repeatable pH-measurements possible, the influence of drift effects and the cross-sensitivity were characterised and the pH-sensitivity of the sensors was determined. For that purpose, impedance-voltage profiles of EIHS sensors were recorded. In addition to the light-induced drift due to persistent photoconductivity, a slow electrochemical corrosion of the sensor was detected. For the determination of pH-sensitivity, three different analysis methods were evaluated. The method that employs the inflection point of the capacitance-voltage profile was found to be very well suited. A specific cross-sensitivity to ionic strength was not observed.

For the reduction of light-induced drift, a continuous illumination of the EIHS sensor was investigated. It was found that violet light is unsuitable, as it induces a pronounced photoelectrochemical corrosion process. However, additional insight into the electrical and sensory properties of the AlGaN/GaN heterostructure was gained from the characterisation of the corroded sensor. A significant reduction of

the light-induced drift duration was demonstrated for red light without an amplification of the corrosion process. The corrosion resistance of the senors was increased by increasing the thickness of the GaN cap layer to 10 nm and reducing the aluminium-content of the AlGaN barrier layer to 20%. It was discovered that the dislocation density at the sensor surface is directly proportional to the magnitude of the corrosion drift. The pH-sensitivity was not influenced by the optimisation steps, with the exception of a reduced sensitivity of the 2DEG sheet carrier density, which was observed for the optimisation of the heterostructure itself.

The measurement of pH-value with AlGaN-EIHS and ISFET sensors revealed that an accuracy of ± 0.03pH can be achieved for several different aqueous solutions as well as umbilical cord blood. It was found that controlled ambient conditions are especially important in order to obtain high measurement accuracy.

The obtained results contributed to the development of a micro-blood-pH analyser. A prototype was successfully realised that requires a sample volume of only 10 µl. Statistical analysis of small measurement series of umbilical blood was performed to verify that the prototype satisfies the accuracy and precision requirements of the German Medical Association guidelines.

In this work it was demonstrated for the first time that AlGaN-based pH-sensors are well suited for the accurate and precise determination of pH-value. Thereby, special application fields of medical engineering are opened up that are covered inadequately by common pH-sensors.

Contents

Symbols and Abbreviations

$[B]$	net number of charged surface groups
α	CPE exponent
α_s	ISFET sensitivity parameter
α_{em}	electromotive efficiency
β	stretching exponent of PPC decay
β_{int}	intrinsic buffer capacity
ΔpK	difference of dissociation constants of surface hydroxyl groups (logarithmic)
$\Delta_r G$	difference of the Gibbs energies of products and reactants
δ_r	relative inaccuracy
ϵ_0	permittivity of free space ($8.85 \times 10^{-12}\,\mathrm{A\,s\,V^{-1}\,m^{-1}}$)
ϵ_r	relative permittivity
η	cell polarisation
κ	conductivity
κ_e	electrolytic conductivity
λ	electromagnetic wavelength
λ_D	Debye length
Λ_m	molar conductivity
μ	electron mobility
ϕ	phase angle of the complex impedance
Φ_0	surface potential

Φ_e ..... potential in the electrolyte solution
Φ_{OHP} ..... potential at the OHP
σ_0 ..... surface charge density
σ_P ..... polarization-induced charge density
σ_{2DEG} ..... 2DEG charge density
σ_{CI} ..... charge density of counter ions
σ_{EDL} ..... EDL charge density
σ_{MI} ..... charge density of mobile ions
τ ..... time constant of the PPC decay
τ_t ..... time constant of trap states
$\underline{Z}$ ..... complex impedance
a ..... activity
a' ..... activity of surface groups
A_{sc} ..... area of Schottky contact
$B_{10}^{20}C_{10}$ ..... heterostructure with 10 nm $Al_{0.2}Ga_{0.8}N$ / 10 nm GaN
$B_{10}^{30}C_{10}$ ..... heterostructure with 10 nm $Al_{0.3}Ga_{0.7}N$ / 10 nm GaN
$B_{10}^{30}C_2$ ..... heterostructure with 10 nm $Al_{0.3}Ga_{0.7}N$ / 2 nm GaN
C ..... equivalent capacitance
c ..... concentration
c' ..... concentration of surface groups
C_0' ..... zero bias equivalent capacitance per area
C_t' ..... equivalent trapping capacitance per area
c_v ..... coefficient of variation
C_{dif} ..... differential capacitance
c_{RMSD} ..... coefficient of the root mean square deviation
CPE_b ..... equivalent insulator (cap and barrier layer) CPE
CPE_t ..... equivalent trapping CPE
d_0 ..... insulator thickness
D_{it} ..... density of interface traps

E^N ..... Nernst potential
F ..... faraday constant ($96\,485.3\,\mathrm{C\,mol^{-1}}$)
f ..... activity coefficient
f_{ac} ..... ac frequency
$F_{b,AlGaN}$ ..... electric field in the AlGaN barrier layer
G ..... equivalent conductance
G ..... equivalent conductance
G_0 ..... zero bias equivalent conductance
I ..... dc leakage current
I ..... ionic strength
I_d ..... drain current
J ..... DC leakage current density
K_+, K_- ..... dissociation constants of surface hydroxyl groups
K_a ..... acid dissociation constant
L ..... gate length
N_A ..... Avogadro constant ($6.02 \times 10^{23}\,\mathrm{mol^{-1}}$)
N_s ..... total 2DEG sheet charge density
n_s ..... 2DEG sheet charge density
N_t ..... total sheet charge density lost to trap states
N_{s_i} ..... total sheet charge density in the inner 2DEG
N_{s_o} ..... total sheet charge density in the outer 2DEG
N_{ss} ..... total density of available surface sites
P_{PE} ..... piezoelectric polarization
P_{SP} ..... spontaneous polarization
pH_B ..... bulk pH-value
pH_S ..... surface pH-value
pH_{PZC} ..... pH-value at point of zero charge
pK_+, pK_- ... dissociation constants of surface hydroxyl groups (logarithmic)

pK_a ..... acid dissociation constant (logarithmic)
q ..... elementary charge
R ..... equivalent resistance
R ..... gas constant ($8.314\,\mathrm{J\,mol^{-1}\,K^{-1}}$)
R_b/G_b ..... equivalent insulator (cap and barrier layer) resistance or conductance
R_s/G_s ..... equivalent series resistance or conductance
R_{2DEG}/G_{2DEG} equivalent 2DEG resistance or conductance
S_{pH} ..... pH-sensitivity
SD ..... standard deviation
T ..... absolute temperature (K)
U_{ac} ..... ac voltage
U_{bias} ..... bias voltage
U_{ds} ..... drain-source voltage
U_{gs} ..... gate-source voltage
U_{th_C} ..... threshold voltage of equivalent capacitance
U_{th_G} ..... threshold voltage of equivalent conductance
U_{th} ..... threshold voltage
W ..... gate width
X_0 ..... measured value of either N_s, U_{th_C} or U_{th_G} during illumination
X_{dark} ..... fitted value of either N_s, U_{th_C} or U_{th_G} in the dark
Z_{im} ..... imaginary part of the complex impedance
Z_{re} ..... real part of the complex impedance
2DEG ..... two-dimensional electron gas
AES ..... Auger electron spectroscopy
AFM ..... atomic force microscopy
BGA ..... blood gas analyser
CC ..... current collapse

Cell-FET .... cell-modified field-effect transistor
CNLS ..... complex non-linear least square
CPE ..... constant phase element
CTG ..... cardiotocography
CV ..... capacitance-voltage
DIW ..... deionised water
DMSO ..... dimethylsulfoxide
DNA-FET ... DNA-modified field-effect transistor
EDL ..... electric double layer
EIHS ..... electrolyte-insulator-heterostructure
emf ..... electromotive force E
EnFET ..... enzyme-modified field-effect transistor
FBS ..... foetal blood sampling
FWHM ..... full width at half maximum
HEMT ..... high electron mobility transistors
iμRE ..... integrated micro reference electrode
IHP ..... inner Helmholtz plane
Immuno-FET immunologically-modified field-effect transistor
ISFET ..... ion-sensitive field-effect transistor
LD ..... laser diode
LED ..... light-emitting diode
M ..... $\mathrm{mol\,L^{-1}}$
MIHS ..... metal-insulator-heterostructure
MIS ..... metal-insulator-semiconductor
MOCVD ..... metal organic chemical vapour deposition
MOSFET .... metal-oxide-semiconductor field-effect transistor
MQW ..... multi quantum-well
OCP ..... open-circuit potential
OHP ..... outer Helmholtz plane

PC ..... polycarbonate
PCB ..... printed circuit board
pcH ..... hydrogen exponential (Wasserstoffexponenten p_H)
PDMS ..... polydimethylsiloxane
PEEK ..... polyether ether ketone
pH ..... negative common logarithm of the hydronium activity
POCT ..... point-of-care-testing
PPC ..... persistent photoconductivity
Q ..... CPE magnitude
QC ..... quality control
QRE ..... quasi-reference electrode
REFET ..... pH-insensitive reference ISFET
RiLiBÄK .... Richtlinie der Bundesärztekammer (guideline of the German Medical Association)
SAW ..... surface acoustic wave
SEM ..... scanning electron microscopy
SMU ..... source-meter unit
SQW ..... single quantum-well
TEGa ..... triethylgallium
TMAl ..... trimethylaluminum
UV ..... ultra-violet

1 Introduction

The pH-value is a crucial parameter in nearly all biochemical reactions, influencing e.g. reaction kinetics in general or enzyme activity in particular. Its measurement in aqueous solutions is a standard procedure in the fields of chemistry, biology or medicine as well as environmental or production monitoring. The most common measurement method is potentiometry with a glass electrode, which was developed more than 100 years ago [2] and is widely accepted as the gold standard. An alternative method employs the ion-sensitive field effect transistor (ISFET) that was first described by Bergveld in the 1970s [3]. This semiconductor based device has several advantages compared to the glass electrode, but cannot yet compete in terms of commercial success. The main advantages, miniaturisation and ruggedness, have only been exploited for very few niche applications, e.g. in the food industry where the breakage of glass is unacceptable. Presently, no commercial analysis systems that employ ISFETs are available, although several innovative and miniaturised concepts can be found in the research literature [4].

A special application challenge that can benefit from the miniaturisation advantage of the ISFET is the analysis of the foetal blood pH-value during birth. This method is called foetal blood sampling (FBS) or foetal blood analysis and was introduced by Saling in 1961 [5]. It is widely employed as a foetal monitoring technique in addition to the non-invasive cardiotocography (CTG), which records the foetal heart

rate and uterine contractions. When an abnormal heart rate is observed in the CTG, the FBS makes it possible to identify if the foetus suffers from asphyxia and an instrumental delivery is necessary, e.g. by Caesarean section. Recent studies show that FBS reduces foetal morbidity, as a result of fewer Caesarean sections and transfers to the neonatal intensive care unit [6]. The importance of FBS is also stressed by the statistical data from the "Bundesgeschäftsstelle Qualitätssicherung gGmbH" (federal agency for quality assurance) in Germany, which lists the FBS as a quality indicator for obstetrics [7]. In 2007, for instance, FBS was performed for about a quarter (26,265) of all singleton pregnancies with a pathological CTG (111,042). This amounts to 4% of all singleton pregnancies (647,394).

The difficulty of FBS is that only very small blood samples, in the range of a few 10 µl, can be obtained and air bubbles can become trapped in the sampling capillary. Additionally, the coagulation of the foetal blood is much faster, requiring immediate analysis. Currently, this analysis is performed using commercial blood gas analysers (BGA) that require a sample volume of at least (35–40) µl. This, rather large, minimum volume and the fact that the BGAs, due to their size, are not optimised for point-of-care-testing (POCT) in the delivery room are severe challenges for FBS. A portable analysis system with a minimum sample volume of 10 µl or less would be needed to facilitate its routine application. Additional application fields include the neonatal care of premature infants, where blood sampling can also be difficult. Such a system has a market potential of 2.5 to 3 million euro revenue, considering that about 500 of the larger hospitals in Germany (from a total of 2084 hospitals in 2009 [8]) are interested in a portable analysis system with a price tag of 5000-6000 euro [9].

The pH-ISFET is very suitable for the realisation of a micro-blood-pH analyser, as it is easily miniaturised. Compared to the glass electrode, the sensing area of the pH-ISFET is much smaller and no longer a critical design parameter. In conjunction with an appropriate miniaturised reference electrode a sample volume of less than 10 µl is possible. This shifts the focus from miniaturisation to measurement accuracy and precision, which then become the crucial parameters of such an ISFET-based system. In Germany, the required accuracy and precision is specified by the "Richtlinie der Bundesärztekammer (RiLiBÄK)" (guideline of the German Medical Association) [10]. For the determination of pH-value an accuracy of 0.8% and a precision of 0.4% is mandatory, which corresponds to 0.06pH and 0.03pH for a pH-value of 7.25. In order to fulfil these requirements a very stable and sensitive pH-sensor is needed.

A new type of ISFET based on an AlGaN/GaN heterostructure has first been described by Steinhoff et al. in 2003 [11]. The superior chemical stability, biocompatibility and sensitivity reported for these devices [12, 13, 14] make them ideal candidates for pH-measurements in biochemical fluids such as blood or cell medium. Recent research efforts are mostly focussed on the functionalisation with biomolecules or cells for the construction of biosensors [15]. In the few publications that report on the basic pH-response, it was shown that the pH-sensitivity is approximately linear in a pH-range from 2 to 12 [11, 16], when small pH-steps are performed ($\Delta\text{pH} < 0.5$). In contrast, insufficient linearity and stability was revealed by investigations in our research group for large pH-steps ($\Delta\text{pH} > 2$). Values between 40 and 60 $\text{mV}\,\text{pH}^{-1}$ have been found, depending on the growth method and the sensor geometry [17]. Additionally, a drawn-out drift was observed when the pH-value was changed from neutral (pH7) to alkaline (pH10) [16]. Investigations by Kang et al. also confirm an unstable and drifting pH-sensitivity [18].

As a result of these effects, the reproducibility of pH-measurements was found to be no better than ±0.2pH in preliminary studies [19]. Although the miniaturisation potential of the ISFET is beneficial for very small sample volumes, the encapsulation and passiviation of the electric contact becomes more difficult. Presently, the long-term stability of the passivation layer is still unsatisfactory and may well be one of the reasons for the observed variations of pH-sensitivity and the drift behaviour.

This thesis is aimed at the construction of a micro-blood-pH analyser that satisfies the requirements of the RiLiBÄK, employing AlGaN-based pH-ISFETs. In order to achieve this goal the following steps are performed:

- Simplification of the AlGaN-ISFET to its basic sensing and transducing element, the electrolyte-insulator-heterostructure (EIHS),
- Establishment of electrochemical impedance spectroscopy and electrochemical impedance-voltage profiling of AlGaN-based EIHS sensor chips as a suitable characterisation method,
- Fundamental characterisation of AlGaN-based pH-sensors, with regard to effects that limit the measurement accuracy and precision, and
- Optimisation of the ambient measurement conditions and the heterostructure for accurate and precise pH-measurements.

One of the advantages of the simplification to the AlGaN-EIHS is that the problematic passivation layer can be replaced by a suitable sealing ring. In addition, far more information on the electrical and structural properties of the AlGaN/GaN heterostructure can be obtained from impedance spectroscopy and impedance-voltage profiling.

The thesis is structured into the four main parts: theory and state of the art (chapters 2 to 4), impedance characterisation (chapters 6 and 7), optimisation (chapter 8) and application (chapter 9). In chapter 2 selected electrochemical fundamentals are explained with special emphasis on electrolyte solutions and pH-value. A brief overview of the different methods for pH-measurement and the glass electrode is given in chapter 3, followed by a discussion of the theory, properties, instrumentation and applications of Si-based ISFETs. The reference electrode, as a mandatory element of the measuring chain, and its miniaturisation is also described here. Chapter 4 is dedicated to the AlGaN/GaN heterostructure with its two-dimensional electron gas (2DEG) and summarises the applications as a fluid sensor which have been reported in literature. The experimental results are presented and discussed in the following chapters. After a description of the employed materials and methods (chapter 5), the characterisation of the AlGaN/GaN heterostructure with a reversible mercury probe on whole wafers using impedance spectroscopy is presented in chapter 6. Suitable equivalent circuits are derived and applied to basic impedance-voltage profiling. Subsequently, impedance characterisation is performed on EIHS sensor chips in an electrochemical measurement cell. These electrochemical impedance measurements are taken as a basis for the following characterisation of drift behaviour, pH- and cross-sensitivity in chapter 7. Potential optimisation approaches are identified and their application to ambient measurement conditions and the heterostructure layout is presented and discussed in chapter 8. The construction of a micro-blood-pH analyser with AlGaN-based pH-ISFETs that realises a minimum sample volume of 10 µl is described in the following chapter 9. The results of pH-measurements of simple buffer solutions, commercial quality control (QC) solutions and umbilical cord blood in this analyser

setup are discussed, with regard to accuracy and precision. Chapter 10 summarises the results that were obtained in this thesis and looks at possible further research work.

2 Theoretic Principles

In this chapter the electrochemical concepts and terms that are used in this thesis are described and the basic definitions of acids and bases as well as pH-value are presented. In addition, the concept and relevance of buffer solutions is given.

2.1 Electrochemical Fundamentals

The definitions and terms described in this section were taken from the monographs of Moore et al. [20] and Atkins et al. [21].

Electrolyte Solutions

Aqueous solutions account for nearly all samples that are analysed in medical and pharmaceutical laboratories. In particular, all biological and many chemical systems are aqueous solutions that contain various sorts of ions and are termed electrolyte solutions. Their composition is of great importance, as the concentration and type of ions has a strong impact on these systems, e.g. by influencing (bio-)chemical reaction rates or the stability of biomolecules.

Throughout this work molarity will be used to express the concentration of the solutions. It is defined as the number of moles of a solute dissolved in 1 litre of solution and has the dimension of $1\,\mathrm{mol\,L^{-1}} = 1\,\mathrm{M}$.

As the employed solvent is always water, the concepts of molarity and molality (number of moles dissolved in 1 kg of solution) are nearly interchangeable. Therefore, molarity will be used even when the correct definitions of some terms are based on molality.

Electrolyte solutions are created by dissolving an electrolyte in a solvent (commonly water). The electrolyte can be an acid, a base or a salt, which can dissociate into mobile charged ions or molecules. Therefore, electrolyte solutions conduct electricity by ionic conductance, which is defined analogously to the known electronic conductance G as:

$$G = \frac{1}{R} = \kappa_e \frac{A}{l}, \tag{2.1}$$

where κ_e is the electrolytic conductivity and the ratio $\frac{l}{A}$ is termed the cell constant. For a given setup this constant is usually derived from the measured conductance of an electrolyte solution with a known value of κ_e. The electrolytic conductivity κ_e is primarily determined by the concentration of ions in the electrolyte solution. In order to compare the conductance at equal electrolyte concentrations the specific conductance κ_e is divided by the molar concentration to give the molar conductivity Λ_m:

$$\Lambda_m = \frac{(1000\,\mathrm{cm^3 L^{-1}})\kappa_e}{c}, \tag{2.2}$$

with the electrolyte concentration c. Although this equation might suggest that Λ_m is independent of the concentration, this is not the case. A deviation due to the interionic interaction becomes more pronounced with increasing electrolyte concentration. Plots of Λ_m versus $\sqrt{c}$ for specific electrolytes can for example be found in [20]. The concepts of ionic activity and ionic strength were introduced to account for the

observed deviation. Only in dilute solutions ($c < 0.1\,\mathrm{M}$) is the concentration as defined above effective for chemical reactions and therefore measurable. At higher values the interaction between the ions results in the reduction of the apparent concentration. This effective concentration is termed ionic activity a and can be calculated by the product of the concentration c and the activity coefficient f:

$$a = c \cdot f. \tag{2.3}$$

The activity coefficient f approaches unity at infinite dilution and in itself is dependent on c through the ionic strength I.

The term ionic strength is a net concentration measure that accounts for interionic interactions and encompasses all dissolved ionic charges in a given electrolyte solution. It is calculated as

$$I = \frac{1}{2} \sum_{i=1}^{n} c_i z_i^2, \tag{2.4}$$

where c_i and z_i are the molar concentration and valence of each ion, respectively. For a 1:1 (monovalent) electrolyte like NaCl, the molarity equals the ionic strength. For electrolytes with higher valence, the ionic strength is a multiple of the molarity, e.g. $I = 3c$ for $CaCl_2$. Apart from the calculation of the activity coefficient, the concept of ionic strength is used for example in the description of the electric double layer (EDL). From the preceding discussion it can also be derived that the conductance of the electrolyte solution is determined by the ionic strength.

Electrodes

To measure the chemical properties of electrolyte solutions by means of electronic equipment a transducing element is needed to mediate between the ionic and the electronic realm. This element is called an electrode and, in its simplest form, consists of a piece of metal which is immersed in an electrolyte solution. The reaction at the surface of the electrode is always a transfer of charge in one way or another. It usually takes place in the form of a redox reaction in a broader sense: electrons are transferred from the electrode to ions or molecules in the solution (reduction at an anode) or the other way around (oxidation at a cathode). The combination of an electrode and an electrolyte solution is called a half-cell, when the dissolved ions are in an electrochemical equilibrium with the electrode.

Immersing a metal (e.g. Ag) in a solution containing the corresponding metal ions (e.g. $AgNO_3$) is one way to achieve this equilibrium. This type of electrode is called a metal (or metal/metal ion) electrode with the following electrode reaction:

$$\mathrm{M} \rightleftharpoons \mathrm{M}^+ + \mathrm{e}^-.$$

The cell diagram for this half-cell is given by:

$$\mathrm{M}|\mathrm{M}^+(c),$$

in which the single vertical line represents the phase boundary between the electrode and the solution and c is the concentration of metal ions. A comma is used to separate the different ions in the same phase and a double vertical line represents a salt bridge in complete electrochemical cells.

A second type of electrodes are gas electrodes which are created by a gas (e.g. H_2) flowing past an inert metal (e.g. Pt). The metal acts as a catalyst for the decomposition of the molecular gas and as an electronic conductor. As the gas is much less noble than the metal, the electrode can be treated as being made up of a "metallic gas".

The standard hydrogen electrode, represented by:

$$\mathrm{H_2} \rightleftharpoons 2\,\mathrm{H^+} + 2\,\mathrm{e^-}$$
$$\mathrm{Pt|H_2|H^+}(c),$$

is the most common gas electrode which reacts with the hydrogen ions H^+ in the solution and can therefore be used to determine their concentration.

Redox electrodes are formed when dissolved ions with two different oxidation states (different from zero) are involved in the electrode reaction at a noble metal. In these types of electrodes only electrons pass through the phase boundary and no electrode material is transferred. An example of this kind of electrode is the iron(II)-iron(III)-electrode given by:

$$\mathrm{Fe^{2+}} \rightleftharpoons \mathrm{Fe^{3+}} + \mathrm{e^-}$$
$$\mathrm{Pt|Fe^{2+}}(c_1), \mathrm{Fe^{3+}}(\mathrm{c_2}).$$

An insoluble salt (or metal/insoluble salt) electrode is created when a piece of metal is coated with a corresponding insoluble salt and immersed into a solution containing the anion of the salt. The most com-

mon electrode of this type is the silver/silver chloride electrode with the following electrode reaction and cell diagram:

$$\mathrm{AgCl} + \mathrm{e}^- \rightleftharpoons \mathrm{Ag} + \mathrm{Cl}^-$$
$$\mathrm{Ag}|\mathrm{AgCl}|\mathrm{Cl}^-(c).$$

The insoluble metal electrode is used for the construction of reference electrodes to achieve stable electrode potentials.

Electrochemical cell

An electrochemical cell is formed when two electrodes are immersed in a common electrolyte solution or into different electrolyte solutions that are connected via a suitable ionic conductor, for example a salt bridge. By this connection of two half cells the electrode potential difference can be measured - the electrode potential of a single half cell cannot be measured in any way. Establishing a metallic connection between the electrodes gives a galvanic cell, in which chemical free energy is converted into electrical free energy, i.e., a potential can be measured. In an electrolytic cell electrical, free energy is converted into chemical free energy, i.e., a potential can be applied to drive a chemical reaction. The relation between electrical free energy and chemical free energy is given as:

$$\Delta_r G = -\nu F E, \tag{2.5}$$

with the Faraday constant F, the stoichiometric coefficient ν and assuming constant temperature and pressure. The electrical free energy corresponds to the electrical potential difference between the electrodes and is also called the electromotive force (emf) E of the electrochemical

cell. The chemical free energy is given by the difference of the Gibbs energies of the products and the reactants $\Delta_r G$.

As a negative value of $\Delta_r G$ corresponds to a spontaneous reaction, a positive value of E is obtained for a galvanic cell whereas a negative E is obtained for an electrolytic cell. The emf can be measured by a high impedance voltmeter connected to the electrodes. As no appreciable current will flow through the electrodes in this case, the measured voltage is also called the open-circuit or rest potential (OCP) of the cell. The potential difference that is measured when the current is not negligibly small is commonly termed the polarisation η of the cell. It is made up of the cell's emf and several overpotential terms due to the current flow. When no junctions, such as a salt bridge, are present in the cell and the reaction is based on a redox couple, the open-circuit potential is equal to the equilibrium potential. This potential can be calculated from thermodynamic data via the Nernst equation. The free enthalpy of a general cell reaction $\mathrm{aA} + \mathrm{bB} \rightleftharpoons \mathrm{cC} + \mathrm{dD}$ is calculated as:

$$\Delta_r G = \Delta_r G^0 + RT \ln \frac{a_C^c \cdot a_D^d}{a_A^a \cdot a_B^b}, \tag{2.6}$$

where R is the gas constant, T is the temperature and a_X^x denotes the activity of agent X with valence x. Applying equation 2.5 to 2.6 the Nernst equation is obtained:

$$E = E^0 + \ln 10 \frac{RT}{\nu F} \log \frac{a_C^c \cdot a_D^d}{a_A^a \cdot a_B^b}. \tag{2.7}$$

The term E^0 is called the standard emf of the cell and is obtained when the activities of the reactants and products are unity. It should be noted that this equation is valid only for constant pressure and temperature.

For $T = 298\,\mathrm{K}$ and $\nu = 1$, the term $ln(10)\frac{RT}{\nu F}$ can be evaluated to give $59.2\,\mathrm{mV}$ and is called the Nernst potential or the "Nernstian" slope E^N. This potential is the theoretical thermodynamic limit that can be achieved for the given cell reaction.

Electrical Double Layer

The charge and potential distribution at the solid/liquid interface can be divided into three sections: the solid, a fixed and a diffuse charge layer in the liquid. For this work it is assumed that the solid consists of an insulator on top of a semiconductor and the liquid is an aqueous electrolyte solution. The fixed charge layer is called the Helmholtz or Stern double layer and the diffuse layer is termed the Gouy-Chapman layer. The combination of both layers is referred to as the Gouy-Chapman-Stern model. In Fig. 2.1 the schematic ion, charge and potential distribution at the interface and in the liquid is illustrated for a positive surface charge σ_0. In accordance with Siu and Cobbold [22] and Bousse et al. [23] this surface charge is assumed to belong to the immediate interface rather than be located at the inner Helmholtz plane (IHP). The origin of the specifically adsorbed surface charge for a metal oxide insulator and the charge and potential distribution in the solid will be discussed in sections 3.3.1 and 4.2, respectively.

As a result of charge neutrality the positive charge at the interface must be balanced by a negative charge either from the liquid or the solid. As no free charge carriers are available in the insulator, no balancing from the solid side is possible in the direct vicinity of the interface. From the electrolyte solution this can be achieved in three different ways. Firstly, via binding of counter ions from the electrolyte to the specifically adsorbed ions at the IHP (σ_{CI}). Secondly, via mobile

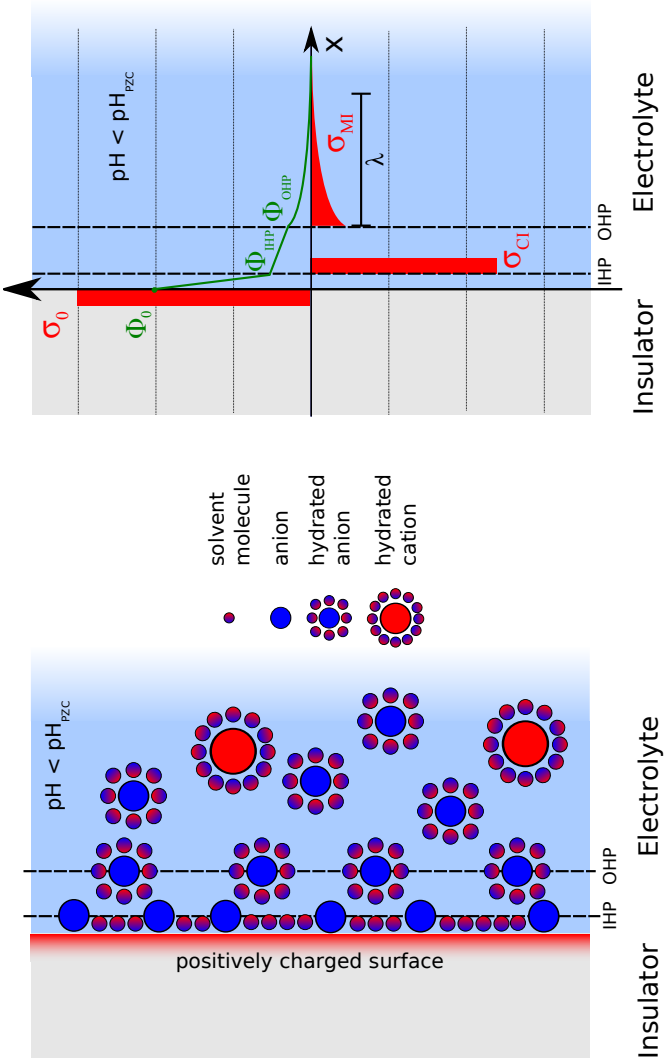

Figure 2.1: Ion, charge and potential distribution in the electrical double layer for acidic solution with low ionic strength.

hydrated ions attracted by electrostatic forces to the plane of closest approach (outer Helmholtz plane - OHP) and thirdly via ions from the electrolyte that contribute to a diffuse region of charge (σ_{MI}). The charge in the Gouy-Chapman layer can be calculated by applying the Boltzmann relation to the mobile ions and inserting this into Poisson's equation. For a monovalent electrolyte such as NaCl this gives:

$$\sigma_{MI} = -(8kT\epsilon_r\epsilon_0 I N_A)^{\frac{1}{2}} sinh(\frac{q(\Phi_{OHP} - \Phi_e)}{2kT}), \tag{2.8}$$

where ϵ_0 and ϵ_r are the permittivity of free space and the relative permittivity, respectively, I is the ionic strength and N_A is Avogadro constant. From this equation it can be seen that the charge in the Gouy-Chapman layer strongly depends on the potential difference between the OHP (Φ_{OHP}) and the electrolyte (Φ_e) and also on the ionic strength. The extent of this diffuse layer is characterised by its Debye length λ_D, which is inversely proportional to the square root of the ionic strength in the bulk solution I:

$$\lambda_D = \sqrt{\frac{\epsilon\epsilon_0 RT}{F^2 I}} \approx \frac{0.304}{\sqrt{I}} \frac{nm}{M}, \tag{2.9}$$

for I given in M. At high ionic strengths ($I > 100\,\mathrm{mM}$) the Debye length falls below 1 nm, i.e. the Gouy-Chapman layer is effectively concentrated at the OHP and can therefore be neglected. In dilute solutions ($I < 1\,\mathrm{mM}$) the Gouy-Chapman layer exceeds 10 nm and has to be taken into account. Especially when the ionic strength is varied over several decades, the influence on the Gouy-Chapman layer becomes important.

The charges at the OHP and IHP can be derived using a parallel plate capacitor approximation and primarily depend on the adsorbed charges and counter charges as well as the ionic strength. The counter ion binding takes place at the IHP and partly balances the surface charge σ_0 through ions of opposite charge. For simplicity, the planes for counter cations and anions are assumed to coincide. It should be noted that counter ion binding can only take place when the counter ions have stripped off their hydration sheath to approach the IHP. Therefore, the electrostatic potential Φ_0 has to be sufficiently high to overcome the solvation energy of the counter ions. When the surface charge is shielded to the extent that Φ_{IHP} is no longer able to overcome the solvation energy, the remaining charge $\sigma_0 - \sigma_{CI}$ is balanced at the OHP and in the Gouy-Chapman layer.

2.2 pH-Value and Buffer Solutions

In this section the primary measurement quantity of this work, the pH-value, is introduced. The fundamental concepts of acids and bases, the definition of the pH-value itself and ways to stabilise the pH-value in solutions through buffer systems are discussed. The monographs of Schwabe [24] and Galster [25] were consulted for this section.

Acids and Bases

A special and important class of electrolytes is formed by acids and bases. Their equilibrium is one of the most widespread and critical parameters in chemical and biological systems. Therefore, many theories have been proposed to describe the phenomenon in the most general and comprehensive way, starting with Arrhenius at the end of the 19th

century [26]. His concept defined acids as substances that produce hydrogen ions and bases as substances that produce hydroxide ions upon dissociation in aqueous solutions. In 1923 Brønsted [27] and Lowry [28] proposed independently that the Arrhenius theory should be expanded to include non-aqueous solutions by defining acids and bases as substances the can donate or accept protons, respectively:

$$\text{acid} \rightleftharpoons \text{proton} + \text{base}. \tag{2.10}$$

A more general definition was also introduced in the same year by Lewis to include reactions in which no hydrogen ions participate. In his concept acids can accept and bases can donate electron pairs. However, the Brønsted-Lowry theory is the most widely used definition and will also be adopted for this work.

The strength of an acid or base is given by their degree of dissociation in solutions. Strong acids (e.g. HCl) dissociate completely, whereas weak acids (e.g. acetic acid (CH_3COOH)) are only partly dissociated. The dissociation of an acid is represented by:

$$HA + H_2O \rightleftharpoons H_3O^+ + A^-, \tag{2.11}$$

and the equilibrium or dissociation constant of this reaction can be calculated as:

$$K_a = \frac{a_{H_3O^+} a_{A^-}}{a_{HA} a_{H_2O}}. \tag{2.12}$$

For sufficiently low ion concentrations the activity of H_2O can be approximated as 1. The other activities can be identified by their con-

centration and the concentration of H_3O^+ is replaced by H^+ for the sake of simplicity, giving:

$$K_a = \frac{[H^+][A^-]}{[HA]}. \tag{2.13}$$

To facilitate the handling of these values they are commonly represented on a logarithmic scale:

$$pK_a = -\log(K_a). \tag{2.14}$$

From equation 2.13 and 2.14 it can be derived that a strong acid corresponds to a K_a close to one (or a small pK_a) and a weak acid to a small K_a (or a high pK_a). In table 2.1 the dissociation constants of several acids are given. The dissociation constant of a base pK_b can be derived in a similar way giving:

$$pK_b = -\log(\frac{[BH^+][OH^-]}{[B]}) \tag{2.15}$$

for the reaction:

$$B + H_2O \rightleftharpoons BH^+ + OH^-. \tag{2.16}$$

pH-value

In the early 20th century, it was discovered that the concentration of hydrogen ions is a crucial parameter for all chemical and biochemical reactions due to its involvement as a reactant or as a catalyst [29, 30]. This fact has had an impact not only on academic research in fields that are related to chemistry, but also in various branches of indus-

Table 2.1: Dissociation constants of various acids at 298 K.

acid	K_a	pK_a
HF	7.1×10^{-7}	3.15
H_2CO_3	4.2×10^{-7}	6.38
HCO_3^-	4.8×10^{-11}	10.32
H_3PO_4	7.5×10^{-3}	2.13
$H_2PO_4^-$	6.2×10^{-8}	7.21
HPO_4^{2-}	4.8×10^{-13}	12.32

try, including chemistry, pharmacy, biotechnology or medicine as well as the food, textile and metal industry and environmental monitoring. The first comprehensive overview of the application fields was given by Kratz in the 1950s [31]. The original definition of the "Wasserstoffexponenten p_H" (hydrogen exponential - today commonly: pcH) by Sørensen in 1909 [32] as the negative logarithm of the hydrogen concentration c_{H^+} in (not necessarily aqueous) solutions greatly simplified the handling of the extraordinarily variable values which span several decades:

$$pcH = -\log c_{\mathrm{H}^+}. \tag{2.17}$$

Due to the logarithmic scaling, it has to be treated as a measure for the potency of the hydrogen ions rather than as an accurate quantification of their concentration. However, it was realised that the activity, or effective concentration, of the hydrogen ions rather than their concentration is the measurable and significant quantity for chemical reactions. This is due to the interionic interaction, which becomes more pronounced at higher ion concentrations. In addition, it was discov-

ered that the hydrogen ion itself does not exist in solutions. It can only be found in its hydrated form - the hydronium ion H_3O^+. These observations led to the correction of the original definition to give:

$$pH = -\log \frac{a_{H_3O^+}}{M}, \tag{2.18}$$

where $a_{H_3O^+}$ is the activity of the hydronium ions. Nevertheless, when the interionic interaction and the hydration of hydrogen ions are negligible, the original definition from Sørensen is often adopted. For the sake of simplicity no differentiation between concentration and activity is made in this thesis and the term "hydrogen ion" (H^+) is used where, strictly speaking, "hydronium ion" (H_3O^+) would be the correct term.

Apart from the presented definitions, which are of a theoretical nature and seldom applied to measurements, a practical pH-scale is commonly used for the actual measurement of the pH-value. This definition is closely linked to the standard measurement method - potentiometry. For potentiometric measurements, an electrochemical cell consisting of a pH-sensitive indicator electrode (commonly a glass electrode) and a reference electrode is employed. The pH-scale relates the cell's measured emf E_x of an unknown solution to the emf E_s of a standardized buffer solution. The pH-value pH_s of the buffer solution is determined very accurately, approaches the true paH value and is invariant with time. Then the pH-value pH_x of the unknown solution is given by:

$$pH_x = pH_s - \frac{E_x - E_s}{\frac{ln(10)RT}{F}}, \tag{2.19}$$

assuming that the indicator electrode exhibits an ideal "Nernstian" response $\frac{ln(10)RT}{F}$. This approach corresponds to a one-point calibration.

A more general approach, which can also be applied if the slope of the pH-sensitivity is unknown, employs two standardized buffer solutions (pH_{s1} and pH_{s2}) to calculate the actual slope using the corresponding emf-values (E_{s1} and E_{s2}). The unknown pH-value is then defined as:

$$pH_x = pH_{s1} - \left(\frac{E_x - E_{s1}}{E_{s2} - E_{s1}} \right) (pH_{s2} - pH_{s1}) = pH_{s1} - \frac{E_x - E_{s1}}{S_{pH}}, \quad (2.20)$$

where

$$S_{pH} = \frac{E_{s2} - E_{s1}}{pH_{s2} - pH_{s1}} \quad (2.21)$$

is the slope of the pH-sensitivity in mV/pH. As two buffer solutions are used, this method is also referred to as two-point calibration. If the pH-sensitivity of the employed indicator electrode is not linear, the calibration can be extended to include three or more buffer solutions. In this case, equation 2.20 is applied to those two neighbouring buffer solutions (pH_{sa} and pH_{sb}) where $E_{sa} < E_x < E_{sb}$. Generally, it should be noted that these practical definitions have an inherent uncertainty that is based on the difference of the diffusion potentials in the measurement chain.

Buffer Solutions

The solutions that are employed to perform calibration routines are called standard or buffer solutions. Their foremost purpose is to supply a constant pH-value and withstand changes of pH due to contamination or dilution. This ability is not only required for calibration, but plays an essential role in many chemical and biochemical reactions. The activity of enzymes, for example, is strongly influenced by the pH-

value with a typical optimal value around 7. In more acidic or alkaline environments the activity is reduced through inhibition of the enzyme or the substrate. Another critical and elaborate buffer system can be found in human blood, whose pH needs to be kept at 7.4 ± 0.05. Deviations from this value have severe pathological and potentially fatal consequences.

Typical buffer solutions are a mixture of a weak acid (e.g. KH_2PO_4) with a corresponding salt (e.g. K_2PO_4) and their function can be explained by looking at the dissociation reaction of the acid:

$$\mathrm{HA} \rightleftharpoons \mathrm{H}^+ + \mathrm{A}^-. \tag{2.22}$$

Here, HA is the undissociated weak acid and A^- the salt anion. The dissociation constant is calculated as:

$$K_a = \frac{[H^+][A^-]}{[HA]}. \tag{2.23}$$

Rearranging for $[H^+]$ and applying the common logarithm gives:

$$pH = pK_a + \log \frac{[A^-]}{[HA]}. \tag{2.24}$$

As the acid is only slightly dissociated its concentration is equal to $[HA]$ and as the salt is dissociated completely its concentration is equal to $[A^-]$. When adding a small amount of a strong acid to the buffer, the equilibrium in reaction 2.22 is shifted to the left to produce more undissociated acid $[HA]$, a strong base on the other hand induces a shift to the right to produce salt anions $[A^-]$. Therefore, only the ratio $\frac{[A^-]}{[HA]}$ varies slightly resulting in a small change of pH that can be derived from equation 2.24. Due to the logarithmic dependency the best buffering

capacity is obtained when salt and acid are mixed in equal shares giving a buffer with $pH = pK_a$. To induce a pH change of 1, for example, the ratio $\frac{[A^-]}{[HA]}$ needs to be 0.1 which requires a fair amount of acid or base. The buffering capacity also increases with higher total concentration of the solution. Other important characteristics of buffering solutions include the dilution value $\Delta pH_{\frac{1}{2}}$, which is the change in pH when diluting the buffer by adding an equal share of water, and the temperature coefficient dpH/dT, which expresses the pH change per Kelvin.

3 Methods for the Measurement of pH-Value

In this chapter a brief historical overview of pH-measurement is given followed by a short discussion of the most commonly applied pH-sensor device - the glass electrode. The measurement of pH-value with the Si-based ISFET is described in more detail, as most of the discussed aspects are also applicable to the investigated pH-sensor based on an AlGaN/GaN-heterostructure. The reference electrode, as a mandatory element for every electrochemical measurement of pH-value, is covered at the end of this chapter. Parts of the material presented here have also been published as a more comprehensive review on the glass electrode in comparison to the ISFET [33].

3.1 Historical Development

Methods to monitor the pH-value go back as far as the 16th century when violet extract was used by alchemists as an indicator for acids - effectively a colorimetric approach which is still applied today in the form of universal indicators. Presently, so-called optodes make use of immobilised indicator dyes [34] and have become established in a few niche applications. The measurement of the pH dependent dissociation kinetics of an ester was proposed by Arrhenius in 1889 [35] as another

non-electrochemical method. Although it is obsolete because of its laborious and time-consuming nature, it is still considered a very accurate method especially in non-aqueous environments [24]. The variety of electrochemical approaches for the determination of pH is illustrated in fig. 3.1. They can be divided into electrodes mainly involving an (immobilised) liquid or gas on the left hand side and all-solid-state devices on the right hand side. Their placement from top to bottom represents an approximate timeline of their first use for pH-measurements. The standard hydrogen electrode was used at the beginning of the 20th century by Sørensen and other researchers. This gas electrode ($Pt|H_2|H^+$) is the ideal hydrogen ion selective electrode by theory and was first applied for the measurement of hydrogen ion concentration in 1904 [36]. Today it is obsolete for practical purposes, due to its rather elaborate measuring setup, but it is still a primary standard for the definition of the pH scale. Another method widely used at that time was the organic redox system Chinhydron, a 1:1 mixture of Chinon and Hydrochinon [37]. The redox potential of this electrode (Pt|Chinhydron, H^+) can be utilised in the pH-range between 1 and 8 and currently still has some relevance for measurements in hydrofluoric solutions [25].

Although the glass electrode was developed in 1909, it took another 30 years before it was recognised as a convenient and accurate device for the determination of pH-value and the first commercial ready-made electrodes were available. This was partly due to the lack of appropriate instrumentation for the potentiometric measurements as the glass electrode exhibits very high impedance (several 100 MΩ). With the increased awareness of the importance of pH-value for academic research as well as industrial processes a less complex and time-consuming setup was needed. This is why investigations mainly concerning practical aspects of the glass electrode were conducted between 1920 and

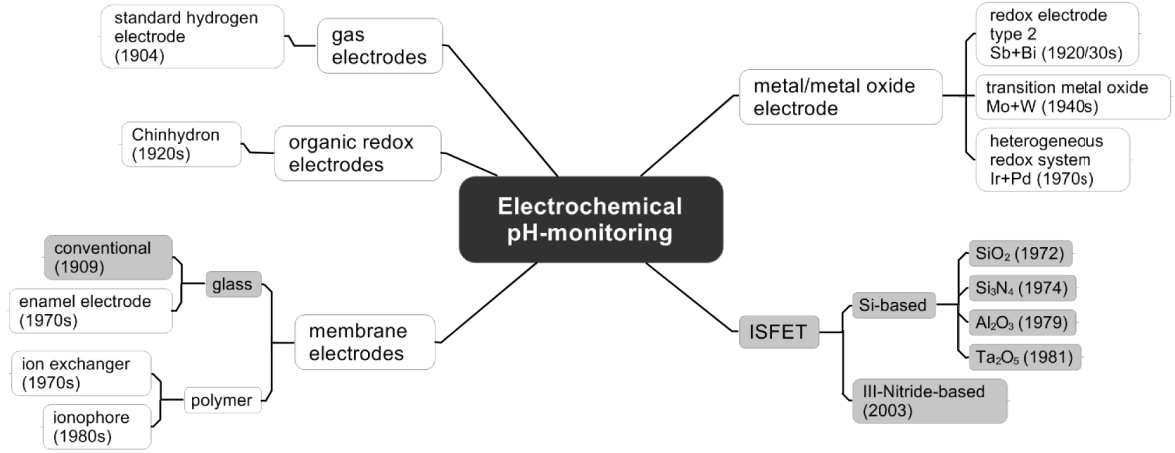

Figure 3.1: Overview of electrochemical methods to determine pH. The methods discussed in this work are highlighted.

1930. This process was further stimulated by the introduction of the MacInnes glass [38] which extended the pH range of glass electrodes and became a standard glass in the following years. The breakthrough came with the development of the vacuum tube in the 1930s and the transistor in the 1950s, resulting in high input impedance voltmeters. As the glass electrode in its conventional form (commonly $Ag|AgCl|Cl^-$, $H^+|$glass membrane$|H^+$) relies on an inner filling solution (typically buffered KCl), attempts to minimise the practical drawbacks of this approach have been made. In the 1970s an all solid-state glass electrode was realised in the form of an enamel electrode [39]. Recent progress on this subject has also resulted in long-term stable pH-sensors with a conducting polymer (e.g. polypyrrole/Nafion®) replacing the inner electrolyte [40]. The replacement of the rather fragile glass membrane by polymer membranes was investigated using cation exchanger membranes [41] as well as membranes doped with ionophores [42].

All-solid-state electrochemical approaches were first realised by metal/metal oxide electrodes, which set themselves apart from the glass electrode by the simplicity and ease of handling. They were therefore intensely studied in the 1920s and 30s (cf. [24]). The antimony electrode ($Sb|Sb(OH)_3$, H^+) [43] relies on hydroxide groups on the surface and resembles a redox electrode of type 2 for hydroxide ions. Its practical pH-range lies between 1 and 10 for temperatures up to 80 °C. Due to its robustness, it is used in harsh environments and hydrofluoric solutions and has additionally found application in microelectrodes for intraoral [44] measurements. The bismuth electrode exhibits similar properties with a measuring range between pH 6 and 14 [45]. Electrodes employing transition metal oxides of tungsten or molybdenum were first reported in 1940 [46] and are based on the change of their oxide valence state corresponding to the pH-value of the solution. Recent research is

also directed at transition metal oxide bronzes [47]. Other metal/metal oxide electrodes include palladium and iridium oxide electrodes (e.g. Pd|PdO, H^+), which are heterogeneous redox systems. With a pH-range of 3 to 10 they are recommended for microelectrodes in medical applications [48]. Ruthenium oxide, screen-printed as a thick film, has also been reported to be a suitable pH electrode [49]. The applicability of further metal oxides has been discussed by Fog [50]. The general drawback of metal/metal oxide electrodes, however, is the relatively pronounced cross sensitivity to oxidising and reducing agents.

The ISFET was originally not intended as a device to measure pH-value. In 1970 Bergveld reported preliminary results of a solid-state device, similar to the metal-oxide-semiconductor field-effect transistor (MOSFET) immersed in an aqueous solution, which was able to measure the activity of sodium ions [3]. Even two years later, when the pH-sensitivity of the ISFET was discovered, it was not seen as an alternative to the glass electrode but firstly as a tool for electrophysiological experiments [51]. The pH-sensitive layer originally used by Bergveld was thermally formed SiO_2. Over the following decade alternative layers like Si_3N_4 [52], Al_2O_3 [53] and Ta_2O_5 [54] were investigated. Much like the glass electrode 60 years earlier, it also took approximately 30 years for the ISFET to be commercialised. In 1994 the review on ISFETs by Janata posed the question: "why have they not yet found a practical application?" [55]; whereas 10 years later Bergveld was able to list some 20 manufactures of ISFETs in his personal historic review [4]. Bergveld's review is also recommended for a more comprehensive historical overview of the development of Si-based ISFETs. The most recent research on alternative material systems has brought forth the group III-Nitrides as promising candidates not only for the now widely available optoelectronic devices [56], but also for sensing applications

[57, 13]. The application of AlGaN transistor devices for the monitoring of pH was first reported in 2003 [11] and there is still considerable interest in these devices due to their favourable material properties.

3.2 Glass Electrode

The design of the conventional glass electrode is illustrated in fig. 3.2. It can be seen that it is a measuring chain in itself consisting of an inner reference electrode (typically Ag/AgCl) immersed in a suitable inner buffer solution (commonly saturated with chloride ions). The glass membrane separates the inner solution from the analyte solution and serves as the actual sensing element of the electrode. The chain is completed by an outer reference electrode that matches the inner one to avoid additional potential differences, giving:

$$Ag|AgCl|\mathrm{Cl}^-, \mathrm{H}^+(\mathrm{a}_{\mathrm{H_3O^+,i}})|glass|\mathrm{H}^+(\mathrm{a}_{\mathrm{H_3O^+,x}})||\mathrm{Cl}^-|AgCl|Ag.$$

The applicability of the glass electrode for pH measurements is based on the phase boundary potential which develops at the glass-solution interface. This potential or emf E_m is nearly exclusively dependent on the hydrogen ion concentration of the solution (within a certain pH range). From thermodynamic considerations the membrane potential is calculated using the Nernst equation, giving:

$$E_m = E^N(pH_i - pH_x), \tag{3.1}$$

where pH_i and pH_x are the pH-values of the inner and outer (unknown) solution, respectively.

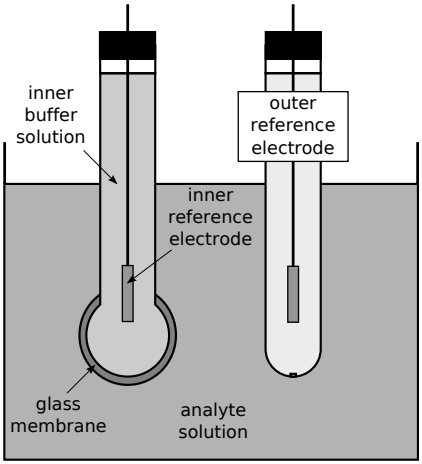

Figure 3.2: Schematic diagram of the glass electrode measurement chain

At present the "dissociation mechanism" as presented by Baucke [58] seems to be the most appropriate model to describe the pH-sensitivity of the glass electrode. It assumes that SiOH groups at the surface of the glass membrane are mainly responsible for the potential generation. The slight deviation from the ideal nernstian sensitivity that is observed in practical measurements is assigned to parasitic potentials in the measurement chain, diffusion processes in the membrane or the so-called alkali error in basic environments. The measurable slope corresponds to:

$$\frac{dE_m}{dpH_x} = -\alpha E^N \tag{3.2}$$

with the electromotive efficiency α_{em} on the order of 0.995 [59].

The properties of the glass electrode include a high impedance on the order of 10-1000 MΩ due to the low electric conductivity of the glass membrane. This fact makes the use of a high input impedance voltmeter as well as sufficiently high insulation resistance mandatory. The pH-sensitivity is generally near-Nernstian in the range of 58 mV/pH with a temperature coefficient of $-0.1983\,\mathrm{mV/(pHK)}$ for an ideal glass electrode. The working temperature of glass electrodes covers the range from -25 to 130 °C, although special designs are needed below 0 and above 100 °C. One of the main advantages of the glass electrode is the fact that its sensing mechanism does not involve redox reactions. Therefore it is not influenced by reducing or oxidising agents. The cross sensitivity towards different cations depends not only on the pH-value but also on the glass composition. With increasing radius of the hydrated cations (K $\longrightarrow$ Na $\longrightarrow$ Li) in the glass the cross sensitivity decreases [60]. The response time (T_{90}) of the glass electrode is typically in the range of several seconds, for aged or contaminated electrodes the response time can be up to 1000 times higher.

As the impedance of glass electrodes is commonly in the range of (10–1000) MΩ, the instrumentation needs to have an input impedance at least a factor of 1000 higher. Suitable devices can be found in the MOSFET and the operational amplifier, an integrated circuit employing MOSFETs with input impedance in the TΩ-range. In their simplest form, they are used as impedance transformers as illustrated in fig. 3.3. Today, commercial pH-meters are based on microprocessors and offer automated temperature compensation, guided calibration with automated buffer recognition as well as recording and output of pH-data. The glass electrode has become by far the most important and widely used measuring device for the determination of pH-value. It is used for monitoring and controlling chemical reactions in various forms, such

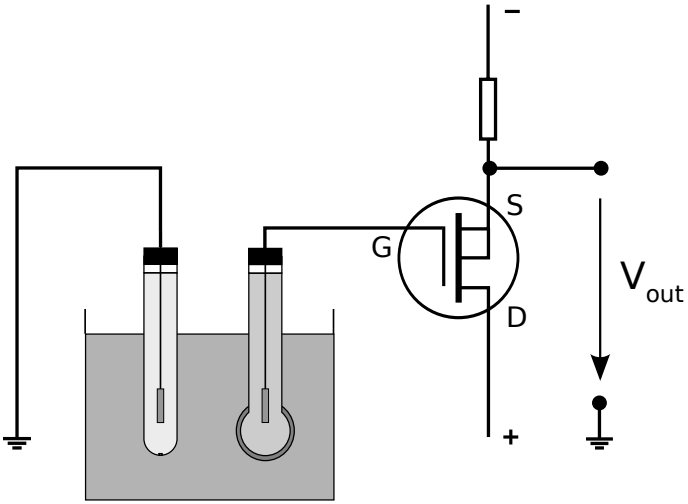

Figure 3.3: Impedance transformation circuit using a MOSFET for the measurement of glass electrode potential.

as controlling the optimal pH-value for enzymatic reactions as well as monitoring production by checking the pH-value of waste water. Due to the vast number of possible applications, the fields where the glass electrode cannot or can only be applied with limitations are briefly discussed. These fields may in turn be filled by alternative devices such as the ISFET. Although the applicability of glass electrodes is not limited to aqueous solutions, non-aqueous solutions may pose difficulties. It is possible to measure pH in liquid ammonium (at -33°C) for the titration of very weak acids [61], however solutions containing hydrofluoric acid are excluded due to the dissolving of the membrane. The miniaturisation of the device is another problem that can only be realised with great effort down to a minimal length of approximately 1 cm [25] because of its discrete and rather elaborate design. This fact also limits the possibility for mass production and results in bulky devices typically with a diameter of 12 mm and a shaft length of several centimetres. Its main restraint however lies in the fragility of the glass membrane, which defines the overall mechanical stability of the glass electrode and hinders the usage, in the food industry for example. It can nevertheless be used in high pressure environments up to 90 bar in the conventional form and up to 1500 bar with special designs [62]. The lifetime of the electrode is limited by the employed glass membranes, which generally belong to the less stable glass types leading to continuous ageing even without usage. As the practical lifetime strongly depends on the operating conditions, especially the temperature, it is difficult to predict, but the value of one year for cool storage can be taken as a guideline [25].

3.3 Si-based ISFETs

The structure of the ISFET is closely related to the MOSFET as illustrated in fig. 3.4. The MOSFET is based on the modulation of current in the semiconductor by an electric field that is capacitively coupled perpendicular to the surface through an insulating oxide layer (commonly SiO_2). For the ISFET the gate metal is replaced by a suitable sensing layer (e.g. Si_3N_4, Al_2O_3 and Ta_2O_5) that is exposed to an electrolyte solution. The gate potential is controlled using a reference electrode. One of the advantages of this device is that its manufacturing can be integrated into commercial semiconductor technology [63] and could therefore be mass fabricated. However, a cost reduction cannot be achieved, as the large number of devices needed for this does not coincide with the current demand for pH-sensors.

Initially, this device was seen as the direct integration of a glass electrode and MOSFET, which combines chemical sensing properties and impedance transformation [3]. This was mainly due to the similarities between the silica-based glass membrane and the SiO_2 insulator, which was the first gate oxide layer to be employed. Therefore, the initial theoretical description of the ISFET was derived form the glass electrode, even though the devices exhibited a clear deviation from the near-Nernstian response [53]. One of the most prominent differences to the glass electrode is that the ISFET is not a measuring chain in itself, i.e. no inner reference system is needed. Additionally, the ISFETs functionality is based on the field effect over the insulating oxide layer, whereas the glass membrane needs to be conducting. The successful use of various other metal oxides and nitrides as pH-sensitive layers [52, 53, 54] also emphasises the differences between the ISFET and the glass electrode. Therefore, the ISFET should rather be viewed as

a combination of the metal/metal oxide electrode and the MOSFET. Both devices share a common charging mechanism, but the charge balancing is fundamentally different. On the one hand, the metal/metal oxide electrode can balance the charge directly through electrons from the metal contact. It is therefore susceptible to redox agents and has a rather low input impedance. On the other hand, the ISFET needs to balance the charge through the ions in the solution as the gate is insulating. It is therefore susceptible to changes in ionic strength and has a high input impedance.

3.3.1 Theory

The pH-sensitive part of the ISFET is the oxide-solution interface. This interface has been extensively studied in colloid chemistry resulting in the "site-dissociation model" by Yates [64] and Healy [65]. It was first applied to the description of ISFETs by Siu and Cobbold [22] and extended by Bousse [66]. For the sake of better comparison to the glass electrode, SiO_2 will be taken as an example for the oxide layer. Similar to the "dissociation mechanism" introduced for the glass electrode by Baucke [58], discrete hydroxyl groups are involved in the interface reaction:

$$SiOH + H_2O \longleftrightarrow SiO^- + H_3O^+.$$

The "site-dissociation model" however describes metal hydroxyls as amphoteric and also takes the reaction

$$SiOH_2^+ + H_2O \longleftrightarrow SiOH + H_3O^+$$

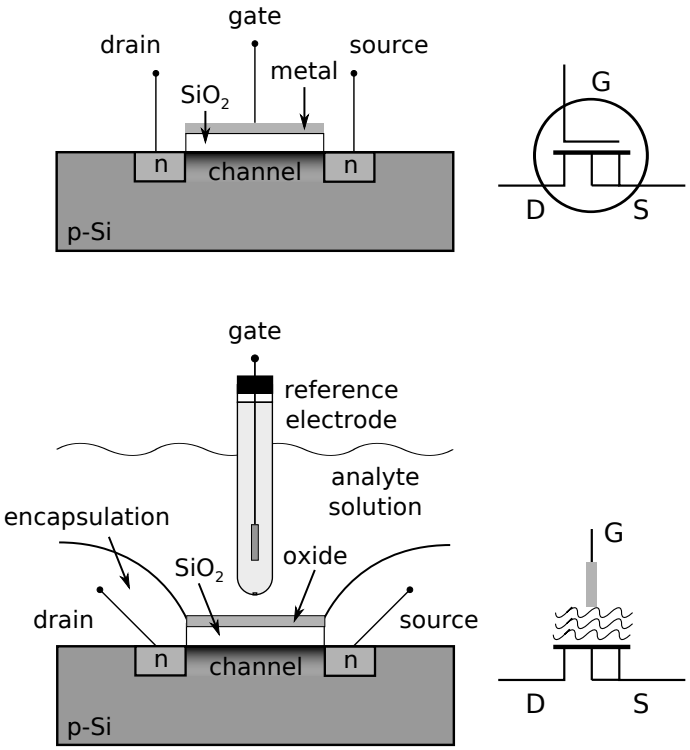

Figure 3.4: Schematic cross section of (a) the MOSFET and (b) the ISFET.

into account, though there is no consensus whether the silica surface is really amphoteric [67]. The dissociation constants of these reactions are given as:

$$K_+ = \frac{a'_{\mathrm{SiOH}} \cdot a_{\mathrm{H_3O^+},S}}{a'_{\mathrm{SiOH_2^+}} \cdot a_{\mathrm{H_2O}}} = \frac{c'_{\mathrm{SiOH}} \cdot a_{\mathrm{H_3O^+},S}}{c'_{\mathrm{SiOH_2^+}}}, \tag{3.3}$$

$$K_- = \frac{a'_{\mathrm{SiO^-}} \cdot a_{\mathrm{H_3O^+},S}}{a'_{\mathrm{SiOH}} \cdot a_{\mathrm{H_2O}}} = \frac{c'_{\mathrm{SiO^-}} \cdot a_{\mathrm{H_3O^+},S}}{c'_{\mathrm{SiOH}}}, \tag{3.4}$$

assuming that the activity of surface groups a' is equal to the surface concentration c' expressed in number of sites per unit area and taking the activity of water as unity. The index S for the hydronium activity $a_{\mathrm{H_3O_S^+}}$ indicates that the surface activity is considered.

The total surface charge density σ_0 may then be written as:

$$\begin{aligned} \sigma_0 &= q(c'_{\mathrm{SiOH_2^+}} - c'_{\mathrm{SiO^-}}) \\ &= qN_{ss}\frac{a^2_{\mathrm{H_3O^+},S} - K_-K_+}{a^2_{\mathrm{H_3O^+},S} + K_+a_{\mathrm{H_3O^+},S} + K_-K_+} = -q[B], \end{aligned} \tag{3.5}$$

where $N_{ss} = c'_{\mathrm{SiOH_2^+}} + c'_{\mathrm{SiO^-}} + c'_{\mathrm{SiOH}}$ is the total density of available surface sites, q the elementary charge and $[B]$ the net number of charged groups. The relation between the surface and bulk hydronium activity (index B) is given by:

$$\begin{aligned} a_{\mathrm{H_3O^+},S} &= a_{\mathrm{H_3O^+},B} \cdot \exp(-\frac{q\Phi_0}{kT}) \\ pH_S &= pH_B + \frac{q\Phi_0}{2.3kT} \end{aligned} \tag{3.6}$$

with the surface potential Φ_0.

This mechanism of charge adsorption needs to be balanced by some form of countercharge to maintain electroneutrality. As the oxide is an insulator no charge transfer is possible through the semiconductor and the countercharge needs to be supplied by the electrical double layer in the electrolyte solution. For the sake of simplicity the Gouy-Chapman model will be used here. In this model a diffuse charge layer is formed electrostatically with opposite sign compared to the surface charge (fig. 3.5). Employing equation 2.8 this can be expressed by:

$$\sigma_{EDL} = -(8kT\epsilon\epsilon_0 I N_A)^{\frac{1}{2}} sinh(\frac{zq\Phi_0}{2kT}) = -\sigma_0, \tag{3.7}$$

for $\sigma_{EDL} = \sigma_{MI}$ and $\Phi_0 = \Phi_{OHP} - \Phi_e$. The fact that the ions can only approach the surface to a finite distance could be accounted for by the inclusion of a Helmholtz layer (Gouy-Chapman-Stern model), but for the discussion of the general approach the simple model is sufficient. Several rather complex derivations for the surface potential with respect to bulk pH-value have been published which require some assumptions [68, 69]. However, a remarkably simple approach to calculate the relationship between the surface potential and the bulk pH-value using equations (3.5) to (3.7) has also been published recently by van Hal [70]. He introduces the concept of the intrinsic buffer capacity β_{int} as the capability of the surface to store charge as a result of an infinitesimal change of pH:

$$\frac{\delta\sigma_0}{\delta pH_S} = -q\frac{\delta[B]}{\delta pH_S} = -q\beta_{int}. \tag{3.8}$$

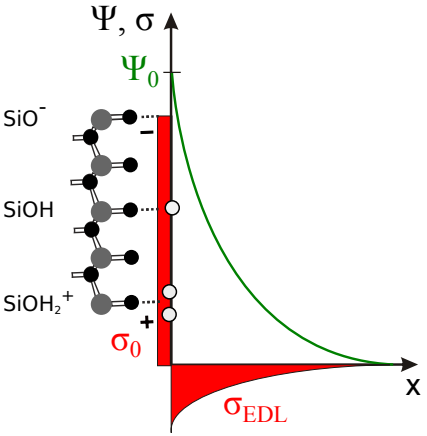

Figure 3.5: Assumed structure of the metal oxide/electrolyte solution interface with charges and potentials.

Using equation (3.5) the intrinsic buffer capacity can be calculated. The capability of the solution to store charge with respect to a small change in the surface potential is the differential capacitance:

$$\frac{\delta\sigma_{EDL}}{\delta\Phi_0} = -\frac{\delta\sigma_0}{\delta\Phi_0} = -C_{dif} \tag{3.9}$$

This capacitance is calculated using equation (3.7). Combining equations (3.8) and (3.9) yields the relationship between surface potential and surface pH:

$$\frac{\delta\Phi_0}{\delta pH_S} = \frac{\delta\Phi_0}{\delta\sigma_0}\frac{\delta\sigma_0}{\delta pH_S} = -\frac{q\beta_{int}}{C_{dif}} \tag{3.10}$$

Using equation (3.6) to relate the surface potential to bulk pH instead gives:

$$\frac{\delta\Phi_0}{\delta pH_B} = -\frac{2.3kT}{q}\alpha_s = -\alpha E^N, \tag{3.11}$$

with

$$\alpha_s = (\frac{2.3kTC_{dif}}{q^2\beta_{int}} + 1)^{-1}. \tag{3.12}$$

This expression is the ISFET analogy to equation 3.2 from the theoretical description of the glass electrode. The sensitivity parameter α_s is the equivalent to the electromotive efficiency of the glass electrode α_{em}. For the sensitivity to be close to the Nernstian limit α_s needs to approach unity. This can be achieved by a high intrinsic buffer capacitance and a small differential capacitance. It is worth noting that the approach by van Hal is general in the sense that it can include not only the "site-dissociation model" and the Gouy-Chapman theory, but any combination of a charging mechanism and a double layer model (or the charge balancing in general) and that it is applicable to all metal oxide/solution interfaces [71]. Si_3N_4 for example is best described by an extended "site-dissociation model" with SiO_2 and amine groups as suggest by Harame [72].

Possibly, this model may also be applied to the glass electrode where the charging mechanism is similar to the oxide/solution interface [58]. For this purpose, suitable descriptions of the surface potential depending on pH-value and the surface charge depending on surface potential would have to be derived.

3.3.2 Properties

As mentioned previously, the ISFET incorporates an impedance transformer leading to a high input impedance (typically several 100 MΩ) and a low output impedance (depending on the gate geometry W/L, on the order of 100-1000 Ω). This fact is beneficial for the following measuring instrumentation as its input impedance and the cable insulation are no longer critical parameters.

The sensitivity of the ISFETs is strongly dependent on the nature of the gate oxide. Using the approach by van Hal, the pH sensitivity is characterized by the intrinsic buffer capacity β_{int} which can be calculated from colloid data for the dissociation constants (pK_+, pK_- with $pK = -\log(K)$) and the total density of surface sites (N_{ss}) of the various oxides. Table 3.1 shows the range of values that can be found in literature with the point of zero charge $pH_{PZC} = \frac{1}{2}(pK_+ + pK_-)$ and N_{ss} which are determined experimentally and $\Delta pK = pK_- - pK_+$ which is obtained by fitting measured data to the "site-dissociation model". The ranges of experimental and theoretical pH-sensitivities is also given.

Table 3.1: Published values for pH_{PZC}, ΔpK and N_{ss} (obtained from colloid experiments) and experimental and theoretical pH-sensitivity for selected insulators.

insulator	pH_{PZC}	ΔpK	N_{ss} (10^{14} cm^{-2})	experimental $\delta\Psi_0/\delta pH_B$ (mV/pH)	theoretical $\delta\Psi_0/\delta pH_B$ (mV/pH)
SiO_2	1-3 [67]	6-10 [68]	5 [73]	20-35 [53] (pH4-7)	5-45 [70]
Si_3N_4	4-6 [67]			46-56 [53] (pH1-10)	
Al_2O_3	7-9 [67]	3-4 [68]	8 [74]	52-48 [53] (pH1-13)	50-55 [70]
Ta_2O_5	2.7-3 [67]	2 [75]	10 [75]	58 [71] (pH2-12)	57-59 [70]
Ga_2O_3	5.95 [76], 7.5 [77], 9 [78]	2 [79]	8 [79]	55-57 [11] (pH2-12)	
		fitted values			

From equations (3.5) and (3.8) it can be seen that β_{int}, and with it the pH-sensitivity, is dependent on pH-value. This has also been confirmed experimentally for several oxides as shown in figure 3.6a. Apart from the observed non-linearity, which is most prominent for SiO_2, the slopes vary considerably. The theoretically predicted ranges are in good agreement with the measured ones and it was found that the pH dependency of the sensitivity is reduced with decreasing ΔpK and increasing N_{ss} of the insulator [70]. It is clear from table 3.1 that Al_2O_3 and Ta_2O_5 have become the preferred insulator materials for the fabrication of ISFETs. The recent research on III-Nitrides, however, suggests that Ga_2O_3 is a promising candidate too. The selectivity of ISFETs is dictated by the choice of the insulator material. Ion selectivity constants towards alkali ions ($K_{H,Na}$ and $K_{H,K}$) have been determined by Abe [53] to be approximately 10^{-5} for SiO_2, 10^{-7} for Si_3N_4 and negligible (presumably on the order of 10^{-9}) for Al_2O_3. The cross-sensitivity can be explained similar to the alkali error of the glass electrode by the specific adsorption of alkali ions, extended by the adsorption of halide ions at positively charged $SiOH_2^+$ sites [23]. However, the influence of the ionic strength of the solution on the differential capacitance (through equation 3.7) and the pH sensitivity in turn, has to be taken into account as well and may be the more predominant factor for selectivity [71]. This influence also decreases with increasing β_{int} and is therefore in qualitative agreement with the experimental values by Abe. The response to changes in ionic strength at a constant pH is also illustrated in figure 3.6b. A large, non-linear dependence on electrolyte concentration is found for SiO_2, whereas Ta_2O_5 exhibits only a small, linear response.

The temperature dependence of the ISFET is the sum of several factors. In addition to the thermal behaviour of the reference electrode

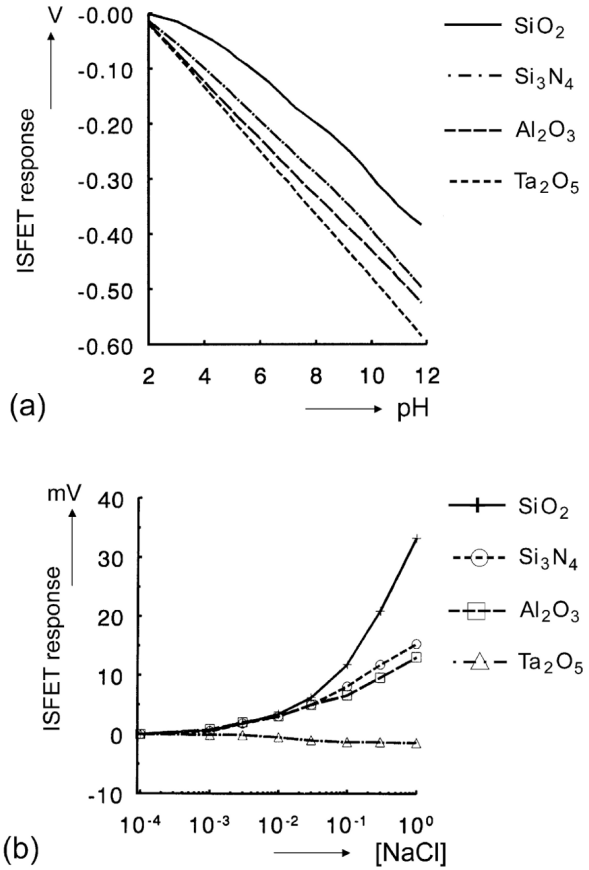

Figure 3.6: The response of an ISFET to (a) electrolyte pH at constant TBACl concentration of 0.1 M and (b) NaCl electrolyte concentration at constant pH of 5.8 [4].

and the thermodynamic dependency of E^N, the FET semiconductor device is also influenced. The main parameters are the threshold voltage U_{th} and the electron mobility μ, for which only empirically derived thermal coefficients are available. Although an athermal point for the drain current exists, it has to be determined individually for each device and cannot be engineered towards a specific value on a larger (wafer) scale. Several concepts to minimise the thermal sensitivity have been devised including the superposition of an AC signal or the on-chip compensation using a paired MOSFET with matched characteristics [80]. Another possible approach is to correct the raw data by previously measured temperature characteristics. Light sensitivity is a challenge that originates from the semiconducting nature of the ISFET and although it has been reduced over the years, it still exists. Especially under conditions of intense illumination, such as direct sunlight, it has to be accounted for. The simplest way to do this is to shield the ISFET from ambient illumination by appropriate housing. The overall response to rapid changes in pH is faster than for the glass electrode and does not deteriorate with time. For high velocity fluid jets, response times (T_{95}) as fast a 5 ms are reported [81] using a special measurement setup. In practical flow-through setups with lower fluid velocities a range of 0.3 to 2 s is typically obtained [82]. Therefore, the response time is thought to be limited by the fluid kinetics rather than the interface reaction kinetics or the underlying FET structure.

3.3.3 Instrumentation

The ISFET itself is part of the amplification system, as its FET part already achieves impedance transformation. Therefore, the electrical resistance needs to be measured as a function of surface potential.

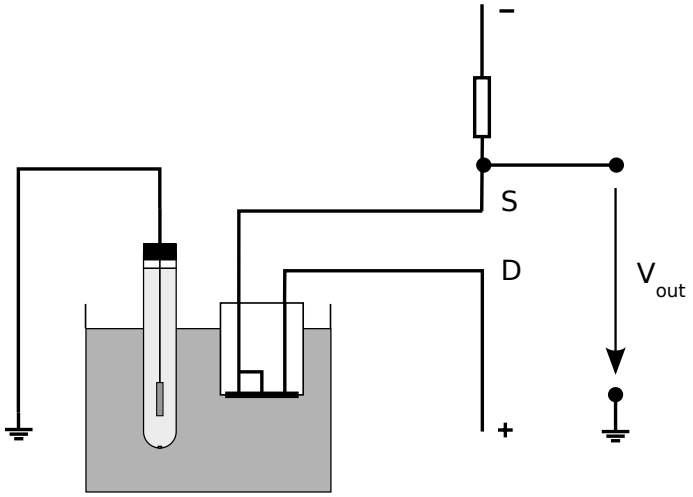

Figure 3.7: Schematic diagram of the ISFET source follower circuit.

This can be achieved by operating the ISFET with constant drain current I_D. A source follower as illustrated in fig. 3.7 is a simple way to do this. It is analogous to the circuit in fig. 3.3 when the glass electrode and the MOSFET are replaced by the ISFET. More elaborate designs include source and drain followers, which employ a constant drain-source voltage in addition to the constant drain current, and differential ISFET/MOSFET pairs as have been suggested by Bergveld [80]. The functionality of the pH-meters for glass electrodes is naturally also available for ISFETs. The possibility to apply common pH-meters to the discussed circuits has brought forth interfacing modules as well as completely modular systems not only for pH but for other ions and conductivity as well.

3.3.4 Applications

The ISFET has found its way to commercial application primarily in fields where the glass electrode cannot be used. This includes fields where the fragility of the glass electrode or its size prohibits its application. Interestingly, the ISFET manufactures have seldom exploited the size advantage of the ISFET but continue to fabricate rod-shaped devices with similar dimensions to the glass electrode. This can partly be attributed to difficulties in miniaturising the reference electrode for which no satisfactory solution has been found. Attempts to manufacture a miniaturised reference electrode have included pH-insensitive ISFETs (termed REFETs) [83] as well as conventional Ag/AgCl electrodes with gelled electrolytes in microcavities [84]. The proper encapsulation of the ISFET sensor chip is another challenge that has to be overcome [85].

The ruggedness of the ISFET has led manufactures to position their devices mainly for the food industry advertising it as "unbreakable". Its fast response, dry storage, easy brush cleaning and the possibility to measure in viscous and solid samples are also highlighted in advertisements. The few examples where miniaturised ISFET systems have made it to the market include a pocket-sized pH-meter introduced by Shindengen (Japan) - today continued by Hach (USA) - in 2004 and an indigestible, wireless capsule for measuring pH, pressure and temperature in the gastrointestinal tract by SmartPill Corp. (USA) that was approved by the U.S. FDA (Food and Drug Administration) in 2006. Interestingly, the latter concept was not introduced with the ISFET but is in fact nearly 50 years old and was also suggested to employ a miniaturised glass electrode [86], although no commercial device resulted from this work. In academic research the ISFET has mainly

been applied in biomedical fields primarily stressing the size advantage e.g. integrated into catheter tips to measure the blood pH in vivo, which came close to commercialisation [87]. Biocompatibility issues, however, made the introduction to the market impossible. Another application example are flow-through cells with four integrated partly functionalised ISFETs (H^+, Na^+, K^+, Ca_2^+) [88] or the combination of pH and pCO_2 ISFETs [89]. The micro flow cell for blood gas analysis fabricated by Shoji et al. [90] employed a pH-ISFET in addition to conventional, but miniaturised, pO_2 and pCO_2 sensors. An impressive reduction of sample volume to 0.34 µl was achieved, but the application to real blood samples was never shown. It is likely that the same biocompatibility and stability issues described earlier have prevented accurate and stable measurements.

More innovative approaches have been demanded and suggested by Bergveld for future development opportunities [4], as the common approaches only exploit the miniaturisation potential but stay conventional in principle. Sensor/actuator systems can be realised by depositing a noble metal electrode around the ISFET which can actuate a pH change through the electrolysis of the water. This way a dipstick titrator can be realised [91] and feedback systems are possible. Due to the fast response time of the ISFET it is also feasible to eliminate drift problems of the device by dynamic measurements [4]. For measurements under uncommon or extreme conditions few results can be found. Similar to the glass electrode, solutions containing hydrofluoric acid are also excluded as metal oxides are etched by them. Results for Si_3N_4 and Ta_2O_5-ISFETs indicate that they can be employed in non-aqueous solvents with good agreement and faster response time compared to the glass electrode [92]. High pressure environments should not pose serious limitations to the application of ISFETs. For commer-

cially available ISFETs a slightly lower temperature range (-5 to 80 °C) is stated, compared to glass electrodes. Ageing of the device even without usage as observed for glass electrodes does not occur for ISFETs. The practical lifetime is mostly determined by the device packaging as the bare ISFET chip itself is essentially non-ageing [93], does not require special storage conditions and can easily be brush cleaned. Therefore the lifetime, again depending on the operating conditions, should be on the order of several years.

3.4 Reference Electrode

All electrochemical methods for the measurement of pH-value share a common element in their measuring chain: the reference electrode. This second half-cell in conjunction with a pH-electrode completes the measurement circuit and forms the measurement cell. It should be noted that a reference electrode is mandatory for every type of pH-electrode, be it a glass electrode, a metal/metal oxide electrode or an ISFET.

3.4.1 Conventional Design

Reference electrodes based on insoluble salts are utilised most frequently as they are easy to manufacture and exhibit very good reproducibility. The silver/silverchloride electrode (Ag/AgCl) has found the most widespread application followed by the mercury/calomel electrode ($Hg/HgCl_2$). The potential of the Ag/AgCl electrode in an electrolyte

solution containing chloride ions can be derived using the Nernst equation (eq. 2.7):

$$E = E^0_{Ag} + E^N \log L_{AgCl} - E^N \log a_{Cl^-} = E^0_{AgCl} - E^N \log a_{Cl^-}, \quad (3.13)$$

with the solubility product $L_{AgCl} = a_{Ag^+} a_{Cl^-}$. It is easily seen that the electrode potential only depends on a_{Cl^-} for given environmental conditions. The potential is reversible in a temperature range from -30 to 130 °C.

An Ag/AgCl reference electrode commonly consists of a glass body in which a silver wire coated with silver chloride is immersed in a concentrated (3 M) or saturated (∼3.5 M) potassium chloride (KCl) solution that is also saturated with AgCl (fig. 3.8). The internal electrolyte solution establishes a stable potential that is passed to the sample via the junction. The junction is required to balance the internal and external potential by exchanging ions, but also needs to prevent contamination of the internal electrolyte solution, as this would impair the potential stability at the internal electrode.

The junction can be realised as an open junction or with various types of diaphragms. To minimise the contamination of the internal electrolyte solution from the sample, an additional junction can be added via a salt bridge (double junction reference electrode). The potential equilibrium between the internal and external solution is ensured by leaking internal solution through the junction by a slight internal overpressure. This is normally achieved using the hydrostatic pressure by opening the filling hole. The leakage rate ranges from 2 ml/d for glass frits to less than 0.05 ml/d for ceramic diaphragms and capillary junctions. The conductivity of the junction, and subsequently the impedance of the whole reference electrode, is inversely propor-

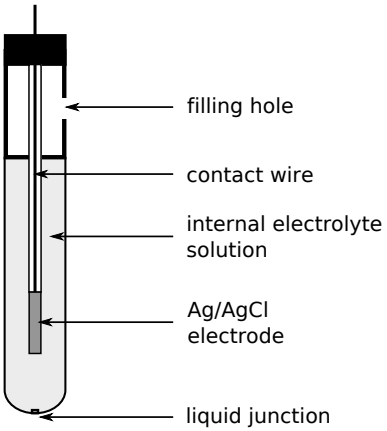

Figure 3.8: Schematic drawing of a conventional reference electrode.

tional to the leakage rate. The most common type of junction is the ceramic diaphragm, which is made up of a porous ceramic plug with a diameter of 1 mm that is melted into the glass body. This junction is also commonly applied for the construction of combination electrodes, which incorporate a glass and a reference electrode in a single probe. However, the porousness (diameter $<1\,\mu m$) and the low leakage rate make the ceramic junction susceptible to contamination and clogging and it exhibits a rather high impedance of about $5\,k\Omega$. To minimise clogging of the junction higher leakage rates and/or bigger pores have to be employed. This is the case for open junctions like the capillary junction with an inner diameter of approximately $10\,\mu m$ and leakage rates down to 0.03 ml/d. Clogging is reduced as only a single pore is used which can be cleaned by a short overpressure impulse. This makes them a suitable choice for the application in blood gas analysers where the junction can become blocked by blood clots. The disadvantage of

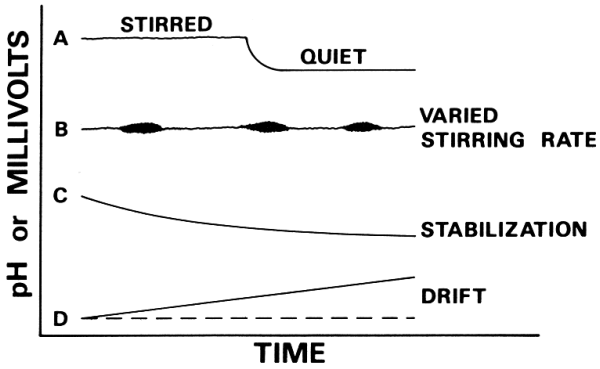

Figure 3.9: Typical measurement artifacts related to the liquid junction potential [94].

this junction is the extraordinarily high electrode impedance (>10 MΩ) leading to more strict isolation and shielding as well as instrumentation requirements. Furthermore, it also distorts the impedance spectrum at high frequencies in electrochemical impedance spectroscopy. In general, many measurement artifacts in electrochemical pH-measurements can be related to the reference electrode junction, as illustrated in fig. 3.9. The solution kinetics influence the junction potential, e.g. by stirring, and a stabilisation period or overall drift may be observed. The stability of the junction potential is also influenced by the choice of the internal electrolyte solution. By using concentrated or saturated electrolyte solutions the charge transfer is determined by these ions and independent of the ions in the sample. The inner electrolyte solution should exhibit nearly equal diffusion constants for cations and anions to establish a stable potential. Otherwise, the charge transfer across

the junction would be unequal, resulting in a drifting potential. Other requirements for the internal electrolyte include: no reaction or contamination of the sample and solubility in the employed solvent. For the Ag/AgCl reference electrode in aqueous solutions, potassium chloride fulfils these requirements when no Ag ions are present in the sample. Otherwise the sample may be contaminated through the formation of AgCl.

For the application of conventional reference electrodes in harsh environments the internal electrolyte solutions can be solidified using gels or polymers. The closed glass body makes the electrode more resistant to external pressure and only a very small amount of sample solution can enter the electrode. The gel matrix does not impede the diffusion of ions and the conductivity of the internal electrolyte solution appreciably. Commonly employed gels include agar-agar, agarose, polyvinyl alcohol or polyacrylamid in concentrations of up to 20% in connection with an open junction (diameter 0.5 to 1 mm). Although no exchange of electrolyte solution takes place across the junction, the diffusion of ions from and to the sample solution is not restricted, which leads to a slow contamination and dilution of the internal electrolyte solution. This is why every sample leaves a trace in the gel. The temperature and time dependent phase separation in the gel with the subsequent loss of water and shrinking of the gel is another effect that limits the lifetime of gel-based electrodes.

3.4.2 Miniaturisation

One of the advantages of the ISFET, the small dimensions of the active sensor area and the possibility of miniaturisation, is seriously hampered by the dimensions of conventional reference electrodes. Therefore many

attempts have been made to overcome this challenge by the development of micro reference electrodes. Three different approaches can be found in literature: quasi-reference electrodes (QRE), miniaturised conventional reference electrodes (integrated micro reference electrodes - iμREe) and the previously mentioned REFETs.

The first miniaturisation approach is based on omitting parts of the conventional design. This automatically implies a deterioration of the electrodes properties, especially with respect to potential stability and lifetime. The quasi-reference electrode only consists of the internal electrode (Ag/AgCl or a noble metal) in direct contact with the sample solution. They can easily be integrated on-chip with the ISFET but exhibit a pronounced sensitivity to the transfer ions for insoluble salt electrodes (e.g. Cl^- for Ag/AgCl) or are susceptible to redox couples. If the reference potential stability is not too critical and the sample composition can be assumed constant with respect to transfer ions and redox couples the QRE is the most straightforward approach that can be manufactured in a very simple way. It is also employed as a secondary reference electrode to establish a reference point for differential measurements between an ISFET and a REFET or a true reference electrode. A slightly more stable reference electrode can be realised by covering a QRE with a polymer-, epoxy- or gel-based electrolyte similar to the conventional gel reference electrodes mentioned earlier, but omitting a discrete junction. The solidified electrolyte is coated onto the QRE and contacted by the sample solution over the whole surface [95, 96]. This way the influence of the transfer ions is reduced. However, due to the relatively large wetted area the electrode potential is influenced by the solution composition and the lifetime is limited.

A miniaturised conventional reference electrode is created when a small open junction is used to minimise the contact area with the

sample [97, 98]. Therefore, this second approach achieves miniaturisation by reducing the actual dimensions of the conventional design and retains the properties of a conventional reference electrode. The realisation of the open junction, however, is a technological challenge especially with respect to the integration into an established production process [84, 90]. In general, the lifetime of the iμRE is reduced as there is little space available for the internal electrolyte solution. This results in a much faster depletion and/or contamination of the electrode. When only the dimensions directly at the sample have to be minimised, but the main body of the electrode can be realised conventionally, the capillary reference electrode is best suited.

The third approach combines the QRE with the possibility to monitor the reference potential using a REFET. The REFET itself is a modified ISFET that is insensitive to ions in general and to pH in particular. A near perfect integration of a reference electrode can be achieved by realising the ISFET, the REFET and a small metal QRE (e.g. Pt) directly on the chip. The rather unstable potential of the QRE is measured by both the ISFET and the REFET and can be suppressed using a differential amplifier system with a high common-mode rejection ratio. The amplified signal only contains the response of the ISFET to changes in ion concentration, assuming that the REFET is insensitive to ions but otherwise identical to the ISFET. The challenge that has not been overcome so far is to develop a modification for the ISFET that eliminates the ion sensitivity but maintains all other properties. For the elimination of ion sensitivity the sensor surface has either been coated using inert and ion-blocking layers like parylene [83], teflon [99] and or directly modified by grafting with long-alkaly-chain silanes [100]. These modifications only reduced the pH-sensitivity either in a small pH range [83] or by a factor of 5 [99] which is not sufficient for

practical applications. However, even a perfectly inert surface of the REFET changes its electrical properties compared to the ISFET due to the different charge and potential distribution at the surface resulting in different surface potentials and a differential signal. A possible solution to this problem is to bias the REFET in such a way that it behaves electrically identical to the ISFET, as suggested by Bergveld [4]. For flow-through systems with a relatively high sample frequency a diffusion barrier which retards the response time of the REFET has been applied [101]. This pseudo-REFET can act as a reference sensor during the passage of the sample as is reacts slowly enough to changes in the sample. Although the REFET is a promising approach, no breakthrough has been achieved so far and only very few publications still investigate the topic.

In conclusion, the miniaturisation of the reference electrode can be achieved for specific applications but there is no universal solution available that would enable the construction of a miniaturised and integrated ISFET-based pH-sensing device with comparable versatility as the combination glass electrode.

4 AlGaN-based Fluid Sensors

In this chapter the material properties of Group III-Nitrides and the structure of the used sensor devices are presented. An overview of the state of the art in AlGaN-based fluid sensors for pH-value, anions and functionalised (bio-)sensors is given and their theoretical description is discussed.

4.1 The III-Nitride Material System

The III-V compound semiconductor GaN and its ternary and quaternary alloys with Al and In form the III-Nitride material system which is nowadays considered one of the most important semiconductors after Si [102]. They can form a hexagonal (wurzite) or a cubic (zincblende) crystal structure. The wurzite structure is the more stable and commonly employed configuration. In this work, the term "III-Nitrides" will be used to refer to GaN and $Al_xGa_{1-x}N$ with a wurzite crystal structure. InN and $In_xGa_{1-x}N$ will not be discussed.

The fabrication of large area GaN samples was first described about 50 years ago [103], but initially their potential was dismissed due to insufficient material quality and the inability to produce p-type material. It took about 30 years to improve the growth techniques and, consequently, the structural properties. This improvement lead to increasing research activity on III-Nitrides and their commercial breakthrough

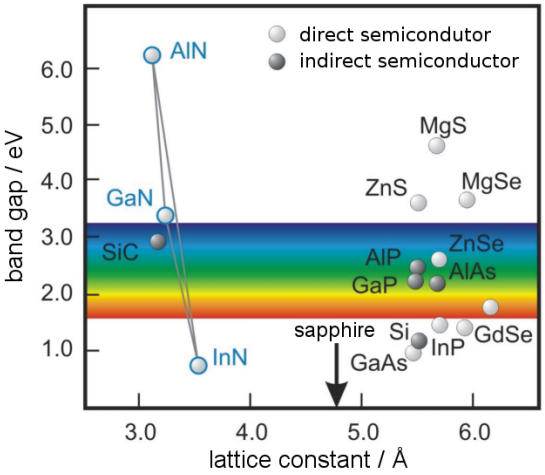

Figure 4.1: Bandgap and lattice constants of III-Nitrides and other selected semiconductors [16].

in 1994 with the introduction of the blue GaN-based light-emitting diode (LED) [104]. Since then a multitude of application fields have been discovered, with optoelectronic devices as the undisputed leader in terms of commercial success and research activity. High-power and high-frequency transistors, devices for harsh and high temperature environments and especially sensor devices have also received increasing research interest in the past 10 years.

Properties and Advantages

One of the most prominent properties and advantages of III-Nitrides compared to Si or other III-V semiconductors (e.g. GaAs) is the possibility to obtain so-called wide band gap semiconductors like GaN and

AlN with a band gap of 3.44 eV [105] and 6.2 eV [106], respectively, as well as semiconductors with a small band gap like InN with 0.7 eV [107]. Additionally, the band gap can be engineered over a broad range to any value between 0.7 and 6.2 eV using the ternary alloys $Al_xGa_{1-x}N$ and $In_xGa_{1-x}N$ via adjustment of x (fig. 4.1). All III-Nitrides are direct semiconductors and can therefore be used to build optoelectronic devices. The large band gap of GaN and $Al_xGa_{1-x}N$ in conjunction with substrates like sapphire and undoped SiC enables the fabrication of devices that are transparent in the visible light spectrum.

The high bond strength of GaN and $Al_xGa_{1-x}N$ results in a high chemical stability, which is beneficial for devices in harsh or high temperature environments. However, it also presents a technological challenge when structuring the material. Biocompatibility of GaN and AlGaN was shown to be superior to common semiconductors like Si [108, 109]. In the corresponding publications, the term biocompatibility was defined in the sense that cell cultures adhere well to the semiconductor and no signs of toxicity or change in cell morphology can be observed.

The spontaneous and piezoelectric polarization of III-Nitrides is up to ten times larger in comparison to other III-V and II-IV semiconductors [110]. This property was exploited for the construction of surface acoustic wave (SAW) devices [111]. The polarization is also used for the fabrication of AlGaN/GaN heterostructures with a highly conducting 2DEG channel. This heterostructure is the basis for the sensor devices employed in this work. As the wurzite structure is noncentrosymmetric, two different stacking sequences are possible on GaN and AlGaN. This results in a polarity of the surface that can be influenced by the choice of growth parameters [110]. For a Ga-face surface the spontaneous polarization is orientated towards the substrate, whereas for

an N-face surface its is orientated towards the surface. Other electrical properties include a reasonable electron mobility and high electron drift velocity [112] as well as the possibility to achieve n-type material using Si and p-type material using Mg as dopants. As-grown material can exhibit unintentional n-type doping (due to N-vacancies), p-type doping (due to the incorporation of C) or be compensated, depending on the growth method.

Applications

As stated earlier optoelectronic devices are the primary applications of III-Nitrides and light emitting devices were the first to be developed. Especially the blue p-n LED developed in 1994 by Nakamura [104] and its subsequent, very successful commercialisation by Nichia Corp. was a milestone for LEDs in the blue and (ultra-)violet spectral range. This success also allowed for the development of white LEDs that use high-intensity blue InGaN-LEDs to excite yellow fluorescence in a phosphor layer giving the overall impression of white light. These LEDs are now commercially widely available and are used as energy saving alternatives for room lighting or in the automotive industry. Following the blue LED the fabrication of continuous wave laser diodes (LD) based on III-Nitrides was achieved in 1996 [113]. Especially the information technology industry benefited from this development, as the blue LD made the construction of optical storage devices (e.g. the Blu-ray disc) with a much higher data density (factor 4) possible, due to the shorter light wavelength. The direct, large and tunable band gap of the III-Nitrides and the possibility to grow single and multi quantum-well (SQW/MQW) structures enabled the manufacturing of blue and green LEDs and LDs. The aforementioned advantages are also exploited for

the construction of photodetectors especially in the ultra-violet (UV) region. On the one hand, the band gaps of GaN and $In_xGa_{1-x}N$ are well suited to achieve solar-blind characteristics. By employing a relatively thick (approx. 1 μm) epitaxial filter layer and using backside illumination through the transparent substrate an upper cut-off wavelength of less than 365 nm is realised. On the other hand, the possibility to fabricate MQW structures increases the sensitivity of the detector [114]. These devices have found commercial application in for example flame sensors or medical UV monitoring, and are available as low-cost devices from manufacturers like Advanced Photonix Inc., sglux SolGel Technologies GmbH or Kyosemi Corp.

Electronic devices based on III-Nitrides can be found mainly in the form of high electron mobility transistors (HEMT). They employ heterojunctions which are formed by different compositions of the ternary alloys. This allows for the local optimisation of charge transport properties especially for high frequency applications. Their wide band gap and fairly good thermal conductivity [112] also makes them applicable at high temperatures and for high power applications. III-Nitride HEMTs are commonly based on an AlGaN/GaN heterostructure and the first promising research results were published in 1996, demonstrating high maximum current, transconductance, breakdown voltage and cut-off frequencies in the range of 50 GHz [115]. About a decade later a multitude of companies started to announce GaN high-power and/or high frequency HEMTs [116] and the first commercially available GaN radio frequency HEMTs were introduced in 2006. Currently GaN HEMTs are available from Cree Inc., Nitronex Corp., Toshiba America Electronic Components Inc. or RF Micro Devices, with a frequency and power range of up to 14 GHz and 50 W, respectively. These devices are

mainly targeted at the communication market with next generation mobile communication standards like UMTS/HSPA, WiMAX or LTE.

Other application fields, which have not been commercialised yet, include SAW devices for electronic analog filtering [117] as well as sensors for gases. One of the advantages of the III-Nitrides for gas sensors is the capability to operate at high temperatures, e.g. in engine exhaust gases. These devices consist of a catalytic metal Schottky contact either directly on GaN, forming a Schottky diode, or on an AlGaN/GaN heterostructure transitor, acting as a catalytic gate. First investigations on Pt:GaN Schottky diodes were carried out in 1999 [118] and the research progress has been reviewed by Eickhoff [57] and Pearton [13]. The application of AlGaN/GaN heterostructures for fluid sensing is the main topic of this work and is therefore discussed in more detail in section 4.4, after the discussion of the basic AlGaN/GaN heterostructure, the formation of the 2DEG and significant defect-related phenomena.

4.2 AlGaN/GaN-Heterostructure and the Two-Dimensional Electron Gas

The general structure employed in this work consists of a GaN buffer and an AlGaN barrier layer (fig. 4.2). Commonly, this structure is deposited on a sapphire wafer with a AlN nucleation layer, to reduce lattice mismatch, and terminated by a thin GaN layer, to increase the chemical stability of the device. For the principal description of the 2DEG generation that is given in this section, however, the GaN cap layer is disregarded. The piezoelectric and spontaneous polarization properties of the III-Nitrides are employed for the construc-

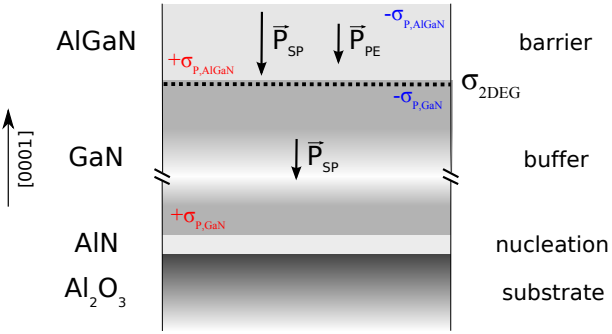

Figure 4.2: Schematic drawing of an AlGaN/GaN heterostructure (Ga-face) with spontaneous and piezoelectric polarization field and induced charges.

tion of AlGaN-based field effect devices, such as HEMTs or Schottky diodes. The discontinuity of the spontaneous polarization P_{SP} and piezoelectric polarization P_{PE} at the GaN/AlGaN interface induces stationary charges σ_P. For the crystal orientation [0001] (Ga-face) a negative charge is generated at the upper and a positive charge at the lower interface. For GaN and $Al_{0.3}Ga_{0.7}N$ the charge induced by spontaneous polarization $\sigma_{P_{SP}}$ is approximately $1.8 \times 10^{13}\,\mathrm{cm}^{-2}$ and $2.8 \times 10^{13}\,\mathrm{cm}^{-2}$, respectively, estimated using equation 7 given in [115]. An additional piezoelectric polarization is generated by the tensile strain in the barrier due to the lattice mismatch of GaN and AlGaN. The charge $\sigma_{P_{PE}}$, induced by piezoelectric polarization, typically amounts to about $6 \times 10^{12}\,\mathrm{cm}^{-2}$, for $Al_{0.3}Ga_{0.7}N$ on GaN [119], and adds to the polarization of the AlGaN barrier. The resulting charges $\sigma_{P,AlGaN}$ and $\sigma_{P,GaN}$ are shown in figure 4.3. At the GaN/AlGaN interface $+\sigma_{P,AlGaN}$ is not fully compensated by $-\sigma_{P,GaN}$, resulting in a remaining positive stationary charge density σ_{diff} of more than

$1 \times 10^{13}\,\mathrm{cm}^{-2}$. To maintain charge neutrality free electrons accumulate near the interface in the GaN buffer shielding σ_{diff} and generating a very thin sheet of electrons, the so called two-dimensional electron gas (2DEG) with a carrier density σ_{2DEG} on the order of $1 \times 10^{13}\,\mathrm{cm}^{-2}$ [110]. Most of the electrons are supplied by surface states at the upper AlGaN/air interface which in turn compensate $-\sigma_{P,AlGaN}$ [120]. It should be noted that the compensation at the lower and the upper AlGaN interface is not complete and an electric field $F_{b,AlGaN}$ on the order of $-300\,\mathrm{kV\,cm}^{-1}$ exists in the barrier. Therefore, the surface of such a heterostructure without a GaN cap layer in air exhibits a positive surface potential Φ_0 of approximately 0.7 V. When the structure is capped with an additional GaN layer a surface potential of about 0.3 V is observed [119]. It should be noted that the value of the surface potential depends on the growth method as shown by Köhler et al. [121]. Owing to the advances in epitaxial growth, the 2DEG can be confined about (10–30) nm below the surface - compared to several 100 nm in Si-based devices - enabling a more effective modulation of the charge density through electric fields. Additionally, the AlGaN/GaN heterostructure exhibits a captivating simplicity in its structure without the need for doping and has superior sensitivity, noise characteristics, and chemical and thermal stability.

4.3 Defect-related Phenomena

As the epitaxial growth of the AlGaN/GaN-heterostructure does not result in perfect crystalline layers, the crystal quality is influenced by several structural and energetic defects, which can be either intrinsic or extrinsic. The most common point defects (one-dimensional) include nitrogen vacancies as well as contamination with oxygen, carbon or

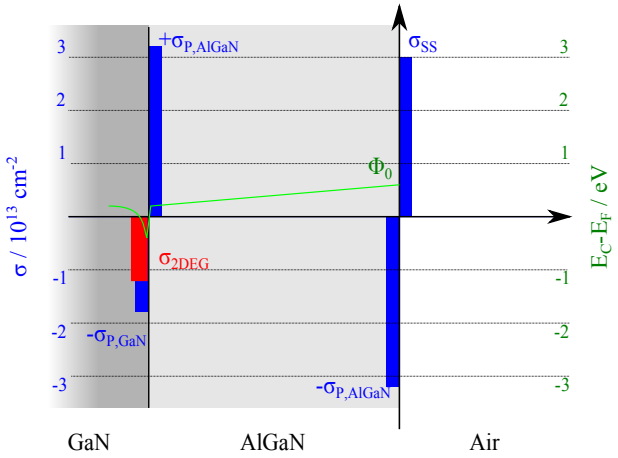

Figure 4.3: The charge and potential distribution in an AlGaN-heterostructure (stationary charges - blue, free charge - red, difference conduction band to Fermi level - green)

silicon [56]. Their energetic levels within the band gap influence the electronic properties of the devices, especially for deep-level defects. The phenomena of persistent photoconductivity and current collapse are mainly attributed to these defects.

Two- and three-dimensional defects are mostly of a structural and intrinsic nature, but nevertheless have a profound influence on the energetic structure. These defects include dislocations, stacking faults and grain boundaries, as well as interfaces in general. For example, the so-called threading dislocations are always present in GaN-based layers that have been deposited on mismatched substrates like sapphire [122]. For heterostructures grown with metal organic chemical vapour deposition (MOCVD) the dislocation density is in the range of $(1 \times 10^9 – 1 \times 10^{10})\,\mathrm{cm}^{-2}$ [123, 124]. It should be noted that the dislo-

cations originate from the substrate/semiconductor interface and run vertically through whole heterostructure up to the surface. Although appropriate measures can be taken to minimise the number of dislocations reaching the surface, these types of defects always permeate the whole structure. As the dislocations interrupt the crystal structure they are also the more reactive sites, which in turn leads to the incorporation of impurity atoms (point defects). The most important aspect for this work, however, is their influence on the chemical stability of the sensors, as intentional (etching) and parasitic (corrosion) wearing out of the surface always starts at those sites.

In the following section a brief overview of the defect-related phenomena persistent photoconductivity (PPC), current collapse (CC) and photoelectrochemical etching is given.

4.3.1 Persistent Photoconductivity

A drawn-out decay of the photoconductivity after darkening has been observed for semiconductor materials like AlGaAs [125] as well as GaN and AlGaN [126, 127]. This characteristic is commonly referred to as persistent photoconductivity. For these material systems the generation/recombination process is disturbed by an additional energy barrier. As energetic defects in the band gap have been identified to be responsible for the PPC, it is also observed for sub-band gap illumination. Although there is some debate about the exact origin and mechanism, it is agreed that the additional charge carriers originate from one or more types of deep-level defects. The PPC has been observed in both n-type [126, 128, 129], p-type [130] and undoped GaN [131] as well as AlGaN/GaN-heterostructures [127, 132]. However, it should be noted that n-type GaN without PPC has also been reported [128], whereas

no such observation has been made for AlGaN/GaN heterostructures. Apart from gallium vacancies [133] or specific surface states [134], especially the contamination with oxygen has been suggested as the cause for the PPC [135, 136]. Additionally, the frequently observed yellow luminescence in photoluminescence measurements of GaN is thought to be connected to the PPC [131]. A detailed discussion of the possible mechanisms, which include macroscopic potential fluctuations or microscopic potential barriers, has been given by Seifert [136].

The typical course of the photocurrent upon changing the illumination conditions is given in figure 4.4, for an AlGaN/GaN Schottky diode. The drawn-out decay after photoexcitation can be described by a stretched exponential function [127]:

$$I(t) = I_{dark} + (I_0 - I_{dark}) \exp((-\frac{t}{\tau})^{\beta}) \tag{4.1}$$

with the dark or equilibrium current I_{dark}, the current upon illumination I_0, the time constant τ and the exponent β. Values between 0.2 and 0.4 have been reported for β and τ was found to be on the order of $(1 \times 10^3$–$1 \times 10^4)$ sec [127, 126, 132, 16]. Although all semiconductor sensor devices exhibit a light sensitivity to some extent and should therefore be kept under constant illumination conditions, the PPC complicates matters considerably. The most obvious choice of illumination - none or darkness - will lead to a prolonged and non-linear drift of the output signal. This is why an optimisation of either the semiconductor or the measurement conditions are mandatory for accurate and reproducible measurements. First optimisation steps for AlGaN-based pH-ISFETs have been performed by Kittler [16], including modulation doping with Si, compensation circuits with passivated sensors and the continuous illumination with an LED. The optimisation of the semicon-

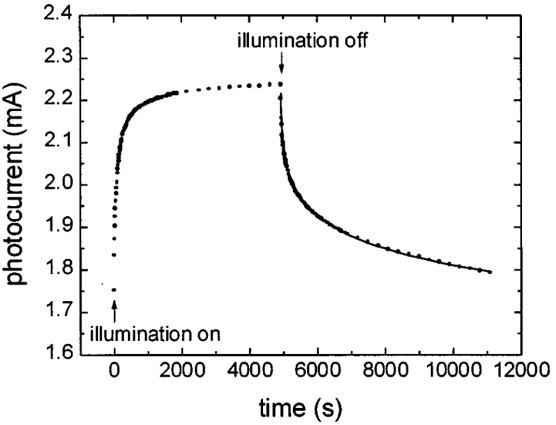

Figure 4.4: Transient response of an AlGaN/GaN-diode upon switching the illumination on and off that demonstrates the impact of PPC [132].

ductor structure by modulation doping with Si succeeded to increase the absolute value of the sheet carrier density N_s and thus decreased the relative influence ambient illumination changes by a factor of up to 3. Additional compensation with a simple difference circuit of a pH-insensitive and an active sensor achieved another decrease by a factor of 5. This decreased the light-induced change of the sensor signal equivalent to 0.2 pH. The continuous illumination of the pH-ISFET with an LED was used to excite as many charge carriers as possible into the conduction band. The variation of the drain current that is measured when the ambient illumination is switched off is plotted in figure 4.5 versus the wavelength of the employed LED. A pronounced decrease of ΔI_{DS} is observed for wavelengths close to the band gap of GaN. A pH-equivalent of 0.07 pH was found when a violet LED ($\lambda_{Peak} = 400\,\mathrm{nm}$)

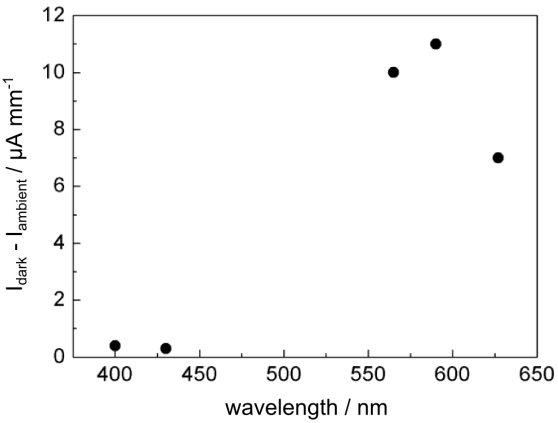

Figure 4.5: Variation of the drain current in an AlGaN-based pH-ISFET upon switching off the ambient illumination plotted versus the wavelength of the additional, continuous LED illumination [16].

is employed. For other wavelengths the variation is larger by a factor of 10. It should be noted that all optimisation approaches discussed in this publication are targeted at reducing the symptoms of the PPC, rather than eliminating its cause. For a true reduction of the PPC the growth of the heterostructure needs to be optimised. Only in this way can the responsible energetic and structural defects be minimised. Nevertheless, the results for the modulation doping and the continuous illumination were taken as a starting point for the optimisation steps presented in this thesis.

4.3.2 Current Collapse

Another kind of trap-related instability that has been observed in GaN-based devices is the so-called current collapse (CC). This phenomenon severely limits the output power of HEMTs and has also been reported for Si- and AlGaAs-based devices [137, 138]. It manifests itself as a reduced drain current characteristic after previous high drain bias [139, 140, 141] or for high frequencies [142, 143, 144]. From the $I_d(U_{ds})$ characteristic in figure 4.6 the large extent of the CC is evident, as the drain current for short pulses of U_{gs} (line + dots) is much smaller in comparison to the values obtained for a constant (dc) U_{gs} (solid line). Similar characteristics have been observed when the device was stressed with a high drain bias. To explain the CC, different mechanisms have been suggested, which focus on the outer 2DEG portion that is not directly influenced by the gate (location z in 4.7c). In general, a partial depletion or pinch-off of the intermediate 2DEG - between gate and drain - is assumed. This depletion is thought to be due to either the trapping of hot carriers by deep centers in the GaN buffer layer [140, 141] or trapping in surface states [142, 143, 145].

The latter mechanism is often modelled as a virtual gate, which induces a depletion of the intermediate 2DEG and reacts with much larger time constants to bias voltage changes, compared to the gate. The increased time constant is caused by the carrier capture/emission characteristic of the associated surface charges. The charging and decharging mechanism of the surface states is assumed to take place via leakage or tunneling currents from the metal gate electrode [144, 145]. In figure 4.7 the CC induced by surface states and charged by tunneling is illustrated. By spatially resolved measurements of the surface potential (fig. 4.7b) an increased negative potential was found near the gate after

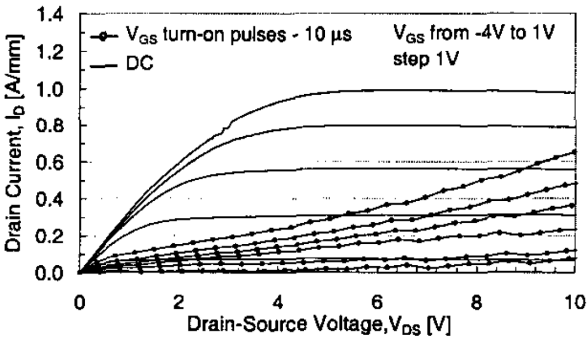

Figure 4.6: Output characteristic $I_d(U_{ds})$ obtained at DC and by pulsing U_{gs} from $-4\,\mathrm{V}$ to a specific U_{gs} that demonstrates the impact of the CC. [144]

stressing the device. This charge accumulation at z (fig. 4.7c) acts as a virtual gate that depletes the underlying 2DEG. Figures 4.7d-f show the band diagrams and sheet charge distributions before stress, after stress and the compensation with UV light.

It was found that the CC can be reversed by liberating the trapped carriers through thermal or optical energy. Especially the restoration of the drain current characteristic by incident light of near-or super-band gap energy is reported in the literature [140, 143, 145]. From this observation and the correlation of the deep-level trap energies derived for the CC with trap energies assigned to the PPC [131, 129], Klein et al. suggest that the traps responsible for the CC and the PPC may be the same [140]. This connection would imply that the PPC is also induced by surface states, arguing for the explanation put forth by Horn et al. [134]. In addition to optical restoration, it was found that the passivation of the free surface with SiN_x [143, 145] as well as the appli-

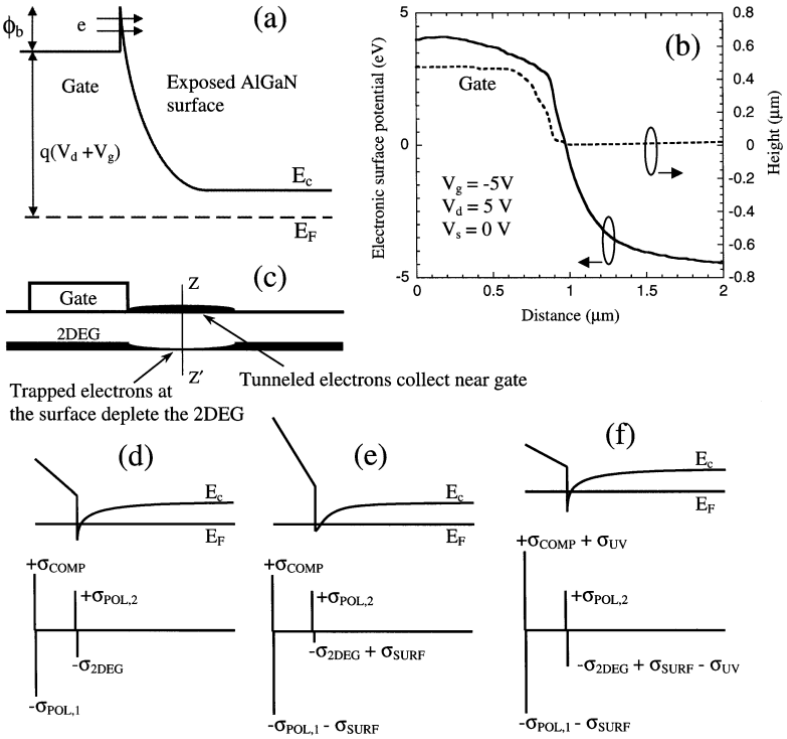

Figure 4.7: (a) Schematic band diagram explaining the tunnelling of electrons from the gate to the surface when a device is stressed by applying biases $-V_g$ and V_d to the gate and the drain, respectively. (b) Measurement of the surface potential variation from the gate toward the drain. (c) Schematic cross section illustrating the concept of a virtual gate. Band diagrams and sheet charge distribution along the z-z' line are shown (d) before stress, (e) after stress, and (f) after UV illumination of the stressed device. [145]

cation of field plates [146, 147] results in a reduction of the CC effect. The passivation is thought to prevent charge from being trapped in surface states, due to a reduction of the surface trap density, alteration of the surface donor states or a decrease of the surface barrier [145].

4.3.3 Defect etching

Although the chemical stability of III-nitride based devices is highlighted in the introductory remarks of nearly every publication on AlGaN fluid sensors, it is clear that every device is only as stable as its weakest link. Leaving aside the aspects of device passivation and packaging for the moment, the structural defects in the crystalline layers themselves are especially critical locations. The defect-free portions of e.g. GaN layers are indeed very hard to etch, with the Ga-face exhibiting a higher stability than the N-face. The 2-dimensional defects, however, are susceptible to acidic and alkaline etching solutions. These properties have been exploited to determine the dislocation density by counting the number of etch pits after exposing samples to contrated H_3PO_4 or KOH at elevated temperatures [148, 124, 122]. The exact assignment of the etch pits to specific types of dislocations is controversial [122], but they are believed to include nanopipes [148] and threading dislocations [123]. A typical AFM image that reveals etch pits in GaN after exposure to molten KOH at 200 °C is given in figure 4.8 for different etch durations. The hexagonal shape of the etch pit is an indicator that lateral etching prevails for this process.

It is apparent from these images that this etching procedure is not suitable for the selective structuring of III-nitrides. To achieve more homogenous results and control the lateral and vertical etch rates, bias-assisted and photo-enhanced etching techniques have been developed,

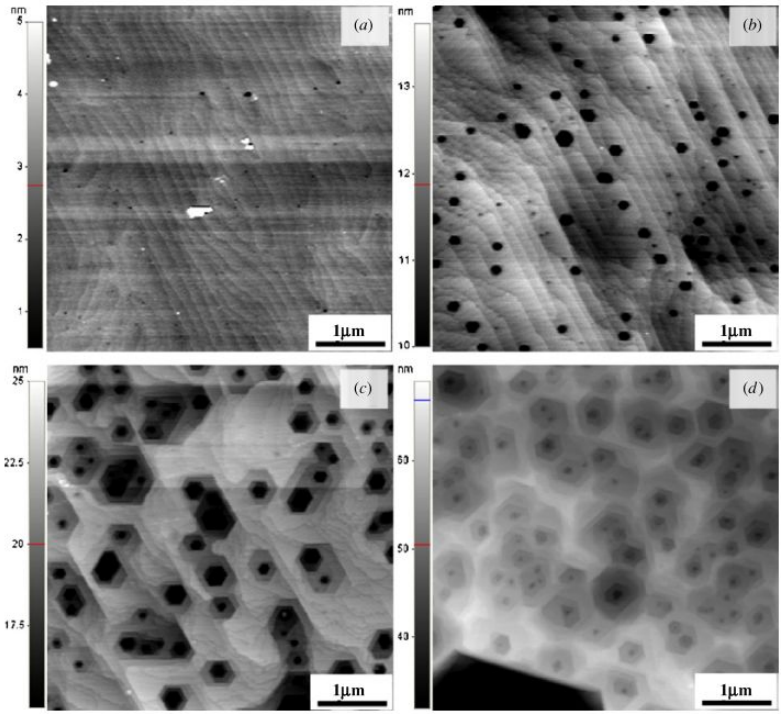

Figure 4.8: AFM images of GaN samples etched in molten KOH at 200 °C for 60 s (a), 180 s (b), 360 s (c) and 900 s (d). [122]

commonly referred to as photoelectrochemical etching. Using diluted solution of KOH and UV illumination at specific intensities, rough surfaces at high vertical etch rates [149, 150, 151] and smooth surfaces with low vertical etch rates [152, 153] were achieved. The additional application of a bias voltage can be used to optimise the undercutting of GaN-based MEMS [153] and allows for etching with solutions that were commonly not considered as etchants, like CO_3COOH or HNO_3 [154]. The mechanism of photoelectrochemical etching is thought to be the following: upon illumination, as well as for the applied bias voltage, positive charge (holes) accumulate at the surface of the semiconductor, which support the oxidation of Ga [149]. This Ga_xO_y is then removed by the acidic or alkaline etchant. For the overall reaction of GaN Youtsey et al. [150] give the following equation:

$$2\,\mathrm{GaN} + 6\,\mathrm{h}^+ \longrightarrow 2\,\mathrm{Ga}^{3+} + \mathrm{N}_2. \tag{4.2}$$

When the oxide etch rate is reduced by dilution of the etching solutions the ratio of oxide growth and oxide etch can be shifted towards photoelectrochemical oxidation. For GaN, photoelectrochemical oxidation has been reported with (deionised) water when the bias voltage exceeds 3 V [155]. With a subsequent etching surfaces with low etch damage were obtained [156].

4.4 Applications as Fluid Sensors

The development of AlGaN-based fluid sensors is illustrated in this section with respect to their historical background and the state of the art in the application fields pH-, anion- and functionalised bio-sensing.

4.4.1 Historical Background

For the construction of chemical sensor devices the modulation of the 2DEG charge density by variation of surface potential is exploited. For this purpose the gate metallisation of the known AlGaN/GaN HEMT heterostructure are omitted, exposing the bare GaN capped surface. A modulation of the channel current I_d was observed by Neuberger et al. [157] when ions generated by a plasma spray device were directed at the surface. This was attributed to the change in the surface charge by incident ions which in turn enhanced or depleted the 2DEG. It was observed that every incident negative ion displaces one electron from the 2DEG. As cyclic changes were found to be completely reversible [158], irreversible processes like trap formation or surface oxidation could be ruled out. Although the strong response on charges was first termed a parasitic effect, which had to be eliminated or controlled for the optimization of HEMTs, the potential for sensor applications was demonstrated shortly afterwards.

The first application of the AlGaN/GaN heterostructure as a fluid sensor was reported for different organic solvents applied to the surface. It was found that the drain current is affected by the dipole moment of the solvent p [159]. However, it was also noted that the molecule size yielded different results for similar dipole moments. This and the unordered dipole orientation in liquids impaired quantitative determination of dipole moment but allows for qualitative evaluation of polar contaminations in nonpolar liquids (e.g. hydraulic oil). Similar results were later reported for the exposure to organic solvents [160, 161], polymer and block copolymer solutions [162]. A linear relationship between the drain current and the ratio of the solvent's dipole moment and dielectric constant p/ϵ was shown by Kokawa et al. [161].

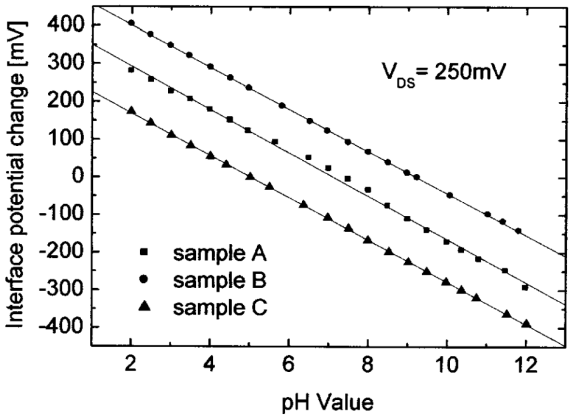

Figure 4.9: pH-dependence of the surface potential of different AlGaN/GaN-heterostructures (A) with Mg-doping, (B) with Mg-doping and additional thermal oxide, and (C) without doping and oxidation [11].

Reproducible and quantitative results for an AlGaN/GaN fluid sensor were first reported in 2003 by Steinhoff et al. [11]. They compared different transistor structures with respect to their pH response and proposed that even the thin surface oxide layer forming upon exposure to atmosphere is sufficient for a linear response in the range from pH 2 to 12 (fig. 4.9). X-ray Photoelectron Spectroscopy analysis of as-deposited GaN revealed the formation of a thin oxide film at the surface [163, 164]. However, the claim made by Steinhoff et al. that no systematical investigation on the ion sensitivity of III-Nitride-based chemical sensors had been done before was not correct. In 1995 Kocha et al. used electrochemical impedance spectroscopy to investigate the GaN-electrolyte interface of MOCVD grown 2 µm Si-doped GaN layers

[165]. They found a linear pH-sensitivity of 55 mV/pH in the pH range from 2 to 14, although no further research was published afterwards.

Recently, the advantageous transparency of the material system has been utilised by Lübbers et al. [166] for the construction of a multiparameter analysis system for biochemical reactions. Simultaneous measurement of pH-value and optical absorption was shown for sample volumes down to 700 nl, employing an AlGaN-based pH-ISFET in combination with GaN-based optoelectronic components (laser diode, photodetector). The results obtained for the investigated enzymatic reaction agreed well with published values, demonstrating the feasibility of the combined opto-electrochemical approach.

Since the first publications on GaN-based fluid sensors in 2001 about fifty publications in international journals and some ten proceeding contributions on their research progress have been published. Apart from very few fundamental research papers on the sensing mechanism or theoretical descriptions, most publications focus on functionalisation or surface modification for innovative devices like biosensors. Some of those investigations, however, lack a certain scrutiny and present disputable conclusions. Therefore, more systematic research is needed if not only innovative, but also accurate and reproducible devices are to be developed.

4.4.2 Sensors for pH-Value

The pH-sensing properties of $Al_xGa_{1-x}N$ that have been reported by several different research groups are summarised in table 4.1. As no marked differences in the pH-sensitivity have been reported for different underlying structures, e.g. bulk GaN or (GaN)/AlGaN/GaN-heterostructures, and measurement techniques, e.g. electrochemical

impedance spectroscopy or potentiometry, the sensing mechanism can be attributed to a pure surface effect. Furthermore, the exact composition of the immediate surface layer does not seem to influence the pH-sensitivity appreciably as long as $Al_xGa_{1-x}N$ with $0 \leq x \leq 1$ and no or only moderate Si-doping is used. Interestingly, similar results had been reported for a Si-ISFET with an AlN sensing layer, even before the first AlGaN-ISFET had been developed [167]. The pH-response is attributed to the presence of a metal oxide layer on the AlGaN/GaN heterostructure, formed either simply by exposure to the atmosphere or due to other oxidation procedures. Therefore the site-dissociation model can also be applied to these devices.

One of the advantages of AlGaN-based pH-sensors compared to Si-based ones is that neither thermal oxidisation nor a specific ion sensitive oxide layer, e.g. Ta_2O_5 or Al_2O_3 are needed. Whether the native oxide is really suitable for stable, reproducible and accurate measurements cannot be derived from most publications. The results on AlGaN-ISFETs with native oxide published by Kang et al. indicate that high concentrations of HCl (5 and 10%) lead to a depletion of the 2DEG [160] contrary to the commonly observed enhancement. Additionally, they observed that measurements are prone to drift and artifacts [18]. Doubts about the suitability and stability of the native oxide have also been raised by Kokawa et al. [161] and Alifragis et al. [168]. The former argue that Ga oxides are soluble in alkaline solutions and can therefore not serve as a stable pH-sensitive layer, whereas the latter propose a fundamentally different theory for the pH-sensitivity. They assume that an anion selectivity is responsible for the pH-dependence. This is also thought to account for the seemingly reversed behaviour at high concentrations of HCl reported by Kang et al. [162].

Table 4.1: Published experimental pH-sensitivities of GaN-based fluid sensors.

structure	measurement technique	pH-sensitivity (mV/pH)	ref.
GaN (2 µm) bulk	electrochemical impedance spectroscopy	55.0	[165]
GaN (1 µm) bulk	potentiometric	51.0 ± 3	[169]
GaN:Si (2 µm) bulk		54.0 ± 4	
AlN (100 nm) on Si-ISFET	transfer characteristic	55.8	[167]
GaN:Si (60 nm)/GaN:Mg HEMT		57.3	
oxidised GaN:Si (60 nm)/GaN:Mg HEMT	constant voltage (dyn.)	56.6	[11]
GaN (3 nm)/AlGaN/GaN HEMT		56.0	
$Al_{0.23}Ga_{0.77}N$ (22 nm)/GaN HEMT	transfer characteristic	57.5	[161]
GaN (2 nm)/AlGaN/GaN HEMT	transfer characteristic	50.0	[166]
GaN (3 nm)/AlGaN/GaN HEMT	transfer characteristic	57.0	[170]

However, HCl concentrations of 5% (approx. 1.5 M) correspond to a theoretical pH-value below zero which is far beyond the commonly claimed pH range of 2 to 12. Therefore, wet etching of the oxide layer is likely to take place reducing the number of amphoteric hydroxyl groups at the surface and in turn the number of positively charged groups. Additionally, the etching process can reduce the surface-to-2DEG distance leading to an effective depletion of the 2DEG. The reported solubility of GaN in alkaline solutions like NH_4OH [163, 171] is also an example for wet etching that takes places outside the claimed pH range and at elevated temperatures. However, the stability of metal oxides in warm alkaline solutions [172] is a general challenge shared by almost every pH-sensor - from the glass electrode to metal/metal oxide electrodes and Si-ISFETs.

Scandium oxide (Sc_2O_3) [18] and silicon nitride (SiN_x) [161] have also been deposited on AlGaN HEMTs as alternative sensing layers. For Sc_2O_3 superior properties are claimed with respect to stability and resolution compared to the native or thermal oxide on AlGaN structures. However, the presented data in [18] for the native oxide seems to be a single worst case rather than a typical measurement, exhibiting drift and measurement artifacts, whereas the data for Sc_2O_3 is likely to be a selected optimal measurement. Especially the comparison to the data of Steinhoff et al. [11] or Kokawa et al. [161] show that Sc_2O_3 is not superior to the native oxide (fig. 4.10).

4.4.3 Sensors for Anions

Another issue that is not agreed on in literature is whether GaN exhibits anion selective properties and its pH-response should be explained by the binding of hydroxide ions (OH^-). This is contradictory to the

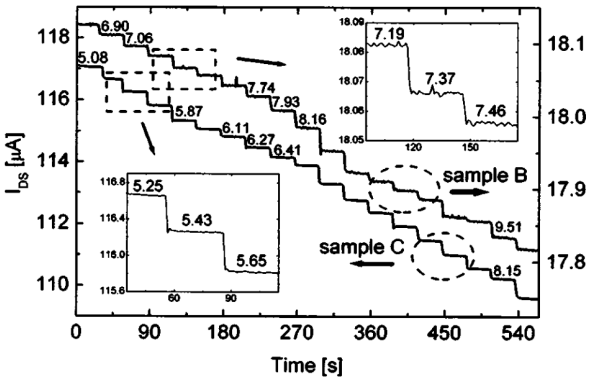

(a)

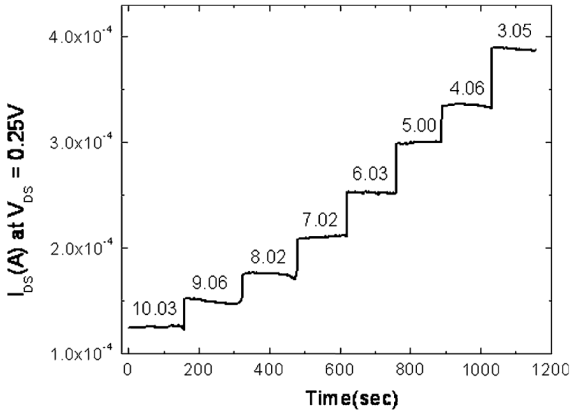

(b)

Figure 4.10: Transient response of the drain current I_d to changes of pH-vlaue for (a) AlGaN-ISFETs with thermal (sample B) and native oxide (sample C) [11] and (b) AlGaN-ISFETs with a Sc_2O_3 layer [173].

commonly accepted binding of hydronium ions H_3O^+ as described by the site-dissociation model. Several investigations on the anion selectivity and sensitivity were published by the Chaniotakis group in 2004 and 2005 [174, 175, 176]. Potentiometric measurements and electrochemical impedance spectroscopy were performed on MOCVD grown Ga-face GaN samples in deionised water (DIW) with added potassium salts versus an Ag/AgCl reference electrode and a $1\,cm^2$ Pt counter electrode. The samples were not pretreated, contacted with indium and encapsulated in epoxy glue. Adding aliquots of 0.1 M salt stock solutions to 50 ml DIW (Nanopure, approx. $18\,M\Omega\,cm$) the potentiometric response for KF, KCl, KNO_3, KSCN, K_2HPO_4 and $KClO_4$ was recorded from $1\,\mu M$ to 10 mM. The slope for these potassium salts was approximately 40-50 mV/decade in the linear region from 0.1 to 10 mM with a slightly higher slope of 70 mV/decade for KSCN 4.11a. The total potentiometric response ($1\,\mu M$ to 10 mM) varies from 140 mV for KF to 227 mV for KSCN. From this data an anion selectivity is claimed with selectivity coefficients $K^{pot}_{Cl,X}$ from 0.09 to 1.94. Interestingly, the potential slope for the pH-sensitivity is much lower with approximately 10 mV/pH.

The proposed theory for this response is based on the assumption that the sample is Ga-terminated and that its surface "...remains clean down to atomic level" [174]. In this case the gallium atom is found to be more electron deficient than the nitrogen atom from theoretical studies [177] and therefore a better Lewis acid. The anions in the electrolyte can coordinate with the gallium leading to a preferential adsorption of anions in the Helmholtz layer and the observed potentiometric response. To prove their point the interfacial capacitance is calculated from impedance spectra at different concentrations of KCl and compared to the measured potential. From the good relationship between

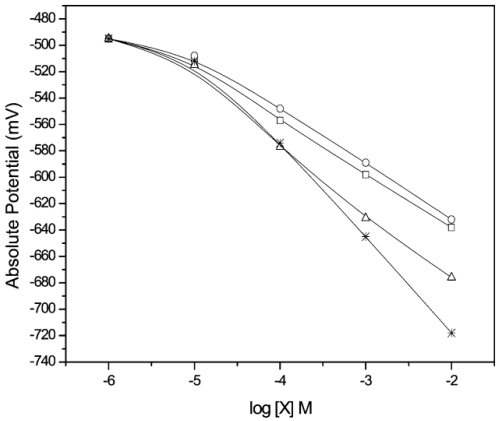

(a)

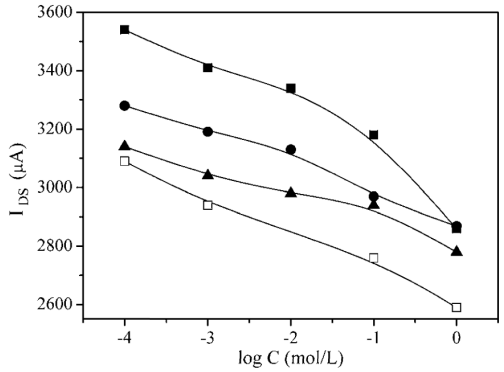

(b)

Figure 4.11: (a) Surface potential of a GaN-bulk electrode versus the concentration of KF (open circle), KCl (open square), KNO_3 (open triangle) and KSCN (star) [174].
(b) Drain current of an AlGaN-ISFET versus the concentration of KCl (filled squares), KBr (filled circles), KNO_3 (filled triangles) and KSCN (empty squares) [168]. All electrolytes were dissolved in DIW.

both traces the validness of the theory is claimed. However, several details in the theoretical discussion and the experimental procedure are questionable. Firstly, it is nearly impossible to obtain atomically clean surfaces, especially without pretreatment. It has been shown in many publication [178, 163, 179] that a native oxide is present on GaN once it has been exposed to air. This layer can only be removed by specific pretreatments like wet chemical etching with NH_4OH [163], HCl [180] or HF [181]. Therefore the surface that is exposed to the electrolyte is more likely to be a non-stochiometric Ga_xO_yN. Secondly, the preparation of electrolyte solution from DIW and salt stock solutions without the control or monitoring of pH-value is inadequate for a material with known pH-sensitivity. The pH-value of DIW only theoretically equals 7 but practically ranges from 7.5 to 5.5 and especially ultra-pure water is very susceptible to atmospheric CO_2, which leads to an acidification of the solution. Other influences that can change the pH-value include the huge increase of ionic strength within the concentration series and the diluting effect when adding the stock solutions. The results for K_2HPO_4 are especially dubious as this solution is used as an pH-buffer and definitely changes the pH-value with increasing concentration. Simulations with CurTiPot [182] give pH7.5 for 1 μM and pH9.3 for 0.1 M. The close agreement of interfacial capacitance and potential cannot prove the elaborated theory as it is unclear whether the main contribution to the capacitance is really due to specific adsorption in the Helmholtz layer or if it originates from the diffuse Gouy-Chapman layer. The discussion in [176] even contradicts the assumption of specific adsorption by stating "... that the measured capacitance is due to the Gouy diffuse layer". Therefore the observed anion sensitivity is more likely to be induced by the varying ionic strength, which in turn has a major influence on the capacitance of the Gouy-Chapman layer

(Eqs. 3.7 and 3.9). Nevertheless, the exact origin of the pronounced slope around or even above the Nernstian limit still remains unclear.

The Chaniotakis group also reported on the anion response of AlGaN/GaN-HEMTs applying the same theoretical background [168]. The measurement results show a slight decrease of the drain current with increasing salt concentration which is similar for all employed electrolytes (KCl, KBr, KNO_3 and KSCN) and much lower than the observed pH-dependence of I_d (fig. 4.11b). Another investigation from the Pearton group employing HEMT structures in NaCl and NaF solutions also confirms that no pronounced anion sensitivity or selectivity exists [183]. This publication also suffers from experimental shortcomings by not monitoring the pH-value and failing to state whether and what kind of reference electrode was used. On top of that the conclusion of this article was copied word for word from Mehandru et al. [160] and therefore summarises completely different results.

A more recent study reports on similarly prepared Ga-face GaN bulk electrodes with potential slopes between 33 and 52 mV/dec for different potassium electrolyte solutions and about 10 mV/decade for the pH-sensitivity [184]. This confirms the experimental results from the Chaniotakis group, but not necessarily their conclusions. However, more care was take in the experimental setup of this study by purging the solutions and the measurement cell with argon. This way it was ensured that no CO_2-induced pH drift could occur in the electrolyte solutions. Nevertheless, the fact that the slope for all tested electrolyte solutions is comparable once again argues for the general influence of the ionic strength rather than a specific adsorption of anions.

The impact of the polarity of the GaN electrode was investigated by Ba et al. [169] by comparing their results for a N-face GaN electrode to the results of the Chaniotakis group. For potassium (KCl, KBr,

KNO_3, KSCN, $KClO_4$, KH_3PO_4 and KSO_4) and chloride electrolytes (NaCl, KCl, Mg_2Cl and Ca_2Cl) no pronounced response was measured between 1 μM and 10 mM. A pH-response of about 53 mV/pH was reported. Based on these results it is concluded that N- and Ga-face GaN can be discriminated by their potentiometric response to anions and pH. However, it has to be noted that all measurements were carried out using a 10 mM LiCl background electrolyte, claiming that LiCl does not exhibit any potentiometric response. Even if this assumption holds true, the background electrolyte will still determine the overall ionic strength for most part of the concentration series, as its concentration is equal to the highest concentration investigated. Therefore, the observation that no pronounced dependence towards specific cations or anions exists is indirect proof for the general dependence to ionic strength. The discrimination between N- and Ga-face is not proven as the authors did not repeat their experiments for Ga-face material. The direct comparison to [176] is invalid, due to the different composition of the employed electrolyte solutions.

It can be summarised that published articles on GaN-based anion sensors reveal a different response to ions for Ga-and N-face GaN bulk electrodes compared to AlGaN-ISFETs. The pronounced sensitivity to electrolyte concentration series for Ga-face GaN is likely to be due to the change in ionic strength and could also be influenced by a general counter ion adsorption depending on the actual surface charge. A selective anion response can not be derived from the published results. The reason for the low pH-sensitivity of Ga-face GaN electrodes could be the lesser amount of surface oxide groups. Whether the response of N-face GaN electrode to ions deviates from Ga-face cannot be decided due to the discussed differences in the electrolyte solutions. The pH-response of N-face GaN electrodes, however, is high and in agreement

with the results for AlGaN-ISFET structures. These structures do not show significant response to anions but have a pH-sensitivity around 53 mV/pH, although they are commonly based on Ga-face material.

4.4.4 Functionalised Sensors and Biosensors

The AlGaN/GaN heterostructure has also been employed for various forms of functionalised sensors and biosensors. Basic functionalisation approaches have included the oxidation of the surface using dry and wet thermal and wet chemical methods [179, 12, 185] in order to improve the wetting behaviour. The coating with polymeric ion selective membranes has been demonstrated for the fabrication of selective ion sensors [186, 187]. It was also shown that the GaN or AlGaN surface can be functionalised with biomolecules by direct chemisorption [188, 189] or silanisation followed by covalent binding [190, 191, 192]. The principal possibility of cell-on-chip concepts with several different cell lines [12, 108, 14] and the high biocompatibility of the III-Nitrides emphasises the potential of the material system for biosensors.

Biosensors based on AlGaN/GaN heterostructures can be categorised into four classes: immunologically-based sensors (Immuno-FETs), enzyme-modified sensors (EnFETs), DNA-modified sensors (DNA-FETs) and cell-based sensors (Cell-FETs). Immuno-FETs have been reported for biotin-streptavidin binding [190] and prostate specific antigen (PSA) detection [193]. The detection of penicillin with covalently bound penicillinase is an example for an AlGaN-EnFET [191, 166]. The very specific hybridisation of DNA strands was also reported, employing an AlGaN-DNA-FET with immobilised single stranded DNA [194]. The label-free measurement of reactions of adhering neuronal cells to ion channel inhibitors [195] demonstrates that Cell-FETs can be fabricated.

A comprehensive treatment of III-Nitride biosensors can be found in the review published by Cimalla and Lübbers et al. in 2010 [15].

4.5 Theoretical Description

For the theoretical description of AlGaN-based ISFETs the principles from the Si-based ISFETs are applied with regard to charge adsorption and charge balancing. Therefore the equations from section 3.3.1 can in principal be applied using the values for Ga_2O_3 from table 3.1. There is, however, a difference in the underlying semiconductor structure due to the large polarization fields in the heterostructure, which induce the 2DEG. Additionally, the much smaller insulator thickness results in a conducting channel (2DEG) very close to the surface. These two differences have been discussed by Bayer et al. [79] using the site-dissociation model and self-consistently solving the Poission-Boltzmann equation for the semiconductor-oxide-electrolyte structure that is shown in figure 4.12. The heterostructure is very similar to one employed in this thesis, but for a thicker AlGaN barrier layer.

The fixed charges $\sigma_{polarization}$ arise from the spontaneous and piezoelectric polarization fields at the GaN/AlGaN interfaces resulting in the 2DEG at the lower interface. An additional polarization charge is assumed at the GaN/oxide interface, which is compensated at the nucleation layer. The actual pH-dependent charge $\sigma_{adsorbed}$ is situated at the oxide/electrolyte interface and is described using the site-dissociation model. It is claimed that some part of the adsorbed charge (termed σ^*) reaches the GaN/oxide interface through voids in the oxide. This is done to account for the observation that the value $\sigma_{adsorbed}$ needs to be higher than initially calculated. Although this assumption may be valid, the high values of the surface charge at metal oxide/electrolyte

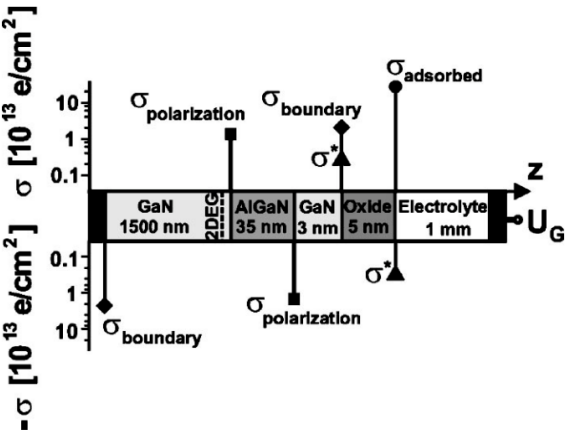

Figure 4.12: Schematic drawing of the AlGaN/GaN-heterostructure simulated by Bayer et al. with corresponding interface charge densities [79].

interfaces are commonly modelled using counter ion binding (cf. section 2.1), which is not considered in this publication. The compensation of the adsorbed charge in the electrolyte is solved numerically using the Poission-Boltzmann equation for a mono- and a divalent electrolyte. Therefore the modeling of the electric double layer only accounts for a diffuse ionic layer and corresponds to the Gouy-Chapman theory.

The best fit to the experimental data of Steinhoff et al. [11] was obtained for $pK_+ = 6$, $pK_- = 8$, N_{ss} =$9 \times 10^{14}\,\mathrm{cm}^{-2}$ and $\sigma^*/\sigma_{adsorbed} = 0.02$ resulting in a sensitivity of 55.9 mV/pH. Furthermore they found that N-face material results in a more pronounced manipulation of the 2DEG with changing pH as the channel is located more closely to the surface (20 nm compared to 43 nm for the Ga-face). The variation of the Al-content in the barrier is also discussed with the conclusion that

a lower content reduces the sheet carrier density in the 2DEG whereas the absolute pH-induced change in σ_{2DEG} remains the same. Therefore the relative change is thought to be more pronounced. Therefore, the specific differences between the AlGaN- and the Si-based ISFET (high polarization fields and proximity of the channel to the surface) can mainly be applied to tailor the transducing part. The potential generation/charge adsorption as well as the charge balancing in the electrolyte solution are not affected. Only the overall sheet carrier density in the 2DEG and the absolute (and relative) pH-induced change of the same are influenced, by variation of the Al-content and thickness of the AlGaN barrier or employing N-face material to minimise the 2DEG-surface distance. In other words, the conversion of the surface potential/charge to the channel conductivity can be made more efficient in AlGaN-based ISFETs.

5 Materials and Methods

In this chapter the fabrication steps of the employed pH-sensor devices are illustrated. Furthermore, the instrumentation and measurement setups and the corresponding characterisation methods are presented.

5.1 Fabrication of AlGaN-based pH-Sensors

The fabrication process for AlGaN-based pH-sensor devices can be divided into the following steps: growth of the AlGaN/GaN heterostructure, contacting and structuring of the 2DEG, passivation of the electrical contacts and encapsulation of the sensor chips. All steps except the last one are performed on wafer scale. For the general electrochemical characterisation an EIHS is used. The EIHS is a simple capacitance structure that allows for the characterisation of the basic pH-sensing mechanism as well as light-induced drift and corrosion phenomena. The pH-measurements in the developed micro blood-pH analyser are performed employing an ISFET pH-sensor. Due to the larger dimensions of the EIHS, the passivation steps can be skipped when the encapsulation is performed using an appropriate sealing ring. For the ISFET all steps are needed as very small active sensor areas are realised. As the technological steps are not the focus of this work, a general and brief overview will be given and only specific details that are important for the optimisation are highlighted.

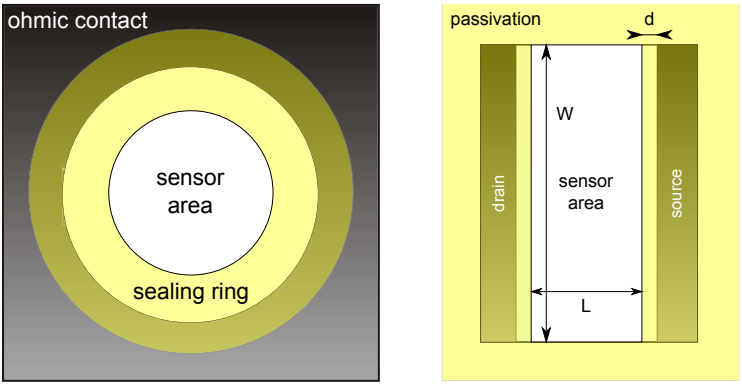

(a) EIHS (b) ISFET

Figure 5.1: Schematic top view of the basic EIHS and ISFET structure.

Design and Layout

The layout of the AlGaN-EIHS is a simple ohmic ring contact with an inner diameter of 4 mm (fig 5.1a). For the passivation of the electrical contacts an O-ring sealing with an inner diameter of 2.5 mm is used, resulting in a sensor area of 4.9 mm^2. The basic structure of the ISFET consists of two separate ohmic contacts, drain and source, on either side of the rectangular sensor or gate area (fig. 5.1b). The passiviation layer covers the drain and source contacts and overlaps the gate area by $d = 10\,\mu m$ to ensure sufficient insulation of the electrical contacts. For the employed ISFETs a W by L ratio 10 ($W = 500\,\mu m$) was used. Two sensor areas as well as a resistance thermometer, a Hall test structure and a quasi-reference metal electrode have been integrated onto the 5x5 mm^2 sensor chips.

Growth

AlGaN/GaN heterostructures can be grown epitaxially using either (plasma induced) molecular beam expitaxy or metal-organic chemical vapour deposition. The structures in this work were grown by MOCVD, as this method is also employed on an industrial scale due to the possibility of batch processes. The use of molecular beam epitaxy is mainly limited to research institutions as only single substrates can be processed. The first challenge in the epitaxial growth of III-Nitrides in general is the choice of a suitable substrate material. Although native GaN substrates are principally available, their fabrication is technologically complex and costly and only yields substrates in small dimensions [196]. Therefore substrates like sapphire and SiC and Si are employed that exhibit a thermal and lattice mismatch to some extent. This mismatch has a great impact on the quality of the grown epilayers which is why a thin low temperature AlN nucleation layer is commonly employed before the deposition of the GaN buffer. Although the lattice mismatch of 6H SiC is small ($\approx 3.5\%$ to GaN) resulting in a higher crystal quality, sapphire (lattice mismatch to GaN $\approx 15\%$) is commonly employed due to its cost advantage (factor 10). Both materials are transparent in the visible light spectrum which is beneficial for the fabrication of transparent sensor chips. Comprehensive reviews on the growth of III-Nitrides were published by Ambacher [115] and Jain et al. [112].

The MOCVD is based on metal-organic precursors like triethylgallium (TEGa) and trimethylaluminum (TMAl) as sources for Ga and Al and ammonia (NH_3) as a N-source. For n-type doping silane (SiH_4) can be added. A mixture of the evaporated precursors and NH_3 is diluted in the carrier gas H_2 and led over the heated rotating substrate.

There they are decomposed and the free metal atoms and nitrogen are deposited. The most important parameters of this process are the temperature of the substrate, the concentration and mixing ratio of the precursors and NH_3 and the reactor pressure. High quality layers can be grown using a two-step method which consists of a low temperature (460℃) deposition of thin AlN nucleation layer followed by high temperature annealing and the subsequent deposition of the main epilayers at high temperature (1120℃). The Al-content in the barrier layer can be adjusted by ratio of TEGa to TMAl. More details on the growth parameters of the employed AlGaN/GaN heterostructures and their optimisation have been published by Tonisch [197].

The heterostuctures that were investigated in this work were all grown on a 2" c-plane sapphire substrate (330 µm thickness) starting with a 20 nm AlN nucleation layer and a GaN buffer with a thickness of $\sim 1.2\,\mu m$. The following 10 nm thick $Al_xGa_{1-x}N$ barrier layer was deposited with an Al-content of either 30% ($x = 0.3$) or 20% ($x = 0.2$). A thin GaN cap layer of 2 or 10 nm thickness was used. For the reduction of the light sensitivity an additional Si-doping ($2 \times 10^{17}\,cm^{-3}$) of the GaN buffer from 50 to 5 nm below the GaN/AlGaN interface was used (fig. 5.2).

Contacting and Structuring the 2DEG

To establish an electric contact with the 2DEG a sputtered Ti/Al/Ti/Au metallisation sequence with thicknesses of 20 nm/80 nm/30 nm/100 nm was employed. The contacts were structured using a lift-off process. In the subsequent tempering step ohmic contacts with the 2DEG are formed through the diffusion of Al into the semiconductor and the generation of nitrogen vacancies due to the formation of TiN. The struc-

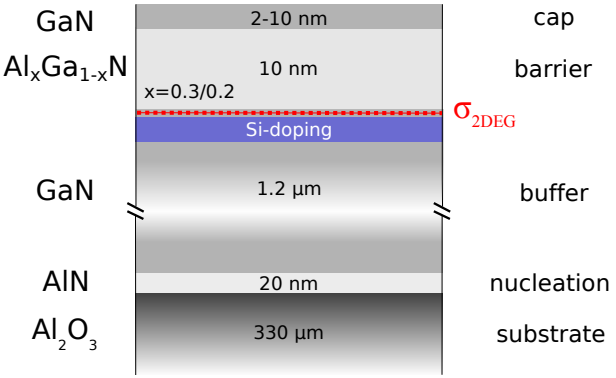

Figure 5.2: Schematic cross-section of the employed GaN/AlGaN/GaN heterostructure.

turing of the 2DEG is achieved using a Cl_2-plasma in an inductively coupled plasma dry etch system after masking the desired 2DEG structures with a photoresist [198]. In the unmasked areas the cap and barrier layers and a small part of the GaN buffer are removed to ensure that no parasitic conductivity is present outside the 2DEG structures. A second metallisation of Ni(30 nm)/Au(200 nm) is applied and structured by lift-off. This layer overlaps the ohmic contacts and facilitates Au-wire bonding at the edges of each sensor chip.

Passivation and Packaging

For the immersion of the ISFET into a liquid an appropriate passivation of the source and drain contacts is mandatory. This way parasitic conductivity via the solution and electrochemical reactions of the contacts are prevented. The passivation layer needs to meet several requirements: chemical stability in acids and bases, high electrical insulation,

mechanical stability and sufficient adhesion to the sensor surface, as well as the possibility to structure the layer on a micrometer scale. A suitable material is polyimide (PI2610, HD MicroSystems) that can be applied using spin coating. It is structured by a plasma dry etch process and tempered in a nitrogen atmosphere. Polyimide passivation layers have a high chemical stability in acids and bases, exhibit good electrical insulation properties and can be structured with a resolution of $\sim 1\,\mu m$. Potential disadvantages of these layers are their mediocre mechanical stability and a small but not negligible hygroscopicity, i.e. water take-up from the solution. This makes the passivation susceptible to scratching and may lead to a carry-over of solution especially in small volumes. For the passivation of the ohmic ring contact of the EIHS a sealing ring (300 µm) was cast from a polydimethylsiloxane (PDMS) elastomer (Sylgard 184, Dow Corning) with an inner diameter of 2.5 mm.

After sawing the wafer into single chips (5x5 mm^2) the ISFET chips are glued to a printed circuit board (PCB), whereas the EIHS chips are mounted on an aluminium frame (fig. 5.3). The electrical contact for both sensor types is established using conductive silver lacquer.

5.2 Measurement Setups and Instrumentation for Impedance Analysis

The employed impedance analysers and measurement setups for impedance characterisation of the AlGaN/GaN-heterostructure are described in this section. This includes the metal-insulator-heterostructure, which is created using a mercury probe, and the EIHS, which is measured in an electrochemical measurement cell. The developed micro blood-pH

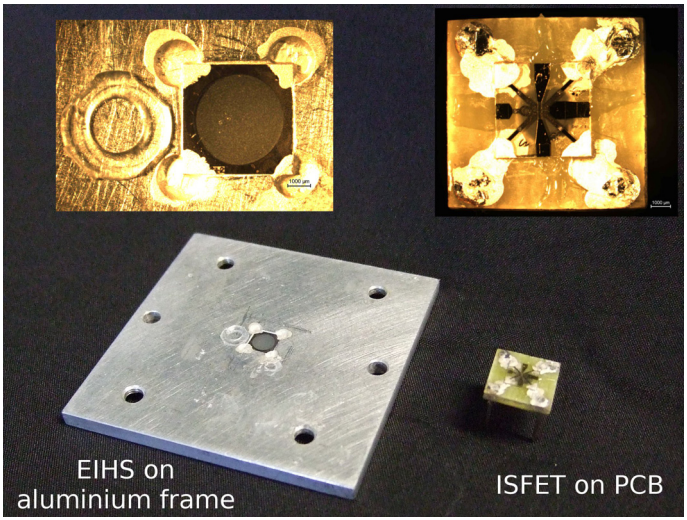

Figure 5.3: Packaged EIHS (with silcone sealing ring) on an aluminium frame and ISFET sensor chip on a PCB frame.

analyser and the employed source-meter units (SMUs) that are used to measure the ISFET pH-sensor are described in chapter 9.

5.2.1 Wafer-level Characterisation

For the characterisation of the MIHS an impedance/gain-phase analyser (1260A, Solartron) in conjunction with a preamplifier interface system (1296A, Solartron) was used. A simple two-electrode interface with HIGH and LOW connectors is available. The standard Solartron Impedance Measurement Software was used for the recording of impedance spectra and profiles. Whole 2" wafers were contacted with a mercury probe (802-150, MDC) with a dot-ring layout. The nominal dot diameter is 760 µm (Schottky contact), the dot-ring spacing is 400 µm and the area of the ring (ohmic contact) is approximately 50 times larger than the dot area. The repeatability of the contact area is given as 1.1%. The dot contact and the ring contact were connected to HIGH and LOW, respectively.

5.2.2 Electrochemical Characterisation

The impedance of the EIHS was analysed using an electrochemical workstation (Zennium, Zahner) with a preamplifier interface system (HiZ probe). The Zennium system supports two-, three- and four-electrode configurations via reference electrode (RE), counter electrode (CE) and two test electrode (TE) ports. For the employed two-electrode configuration both TE ports are interconnected as well as the RE and the CE ports. The Thales Z software was used for the recording of impedance spectra. The standard method for impedance profiles was not suitable for recording the time series that were necessary for drift

measurements. Therefore a measurement program was developed and implemented using LabView 8.6 (National Instruments).

The setup for the electrochemical characterisation is made up of the measurement cell that holds the electrolyte solution, the reference electrode that defines the solution's potential and a fluidic system that supplies up to three electrolyte and a rinsing solution (Fig. 5.4).

The body of the measurement cell is made from polyether ether ketone (PEEK) and a polycarbonate (PC) cover plate. The transparency of the cover plate allows for visual inspection of fill level and possible trapped air bubbles. Additionally, the sensor chip may also be illuminated from the front side. The cell has openings for the sensor chip, the reference electrode and for the in- and outlets of the fluidic system. A standard glass body reference electrode (InLab Reference, Mettler Toledo) with a ceramic double junction and a 3 M KCl inner electrolyte was employed. As the filling is implemented using low pressure the cell is sealed using O-ring gaskets at the PC cover plate and the reference electrode. The EIHS sensor chip is sealed with the silicone sealing ring. In addition to the thin seal the PEEK body has a broad conic recess towards the sensor chip to minimise the chance of air bubbles being trapped. Sedimentation from the electrolyte onto the sensor surface is avoided by fixing the sensor vertically at the measurement cell. The inlet is situated opposite the sensor and the outlet at the bottom of the cell to facilitate filling and emptying. The EIHS sensor chip in the aluminium frame is fastened at the measurement cell and placed onto a thick aluminium block that is connected to the TE ports of the impedance analyser. This block also holds a LED that illuminates the sensor chip from the backside. The reference electrode is connected to the CE and RE ports. A Faraday cage, grounded at the impedance analyser, is used to shield from electromagnetic interference.

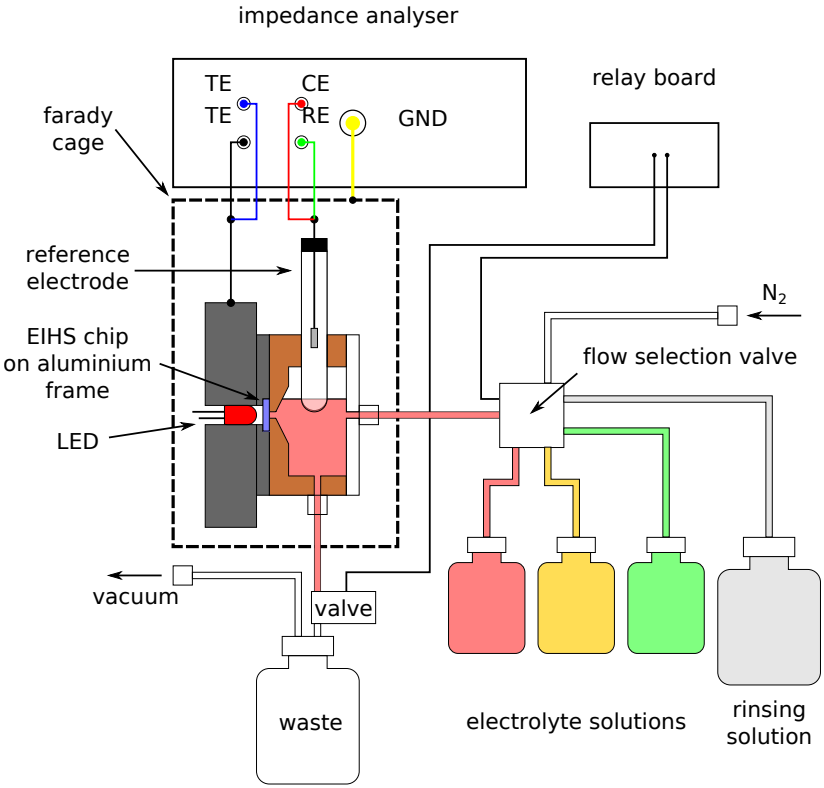

Figure 5.4: Schematic illustration of the electrochemical characterisation setup for AlGaN-EIHS sensor chips

The filling is implemented using the house vacuum supply to generate underpressure in the measurement cell via a waste flask. After the evacuation, the waste valve is closed and the cell is filled via a flow selection valve (080T612-62, Bio-Chem Valve), which selects one of the solutions. The measurement cell is emptied by opening the waste valve while the purging gas nitrogen is selected. After the emptying and purging procedure the selection valve is closed to evacuate the cell for the next filling sequence. In between each electrolyte solution two rinsing steps with DI water are performed to avoid a carry-over of solution. The filling, emptying and purging procedures are automated using a relay board (8fach-Relaiskarte 24V/7A, Conrad) to which the valves are connected. The developed LabView program allows for completely automated measurement cycles of up to three different electrolyte solutions. The standard measurement cycle for three different electrolyte solutions was defined in a way that all possible changes between the solutions are covered. For three solutions with low (L), medium (M) and high (H) arbitrary parameter values (e.g. pH), seven steps are performed in the sequence: $M \rightarrow H \rightarrow L \rightarrow M \rightarrow L \rightarrow H \rightarrow M$. This way carry-over or drift effects depending on the previously measured solution can be characterised .

The Labview program also controls the impedance analyser to measure the electrochemical impedance-voltage profile. The complex impedance $\underline{Z}$ of the sensor is recorded versus the applied bias voltage U_{bias} at a fixed ac frequency and amplitude (f_{ac}, U_{ac}). To ensure near steady-state conditions the dc leakage current I is recorded and analysed with regard to drift before each impedance measurement. The stability criteria for I are a relative drift of less than 2% or an absolute drift of less than 5 nA compared to its running average. A minimum of 3 and a maximum of 15 dc current measurements was preset to limit

measuring time. The additional advantage of this procedure is that the dc current-voltage characteristic of the sensor is recorded in addition to the electrochemical impedance-voltage profile.

The analysis of impedance data is performed in Origin Pro 7.5 (OriginLab) employing an OriginC script that calculates the equivalent elements C and G. For each measurement the parameters insulator capacitance $C_0' = C'(0\,\mathrm{V})$, zero bias conductance G_0, total 2DEG sheet charge density N_s and threshold voltages U_{th_C} and U_{th_G} are determined. Details on the calculation of the equivalent elements and the derivation of the parameters are given in section 6.1. This script-based data analysis facilitates the handling of large measurement series with several hundred datasets, that are obtained for drift measurement, as the data files can simply be processed using "drag-and-drop".

5.2.3 Employed Buffer, Sample and Cleaning Solutions

For the electrochemical characterisation simple phosphate buffer solutions and commercially available calibration, cleaning and quality control solutions were used.

During the initial phase of the investigations very simple phosphate buffer solutions with (PB6.5K, PB7.0K, PB7.5K) and without (PB6.5, PB7.0, PB7.5) added KCl were employed. Once it became clear that the ionic strength does influence the sensor signal, phosphate buffer solutions with equal ionic strength were used for the standard pH-sensitivity cycles. The solutions are fabricated based on the standard buffer solution pH6.86, following the National Institute of Standards and Technology and the DIN 19266 [199], but for the use of only potassium phosphates. The ionic strength was adjusted to 100 mM for the

solutions PB6.88, PB7.25 and PB7.64, by the ratio of KH_2PO_4 and K_2HPO_4. Modified phosphate buffers with added NaCl (MPB6.81 and MPB7.36) are more suitable for calibration when blood samples are measured, as their ionic composition is adjusted to physiological conditions [200]. The ionic strength measurement series were performed with PB6.88 buffer solution as the starting point for 100 mM (PBI100). The solutions for 10 and 1 mM (PBI10 and PBI1) were calculated by scaling the concentrations of KH_2PO_4 and K_2HPO_4. The properties of the phosphate buffer solutions are summarised in table 5.1. The theoretical pH-values and the ionic strength were calculated using the pH-calculator CurTiPot [182]. For the micro blood-pH analyser the calibration solutions S1545 (pH7.383) and S1555 (pH6.841) and the cleaning solution S4930 (all from Radiometer) were employed. Quality control measurements were performed using the multi-parameter QC solutions ISETROL Level 1-3 (Roche).

Table 5.1: Composition, calculated pH-value and ionic strength (CurTiPot [182]), and measured pH-value of the employed phosphate buffer solutions.

buffer solution	composition	pH-value	ionic strength (mM)	measured pH-value
PBI1	0.193 mM KH_2PO_4 + 0.364 mM K_2HPO_4	6.879	0.94	6.86 ± 0.02
PBI10	3.27 mM KH_2PO_4 + 2.12 mM K_2HPO_4	6.879	9.61	6.86 ± 0.02
PB6.88/PBI100	25.0 mM KH_2PO_4 + 25.0 mM K_2HPO_4	6.878	100.0	6.87 ± 0.02
PB7.25	12.5 mM KH_2PO_4 + 29.3 mM K_2HPO_4	7.247	100.4	6.25 ± 0.02
PB7.64	5.5 mM KH_2PO_4 + 31.5 mM K_2HPO_4	7.636	100.0	6.63 ± 0.02
MPB6.81	25.0 mM KH_2PO_4 + 25.0 mM K_2HPO_4 + 130 mM NaCl	6.809	230.0	6.67 ± 0.02

continued on next page

continued

buffer solution	composition	pH-value	ionic strength (mM)	measured pH-value
MPB7.36	8.7 mM KH_2PO_4 + 30.4 mM K_2HPO_4 + 120 mM NaCl	7.356	100.4	7.26 ± 0.02
PB6.5(K)	45.3 mM KH_2PO_4 + 20.7 mM Na_2HPO_4 (+ 100 mM KCl)	6.501	106.4 (206.4)	6.5 ± 0.3 adjusted with HCl
PB7.0(K)	2.56 mM KH_2PO_4 + 40.4 mM Na_2HPO_4 (+ 100 mM KCl)	7.001	145.3 (245.3)	7.0 ± 0.3 adjusted with HCl
PB7.5(K)	9.77 mM KH_2PO_4 + 56.2 mM Na_2HPO_4 (+ 100 mM KCl)	7.500	176.7 (276.7)	7.5 ± 0.3 adjusted with HCl

5.3 Characterisation Methods

In this section the methods that are applied to characterise the AlGaN-MIHS and EIHS are described. Compared to the AlGaN-ISFET, the characterisation methods are more complex for these capacitor structures. However, much more information on structural and electrical properties of the underlying heterostructure can be obtained from the application of impedance spectroscopy and impedance-voltage profiling. As the AlGaN-EIHS is the basic transducing element of the AlGaN-ISFET, the results obtained for the EIHS can directly be applied to the ISFET. Additionally, the passiviation layer, which is problematic but mandatory for the ISFET, can be replaced by a simple sealing ring. In general, the simplification to the EIHS is a very suitable approach to reduce the investigated AlGaN-ISFET to its basic structure, in order to perform a fundamental characterisation of its properties.

The complex impedance $\underline{Z}$ of the AlGaN-MIHS and EIHS is measured as a function of ac frequency f_{ac} and dc bias voltage U_{bias}. The measurement of $\underline{Z}(f_{ac})$ at a fixed U_{bias} is called impedance spectrum and $\underline{Z}(U_{bias})$ at a fixed f_{ac} is called impedance-voltage profile. Impedance spectroscopy is applied for the initial, static characterisation and to determine a suitable equivalent circuit for the heterostructure. Impedance-voltage profiling is used to characterise dynamic processes like light-induced drift or corrosion phenomena and to measure pH-value. The methods and instrumentation that are employed for the measurement of pH-value with the ISFET will be described briefly in section 9.4.

To obtain the complex impedance of a material sample, it is connected to at least two electrodes, forming a measurement cell. In case

of the MIHS, the electrodes are reversible mercury contacts that are applied to the surface of the as-grown wafer. Therefore, the measurement chain comprises the large Hg ohmic contact, the 2DEG channel, the barrier and cap layer and the Hg Schottky contact. The measurement chain of the EIHS includes the Ti/Al/Ti/Au ohmic contact, the 2DEG channel, the barrier and cap layer, the semiconductor-electrolyte interface, the electrolyte solution and the reference electrode.

The most widespread method for the measurement of $\underline{Z}$ is the application of a small ac voltage with the amplitude U_{ac} and the frequency f_{ac}. The ac current that is measured as the systems response to the ac voltage, with amplitude I_{meas} and phase angle ϕ, is then used to calculate the transfer function or impedance. This principal method is expressed by the following equation:

$$\begin{aligned} \underline{Z} = \frac{\underline{U}}{\underline{I}} &= \frac{U_{ac} e^{j2\pi f_{ac} t}}{I_{meas} e^{j(2\pi f_{ac} t + \phi)}} \\ &= \frac{U_{ac}}{I_{meas}} e^{-j\phi} = |Z| e^{-j\phi} = Z_{re} + j Z_{im}, \end{aligned} \tag{5.1}$$

where $|Z|$ is the magnitude and Z_{re} and Z_{im} are the real and imaginary part of the impedance. For this analysis different approaches are used, ranging from analog circuits for digitising the output signal and the use of fast Fourier transformation. A constant bias voltage U_{bias} can be superimposed onto U_{ac} to obtain the voltage-dependence of the impedance spectra or to record impedance-voltage profiles. In electrochemistry the open-circuit potential of the measurement cell is commonly used for U_{bias} to minimise the dc current flow or U_{bias} is set to 0 V. The ac amplitude U_{ac} has to be set large enough to induce a measurable ac current, but also small enough to minimise the disturbance from the equilibrium condition of the sample. For conducting

electrodes U_{ac} can be as small as (1–5) mV, for semiconducting or insulating electrodes larger amplitudes around (20–50) mV are necessary to achieve a reasonable signal-to-noise ratio.

5.3.1 Impedance Spectroscopy

Impedance spectra are obtained when the frequency f_{ac} is varied, commonly from high to low frequencies. The frequency of impedance analysers ranges from a few milli- or microhertz to several MHz. Generally, impedance spectroscopy can be employed to characterise properties that have an influence on the conductivity of the investigated system. This includes material properties, such as electrical/ionic conductivity, the dielectric constant or charge carrier generation-recombination rates, and interface properties, such as adsorption reaction rates, interfacial capacitance or diffusion coefficients. In addition, structural properties, such as insulator thickness or charge carrier depth profiles, can be estimated. The determination of structural and material properties of the MIHS will simply be termed impedance spectroscopy in this thesis. For the characterisation of the EIHS, the term electrochemical impedance spectroscopy will be used.

The measured impedance represents the overall electrical response of the measurement cell. This means that all elements in the cell - the investigated sample as well as metal and electrolyte conductivity, reference electrode or parasitic capacitors - contribute to this response. Therefore, a separation of these elements is essential for interpretation. Additionally, the electrical response of each element can include a distribution of microscopic processes and reactions (e.g. different forms of charge transport, charge carrier generation-recombination or adsorption reactions). These considerations imply that a mathematical model

is needed based on plausible physical theory. The extent to which distributed elements have to be used in this model depends on material properties like interface roughness or structural and energetic defect density.

The mathematical model that is used for impedance spectroscopy is an equivalent circuit consisting of well-known elements like resistors or capacitors in series or parallel connection. To account for distributed processes additional elements have been introduced, e.g. the Warburg impedance for diffusion processes or the constant phase element (CPE). As the latter will be used in the equivalent circuit of the AlGaN-MIHS and EIHS, it shall be presented in more detail here. The CPE is a generalisation of the capacitor and has a similar mathematical description, but for an added exponent α. Its impedance is given by:

$$Z_{CPE} = \frac{1}{(j\omega)^{\alpha} Q} = \frac{1}{(j2\pi f)^{\alpha} Q}, \tag{5.2}$$

where Q has the numerical value of the admittance $(1/|Z|)$ at $\omega = 1\,\mathrm{rad/s}$ and $0 \leq \alpha \leq 1$. The units of Q are $\mathrm{S \cdot s^{\alpha}}$. For $\alpha = 1$ the CPE becomes an ideal capacitor with a phase angle $\phi = -90°$ and for $\alpha = 0$ an ideal resistor is obtained. For $0 < \alpha < 1$ the phase angle is still constant and independent of frequency, but deviates from $-90°$. The phase angle of the CPE is calculated as $\phi = -90° \cdot \alpha$. Simply put, the CPE is a non-ideal capacitor with a constant phase angle of less than $-90°$. This also implies that the impedance of the CPE will always comprise an imaginary and a real part, in contrast to the capacitance, which only has an imaginary part. Both Z_{re} and Z_{im} of the CPE decrease with increasing frequency. As an equivalent element the CPE is very useful to describe distributed processes and was first mentioned by Cole and Cole [201]. The origin of CPE-like behaviour is thought to be

inhomogeneous current or potential distributions in the measurement cell. This includes structural characteristics (e.g. interface roughness or varying material thickness or composition), chemical characteristics (e.g. distributed reaction rates) or electrical characteristics (e.g. relaxation times and nonuniform diffusion or current distribution). A comprehensive discussion of the CPE and other distributed elements can be found in [202].

Once a physically plausible equivalent circuit has been found a complex non-linear least square (CNLS) fit is commonly applied with appropriate weighting methods. For this thesis the fitting procedure was performed with ZView (Scribner Associates) using data-proportional weighting. The results of the fit can then be used to characterise the different elements in the investigated sample system. The advantages of impedance spectroscopy are the relative simplicity of the methods themselves, its possible automation and the characterisation of various material and interface properties. It can be employed in a multitude of application fields including corrosion analysis, characterisation of biological membranes or dielectrics as well as predicting the performance of electrochemical sensors or fuel cells. Its disadvantage is mainly found in the difficult and ambiguous interpretation of the impedance data. For a single impedance spectrum an infinite number of suitable equivalent circuits can be derived that model the observed characteristic equally well. It can even be shown that a single equivalent circuit consisting of three or more elements can be rearranged in various ways and still yield exactly the same fitted impedance spectrum [202]. Therefore, the plausible physical theory becomes very important when impedance spectra are interpreted. The choice of the appropriate equivalent circuit can be facilitated when several impedance spectra are recorded under different conditions. In this work, complete impedance spectra at varying ap-

plied bias voltage U_{bias} are recorded, which is effectively a combination of impedance spectroscopy and impedance-voltage profiling.

5.3.2 Impedance-Voltage Profiling

The measurement of impedance versus varying bias voltage U_{bias} at a fixed frequency f_{ac} is termed impedance-voltage profiling. Although this method is not a standard method in electrochemistry it yields valuable information concerning the voltage dependence of sample systems. In semiconductor physics, it is applied to determine properties like the doping profile, insulator thickness or threshold voltage. In this context it is commonly referred to as capacitance-voltage (CV) profiling [203]. This term implies that the dominant element of the equivalent circuit is a capacitor, as it is the case for the metal-insulator-semiconductor (MIS) structure that represents an important cornerstone of modern semiconductor technology. When the resistive equivalent elements are taken into account and a conductance-voltage profile is derived from the impedance-voltage profiling, additional parasitic properties like the trap density can be determined. A comprehensive treatment of Si-based MIS device in general and their characterisation with capacitance- and conductance-voltage profiling can be found in [204]. In this work the general term impedance-voltage profiling will be used, as not only the capacitance but also the conductance of the heterostructure will be investigated. It should also be noted that U_{bias} will always be referenced to the Schottky contact and therefore has an inverted sign compared to the convention that is commonly used in semiconductor physics. This is done to avoid confusion when the electrochemical impedance-voltage profiles are discussed, where the low potential is always assigned to the reference electrode by the impedance analyser.

The principal mechanism of impedance-voltage profiling is the variation of the depletion region width below a Schottky contact with the applied bias voltage. The charge carrier concentrations in the semiconductor influence the width of the depletion region and affect the measured impedance. Commonly, a simple parallel equivalent circuit with a capacitor and a resistor is assumed, to derive the capacitance- and conductance-voltage profile. This equivalent circuit is subjected to critical analysis in section 6.1, where the complete equivalent circuit of the AlGaN/GaN heterostructure is derived from impedance spectroscopy. The application of CV-profiling to AlGaN/GaN heterostructructures has been described e.g. by Ambacher et al. for different barrier thicknesses, Al-contents and crystal polarities [110]. There it was used for the determination of the sheet carrier density and the location of the 2DEG depending on crystal polarity and barrier thickness. It is also applied for the non-destructive characterisation of wafers directly after the epitaxial growth using a reversible mercury probe [197]. The conductance-voltage profiles have been disregarded for these applications. The parameters that are derived from the CV-profiles include the sheet carrier density N_s, the insulator thickness d_0, which comprises the cap and barrier layer, and the threshold voltage U_{th}. Additionally, it is thought that depth profiles $n(z)$, which reach into the GaN bulk, can be derived and bulk doping concentration can be estimated. The basic equations for these parameters are given in the following paragraph.

For the capacitance a simple plate capacitor geometry is assumed that can be described by:

$$C = \epsilon_0 \epsilon_r \frac{A_{sc}}{d}, \tag{5.3}$$

where A_{sc} is the area of the Schottky contact, d is the thickness of the dielectric, and ϵ_0 and ϵ_r are the vacuum and relative permittivity, respectively.

The sheet carrier concentration $n_s(U_{bias})$ is calculated from the capacitance through integration using:

$$C'(U_{bias}) = \frac{C(U_{bias})}{A_{sc}} = \frac{dQ(U_{bias})}{dU \cdot A_{sc}} = \frac{-e \cdot dn_s(U_{bias})}{dU} \tag{5.4}$$

and

$$n_s(U_{bias}) = -\frac{1}{q} \int_{\infty}^{U_{bias}} C'(U) dU, \tag{5.5}$$

assuming that charge conservation is fulfilled and background doping of the heterostructure is small compared to the sheet charge density in the 2DEG. At zero bias voltage the total sheet charge density $N_s = n_s(0\,\mathrm{V})$ is obtained, which is commonly used as a characteristic parameter of the 2DEG.

The distance z between the Schottky top and 2DEG back electrode can be calculated using:

$$z = \frac{\epsilon_0 \epsilon_r}{C'(U_{bias})}, \tag{5.6}$$

with $\epsilon_r = 8.8$ for $Al_{0.3}Ga_{0.7}N$, approximated linearly from the values of AlN (8.5) and GaN (8.9) [205]. As this value is very close to the relative permittivity of the GaN cap layer, the cap and barrier layer can be treated as one layer. The total thickness of the cap and barrier layer d_0 is obtained for $C'_0 = C'(0\,\mathrm{V})$.

The threshold voltage U_{th} is commonly estimated by extrapolating the linear portion of $n_s(U_{bias})$ and determining its intersection with the

voltage axis. Several other methods for the determination of threshold voltage can be found in the monograph of Schroder [203].

Ambacher et al. [110] also state that a depth profile can be obtained using equation 5.6 and the following equation that can be found in [203]:

$$n(z) = \frac{C'^3}{e\epsilon_0\epsilon_r}\frac{dU}{dC'} = \frac{1}{z}\frac{C'^2}{e}\frac{dU}{dC'}. \tag{5.7}$$

The validity of this claim for the common AlGaN/GaN heterostructure and its specific contact geometry will be discussed in section 6.1.

An example for trap characterisation with capacitance and conductance profiles has been published by Miller et al. [206] for heterostructures with an 30 nm Si-doped $Al_{0.15}Ga_{0.85}N$ barrier and a 10 nm $Al_{0.15}Ga_{0.85}N$ spacer layer on top of 3 µm GaN. The profiles are given in figure 5.5 and show that the capacitance profile shifts towards higher gate-drain voltage at higher frequency. The conductance profile reveals that a pronounced frequency dispersion is present that increases the conductance by about two decades in addition to a voltage shift.

The conductance method described by Nicollian and Brews [204] is applied to determine the interface trap density D_{it}. The frequency dispersion of both the capacitance and the conductance is analysed with an equivalent circuit that includes the interface trap capacitance C_{it} and resistive loss term R_{it}, in addition to the capacitance of the barrier C_b, the capacitance of the spacer layer C_s and a series contact resistance R_s. The equivalent circuits for the measurement with $C_m||G_m$, the assumed model with trap states and a simplified circuit with trap states is illustrated in figure 5.6. The full equivalent circuit with trap states (fig. 5.6b) is simplified, as the C_p and G_p can be derived more easily from the measurement circuit. To do this C_b and R_s were deter-

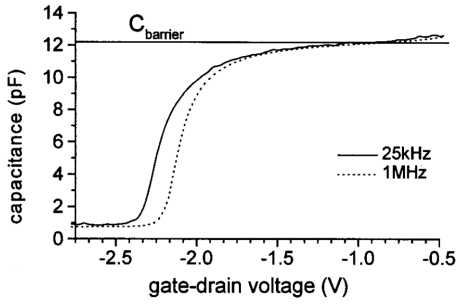

(a)

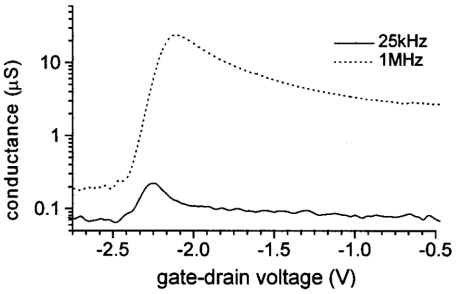

(b)

Figure 5.5: Capacitance and conductance profiles of a modulation-doped $Al_{0.15}Ga_{0.85}N/GaN$ heterostructure that demonstrate the trap-related frequency dispersion [206].

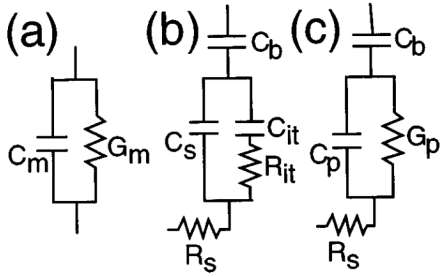

Figure 5.6: Commonly employed equivalent circuits of the AlGaN/GaN heterostructure that account for interface traps: a) measurement circuit, b) circuit with interface traps and c) simplified circuit with lumped interface trap elements. [206]

mined independently from the enhancement plateau in the CV-profiles ($C_{barrier}$ in fig. 5.5a) and from dc current-voltage measurements, respectively. The calculated values of C_p and G_p/ω were plotted versus angular frequency ω and analysed using different models for the trap states. The best fit of the data was obtained for a model that accounts for a continuous distribution of trap levels. From this analysis a trap density of $D_{it} = 1 \times 10^{12}\,\mathrm{cm}^{-2}\,\mathrm{eV}^{-1}$ with a time constant of $\tau_t = 1\,\mu\mathrm{s}$ was estimated. The exact location could not be determined unambiguously, as similar values for D_{it} and τ_t were obtained for the case of traps at the metal-semiconductor interface and in the AlGaN barrier layer. From the comparison to the data reported by Kohn et al. for a modulation-doped $Al_{0.3}Ga_{0.7}N$/GaN-FET [207], it is suggested that an increased Al-content in the barrier layer results in large time constants. Shealy et al. give a value of $\tau_t = 4\,\mu\mathrm{s}$ for an AlGaN/GaN heterostructure, without stating the Al-content of the barrier [208].

6 Impedance Characterisation of the AlGaN/GaN Heterostructure and Derivation of Equivalent Circuits

The heterostructure layout that was chosen for the fundamental impedance characterisation in this section is mainly derived from the thesis of Kittler [16] and Cimalla [17] and the initial publication on AlGaN-based pH-ISFETs by Steinhoff [11]. It is based on the following primary requirements:

1. high chemical stability of the surface, which is achieved using a GaN cap layer,

2. low operating voltage to minimise electrostatic stress to the passivation layer, which is achieved using a small AlGaN barrier and

3. reduced light sensitivity, which can be achieved by doping the GaN bulk with Si slightly below the GaN/AlGaN interface.

From these requirements a standard heterostructure with a 1.2 µm GaN buffer (doped with $2 \times 10^{17}\,\mathrm{cm}^{-3}$ Si from 50 to 5 nm below the GaN/AlGaN interface), a 10 nm $Al_{0.3}Ga_{0.7}N$ barrier and a 2 nm GaN cap layer is derived. The abbreviation $B_{10}^{30}C_2$ will be used for this structure to indicate the parameters barrier Al-content, barrier thickness and cap thickness. The measurement series were carried out after the sensor chip had been kept in the dark for at least 12 h, except for the investigations on light-induced drift.

6.1 Wafer level characterisation of the MIHS

In this section the characterisation of $B_{10}^{30}C_2$ wafers by impedance spectra and impedance-voltage profiles is presented to gain insight into the fundamental properties of the AlGaN/GaN heterostructure. Using reversible mercury contacts, the metal-insulator-heterostructure (MIHS) is analysed before any further processing steps are applied. An equivalent circuit is derived from impedance spectra and the differences between the AlGaN/GaN heterostructure and common Si-based metal-insulator-semiconductor (MIS) structures are highlighted. High resolution scanning electron microscopy (SEM) images are shown to illustrate the surface morphology of the as-grown wafers.

6.1.1 Impedance Spectroscopy

A fundamental step for the interpretation of impedance-voltage profiles is the derivation of an appropriate equivalent circuit, which is also very useful to obtain additional structural and electrical properties of the investigated sample. Commonly, the heterostructure is reduced to the

barrier layer and treated as a plate capacitor with a parallel resistor, as described in section 5.3.2. However, the validity of this equivalent circuit is put into question by the following considerations:

- Firstly, semiconductor structures that are commonly investigated can be approximated by a simple 1-dimensional layout, e.g. a MIS capacitor with a Schottky top contact and an Ohmic back contact conveyed by the conducting Si substrate (fig. 6.1 left). In contrast, the investigated AlGaN/GaN heterostructure is grown on insulating sapphire, which prevents the simple fabrication of a back contact. The back contact is provided by the 2DEG channel at the AlGaN/GaN interface (fig. 6.1). This imposes serious limitations on the application of common impedance-voltage profiling as the 2DEG is not only the charge distribution of interest but also the back contact. This implies that the profiling of the 2DEG by the applied bias voltage degrades the back contact and a severe deviation from the one-dimensional geometry can be expected. Due to this distortion, the one-dimensional treatment of the impedance-voltage profile (e.g. for a depth profile), which has been commonly applied to AlGaN/GaN heterostructure [110], is only valid for as long as the 2DEG is sufficiently conducting.

- Secondly, the phase angle ϕ of the impedance deviates from the ideal capacitive value of $-90°$ when the 2DEG is depleted by the applied bias voltage. This deviation is depicted in the impedance-voltage profile (fig. 6.2) taken at the initial standard parameters for the wafer characterisation ($f_{ac} = 10\,\mathrm{kHz}$, $U_{ac} = 50\,\mathrm{mV}$). The depletion of the 2DEG is signified by the large increase of Z_{re} and $|Z_{im}|$ around 1.5 V. The course of the phase angle is determined by the ratio of Z_{im} to Z_{re} and it can therefore be used

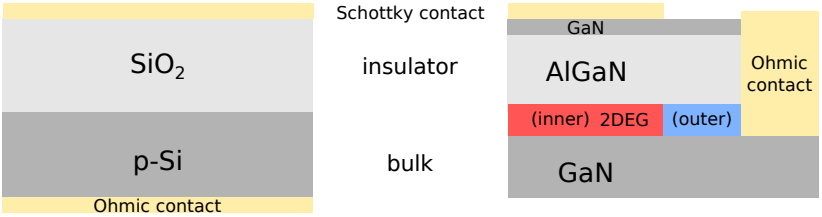

Figure 6.1: Structural comparison between a Si-based MIS and an AlGaN/GaN-MIHS

to determine which part of the impedance is dominant. At a bias voltage of 0 V the impedance is dominated by Z_{im} and ϕ is close to -90°. With increasing U_{bias} the real part Z_{re} rises earlier and faster than Z_{im}, which results in an increasing phase angle. At the intersection of the real and imaginary part, ϕ equals -45° and $\underline{Z}$ is dominated by Z_{re} ($\phi > -45°$) until the curves intersect again. For higher U_{bias}, the phase angle approaches -90° and stays constant. This phase deviation is disregarded in literature on impedance-voltage profiling of AlGaN/GaN heterostructures and its origin has not been discussed.

- Thirdly, the known pronounced frequency dispersion (cf. fig. 5.5) cannot be accounted for with a simple parallel equivalent circuit. The interface trap model employed by Miller et al. (cf. section 5.3.2) is one possibility to account for the frequency dispersion; other approaches and equivalent circuits for trap modelling in MIS structures can be found in the monograph of Schroder [203]. However, these models are not adopted as a starting point, as they are all based on a one-dimensional geometry.

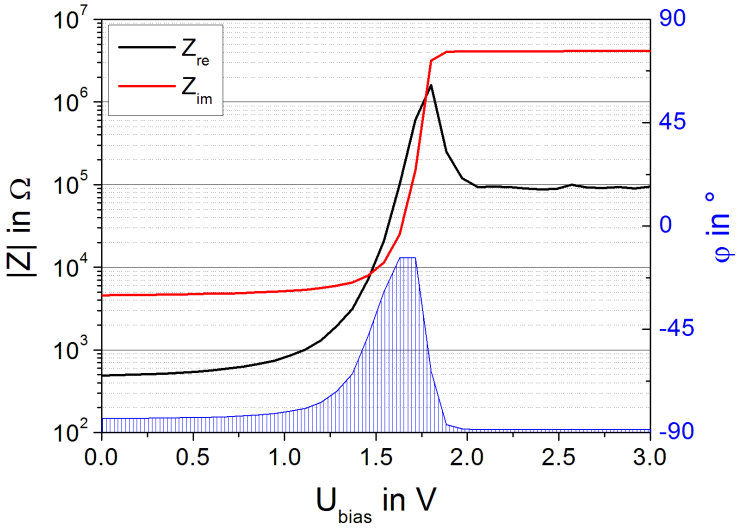

Figure 6.2: Plot of Z_{re}, $|Z_{im}|$ and ϕ versus U_{bias} for an as-grown $B_{10}^{30}C_2$ heterostructure measured with a mercury probe.

In order to identify the influence of the two-dimensional geometry of the AlGaN-MIHS, an appropriate equivalent circuit is derived from impedance spectra $\underline{Z}(f_{ac})$ at various bias voltages U_{bias}. Effectively, this approach corresponds to a combination of impedance spectroscopy and impedance-voltage profiling and could be termed impedance spectra-voltage profiling.

The real and imaginary spectra of a $B_{10}^{30}C_2$ heterostructure are shown in fig. 6.3 for $f_{ac} = 100\,\mathrm{kHz}$ - $1\,\mathrm{Hz}$ and $U_{ac} = 30\,\mathrm{mV}$. The bias voltage is swept from 0 to $2.5\,\mathrm{V}$ in steps of $0.1\,\mathrm{V}$. The real impedance spectrum reveals a two-fold behaviour at low U_{bias}: at low frequency a linear decrease with increasing frequency is observed, whereas the high frequency portion is constant and independent of frequency. When U_{bias} is increased this constant plateau of Z_{re} is shifted towards higher impedance and lower frequencies. Additionally, a second decreasing slope appears at high frequencies. During the course of this shift the first slope is eliminated and the plateau is smoothed out. The second slope becomes steeper and dominates the spectrum. With a further increase of U_{bias} a turning point is reached and Z_{re} starts to decrease slightly at all frequencies. Nearly ideal capacitive behaviour is suggested by the linear decrease of the imaginary impedance spectrum with a slope close to -1 (decade per decade) at low U_{bias}. Increasing U_{bias} also shifts these spectra towards higher impedance and the slope is split into two, slightly different, portions. Unlike the real impedance spectra, no decrease is observed at high U_{bias}. These rather complex characteristics of the impedance spectra reveal that a single parallel circuit $C||R$ is not sufficient to describe the heterostructure in the investigated frequency range. The two decreasing slopes of Z_{im} indicate that two capacitive elements are needed in addition to at least one resistive element for the plateau of Z_{re}. The frequency dispersion of Z_{re} can be modelled

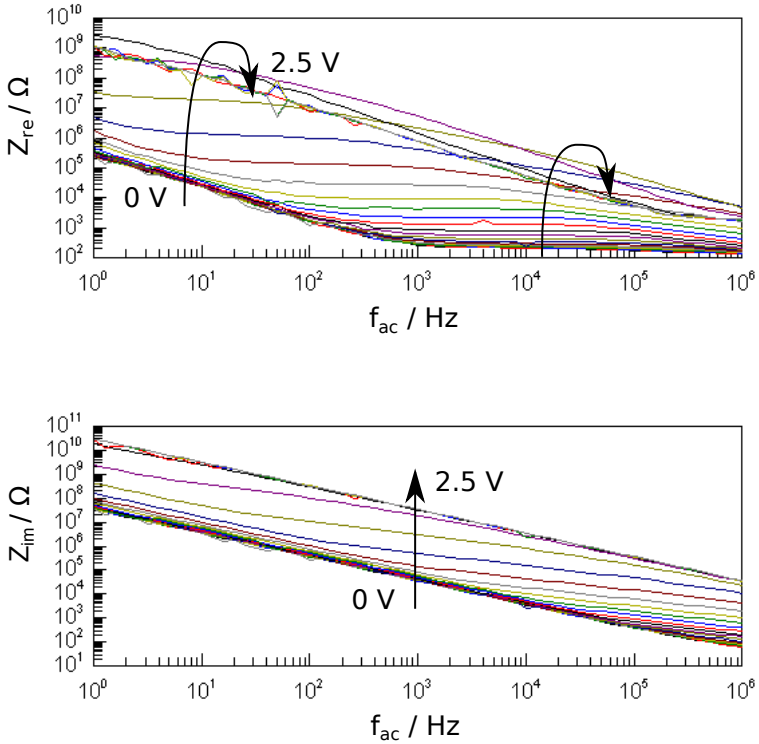

Figure 6.3: Real and imaginary impedance spectra of an AlGaN-MIHS ($B_{10}^{30}C_2$) with increasing bias voltage.

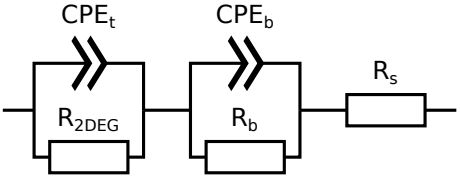

Figure 6.4: Full equivalent circuit derived from the impedance spectra of an AlGaN-MIHS by CNLS fitting.

by CPEs. These capacitive elements also account for the slight deviation from -1, which is found for the slopes of Z_{im}. The best fit to the impedance data was obtained for a series connection of two parallel circuits $CPE_b||R_b$ and $CPE_t||R_{2DEG}$ and a series resistance R_s, as given in figure 6.4.

The equation of this equivalent circuit is:

$$\begin{aligned}\underline{Z} &= Z_{re} + jZ_{im} \\ &= R_s + \frac{1}{\frac{1}{R_b} + (j2\pi f_{ac})^{\alpha_b} \cdot Q_b} + \frac{1}{\frac{1}{R_{2DEG}} + (j2\pi f_{ac})^{\alpha_t} \cdot Q_t}.\end{aligned} \tag{6.1}$$

Before the voltage profiles of the equivalent elements are presented and discussed, the general plausibility of the derived equivalent circuit needs to be confirmed. This is done by correlating the equivalent elements with the actual device structure. Along the measurement path the heterostructure can be divided into capacitive and resistive elements. The barrier and cap layer, which are depleted of mobile charge carriers due to the internal polarisation fields, exhibit capacitive behaviour. The resistive elements are formed by the inner 2DEG below the Schottky contact and the outer 2DEG between the Schottky and the Ohmic contact, as well as the Ohmic contact itself (fig. 6.1). The series resistance R_s can be assigned to the Ohmic contact, which is as-

sumed to be ideal and therefore independent of the applied voltage. Its value is expected to fall in the range of a few Ω up to 100 Ω, depending on the quality of the ohmic contact. The parallel circuit $CPE_b||R_b$ can be assigned to the insulator, consisting of the barrier and cap layer. The insulator capacitance is seen in CPE_b and its resistance can be approximated by R_b. A high value, on the order of several GΩs, is expected for R_b, whereas CPE_b will depend on the insulator thickness and the area of the Schottky contact. The resistor R_{2DEG} can be assigned to some portion of the 2DEG, as the rather low value of the Z_{re} plateau ($\approx 200\,\Omega$) suggests this connection. Whether the inner and/or the outer 2DEG are reflected in this equivalent element cannot yet be determined. The parallel CPE_t is connected to the 2DEG in a way that will be discussed later on.

As the CPE is not commonly used in semiconductor physics, its origin in the investigated heterostructure needs to be discussed. Generally, CPE behaviour is assigned to a non-uniform current and/or voltage distribution that can arise from surface roughness, varying thickness or a distribution of time constants. For the investigated system the surface roughness can be disregarded as atomic force microscopy (AFM) measurements of as-grown heterostructures reveal a very small roughness of (1–1.5) nm (rms - 5x5 µm^2). The aspect of varying thickness does not apply, due to the homogeneous deposition of the layers. Only a monotonous, radial variation of the overall heterostructure thickness is observed, with a maximum variation of 10% between the centre and the edge of a 2" wafer. However, a variation of the effective thickness of the insulator results from the previously presented consideration that the depletion of the 2DEG will at some point be lateral instead of vertical. In this case the electrical field lines no longer run perpendicular to the insulator, but are skewed towards the ohmic contacts.

This field distortion and inhomogeneous field density could be a reason for the CPE behaviour. The most likely explanation, however, is a distribution of charge generation/recombination time constants, due to defect levels or trap states in the band structure of the semiconductor. The presence of these states and their impact on the electronic properties of the heterostructure is known and has been discussed in section 4.3. In addition, the analysis of the frequency dispersion by Miller et al. [206] revealed that a broad distribution of trap levels exist in the AlGaN/GaN heterostructure. In order to derive the trap density and time constant, Miller et al. needed to fit the calculated G_p/ω spectra with a function for a continuum of trap levels. The CPE, however, accounts for the distribution characteristic by its definition and is therefore an ideal equivalent element to model trap-related dispersion phenomena. Nevertheless, except for the characterisation of interface traps in GaAs-based MIS structures reported by Kochowski et a. [209, 210], no publications can be found on this topic.

Now that the physical plausibility of the equivalent circuit is established and interpretation of the CPE has been considered, the voltage dependence of the equivalent elements will be presented in the following. Figure 6.5 shows the voltage profiles of CPE_b, CPE_t, G_s, G_b and G_{2DEG} obtained from CNLS fitting of the impedance spectra. The resistive elements are given by their conductance $G = \frac{1}{R}$ to facilitate the plotting of all traces on one graph. From these profiles three primary ranges can be identified, which correspond to the enhancement and depletion of the 2DEG channel and the transition between both states. The enhancement range extends from zero bias voltage to the beginning of the logarithmic decrease of Q_b, Q_t and G_{2DEG}, the transition range spans the decreasing portion and the depletion range is characterised by the constant values of Q_b at high U_{bias}. For the given ex-

ample (fig. 6.5) the ranges are approximately (0–1.5) V (enhancement), (1.5–2) V (transition) and >2 V (depletion). Generally, it is observed that the voltage profiles of all equivalent elements are monotonous and the uncertainty of the fitted values is very low. These observations suggest that the derived model is correct and that its elements can be employed to characterise physical processes in the heterostructure. The slightly erratic characteristic of Q_t and large error bars of α_t in the enhancement range suggest that their influence on the overall impedance is very low. A similar effect is observed at high U_{bias} for most of the equivalent elements. At some point their influence on the overall impedance becomes marginal and they are therefore no longer included in the voltage profile. Only Q_b and α_b can be derived for the entire bias voltage range. Their almost negligible uncertainties emphasise that CPE_b is the most important and dominant element of the equivalent circuit.

After this general discussion, the bias voltage dependence of each equivalent element is discussed in detail. In order to facilitate this discussion, the assumed changes in the electrical field (blue arrows) and the sheet carrier concentration in the 2DEG (red bar) with increasing bias voltage are illustrated in figure 6.6. The overlaid equivalent circuit demonstrates the correlation to the heterostructure. In addition, single elements are greyed out when they no longer influence the overall impedance of the MIHS.

The resistive elements G_s and G_b reveal a true ohmic characteristic, as they are not influenced by U_{bias}. Their constant values correspond to resistances of 100 Ω and 10 GΩ for R_s and R_b, respectively. This confirms that R_s represents the ohmic contact and R_b represents the resistance of the insulator, as their values agree with the initial considerations. The insulator capacitance is represented by CPE_b, as it is

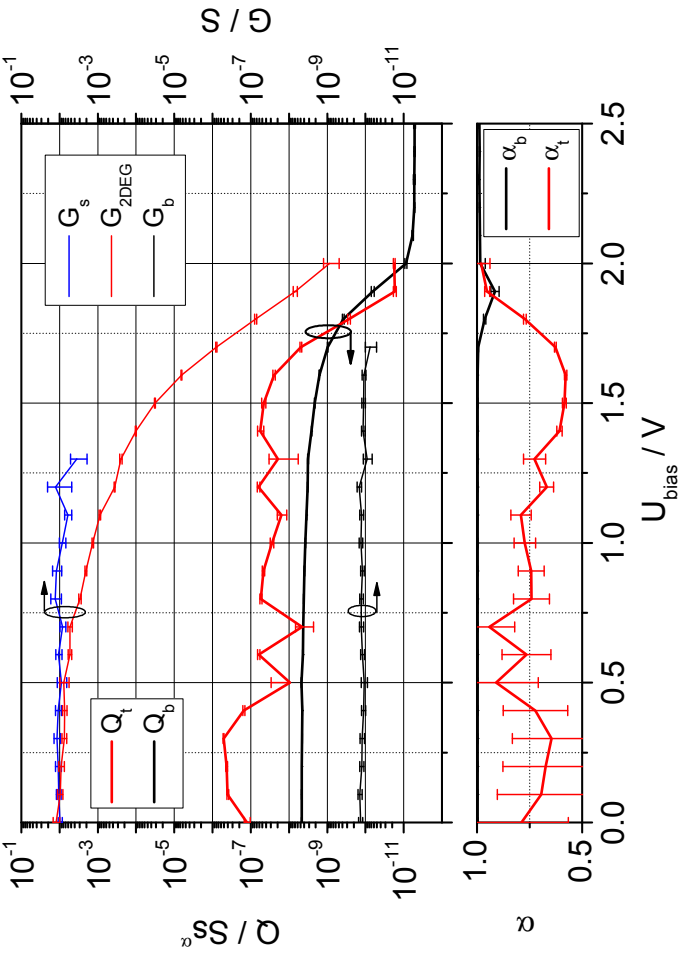

Figure 6.5: Voltage profiles of the equivalent elements CPE_b and G_b (black), CPE_t and G_{2DEG} (red) and G_s (blue) for an AlGaN-MIHS, derived from impedance spectra.

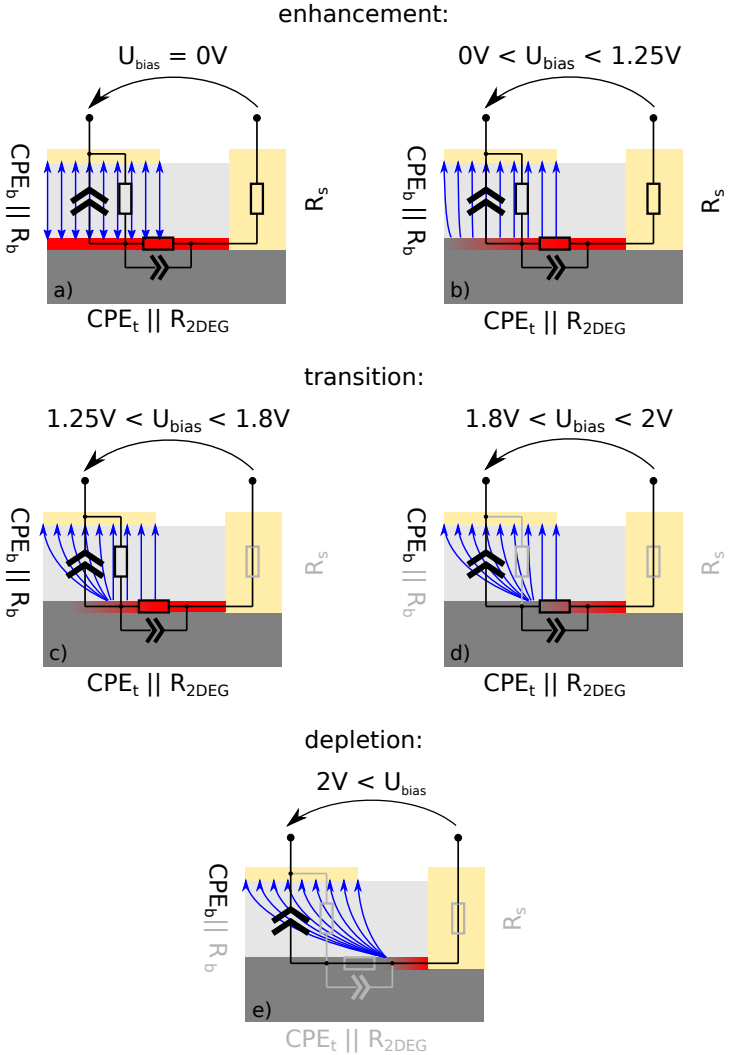

Figure 6.6: Schematic cross sections of an AlGaN-MIHS illustrating the simplified course of the electric field (blue) and the sheet concentration in the 2DEG (red) depending on the applied bias voltage. The full equivalent circuit is overlaid and elements with insignificant influence are greyed out.

parallel to R_b. This connection can also be verified by the course of its voltage profile. In the enhancement range, CPE_b can be treated as an ideal capacitor since α_b is very close to 1. It can be assumed that the electric field runs perpendicular to the cap and barrier layer, between the Schottky top electrode and the 2DEG back electrode (fig. 6.6a). At the beginning of the transition range the pronounced decrease of Q_b reflects that the 2DEG back electrode is no longer sufficiently conducting below the Schottky contact. This effectively reduces the area of the plate capacitor and, in turn, its capacitance. In addition, the field lines no longer run perpendicular through the structure and are distorted towards the Ohmic contact (fig. 6.6c). This means that the path along the field lines and the effective thickness of the dielectric is increased, which also decreases the capacitance. At some point the vertical depletion geometry will be expanded by a lateral dimension. The outer 2DEG beside the Schottky contact will begin to deplete, in addition to the inner 2DEG. The exact point of this effect is difficult to determine, but a connection to the decrease of α_b is very likely. Due to the deviation of α_b in this transition range, CPE_b can no longer be treated as an ideal capacitor. Possible explanations for this deviation are the distortion of the electric field in the cap and barrier layer or the impact of trap states. The field distortion, however, cannot explain the subsequent increase of α_b in the depletion range, as the extent of the distortion will increase when U_{bias} is increased further. Therefore, trap states are likely to be responsible for the deviation of α_b. The observation that their influence is not seen at lower U_{bias} can be due to a corresponding energetic level deep in the band gap, which is not excited until U_{bias} has reached a certain value. It might also indicate that these traps only affect the outer 2DEG, which is not depleted before. When the depletion of the inner 2DEG is complete, a further

increase of U_{bias} will only result in a slightly increasing lateral depletion of the outer 2DEG (fig. 6.6e). A constant and nearly ideal capacitive behaviour is observed in this case, as neither the area of the remaining back electrode, provided by the outer 2DEG ring, nor the effective dielectric thickness will be affected to a great extent.

It becomes clear that the CPE_b primarily reflects changes of the lateral geometry of the 2DEG back electrode. As a consequence, no depth profiles that reach into the GaN bulk layer can be derived from the insulator capacitance. When the 2DEG starts to deplete laterally, the capacitance is dominated by the decreasing area of the 2DEG back electrode and the simple plate capacitor geometry can no longer be employed. Therefore, a corresponding depth can no longer be calculated using equation 5.6. Although a three-dimensional conductance via the GaN bulk may be possible, its influence will be marginal as the bulk was found to be compensated in the investigated heterostructures. In addition, a possible bulk conductance does not change the fact that the applied bias voltage will always drop across the insulator, as no bulk contact exists. The conductance of the 2DEG can be linked to G_{2DEG}, on the basis of the derived values and the observed voltage dependence. In the enhancement range a value of about 10 mS or 100 Ω is found. For comparison, an estimate for the resistance of the outer 2DEG $R_{2DEG_{out}}$ can be calculated from the sheet resistance $R_{\square}$, the radius of the Schottky contact r_{sc} and the inner radius of the Ohmic contact r_{oc} using:

$$R_{2DEG_{out}} = \frac{R_{\square}}{2\pi} \ln(\frac{r_{oc}}{r_{sc}}). \tag{6.2}$$

For the $B_{10}^{30}C_2$ heterostructure with a typical sheet resistance of 400 Ω/□ and with the outer radius of the Schottky contact ($r_{sc} = 360\,\mu m$) and

the inner radius of the ohmic contact ($r_{oc} = 760\,\mu m$) of the mercury probe, a value of about $50\,\Omega$ is obtained. The average resistance of the inner 2DEG cannot be calculated as easily since it is distributed below the Schottky contact, but a value of several ten Ωs is a reasonable estimate. The resulting total resistance of up to $100\,\Omega$ agrees very well with R_{2DEG}. Additionally, the depletion characteristic that is observed for G_{2DEG} confirms the connection to the 2DEG. Initially, its approximately linear decrease reflects the decrease of the sheet carrier concentration n_s in the inner 2DEG. The inner 2DEG most likely starts to deplete from the centre of the Schottky contact towards its border (fig. 6.6b). The logarithmic decrease in the transition region signifies that n_s is reduced accordingly (fig. 6.6c-d).

The equivalent element CPE_t can be treated as a phenomenological description of the influence of trap states on the 2DEG. Essentially, it models the frequency dependent trapping of 2DEG charge carriers. The rather unusual placement of this element parallel to 2DEG conductance can be understood as a charge bypass at high frequencies. It does not imply that the trap states are localised at the AlGaN/GaN interface. Nevertheless, it is a very suitable description for charge traps with a broad distribution of time constants. At low frequencies most charge carriers will flow via R_{2DEG}, whereas at high frequencies some portion flows via CPE_t, i.e. it is lost to trap states. The relatively constant values of Q_t and α_t in the enhancement range suggest that trapping process and its distribution is independent of U_{bias}. However, the depletion of the 2DEG decreases Q_t and increases α_t. This deviation does not mean that fewer trap states are present or that their distribution becomes smaller. Instead, the measurement method fails to extract the true properties of the traps, when the back electrode is lost and the field geometry is severely distorted. This emphasises the

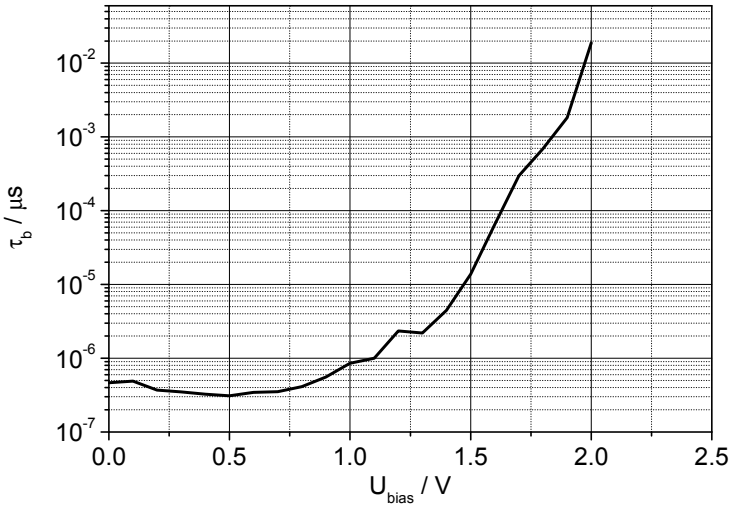

Figure 6.7: Characteristic time constant τ_t of traps states derived from the parallel equivalent circuit $CPE_t||R_{2DEG}$ versus applied bias voltage.

phenomenological character of CPE_t - it cannot describe the charge that is lost from the 2DEG when no 2DEG is present. Nevertheless, for the enhancement and early transition ranges a characteristic value around which the time constants are distributed can be calculated using:

$$\tau_t = (\frac{Q_t}{G_{2DEG}})^{1/\alpha_t}, \tag{6.3}$$

as proposed by Brug et al. [211]. In figure 6.7 this characteristic time constant is plotted versus U_{bias}. Values of (1–10) µs are found towards the end of the enhancement range, which agree very well with the

published trap time constants of 1 µs [206] and 4 µs [208]. The steep increase towards the depletion range has no physical meaning, due to the discussed limits of the model.

An estimate for the total charge lost to traps can be obtained through integration of CPE_t, similar to the calculation of the total sheet charge density N_s (section 5.3.2). However, for the integration a capacitance equivalent is needed for CPE_t. This can be derived for the parallel circuit $CPE_t||R_{2DEG}$ using the estimation by Brug et al. [211]. Normalised by the area of the Schottky contact A_{sc} it yields:

$$C'_t = \frac{(Q_t R_{2DEG}^{1-\alpha_t})^{1/\alpha_t}}{A_{sc}}. \tag{6.4}$$

Applying equation 5.5 to C'_t, a value of $N_t = 1.8 \times 10^{12}\,\mathrm{cm}^{-2}$ is obtained. The good agreement to the trap density of about $1 \times 10^{12}\,\mathrm{cm}^{-2}\,\mathrm{eV}^{-1}$ reported by Miller et al. [206] suggests that the total sheet charge density lost to traps N_t corresponds to D_{it}.

It can be summarised that the derived equivalent circuit is very suitable for the description of the AlGaN/GaN heterostructure. The correlation of the equivalent elements to the actual device structure is as follows: R_s represents the ohmic contact, R_b and CPE_b reflect the insulator resistance and capacitance, respectively, and R_{2DEG} accounts for the resistance of the 2DEG. A phenomenological description of the trapping of 2DEG charge is given by CPE_t. The impedance spectra suggest that CPE_b and R_{2DEG} have the largest influence on the overall impedance, whereas R_s is too small and R_b too large to have significant impact. The influence of CPE_t is frequency dependent and accounts for most of the frequency dispersion of the impedance. In general, the CPE was shown to be an appropriate model to describe the influence of trap states with a broad distribution of time constants. The characteristic

time constant and the trap density that were estimated from CPE_t and R_{2DEG} agree well with published values.

6.1.2 Impedance-Voltage Profiling

Although a very good model for the AlGaN/GaN heterostructure can be obtained, impedance spectroscopy cannot be used for the characterisation of time-dependent processes, such as drift phenomena. This is due to the fact that the recording of impedance spectra with varying bias voltages is a very time consuming process with measurement durations of up to 4 h. Impedance-Voltage profiles, however, typically take (10–15) min and are therefore a more suitable measurement method for this purpose. The inherent trade-off of this method is that only two parameters are measured an, in turn, only two equivalent elements can be estimated. Therefore, the full equivalent circuit, as derived from impedance spectroscopy, needs to be reduced to its most important two elements.

As a first step, the quality of the full equivalent circuit with regard to impedance-voltage profiles is discussed. Subsequently, a reduced equivalent circuit for the interpretation of impedance-voltage profiles is derived and the connection between the full and the reduced equivalent circuit is discussed. The derivation of important parameters for the characterisation of the heterostructure is given at the end of this section. To evaluate the quality of the full equivalent circuit, $Z_{re}(U_{bias})$ and $Z_{im}(U_{bias})$ profiles were calculated from the fitted equivalent elements using equation 6.1 for various frequencies and compared to data obtained by direct $\underline{Z}(U)$ measurements (fig. 6.8). An excellent agreement is obtained for Z_{im} and only minor deviations can be observed for Z_{re}. This confirms that the derived equivalent circuit is very well

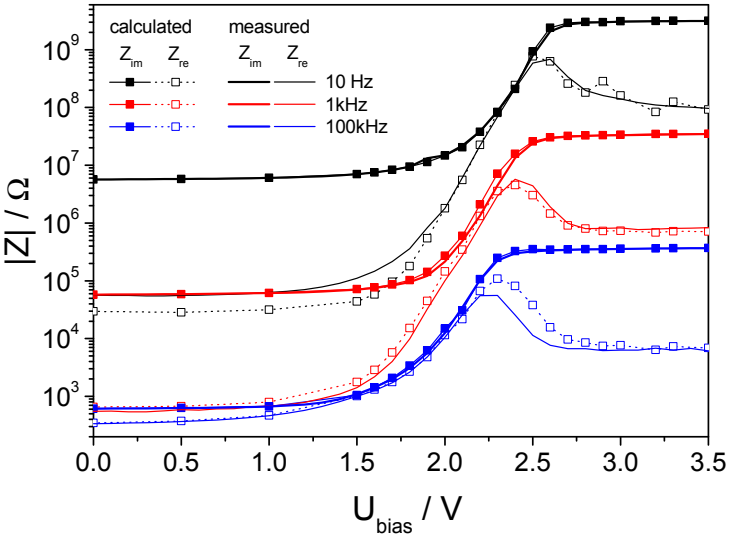

Figure 6.8: Comparison of Z_{re} and $|Z_{im}|$ at 10 Hz, 1 kHz, and 100 kHz, measured directly and calculated from the full equivalent circuit using eqn. 6.1.

suited to describe the AlGaN/GaN-Hg-MIHS over a large frequency range.

One reason for the very good match between the derived model and the measurements is that the full equivalent circuit has a large number of degrees of freedom. Five equivalent elements with a total of seven parameters are used to reproduce the impedance in the investigated frequency range. For the application to impedance-voltage profiling the number of parameters has to be reduced to two, as only Z_{re} and Z_{im} are measured. A simple series connection of a capacitor and a resistor was

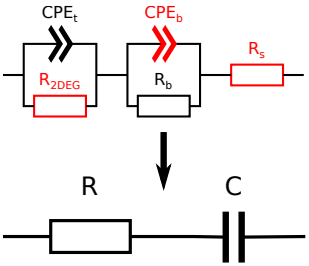

Figure 6.9: Suitable reduction of the full equivalent circuit for the application of impedance-voltage profiling.

chosen (fig. 6.9) since the impedance is mostly dominated by the capacitive contribution of CPE_b and the resistive contribution of R_{2DEG}. This results in the following simple equations for the calculation of C and R from the obtained impedance data:

$$\begin{aligned} C &= \frac{1}{2\pi f_{ac} Z_{im}}, \\ R &= Z_{re}. \end{aligned} \tag{6.5}$$

Due to the discussed frequency dispersion it is reasonable to record at least one profile at low frequency (LF - (1–10) Hz) and one at high frequency (HF - (10–100) kHz). The capacitance C and conductance $G = \frac{1}{R}$ at 10 Hz and 100 kHz were calculated from measured impedance-voltage profiles and are compared to Q_b and G_{2DEG} in figure 6.10. For C a typical depletion characteristic is observed, which shifts towards lower bias voltages at 100 kHz. A close agreement of $C_{10\,\mathrm{Hz}}$ and Q_b is observed for the whole range of U_{bias}, except for a small deviation in the transition range. The conductance G also shows a depletion characteristic that is more pronounced at low frequencies. In addition, a conductance shift towards higher values at high frequency is present.

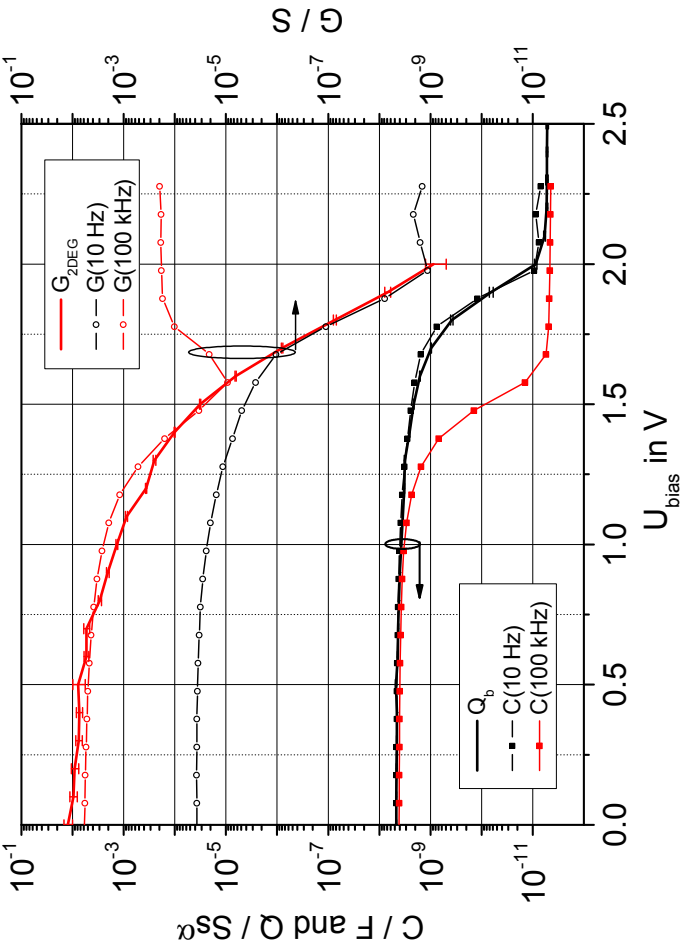

Figure 6.10: Comparison of the elements of the reduced equivalent circuit (C, G) at low and high frequencies to elements of the full equivalent circuit (Q_b, G_{2DEG}) for an AlGAN-MIHS.

In the enhancement range the admittance G_{2DEG} can be approximated by $G_{100\,\mathrm{kHz}}$ and in the transition range its course approaches $G_{10\,\mathrm{Hz}}$.

The good agreements between the elements of the reduced equivalent circuit and Q_b and G_{2DEG} confirm that the insulator capacitance and the 2DEG resistance determine the overall impedance of the MIHS structure to a large extent. The insulator capacitance can be estimated by $C_{10\,\mathrm{Hz}}$ in the investigated voltage range. In order to estimate the 2DEG conductance a single impedance-voltage profile at low frequency is not sufficient. For the enhancement range an additional high frequency profile is needed. This is due to the influence of trap states, which is not accounted for by the reduced equivalent circuit. However, the frequency dispersion that is observed for C allows for the estimation of the amount of charge that is transferred to trap states. It was found that the difference between the sheet charges in the 2DEG at low and high frequency is approximately equal to N_t, calculated from Q_t. The following equation reflects the relation between N_t and the difference $N_s(LF) - N_s(HF)$:

$$\begin{aligned} N_t &= \int_{U_{bias}} \frac{C_t'(U)}{e} dU \\ &\approx \int_{U_{bias}} \frac{C_{LF}' - C_{HF}'(U)}{e} dU = N_s(LF) - N_s(HF). \end{aligned} \tag{6.6}$$

When applied to the data shown in figure 6.10, a value of about $2.0 \times 10^{12}\,\mathrm{cm}^{-2}$ is obtained for $N_s(10\,\mathrm{Hz}) - N_s(100\,\mathrm{kHz})$, which is very close to the $1.8 \times 10^{12}\,\mathrm{cm}^{-2}$ estimated for N_t. The deviation may be explained by the additional trapped charge from the outer 2DEG, which is affected due to the lateral depletion. As CPE_t only characterises the inner 2DEG, this charge is not reflected. The insulator conductance G_b and the conductance of the ohmic contact G_s cannot be reproduced

by either the low or the high frequency impedance-voltage profile. The only possible indication of G_b is the value of $G_{10\,\mathrm{Hz}}$ in the depletion region, which is within one order of magnitude.

As a next step, structural and electrical properties of the investigated heterostructure are estimated from impedance-voltage profiles using the reduced equivalent circuit. The common methods of capacitance-voltage profiling (section 5.3.2) can be applied for this purpose, as $C_{10\,\mathrm{Hz}}$ has been identified as a very good estimate of the insulator capacitance. The sheet charge density N_s can be estimated using equation 5.5 by integration up to $U_{bias} = 0\,\mathrm{V}$. For the $B_{10}^{30}C_2$ heterostructure a typical value of about $8 \times 10^{12}\,\mathrm{cm}^{-2}$ is obtained. The thickness of the insulator can be approximated using equation 5.6 and the capacitance C_0' at zero bias voltage with a value around $800\,\mathrm{nF\,cm}^{-2}$. This corresponds to an estimated insulator thickness of 10 nm, which is significantly lower than the targeted total thickness of the barrier and cap layer (12 nm). The origin of this difference is not yet understood. Possibly, the area of the Hg-Schottky contact is larger than assumed for the calculation or voids in the GaN cap layer reduce the total insulator thickness.

The threshold voltage of the 2DEG can be determined using a linear extrapolation of $n_s(U_{bias})$, which is calculated using equation 5.5. However, this method depends on the choice of the linear region as illustrated in figure 6.11. Here, the intersection with the x-axis shifts towards lower voltages (see arrow) when fewer points are used for the linear fit. The values of U_{th} range from 1.8997 V to 1.7864 V, i.e. a deviation of up to 113.3 mV. This value is unacceptable, as U_{th} will be used to determine pH induced changes of the surface potential. In light of a maximum pH-sensitivity close to $60\,\mathrm{mV\,pH}^{-1}$ this uncertainty would correspond to about 2 pH units. Furthermore, the linear approx-

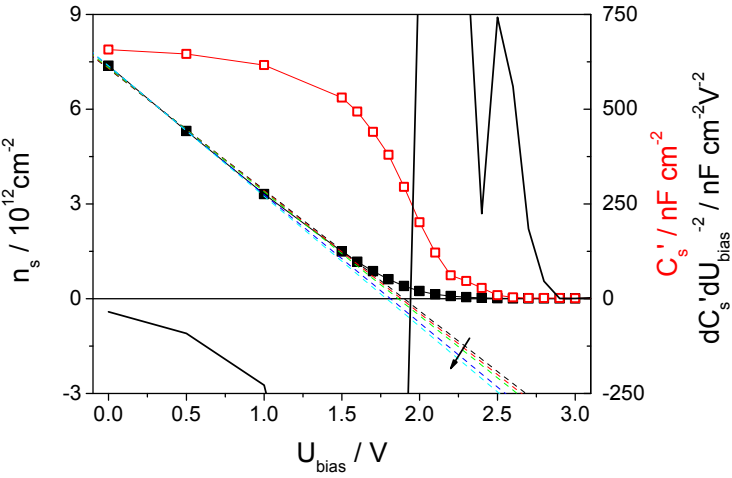

Figure 6.11: Comparison of methods to derive U_{th}: linear extrapolation of $n_s(U_{bias})$ (filled squares) for a differing amount of data points (dashed lines - arrow signifies fewer data points) and determination of the inflection point of $C'(U_{bias})$ (open squares) by calculating the zero-crossing of the second derivative (continuous line).

imation can not easily be implemented for a automated data analysis without ambiguity. Therefore, a different method was developed which is based on the inflection point of $C'(U_{bias})$ as a measure for the threshold voltage. It is calculated by linear interpolation of the zero-crossing of the second derivative. The advantage of this method is the unambiguity in the determination of U_{th} and the easy implementation for automated data analysis. For the shown data, $U_{th} = 1.9405\,\mathrm{V}$ is obtained, which is slightly higher than the values obtained using the linear

extrapolation method. However, this small deviation is negligible compared to the absolute value of U_{th} ($\approx 2\%$). Therefore, the inflection point of $C'(U_{bias})$ is a very suitable estimate of the threshold voltage. Additionally, it will be shown later on that this method is capable of providing sub-millivolt resolution for long-term drift measurements and reproducibility tests and that it is robust with respect to shifted and slightly distorted data.

Additional parameters that will be used for the characterisation of drift effects and sensitivity are the zero bias capacitance and conductance C_0' and G_0, as well as the conductance threshold voltage U_{th_G} determined from using the inflection point method.

In summary, it was found that the series connection C+R is the appropriate equivalent circuit to model the AlGaN/GaN heterostructure for impedance-voltage profiling. At low frequency the equivalent series capacitance corresponds to the insulator capacitance and common methods from CV-profiling can be employed to estimate N_s and d_0. For the determination of the threshold voltage an unambiguous and robust method was developed, based on the inflection point of the CV-profile.

6.1.3 Scanning Electron Microscopy

Although the measurements with the mercury probe are assumed to be nondestructive, it was observed that the contact areas exhibit some form of contamination after prolonged measurements. The SEM image shown in Fig. 6.12a illustrates that a darker, more conducting layer has been deposited below the mercury contacts. It also reveals that the small, inner Schottky contact is not a well defined circle but a rather irregular area. Therefore, the reproducibility of the measurements is limited by the uncertainty of this Schottky area, which is assumed to

be ±5%. In addition, the contamination from the mercury contacts can induce drift phenomena within a measurement series.

In order to gain insight into the surface morphology of the AlGaN/GaN heterostructure, SEM images were taken at high magnification. This image is used as a reference to evaluate the extent of the (photo-)-electrochemical corrosion and the influence of the fabrication process. In figure 6.12b the SEM image of an as-grown $B^{30}_{10}C_2$ wafer is given, revealing dark holes on a mottled background. The holes can be attributed to screw dislocations reaching the surface. Counting the defects per square micrometre, a defect density of $1 \times 10^9\,\mathrm{cm}^{-2}$ can be estimated, which agrees well with the values obtained by Tonisch [197]. It should be noted that the published values were obtained using AFM measurements on wafers that were previously etched in H_3PO_4 at 180 °C to emphasise the point defects. This defect etching step is needed as the diameter of the AFM tip limits the lateral resolution to a few tens of nanometres, depending on the quality of the tip. Using high resolution SEM images, however, point defects with a diameter of less than 10 nm can be resolved, due to the much higher lateral resolution of the SEM and the high contrast of the defects. The contrast is induced by the morphology of the defects and their higher conductivity compared to the insulating cap and barrier layers. The mottled background reflects grain boundaries or step dislocations of the deposited crystalline layers, which appear as cloud-like structures in AFM images. These dislocations have a major impact on the crystalline quality of the heterostructure, limiting its resistance to corrosion. As the structural defects also manifest themselves as energetic defects in the band structure of the semiconductor, an influence on related parasitic phenomena such as persistent photoconductivity and current collapse is assumed.

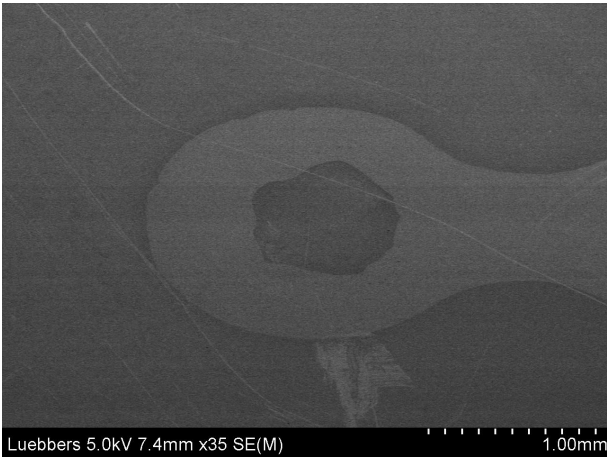

(a)

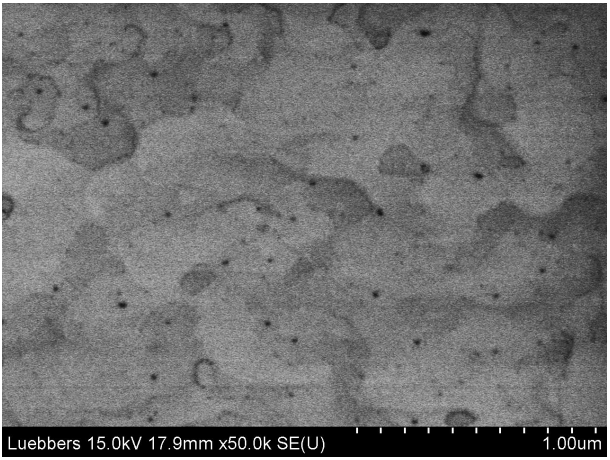

(b)

Figure 6.12: SEM images (a) at low magnification showing the contamination that is introduced by the mercury contact and (b) at high magnification showing the surface of an as-grown $B_{10}^{30}C_2$ wafer.

6.1.4 Summary

In summary, the preceding discussion on the impedance characterisation of as-grown $B_{10}^{30}C_2$ wafers using a mercury probe (MIHS) yielded the following results and conclusions:

- The series connection of R_s, $CPE_b||R_b$ and $CPE_t||R_{2DEG}$ is a very suitable equivalent circuit for the AlGaN/GaN-MIHS in the frequency range from 1 Hz to 1 MHz and in the bias voltage range (0–3) V. A plausible physical interpretation for each element was given and verified.

- The CPE is a good phenomenological description of trap states with a broad distribution of time constants. Estimates of the characteristic time constant and trap density obtained from CPE_t agree with published values.

- For the application of impedance-voltage profiling the full equivalent circuit is reduced to a series connection $C + R$. At low frequencies C is equal to Q_b and corresponds to the insulator capacitance. The resistance of the 2DEG is reflected in R_{2DEG}, which can partly be approximated by R at low and high frequency.

- The sheet charge density N_s and threshold voltage U_{th} can be calculated from the capacitance-voltage profile of the reduced equivalent circuit. The estimation of the insulator thickness d_0 yields significantly lower values than expected.

- The inflection point of the insulator capacitance C is a good and unambiguous measure of the threshold voltage.

- For the interpretation of impedance-voltage profiles of the MIHS, the lateral depletion of the 2DEG towards the ohmic contacts

needs to be considered. Depth profiles are therefore only possible to a limited extent, as the 2DEG is not depleted vertically into the GaN bulk layer.

- Due to the two-dimensional depletion geometry, the MIHS needs to be modelled with a series connection $C + R$, rather than the commonly assumed parallel connection $C||R$.

- A dislocation density of $1 \times 10^9\,\mathrm{cm}^{-2}$ was estimated for the as-grown wafer from high-resolution SEM images. No previous etching step was required to determine this density.

These results and conclusions allow for the clarification of the considerations that were put forth at the beginning of this chapter, concerning the two-dimensional depletion of the 2DEG, the origin of the phase angle peak and the appropriate modelling of the frequency dispersion.

- Firstly, it was assumed that the obvious difference between the common one-dimensional MIS structure with a back contact and the two-dimensional AlGaN/GaN MIHS results in a significant deviation from the one-dimensional depletion characteristic. This assumption is verified by the observation that the suitable reduced equivalent circuit is the series connection $C + R$, instead of the parallel connection $C||R$. The series connection implies that R has to be located outside the insulator layer and that it has a significant impact on the overall impedance. Its depletion characteristic indicates that it reflects some portion of the 2DEG channel. Therefore, R must be related to degradation of the 2DEG and the pinch-off at the outer 2DEG. Figuratively speaking, the input leads to the inner 2DEG are supplied by the outer 2DEG, which becomes the bottleneck, in terms of conductance,

when the 2DEG is depleted. For the one-dimensional MIS structure no impact of a series resistance will be observed, as the bulk material always sufficiently conducts and is generally unaffected by the depletion (or enhancement) region below the insulator.

- Secondly, it was stated that the phase angle deviation in the transition range of the impedance-voltage profiles has been disregarded so far and that its origin has not been discussed. From the results obtained in this section, it can be derived that the two-dimensional geometry of the AlGaN/GaN heterostructure is the source of this phase angle peak. A two-fold 2DEG depletion process can be found: an area-depletion of the inner 2DEG, reflected by CPE_b (or C), and a conductance-depletion mostly at the outer 2DEG, as seen in G_{2DEG} (or G). The fact that these two depletion processes differ with regard to their characteristics is the reason for the deviation of the impedance phase angle ϕ. An increase of ϕ is found, as the 2DEG conductance G is affected before the area of the 2DEG is reduced. This has an important implication for the interpretation of the phase angle peak: the higher the peak, the more dominant the conductance-depletion is compared to the area-depletion. Taking into account the correlation with the outer and inner 2DEG, it can be concluded that a high peak corresponds to a pinch-off at the outer 2DEG, whereas a low peak corresponds to a pinch-off at the inner 2DEG.

- Thirdly, it was suggested that the modelling of the frequency dispersion cannot be achieved with a simple parallel equivalent circuit and that the equivalent circuits that are commonly employed to account for trap states are not suitable. As a different equivalent circuit was found for the two-dimensional depletion

geometry of the AlGaN/GaN heterostructure, the model for the trap states needed to be modified. It was confirmed that the CPE is an appropriate phenomenological model for the impact of trapping on the 2DEG. This model also explains why the pinch-off of the AlGaN/GaN MIHS is influenced to a greater extent by trap states, compared to MIS structures with a back contact. As previously discussed, the outer 2DEG is the bottleneck of the heterostructure. Therefore, the frequency dependent trapping of charge from the outer 2DEG has a pronounced influence on the depletion characteristic. These conclusions may also be applied to gain more insight into the mechanism of the current collapse, which is closely correlated to the observed pinch-off.

In the following section the focus is shifted from the semiconductor structure to its interface with an electrolyte solution. The same impedance measurements as in this section are performed on the EIHS to reveal how the electrolyte Schottky contact influences the semiconductor. Additionally, it is investigated whether information on the electrolyte-semiconductor interface can be obtained.

6.2 Chip level characterisation of the EIHS

Electrochemical impedance spectroscopy and profiling has not been applied to entire as-grown wafers, as no suitable measurement setup, comparable to the mercury probe, was available. Instead, AlGaN/GaN-EIHS sensor chips were fabricated from $B_{10}^{30}C_2$ wafers as described in section 5.1 and characterised using the developed electrochemical measurement cell (section 5.2.2). In accordance with the approach that was used for the wafer level characterisation, the electrochemical impedance

spectrum of the EIHS was investigated as a first step. This way the differences between the metal and the electrolyte Schottky contact can be determined. The same ambient conditions were used, including no illumination. The most apparent difference between the metal and electrolyte Schottky contact is their area, which is about ten times larger for the EIHS ($A_{sc} = 4.91\,\mathrm{mm}^2$ compared to $0.41\,\mathrm{mm}^2$). The ohmic contact of the EIHS exhibits a lower resistivity than its mercury probe counterpart due to the use of an alloyed Ti/Al/Ti/Au metal stack, providing a typical contact resistance of (3–4) $\Omega\,\mathrm{mm}$. However, the contribution that dominates the series resistance by several orders of magnitude is the impedance of the reference electrode which amounts to several kΩ. For the employed standard glass reference electrode, the impedance of the ceramic diaphragm is specified with $< 5.5\,\mathrm{k}\Omega$.

6.2.1 Electrochemical Impedance Spectroscopy

The electrochemical impedance spectra for $U_{bias} = (0\text{–}2.5)\,\mathrm{V}$ are shown in figure 6.13 for the frequency range $f_{ac} = 1\,\mathrm{Hz}$ to $1\,\mathrm{MHz}$. The employed electrolyte is the phosphate buffer solution PB6.88. Similar to the spectra of the MIHS, a plateau is observed for Z_{re} at low bias voltage, which shifts toward lower frequencies and higher impedance with increasing U_{bias}. At very low and high frequencies a decreasing slope is found. The low frequency slope is shifted towards higher impedance and subsequently overlapped by the shifting plateau. The high frequency slope is only shifted slightly towards lower frequencies. At high U_{bias} the EIHS is characterised by a single slope. For Z_{im} a nearly ideal slope of -1 is observed at low U_{bias} and frequencies up to $10\,\mathrm{kHz}$. With increasing bias voltage, the slope is shifted towards higher impedance and a second slope develops, which is less steep. At frequencies

exceeding 10 kHz, the slope reverts to a slight increase followed by another minor decrease. Generally, the shift towards higher impedance is found to be less pronounced for increasing frequency. Near 1 MHz the imaginary part is independent of U_{bias}.

Most of the deviations between the EIHS and the MIHS in the impedance spectra can be attributed to the reference electrode. The plateau of Z_{re} in the frequency range from 100 Hz to 100 kHz indicates that its resistive contribution amounts to about 10 kΩ. Additionally, the course of Z_{im} at high frequencies suggests that the reference electrode also has a parallel capacitive characteristic. Its value was estimated to be about 30 pF, which is rather high for a reference electrode. This implies that additional parasitic capacitive elements are present in the measurement setup. To minimise their influence and to facilitate the fitting procedure, the frequency spectra are only evaluated up to 10 kHz. This way only the resistive part of the reference electrode has to be accounted for.

The fitting procedure revealed that the full equivalent circuit, derived for the MIHS, can also be applied to the EIHS. The voltage profiles of the equivalent capacitive elements CPE_b and CPE_t (thick lines), and the conductive equivalent elements G_b, G_{2DEG} and G_s (thin lines) are plotted versus U_{bias} in figure 6.14. For most equivalent elements the previous correlation to the device structure can be adopted. Only the physical interpretation of R_s has to be extended, as it is now primarily determined by the resistance of the reference electrode. In general, it can be stated that R_s is a lumped representation of all series resistive elements outside the actual heterostructure, such as the ohmic contact, the reference electrode resistance and the resistance of the electrolyte solution. In contrast to the former two, the latter resistance is an important factor that is variable and depends directly on the composition

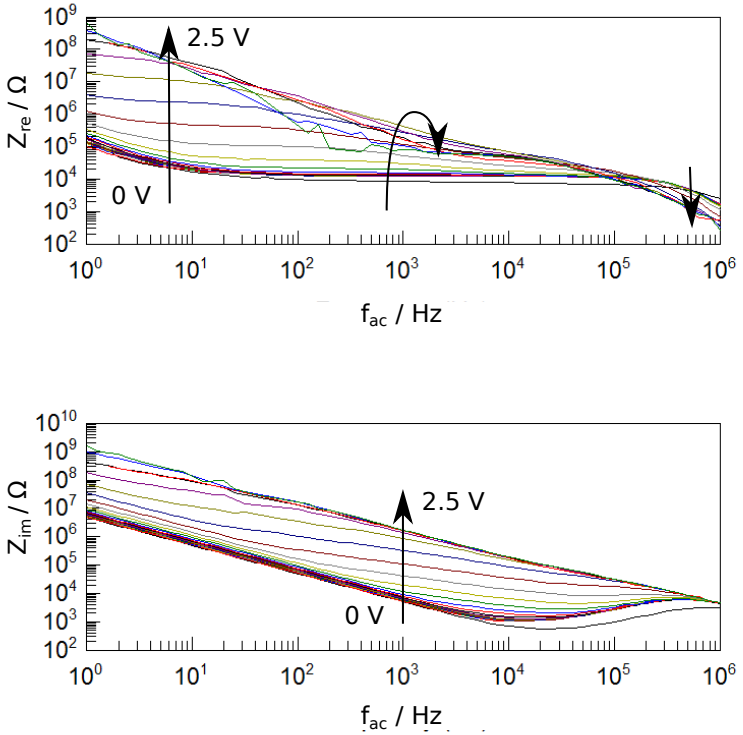

Figure 6.13: Real and imaginary electrochemical impedance spectrum of an AlGaN-EIHS ($B_{10}^{30}C_2$) at pH6.88 with increasing bias voltage

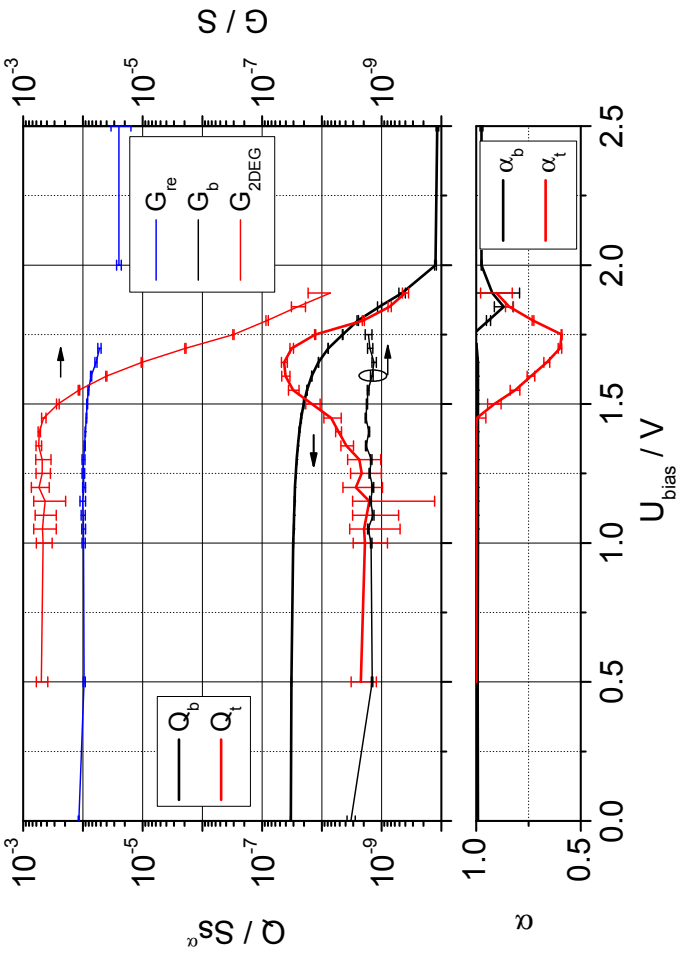

Figure 6.14: Voltage profiles of the equivalent elements CPE_b and G_b (black), Q_t and G_{2DEG} (red) and G_s (blue) of an AlGaN-EIHS, derived from electrochemical impedance spectra.

of the electrolyte solution. At lower ionic strength the influence on R_s is expected to be more significant.

As no additional equivalent element is needed to model the EIHS, it can be assumed that the impedance of the electric double layer cannot be extracted. This is due to the relatively high ionic strength (I = 100 mM) of the employed buffer solution, which reduces the EDL to the Helmholtz layer (cf. section 2.1). Its capacitance is estimated to be in the range of (10–20) µF cm^{-2} for metal oxides [212] and may therefore be too large to influence the measured spectra. In general, the voltage profiles of the EIHS equivalent elements are very similar to the MIHS. In figure 6.15 and 6.16 the equivalent CPE-voltage profiles and conductance-voltage profiles of the EIHS and the MIHS are compared. For this comparison, the insulator capacitance and conductance need to be normalised by the area of the Schottky contact, giving Q'_b and G'_b.

Figure 6.15 illustrates that qualitatively similar characteristics are obtained for Q'_b, except for lower values in the enhancement range and a small voltage shift for the EIHS. The corresponding exponent α_b also exhibits this voltage shift, but is otherwise very similar to the MIHS. Pronounced differences, however, are observed for the profiles of CPE_t. In the enhancement range, a much lower magnitude Q_t is found for the EIHS and the exponent α_t suggests ideal capacitive behaviour. Similar to the MIHS, the uncertainty of Q_t is relatively high, indicating that its influence is minor. In the transition range the Q_t profiles become similar in magnitude and shape, except that the EIHS profile is shifted towards higher U_{bias}. The α_t profiles do not reflect the voltage shift to this extent, but a large difference is found in the enhancement range.

The comparison of the equivalent conductance-voltage profiles in figure 6.16 clearly shows that G_s has decreased by two orders of mag-

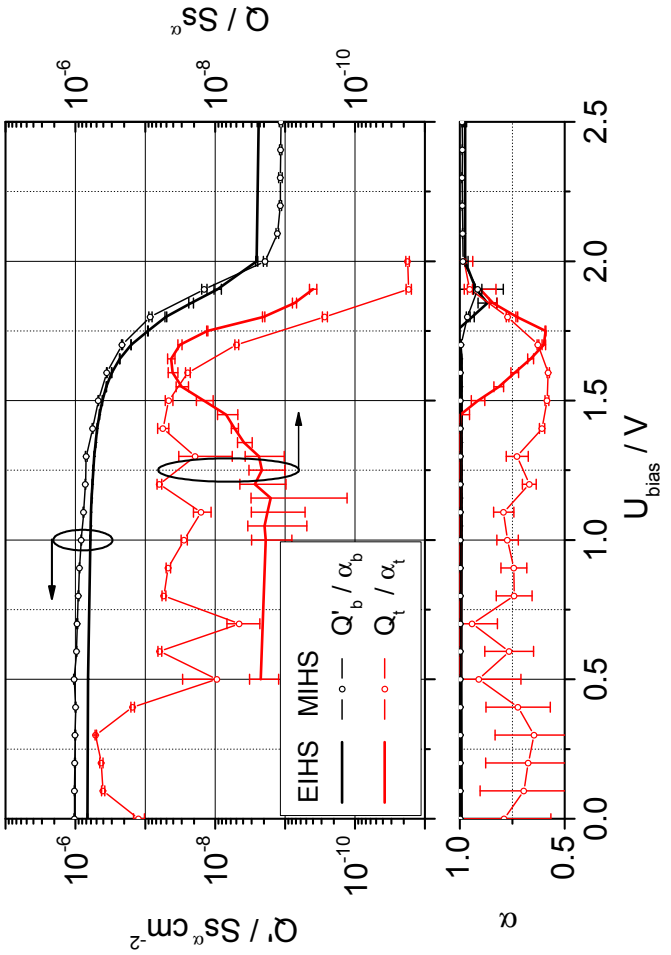

Figure 6.15: Comparison of the equivalent CPE-voltage profiles of the AlGaN-EIHS and the AlGaN-MIHS.

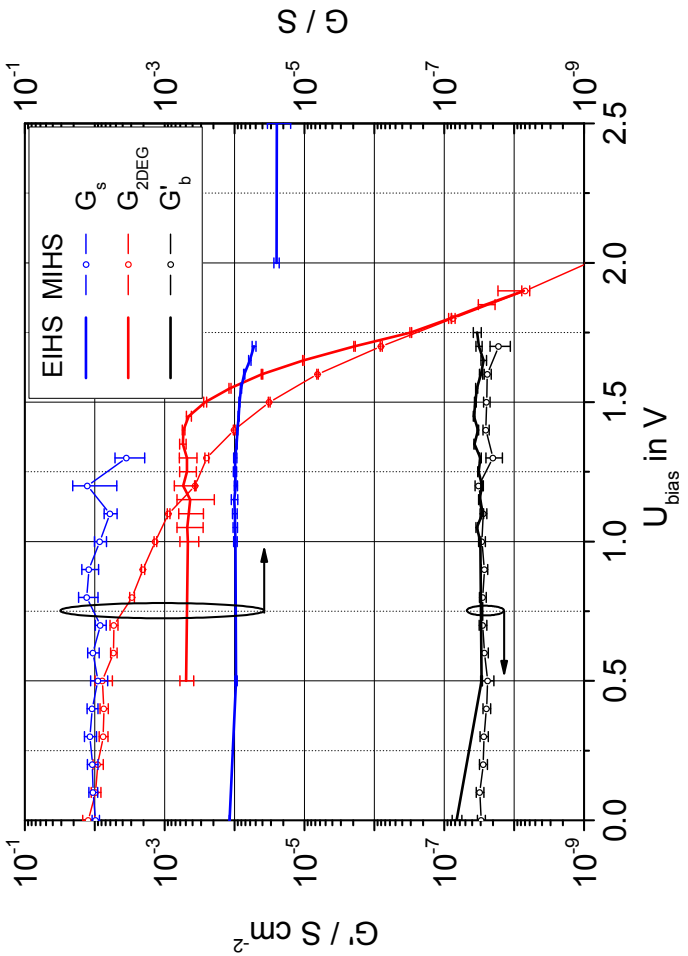

Figure 6.16: Comparison of the equivalent conductance-voltage profiles of the AlGaN-EIHS and the AlGaN-MIHS.

nitude compared to the MIHS, due to the impedance of the reference electrode. In contrast, it is found that G_b is nearly unaffected by the type of the Schottky contact. This is expected, as the insulating properties of the heterostructure should be independent of the Schottky contact. For G_{2DEG}, pronounced differences are observed in the enhancement range. Instead of a decreasing slope, the EIHS exhibits a constant plateau about one order of magnitude below the values of the MIHS. At the beginning of the transition range, a sharp changeover into a logarithmic decrease is found and towards the depletion range the course of G_{2DEG} is equal for the EIHS and the MIHS.

The observed differences can mainly be attributed to the reference electrode, the electrolyte solution and possibly to the interface with the electrolyte. As Q_b is nearly unchanged for the EIHS in the transition and depletion range, it can be concluded that the depletion geometry is not affected. The small voltage shift indicates that the surface potential is slightly higher for the electrolyte solution compared to the mercury contact. Possible explanations for the lower values in the enhancement range are the uncertainty of the Schottky area and the influence of the EDL. The former explanation implies that the estimated contact area is too small for the MIHS and/or too large for the EIHS. The influence of the EDL can be understood by looking at the series connection of the insulator and the EDL capacitance. As the EDL capacitance is larger than the insulator capacitance, this results in a reduction of the measured overall capacitance. A combination of both effects is likely to be responsible for the observed deviation, as the difference is relatively large (about 30%).

The differences in G_{2DEG} and CPE_t are linked to the high impedance of the reference electrode and the limits of measurement method. As long as G_s is smaller than G_{2DEG}, the real part of the overall imped-

ance is dominated by the reference electrode. This cut-off at 10 kΩ can clearly be seen in the real impedance spectra (fig. 6.13). As a consequence, both CPE_t and G_{2DEG} cannot be estimated properly, resulting in the observed deviations in the enhancement range. When the 2DEG is depleted to a sufficient extent, G_{2DEG} falls below G_s and both Q_t and G_{2DEG} approach the values that are observed for the MIHS. The origin of the voltage shift of Q_t is not understood, but the excellent agreement found for G_{2DEG} suggests that impact of the reference electrode is no longer present in this range. Another very interesting conclusion from this agreement is that the terminal depletion of the 2DEG conductance is independent of the area of the Schottky contact. This indicates that either the conductance of the inner 2DEG is also area-independent or that the terminal depletion is only determined by pinch-off at the outer 2DEG.

6.2.2 Electrochemical Impedance-Voltage Profiling

For the application of impedance-voltage profiling, the reduction of the full equivalent circuit to two elements is necessary for the EIHS as well. Once again the voltage profiles of the equivalent elements are compared to a low frequency (10 Hz) and a high frequency (1 kHz) impedance-voltage profile. Compared to the MIHS, the high frequency value needs to be lower in order to minimise the capacitive influence of the reference electrode. The reduced equivalent circuit C+R is also chosen for the EIHS and C and G are calculated using equation 6.5. In figure 6.17 the comparison of C and G at 10 Hz and 1 kHz to Q_b, G_s and G_{2DEG} is shown.

It can be seen that the low-frequency capacitance-voltage profile closely matches Q_b well into the transition region. Only at the end

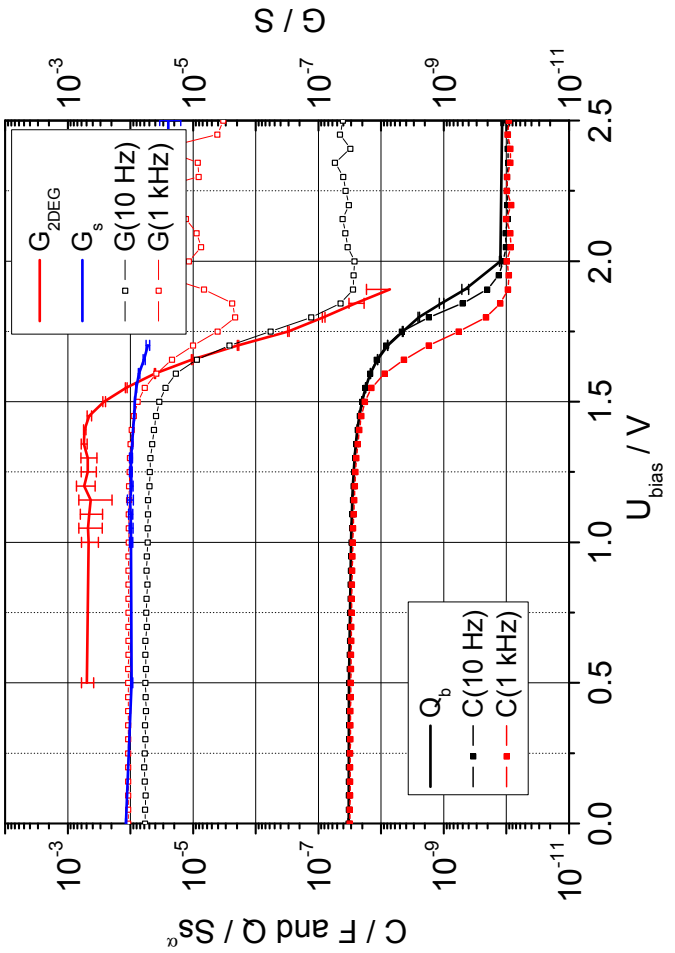

Figure 6.17: Comparison of the elements of the reduced equivalent circuit (C, G) at low and high frequencies to elements of the full equivalent circuit (Q_b, G_{2DEG}, G_s) for an AlGaN-EIHS.

of the transition region and in the depletion region a deviation, due to the decrease of α_b, becomes apparent. Nevertheless, it can be concluded that C is a good estimate of the insulator capacitance. In contrast, the estimation of trap density does not yield plausible results. Although the relation between the trapped charge and the low to high frequency difference of the 2DEG charge, expressed by equation 6.6, also holds for the EIHS, rather low values of $N_t = 0.46 \times 10^{12}\,\mathrm{cm}^{-2}$ and $N_s(LF) - N_s(HF) = 0.43 \times 10^{12}\,\mathrm{cm}^{-2}$ are obtained. These values deviate significantly from the MIHS and suggests that the total trap charge N_t no longer correlates with the trap density D_{it}, as it is unlikely that less charge is trapped by the EIHS. A suitable explanation for the low values is found in the previously discussed limitation of deriving Q_t in the enhancement range. Due to the impact of the reference electrode, Q_t and subsequently N_t are underestimated.

The equivalent conductance elements G_s and G_{2DEG} can, at least partially, be correlated to the reduced equivalent circuit. In the enhancement range $G_{1\,\mathrm{kHz}}$ is equal to the impedance of the reference electrode and the electrolyte solution G_s, as this element is not short-circuited by a parallel capacitive element in contrast to the other conductive elements. This also implies that the enhancement value of G_{2DEG} cannot be derived from impedance-voltage profiles, as it is always masked by G_s. In the transition region, $G_{1\,\mathrm{kHz}}$ deviates from G_s, tending towards lower conductance, as G_{2DEG} decreases steeply and strongly influences the overall impedance. The depletion range can be disregarded, due to the high noise level. A close match of $G_{10\,\mathrm{Hz}}$ and G_{2DEG} is obtained in the transition range. The conductance of the insulator G_b cannot be approximated by either low or high frequency conductance profiles.

The preceeding discussion confirms that the series connection $C + R$ is also an appropriate reduced equivalent circuit for the AlGaN/GaN-EIHS. The 2DEG sheet charge density, insulator thickness and threshold voltage can now be derived from the low frequency capacitance-voltage profile. The obtained values of $N_s = 6.0 \times 10^{12}\,\mathrm{cm}^{-2}$ and $U_{th} = 1.6764\,\mathrm{V}$ show that the 2DEG is depleted slightly when the heterostructure is immersed in an aqueous solution. This depletion is due to charge balancing via dipoles and mobile ions, as discussed in section 4.4. For the insulator thickness d_0 a value of 11.9 nm is obtained, which matches the targeted value of the total cap and barrier layer thickness (12 nm). This close agreement suggests that the EIHS might be more suitable for the determination of d_0. Indeed, electrochemical CV-profiling is an established method for the accurate derivation of doping depth profiles of nearly all common semiconductor. The application of electrochemical CV-profiling to GaN has been reported e.g. by Wolff et al. [213, 214].

6.2.3 Summary

In summary, the following results and conclusions have been derived from the analysis of impedance spectroscopy data and impedance-voltage profiles of the AlGaN-EIHS:

- The same full and reduced equivalent circuits that were derived for the MIHS can be applied to the EIHS. The physical interpretation of the equivalent elements is unchanged, except for the inclusion of the reference electrode impedance and the electrolyte resistance in R_s.
- The high impedance of the reference electrode limits the measured high frequency impedance and hinders the correct derivation of

CPE_t and G_{2DEG} in the enhancement range. As a consequence, the trap density can no longer be estimated from the impedance data.

- No pronounced impact of the EDL at the electrolyte-semiconductor interface on the measured profiles is observed. A possible indicator for the EDL is the decreased value of Q_b in the enhancement range.
- The parameters N_s and U_{th} reveal that the 2DEG is slightly depleted upon exposure to the electrolyte. A very good estimate of the insulator thickness d_0 is obtained.

Generally, the similarities of the EIHS and MIHS suggest that the heterostructure will have a prominent influence on the sensing characteristic of the sensor device. Additionally, it can be assumed that the conclusions derived for the MIHS are also applicable to the EIHS, especially with regard to the pinch-off of the 2DEG and the interpretation of the phase angle peak.

In order to obtain more information on the electrolyte-semiconductor interface, two approaches are possible. Either the insulator capacitance is increased to a value close to the EDL capacitance or the EDL capacitance is decreased by employing electrolyte solutions with lower ionic strength. In both cases the influence of the EDL on the overall impedance is amplified.

It was also concluded that the high impedance of the reference electrode limits the frequency range for impedance characterisation and distorts the values of CPE_t and G_{2DEG}. A possible solution to this problem is the use of low impedance reference electrodes. However, even such electrodes seldom exhibit an impedance below 1 kΩ. In addition, the miniaturisation of the reference electrode, which is necessary

for the targeted application, commonly has the trade-off of a high electrode impedance, as discussed in section 3.4.

7 Drift Behaviour and Sensitivity of the AlGaN-EIHS

In this chapter, impedance-voltage profiling is employed to characterise dynamic processes within the heterostructure and at its interface with the electrolyte solution. Special emphasis is placed on those processes that influence the stability and reproducibility of the sensor signal. This includes residual surface contamination from the fabrication process, PPC drift after illumination and electrochemical corrosion of the sensor surface. Subsequently, the pH-sensitivity and the cross-sensitivity to ionic strength are investigated. For all measurements, EIHS sensor chips with a $B_{10}^{30}C_2$ heterostructure are analysed with the developed electrochemical characterisation setup, which is shielded from ambient illumination and electromagnetic interference.

7.1 Characterisation of Drift Phenomena

Two multiparameter graphs have been developed to evaluate the drift behaviour and the sensitivity of EIHS sensors from measured impedance-voltage profiles. These standard graphs, termed *voltage profile* and

parameter footprint, are rather comprehensive representations that reflect the influences on and the properties of the AlGaN-EIHS. They will be used multiple times throughout this thesis. This is why their layout is explained in more detail in the following paragraph using a measurement series that exhibits the most important drift effects.

The *voltage profile* and *parameter footprint* of a previously unused sensor chip after switching off ambient illumination is shown in figures 7.1 and 7.2. The near neutral standard phosphate buffer solution PB6.88 was employed. The graphs have been derived from the analysis of 300 single impedance-voltage profiles at 10 Hz, which were measured every 15 minutes in direct succession. It should be noted that the developed automated analysis algorithm proved extremely useful and time-saving for this purpose.

The *voltage profile* (fig. 7.1) consists of a large primary graph and two smaller secondary graphs that share either the voltage or the capacitance axis. The primary graph shows the capacitance (solid lines) and conductance (dashed lines) profiles versus the applied bias voltage. The scaling and values on the capacitance axis (far left) and conductance axis (upper right) are equal and only separated to assign the correct units. These two profiles are calculated from the measured impedance-voltage profiles using the reduced equivalent circuit (eqn. 6.5). The capacitance axis is shared with the left secondary graph, which will be called reproducibility profile. The reproducibility profiles show the absolute voltage shift ΔU of the capacitance with respect to elapsed time or measurement count. They are calculated by interpolating all capacitance profiles to the capacitance values of a reference trace (e.g. the first trace) and subtracting the interpolated voltage values from the reference trace. The capacitance is then plotted versus the absolute values of the resulting potential difference (left upper axis). This procedure

is illustrated for exemplary values of ΔU after 1, 25 and 50 h by the bars in figure 7.1. The voltage axis is shared with the lower secondary phase profile graph, which shows the phase angle ϕ of the measured impedance (lower right axis). From the *voltage profile* the shape of the profiles can be evaluated over the entire measurement range and mainly qualitative interpretations can be derived. This includes e.g. the linearity of the voltage shift from the reproducibility profiles, the extent and dynamics of the 2DEG depletion from the capacitance profile and the amount of corrosion from the phase profile.

In contrast to the *voltage profile*, which mainly shows the measured raw data, the *parameter footprint* (Fig. 7.2) is generated from different analysis methods that derive estimates for the threshold voltages (U_{thC} and U_{thG}) and the sheet carrier concentration N_s. The threshold voltages are estimated using the inflection point method introduced in section 6.1 and N_s is calculated applying equation 5.5. Additionally, the absolute values of the capacitance and conductance at zero bias voltage, C_0' and G_0, are plotted. Generally, parameters derived from the capacitance-voltage profiles will be plotted in black, whereas parameters derived from the conductance-voltage profiles are plotted in red. The x-axis in all four subgraphs gives the number of measurements (lower axis) and the corresponding elapsed time (upper axis). The *parameter footprint* allows for the quantitative evaluation of drift effects. It will be shown that application of the inflection point method allows for the determination of very small voltage drifts as low as $0.1\,\mathrm{mV\,meas^{-1}}$. After this general explanation of the *voltage profile* and the *parameter footprint* layouts, the data presented in figures 7.1 and 7.2 is discussed briefly, to highlight the most important drift phenomena. In the subsequent sections, each phenomenon will be discussed in more detail.

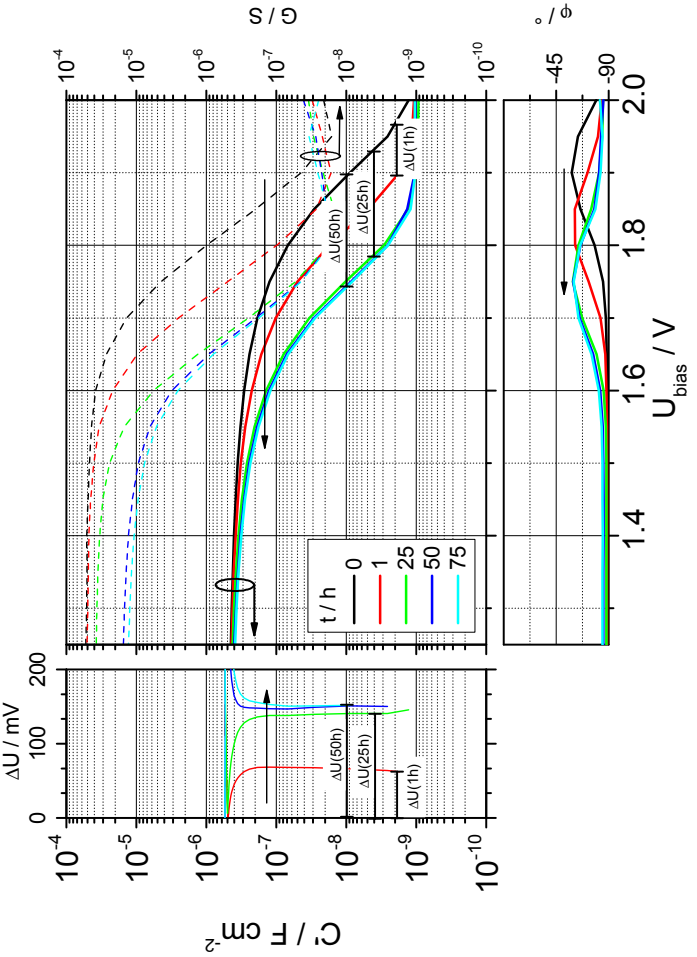

Figure 7.1: *Voltage profile* of an AlGaN-EIHS ($B_{10}^{30}C_2$) upon initial usage and after switching of illumination. The layout of the graphs is explained in the text.

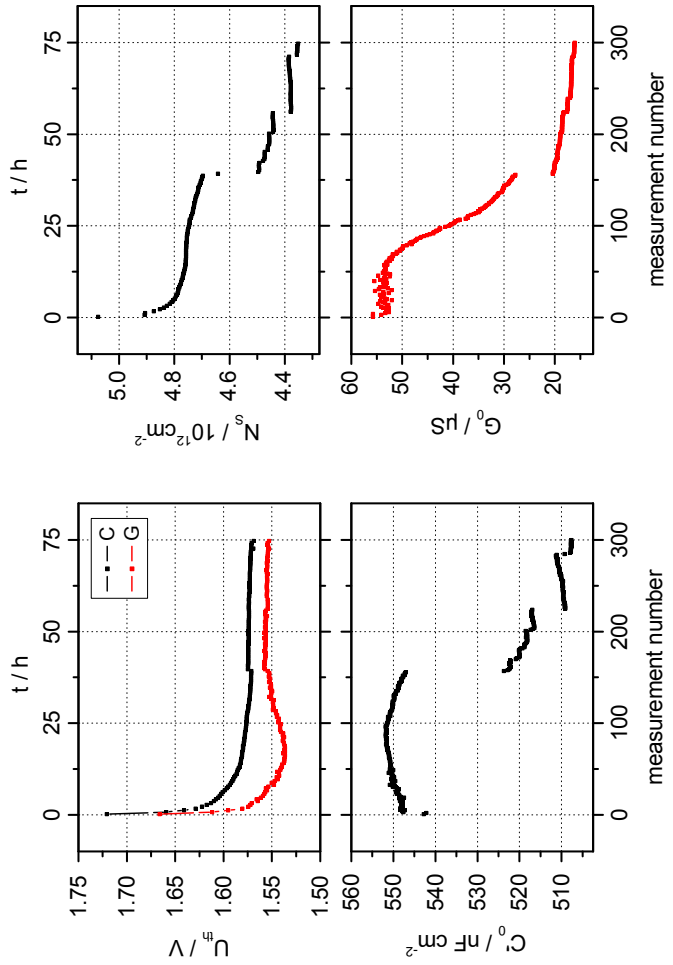

Figure 7.2: *Parameter footprint* of an AlGaN-EIHS ($B_{10}^{30}C_2$) upon initial usage and after switching of illumination. The layout of the graphs is explained in the text.

The primary drift characteristic that can be extracted from the given *voltage profile* and *parameter footprint* is the drawn-out persistent photoconductivity, which results in slowly decreasing U_{th} and N_s. However, the rather low value of C_0', the negative drift of G_0 and the artifact features (e.g. steps, high noise) suggest that additional effects or reactions influence the sensor. It was found that residual surface contamination from the fabrication process is the source of drift behaviour upon the initial usage of a sensor chip. A third kind of drift characteristic is induced by the applied bias voltage, which leads to electrochemical corrosion seen in long-term measurements. An indication of the corrosion process can be found in the ongoing shift of the reproducibility profiles and the long-term drift in the *parameter footprint*.

7.1.1 Surface Contamination Drift

In this section the drift due to a contamination layer from the fabrication process is presented and discussed. To reduce the contamination, an initial cleaning and measurement protocol is suggested. The influence of the contamination layer on the stability and drift of the sensor signal is rather unpredictable, as its dissolution is not a smooth and homogenous process.

The drift and artifact features from figure 7.1 that can be attributed to this process include the steps of N_s, C_0' and G_0 and the low absolute value of C_0'. The existence of a contamination layer on the sensor was confirmed by SEM. In figure 7.3, SEM images of the sensor surface are shown that were taken after the fabrication process (fig. 7.3a) and after prolonged storage ($>$ 2 years, fig. 7.3b). Especially the comparison to figure 6.12b reveals that the typical structure of the surface is no longer visible for the fresh contamination layer. Instead, a uniform and

featureless layer with randomly distributed particles is visible. Upon prolonged storage the layer becomes concentrated in dark dots that are distributed homogeneously and the underlying structure of the semiconductor is partly revealed.

To characterise the composition and thickness of this contamination layer, Auger electron spectroscopy (AES) was a employed. AES depth profiles of the carbon and oxygen signals of an unused sensor are compared to a sensor that had been used for several measurements (fig. 7.4). The profiles have been shifted so that the transitions between the AlGaN barrier and the GaN bulk coincide. The gallium, aluminium and nitrogen signals are not shown, as they do not change appreciably after usage. The composition of the unused sensor surface is dominated by a high carbon and a low oxygen content. After usage, the carbon content is reduced to a third of the initial value and the oxygen signal is more than doubled, leaving both signals at an approximately equal level. Additionally, a shift of about 2.5 nm is found, indicating that the height of the structure has been reduced. A closer look at the fabrication process is necessary to explain the origin and composition of this contamination layer. The fabrication of the sensor chips, as describe in section 5.1, includes several masking steps with photoresist. The complete removal of these masking layers can be problematic and imperfect, especially if the photoresist is exposed to a plasma process like the mesa etching step. During this step, the topmost part of the photoresist can become polymerised, making it difficult to be removed by the standard cleaning procedure with aceton and isopropanol. The high carbon signal in AES measurements of the unused sensor chips confirms that an organic contamination layer is present. The AES depth profile shift of 2.5 nm can be taken as an estimate for the thickness of the photoresist layer. The difference of the C and O signal between the unused and

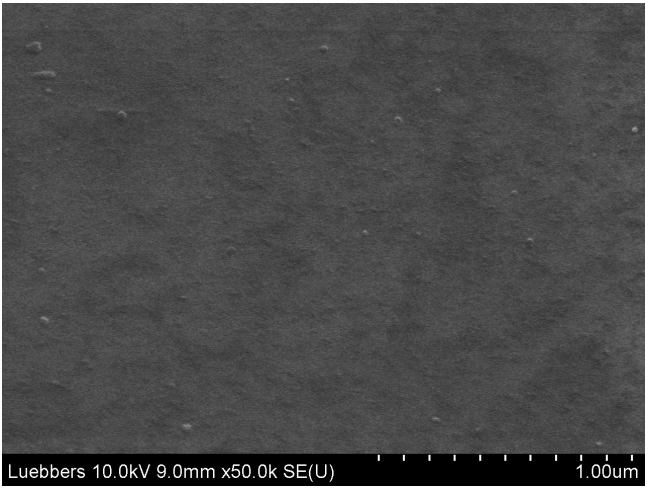

(a)

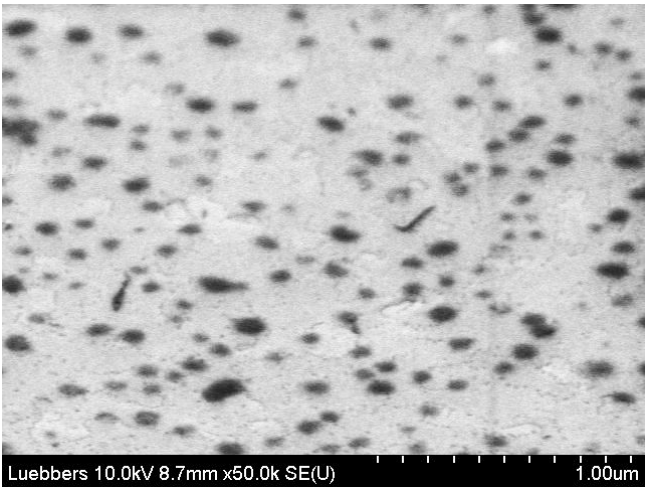

(b)

Figure 7.3: High resolution SEM images that show the surface contamination of an AlGaN-EIHS (a) directly after the fabrication process and (b) after prolonged storage ($>$ 2 years).

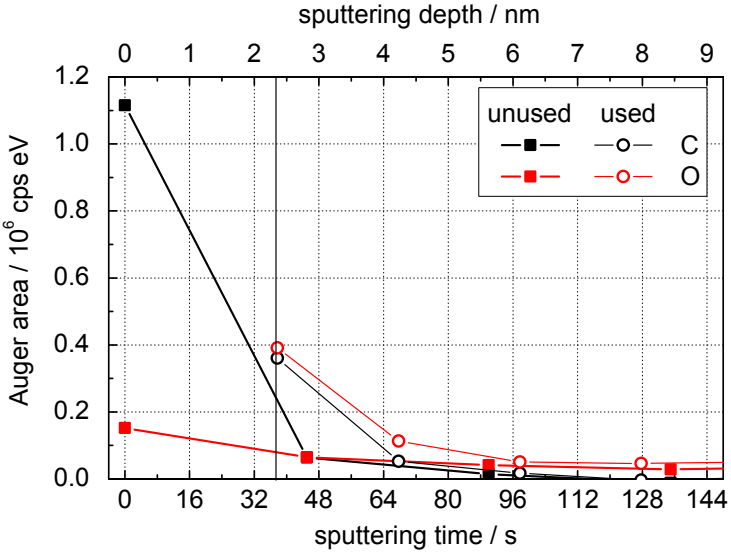

Figure 7.4: AES depth profile of an unused and an used AlGaN-EIHS sensor chip. The profiles of the used sensor chip have been shifted to match the profiles of the unused sensor chip at the AlGaN/GaN interface.

used sensor can be explained by the removal of the organic photoresist layer and the subsequent oxidation of the sensor surface.

Especially the low value of C_0' in the *parameter footprint* (fig. 7.2) can be attributed the impact of the photoresist contamination layer. For this sample, which had been stored for more than two years, an accumulation of the photoresist contamination in small dots (fig. 7.3b) was observed. This resulted in a partial reduction of the effective sensor area. The percentage coverage of the surface with photoresist contamination was estimated to be approximately 30%, from the analysis of the SEM image. This matches the difference that was found for C_0'. The unused EIHS exhibited a value of about $550\,\mathrm{nF\,cm^{-2}}$, whereas after usage and a subsequent cleaning step a value of $750\,\mathrm{nF\,cm^{-2}}$ was obtained. The steps observed in N_s, C_0' and G_0 could indicate that portions of the contamination layer peel off.

To remove the contamination layer before the sensor is employed for measurements, different wet chemical cleaning procedures were investigated. These included the application of the dedicated photoresist remover AZ 100 (MicroChemicals) and dimethylsulfoxide (DMSO) at 80 °C for 30 min, as well as the standard cleaning procedure with aceton and isopropanol. However, only small portions of the photoresist were removed and the SEM revealed that the once homogenous layer becomes spotted with lighter domains. However, SEM images also show that the contamination layer is susceptible to mechanical stress and that it can be scratched off, e.g. with a pair of tweezers. This way the evaluation of the underlying surface morphology and dislocation density is possible.

In figure 7.5 such a scratched area is shown, which reveals the typical dislocation patterns. The dislocations are much more numerous and pronounced, compared to the as grown wafer (fig. 6.12b). In addi-

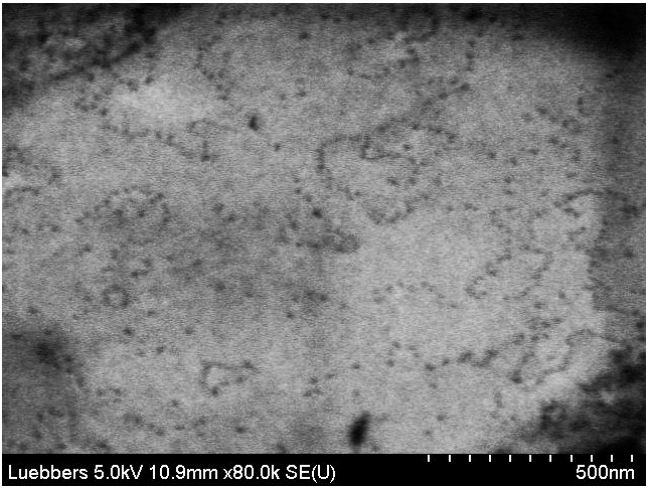

Figure 7.5: SEM image that show an area of an AlGaN-EIHS sensor chip where the contamination layer has been partly removed by scratching.

tion to the few single point defects, the grain boundaries have become pitted and the dislocation density has increased by more than a decade to approximately $1 \times 10^{10}\,\mathrm{cm}^{-2}$. This suggests that some step in the fabrication process severely deteriorates the crystal quality, which in turn makes the sensors more susceptible to corrosion. Most likely, the high temperature annealing of the ohmic contacts is responsible for this deterioration, due to the thermal mismatch between the sapphire substrate and the heterostructure. The rapid heating and the relatively high tensile stress in the barrier may also add to this effect. The removal of the contamination layer is critical for reproducible and accurate measurements, not only with respect to the drift behaviour but also because the metal oxide at the surface is the sensing element of

the device. This implies, that if the surface is covered with a photoresist layer the pH-sensitivity is likely to be influenced. Therefore, the standard cleaning procedure was modified to include a watering step for at least 24 h in a neutral buffer solution and an additional mechanical cleaning step in aceton with a cotton applicator. These additions do not result in a complete removal of the photoresist contamination, but they reduce the drift behaviour upon the initial usage of the sensor chips. An initial measurement series with at least 20 single measurements (corresponding to 5 h) followed by a cleaning step with DIW for 5 min and a final rinsing with DIW were performed, to ensure stable measurement conditions.

Although the initial cleaning and measurement protocol leads to a clean and reproducible sensor surface, it is best to avoid the formation of the contamination layer in the first place. To achieve this the cleaning steps during the fabrication process ought to be revised. Possible optimisation routes include the removal of the topmost polymerised photoresist layer by an oxygen-plasma resist stripper, followed by a wet chemical removal step. Additionally, it should be investigated if the mild standard cleaning process with acetone and isopropanol can be replaced by the dedicated photoresist remover AZ 100 or DMSO for all or most of the cleaning steps during fabrication.

7.1.2 Light-induced Drift and Persistent Photoconductivity

The light sensitivity of the 2DEG is one of the most important influences on the stability of the sensor signal. The persistent photoconductivity manifests itself in a drawn out drift when the sensor is darkened, with time constants in the range of several hours. In AlGaN/GaN

HEMTs the drain current is influenced via the conductivity of the 2DEG. For the MIHS or EIHS capacitor structure, its influence can expected to be observed directly in the drift of the sheet carrier concentration N_s, which in turn determines the threshold voltages. The drift characteristic of the EIHS was recorded after backside illumination with a violet LED ($\lambda = 400\,\mathrm{nm}$, 80 mcd at 10 mA). This wavelength corresponds to near band gap illumination. The measurement series was started after the sensor chip had been kept in the dark for more than 24 h. The illumination was switched on for the duration of a single impedance spectrum ($\approx 15\,\mathrm{min}$) and the decay characteristic was measured for about 24 h, to evaluate the PPC. The impedance profile have an average duration of 15 min and are recorded in immediate succession.

The *voltage profile* before (black), during (red) and after the illumination (blue) with a violet LED are shown in figure 7.6. The reproducibility profiles are calculated with respect to the profile upon illumination. The blue arrows indicate the direction of the drift after the illumination is switched off. The initial dark profile exhibits the typical enhancement, transition and depletion ranges with a capacitance and conductance depletion over more than two and three decades, respectively. In the phase profile a single, well-defined peak with a full width at half maximum (FWHM) of approximately 0.2 V and a maximum of $-49°$ can be found. In the enhancement and depletion range, values of $-88°$ and $-85°$ are observed, respectively. When the violet LED is switched on, all profiles are shifted about 0.4 V towards larger bias voltages. The capacitance and conductance profiles are slightly skewed, resulting in a broader transition region especially towards the depletion region. Generally, the capacitance depletion is less pronounced, which in turn leads to a phase angle well above $-70°$

in the depletion range. The phase peak is slightly flattened and its symmetry is distorted towards high bias voltages, with maximum of -53° and a FWHM of more than 0.4 V. An explanation for the slightly skewed capacitance-voltage profile during illumination can be found in the two-dimensional depletion geometry of the 2DEG. The lower portion of the capacitance-voltage profile was found to primarily reflect the lateral depletion of the outer 2DEG. Due to the backside illumination, charge carriers are induced in both the inner and the outer 2DEG. As a result, the skewing of the capacitance-voltage profile during illumination has to be due to different amounts of charge carriers being induced in the inner and outer 2DEG. The outer 2DEG seems to be enhanced to a larger extend than the inner 2DEG. The shape of the phase angle peak, which is broader and less high, confirms this assumption. As the height and width are indicators for the location of the 2DEG pinch-off, it can be concluded that the pinch-off has shifted towards the inner 2DEG. This is the case when the outer 2DEG has a larger sheet carrier concentration than the inner 2DEG. Figuratively speaking, the bottleneck characteristic of an enhanced outer 2DEG is less pronounced. The difference in the amount of light-induced charge is likely to be linked to the photocurrent that flows vertically through the heterostructure, as discussed later on in this section. When the illumination is switched off, the heterostructure slowly returns to is initial state and the pinch-off shifts back towards the outer 2DEG. However, significant differences are found between the initial dark profiles and the profiles after 24 h. The capacitance- and conductance-voltage profiles are less steep and the phase angle peak is reduced in height. This suggests that irreversible changes of the heterostructure have taken place, most likely due to corrosion processes.

Table 7.1: Results of the PPC stretched exponential fit for an AlGaN-EIHS ($B_{10}^{30}C_2$) after switching of violet illumination.

parameter	$\frac{X_0 - X_{dark}}{X_{dark}}$	τ (s)	β
N_s	21.0%	891 ± 45	0.40 ± 0.01
U_{th_C}	21.4%	1044 ± 45	0.46 ± 0.01
U_{th_G}	19.0%	1314 ± 171	0.39 ± 0.03

In the *parameter footprint* (Fig. 7.7) the influence of the PPC can clearly be seen for U_{th_C}, U_{th_G} and N_s by the drawn-out exponential decay characteristic that lasts for more than 12 h. A very low positive drift is observed for C_0', which becomes continuously smaller. The zero bias conductance G_0 shows no significant drift. It should be noted that the parameters footprint only accounts for variations of the upper portions of the capacitance- and conductance-voltage profiles. Therefore, the previously discussed impact on the outer 2DEG can not be observed.

To quantify the PPC decay characteristic the commonly employed stretched exponential fit (eqn. 4.1) is applied to U_{th_C}, U_{th_G} and N_s in the *parameter footprint*. The obtained values are given in table 7.1. The value of X_0 corresponds to the measured value of either N_s, U_{th_C} or U_{th_G} during illumination and X_{dark} is obtained from the fitting procedure. The ratio $\frac{X_0 - X_{dark}}{X_{dark}}$ is given to evaluate the relative influence of the illumination. The time constant τ is fitted per measurement and converted to seconds assuming an average measurement time of 15 min = 900 sec. In general, comparable results can be derived from N_s as well as U_{th_C}, for the PPC decay characteristic. This similar behaviour can be expected as U_{th_C} is directly linked to N_s. Their course

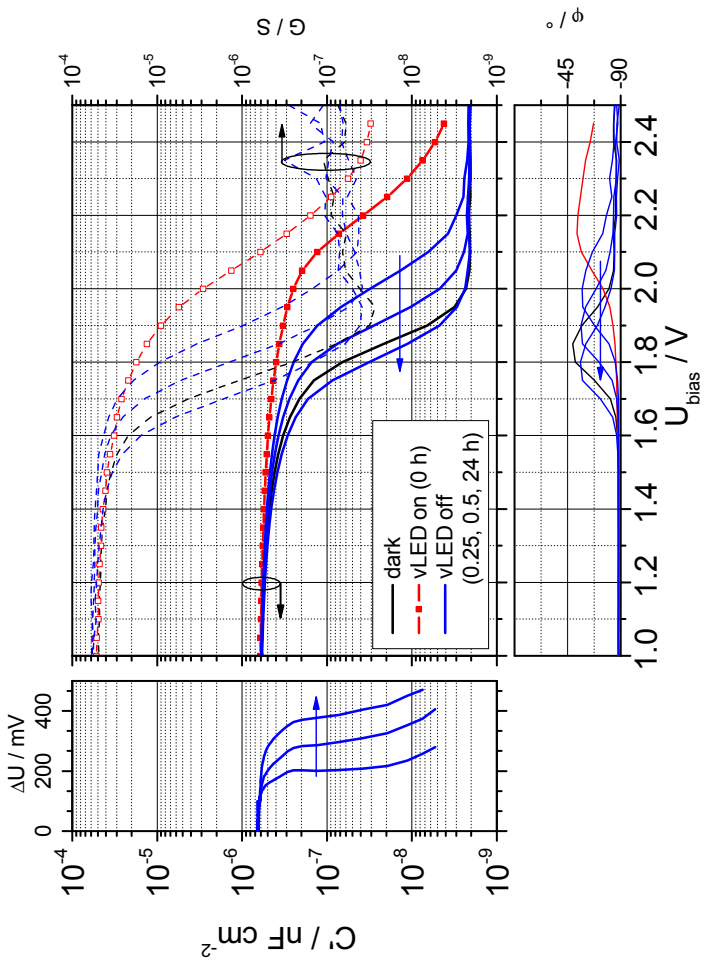

Figure 7.6: *Voltage profile* of an AlGaN-EIHS ($B_{10}^{30}C_2$) after prolonged darkening (black), with violet illumination (red) and after switching off the illumination (blue). Reproducibility profiles are referenced to violet illumination (red squares).

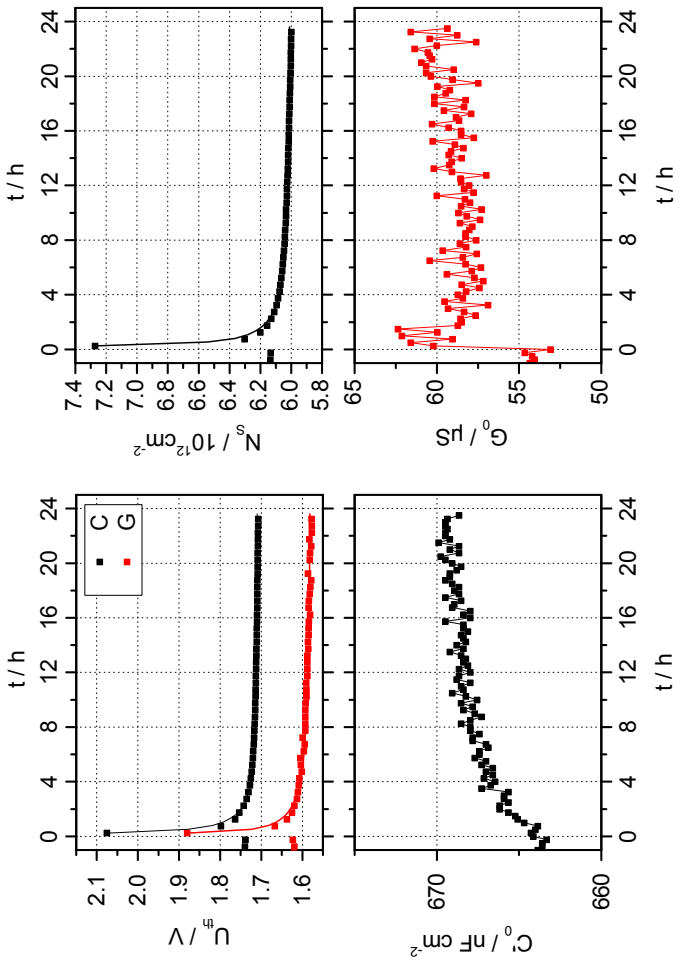

Figure 7.7: *Parameter footprint* of an AlGaN-EIHS ($B_{10}^{30}C_2$) after prolonged darkening, with violet illumination and after switching off the illumination. Solid lines depict stretched exponential approximations of U_{th_C}, U_{th_G} and N_s.

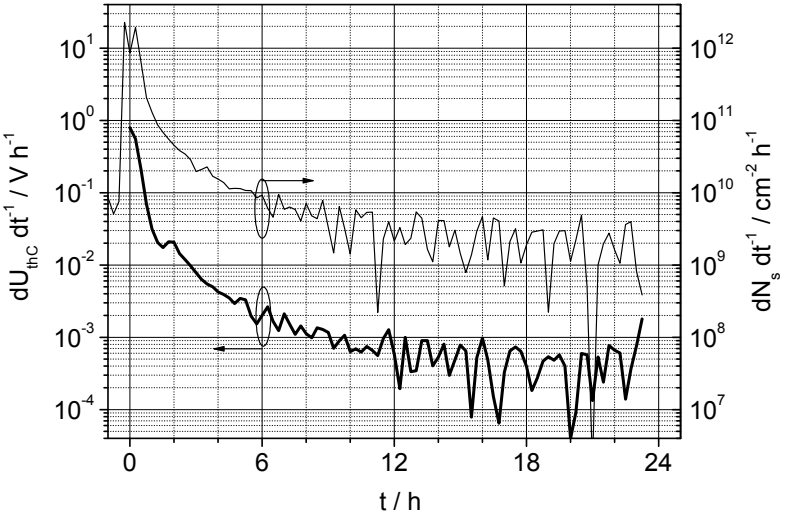

Figure 7.8: Plot of the derivatives of U_{th_C} and N_s versus time after switching off the violet illumination.

is qualitatively equal, as long as the capacitance in the enhancement and depletion range is relatively constant and the voltage shift is reasonably parallel. This can be confirmed by the *voltage profile*. For the fit of U_{th_G} somewhat higher time constants are obtained and the uncertainty is generally higher for τ and β.

The values of τ and β compare reasonably well to the literature values of $(1 \times 10^3$–$1 \times 10^4)$ s for τ and 0.3–0.4 for β [127, 126, 132, 16]. The ratio $\frac{X_0 - X_{dark}}{X_{dark}}$ agrees well with the value of $\Delta n_s = 24\%$ reported by Kittler [16] for a similar AlGaN/GaN heterostructure. For practical measurement purposes, it is important to know after which duration

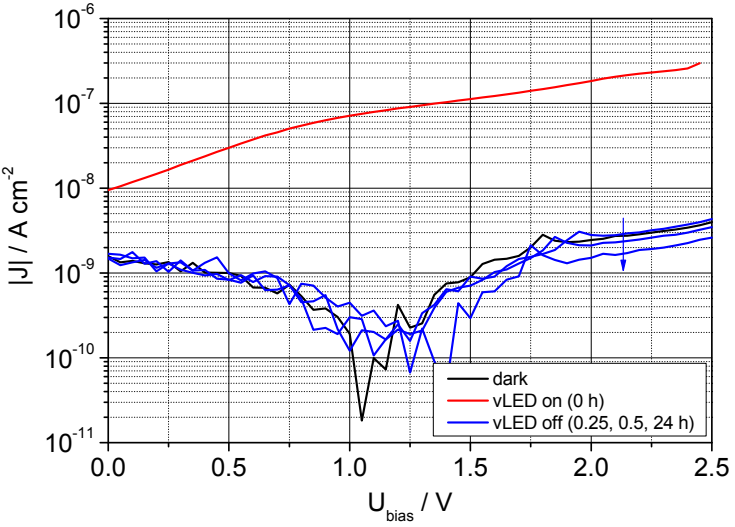

Figure 7.9: DC current density profiles of an AlGaN-EIHS ($B_{10}^{30}C_2$) after prolonged darkening (black), with violet illumination (red) and after switching off the illumination (blue).

the PPC has decayed to an acceptable drift level. In order to estimate this duration, the derivatives of U_{th_C} and N_s were taken (fig. 7.8). A sufficiently low drift is obtained after more than 12 h, with $dU_{th_C}dt^{-1} \leq 2\,\mathrm{mV\,h^{-1}}$ and $dN_s dt^{-1} \leq 5 \times 10^9\,\mathrm{cm^{-2}\,h^{-1}}$. However, after this time the drift of N_s and U_{th_C} does not disappear but becomes linear instead. A continuous linear drift can also be found for C_0' in the *parameter footprint* (Fig. 7.7). These effects can be attributed to electrochemical corrosion.

Another indicator for electrochemical corrosion is the DC leakage current that flows in the electrochemical measurement cell. Due to the insulating properties of the heterostructure in vertical direction this current is usually very small, but it is nevertheless measurable and significant. For the EIHS, the DC current-voltage characteristic was recorded simultaneously to the impedance-voltage profile, by the developed LabView measurement program (cf. section 5.2.2). The DC current was normalised by the area of the electrolyte Schottky contact to give the DC current density J.

In figure 7.9 the plot of DC current density magnitude versus bias voltage is shown for the investigated measurement series. It is found that the violet illumination induces a large photocurrent. When the LED is switched on, J immediately increases by two decades. It drops back to the dark current level just as fast, when the LED is switched off. This means that the photocurrent is not subject to a drawn-out PPC characteristic. Without illumination the current density is very low and it was found that J decreases slightly over the further course of the measurement series. The large photocurrent also explains the difference between the inner and outer 2DEG sheet charge density upon violet illumination. Assuming that at least part of the light-induced charge is generated in the AlGaN barrier layer, the DC current flow through the barrier greatly influences the generation/recombination equilibrium. It will be shifted towards recombination, resulting in a smaller sheet charge density in the inner 2DEG, compared to the outer 2DEG. For the outer 2DEG, no DC current via the barrier is possible and therefore the equilibrium is not influenced. The increased photocurrent also suggest that the corrosion process is more severe, when the EIHS is illuminated with violet light. This photoelectrochemical corrosion is discussed on more detail in section 8.1.1. In the following

section the electrochemical corrosion without illumination is illustrated and discussed.

7.1.3 Electrochemical Corrosion

It was discovered that the electrochemical corrosion of the sensor surface is one of the most important sources of long-term drift phenomena. Although the chemical stability of the III-nitrides is highlighted in nearly every publication concerning AlGaN-based fluid sensors, the corrosion of the sensors has to be considered for the construction of accurate and reproducible devices. The key aspect is that the crystal quality in general and the dislocation density in particular determine how susceptible the sensor is to corrosion, even in neutral aqueous buffer solutions. In addition to that, the applied voltage and the incident light play a major role. The connection to the applied voltage is also the reason why the drift is expressed per measurement.

When the sensor chip is not illuminated, the corrosion is mainly determined by the applied bias voltage and the composition of the electrolyte solution (concentration and pH-value). As the employed buffer solutions are nearly neutral ($6<\text{pH}<8$) and rather diluted, a pronounced wet chemical attack of the semiconductor can be ruled out. Therefore, the corrosion of the sensor surface under these conditions is of an electrochemical nature. Polarising the surface with a positive potential results in the generation of holes and an oxidation and etching mechanism similar to the one described in section 4.3.3 can be assumed. The electrochemical corrosion of the surface is illustrated by the *voltage profile* and *parameter footprint* in figures 7.10 and 7.11. A long-term drift measurement is shown after the EIHS sensor chip had been kept in the dark for more than 36 h.

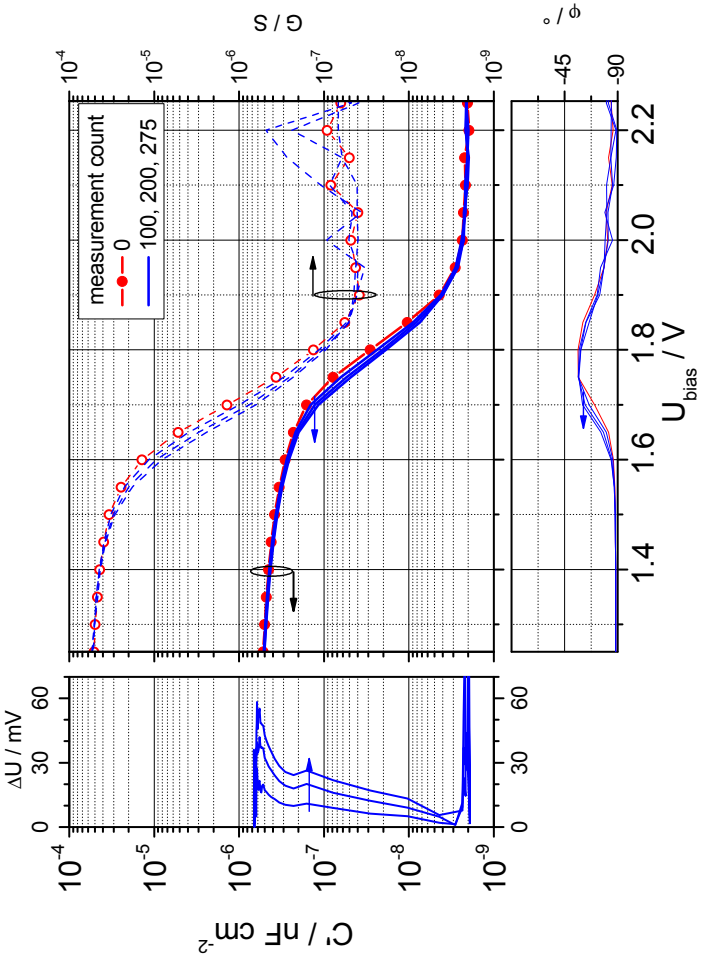

Figure 7.10: *Voltage profile* of a long-term measurement series in the dark with an AlGaN-EIHS ($B_{10}^{30}C_2$). Reproducibility profiles are referenced to measurement count 0 (red circles).

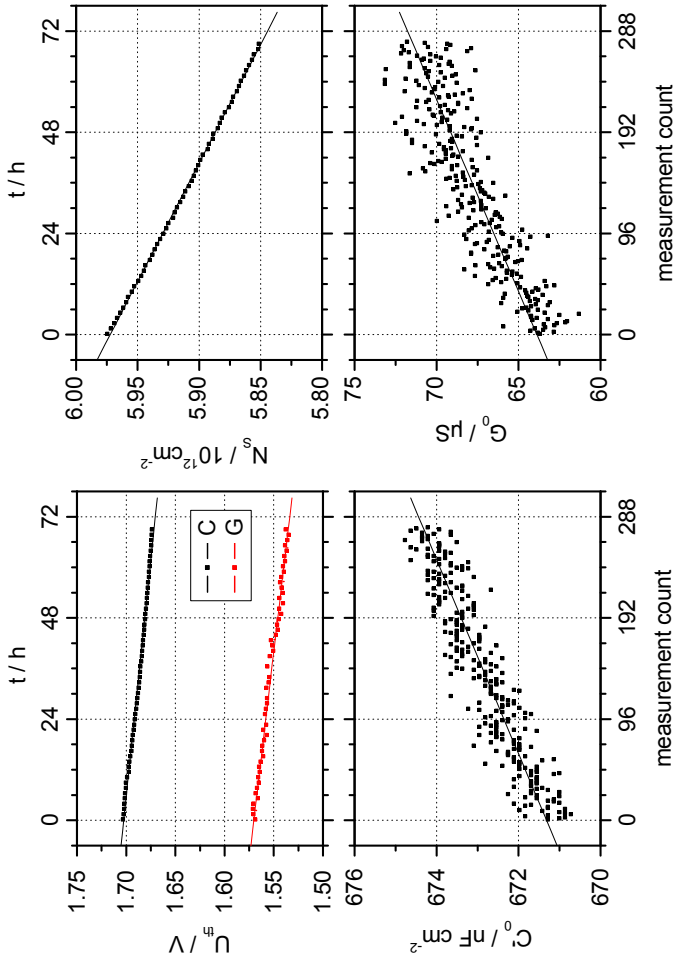

Figure 7.11: *Parameter footprint* of a long-term measurement series in the dark with an AlGaN-EIHS ($B_{10}^{30}C_2$). Solid lines depict linear approximations.

The *voltage profile* (fig. 7.10) shows that, even after more than 250 measurement, the capacitance and conductance profiles shift only to a small extent. The shift is less pronounced close to the depletion region. This leads to a slightly skewed transition slope, although the overall shape of both profiles is not altered significantly and the enhancement and depletion values are unchanged. The change of the transition slope is also discernible in the phase profile, where the height of the peak is marginally reduced and its width slightly increased. From the reproducibility profile it can be seen that the shift is not parallel. A larger shift is found for the upper capacitance portion and a smaller shift for the lower portion. From the *parameter footprint* it can be seen that the threshold voltages U_{th_C} and U_{th_G} and the sheet carrier concentration N_s drift linear towards smaller values. In contrast, the zero bias capacitance C_0' and conductance G_0 increase. The drift for all parameters is constant for the whole measurement series of more than 250 measurements. The obtained values for the shown linear approximations are given in table 7.2. The very small values demonstrate that the electrochemical corrosion is not very pronounced, but nevertheless present. In addition, it can be concluded that the chosen analysis method, and especially the inflection point method, is very suitable for the determination of marginal drift effects. The reason for the electrochemical corrosion drift are structural defects in the semiconductor, such as screw dislocations, grain boundaries and possibly nanotubes. All of those two-dimensional defects impair the insulating nature of the barrier and cap layers, leading to a vertical DC current across the heterostructure and, more importantly, via the semiconductor-electrolyte interface. Due to the transition between electron and ion conductivity at this interface, a charge transfer is always coupled with a material

Table 7.2: Drift slopes of U_{th_C}, U_{th_G}, N_s, C_0' and G_0 for the electrochemical corrosion of an AlGaN-EIHS ($B_{10}^{30}C_2$) in the dark.

parameter	drift (meas^{-1})
U_{th_C} (mV)	−0.1
U_{th_G} (mV)	−0.1
N_s (10^9 cm^{-2})	−0.4
C_0' ($\text{nF}\,\text{cm}^{-2}$)	0.01
G_0 (µS)	0.03

transfer. If this transfer leads to the unwanted removal of material from the surface, it is termed corrosion.

The influence of the corrosion process on U_{th_C}, U_{th_G}, N_s and C_0' can be explained by the enlargement and deepening of dislocation pits. Below a deeper and broader pit, the 2DEG is depleted locally to some extend, due to a thinner insulation layer and the increased electrical field in it. Therefore, the overall sheet charge density and the threshold voltages decrease. The increase of C_0' is connected to the same effect. A thinner barrier leads to a larger capacitance per area, when the simple plate capacitor model is invoked. Although these larger capacitance elements are localised at the dislocations and distributed all over the sensor surface, they are in parallel to the capacitance of the remaining intact barrier layer. Therefore, the overall capacitance will increase, as was observed in this measurement series. In contrast, the increased value of G_0 is unlikely to be due to corrosion, as it was immediately reduced to 50 µS after it was cleaned with DIW and subsequently measured with fresh buffer solution. In order to explain this behaviour the mandatory and constant leakage of internal electrolyte solution from the reference electrode (cf. chapter 3.4) needs to be considered. De-

spite the very low leakage rate of the employed reference electrode, the long measurement duration of nearly three days results in a considerable increase of the ionic strength in the sample solution. For a typical leakage rate of 0.05 ml/d (KCl solution with $I = 3\,\mathrm{M}$) into the sample volume of 10 ml buffer solution ($I = 0.1\,\mathrm{M}$), the ionic strength increases by 14% after one day. After three days an increase by 42% can be expected and after one week it amounts to 98%. An increase of ionic strength results in an increase of the conductance of the electrolyte solution (cf. section 2.1). As G_0 reflects all conductive elements in series with the EIHS, including the electrolyte solution (cf. section 6.2), an increase of the conductance of the electrolyte solution will also lead to an increase of G_0. Thus, the drift of G_0 has to be assigned to the leakage from the reference electrode.

7.1.4 Summary

The investigations on drift phenomena of AlGaN-EIHS using impedance-voltage profiling can be summarised as follows:

- Three main drift mechanisms were found: dissolution of photoresist contamination, persistent photoconductivity and electrochemical corrosion. The first two are temporary drift phenomena upon darkening and for the initial use, respectively. The third is an irreversible process.

- Residual photoresist contamination from the fabrication of the EIHS sensor chips was confirmed by SEM. An initial cleaning and measurement protocol was suggested and successfully performed to remove this contamination.

- The dislocation density of the EIHS surface has increased to about $1 \times 10^{10}\,\mathrm{cm}^{-2}$ after the fabrication process, presumably due to the thermal annealing step of the ohmic contacts.
- The characteristic of the light-induced PPC drift agrees with published results. This demonstrates that impedance-voltage profiling is a suitable method for the determination of drift phenomena. Additionally, it was shown that the EIHS sensor chip has to be darkened for at least 12 h to obtain a stable sensor signal.
- The photocurrent that is induced upon illumination with violet light does not reveal a drawn-out decay characteristic. It is, however, responsible for an accelerated corrosion process.
- Without illumination, a corrosion of the EIHS sensor chip takes place, but it is very slow. The developed analysis methods were shown to be suitable for the monitoring of these small drift rates.

It can be concluded that pronounced drift phenomena are present, but they can be minimised by appropriate ambient conditions and measurement protocols. For the characterisation of pH- and cross-sensitivity, which is presented in the following section, the photoresist contamination was removed and the AlGaN-EIHS sensor chips were kept in the dark for more than 12 h before measurements were performed.

7.2 Sensitivity

In the introduction chapter of this thesis it was stated that the reproducibility of pH-sensitivity is unsatisfactory for AlGaN-ISFETs and that values between $30\,\mathrm{mV\,pH}^{-1}$ and the Nernstian limit of $59.2\,\mathrm{mV\,pH}^{-1}$

have been found. This variation of pH-sensitivity was also found for the AlGaN-EIHS and in the following sections the best and worst case scenarios are illustrated. A measurement series with high pH-sensitivity is presented in section 7.2.1 and three analysis methods for the determination of pH-sensitivity are introduced: the interpolation method, the inflection point method and the integration method. Two examples of diminished pH-sensitivity, due to significantly differing depletion characteristics, are presented in section 7.2.2. Additionally, it is shown that the analysis method strongly influences the obtained pH-sensitivity and the advantages and limits of the different methods are discussed.

For the pH-sensitivity measurement series, the buffer solutions PB6.88, PB7.25 and PB7.64 were used. With the standard measurement cycle (PB7.25 $\rightarrow$ PB7.64 $\rightarrow$ PB6.88 $\rightarrow$ PB7.25 $\rightarrow$ PB6.88 $\rightarrow$ PB7.64 $\rightarrow$ PB7.25) each possible step between the different pH-values is performed. This way the reproducibility of the measurement and the dependence on the previously measured pH-value can be assessed. The ionic strength of the employed buffer solution was kept at 100 mM to avoid a possible cross-sensitivity.

7.2.1 High pH-Sensitivity

The measurement series shown in figures 7.12 and 7.13 is an example for high pH-sensitivity. The impedance-voltage profiles were taken at 10 Hz. The capacitance and conductance profiles exhibit the typical enhancement, transition and depletion ranges. The depletion of C and G amounts to two and three decades, respectively. A distinct and reproducible shift with respect to the pH-value is observed in the transition range, whereas the enhancement and depletion ranges are not affected by the pH-value. In the phase profile a single, well-defined peak is visi-

ble with a maximum value of $-59°$ and an FWHM of slightly less than 0.2 V. The pH-induced voltage shift of these three profiles is nearly parallel. This suggests that the pH-value of the electrolyte solution leads to a linear change of the surface potential, which in turn influences the depletion characteristic of the 2DEG.

In the *voltage profile* (fig. 7.12), the interpolation method was employed to determine pH-sensitivity. It is calculated as the voltage shift between two capacitance profiles divided by the corresponding pH-value difference. A sensitivity profile is obtained when the voltage shifts are calculated over the entire course of the capacitance profiles. This corresponds to a reproducibility profile normalised by the pH-value difference. In figure 7.12, the sensitivity profiles S_{pH} versus C' are shown in the left-hand secondary graph and exemplary shifts ΔU and ΔpH are given to clarify how the interpolation method is applied. The lower left axis gives the pH-sensitivity and the Nernstian limit is signified by the solid vertical line at $59.2\,\mathrm{mV\,pH^{-1}}$. It is important to note that the sensitivity profiles always give a relative sensitivity with respect to the reference capacitance profile used for interpolation (here: pH7.63). In addition to the sensitivity profiles, the reproducibility profiles of the reference pH-value is given in mV by the upper left axis. Their course should run below 3 mV, as this value corresponds to a deviation of about 0.05pH when a Nernstian pH-sensitivity of $59.2\,\mathrm{mV\,pH^{-1}}$ is assumed. When the reproducibility profiles exceed this value the measurement no longer fulfils the accuracy requirement of 0.06pH as stated in the RiLiBÄK. The dashed vertical line signifies this critical deviation.

The sensitivity profiles illustrate that the pH-change induces a parallel shift only for the upper portion of the capacitance profiles. It can be observed that the shift towards pH6.87 is nearly parallel for the whole

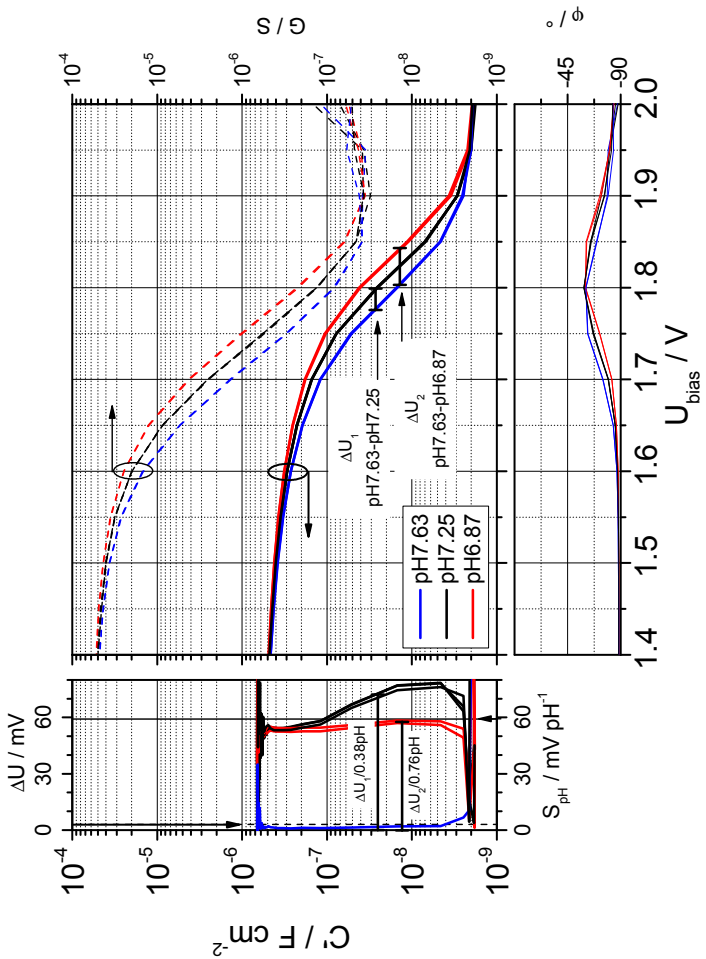

Figure 7.12: *Voltage profile* of a pH-sensitivity measurement series with an AlGaN-EIHS ($B_{10}^{30}C_2$) that exhibits high pH-sensitivity. The calculation of the sensitivity profiles referenced to pH7.63 (blue) is explained in the text.

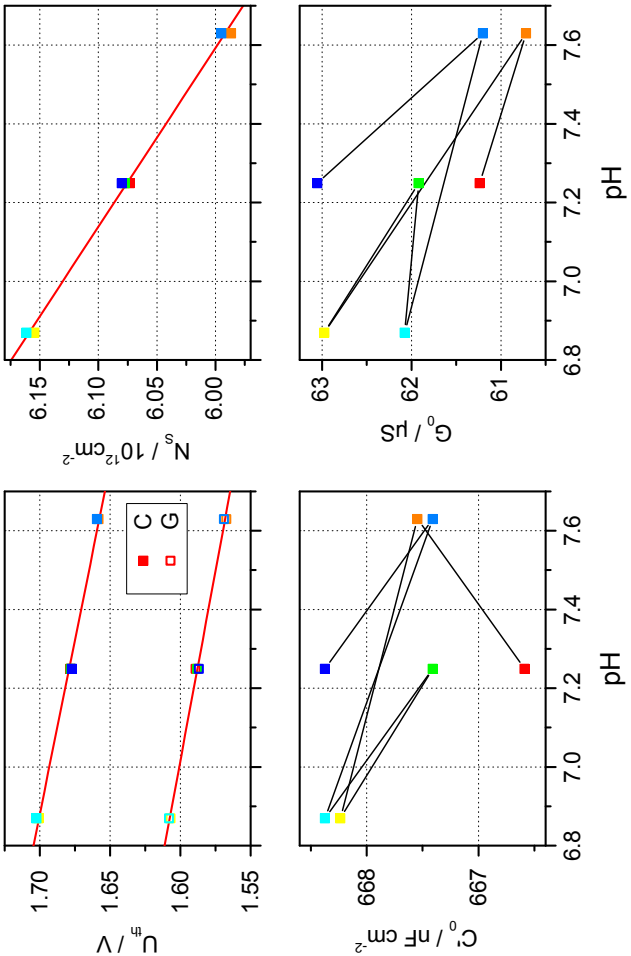

Figure 7.13: *Parameter footprint* of a pH-sensitivity measurement series with an AlGaN-EIHS ($B_{10}^{30}C_2$) that exhibits high pH-sensitivity. Solid lines depict linear approximations.

capacitance range with a slight increase from 55 to 58 mV pH^{-1}. The shift towards pH7.25 yields similar values, but only for the topmost portion of the capacitance profile. In the lower portion it reveals a large deviation with a value of up to 75 mV pH^{-1}. The reproducibility profiles for pH7.63 are below 3 mV and no marked dependency on the prior pH-value is found. For the interpretation of the absolute pH-sensitivity, the sensitivity profiles can be somewhat misleading, as they only give relative values and the choice of the reference profile is critical. For instance, if the sensitivity profiles are calculated with regard to the middle pH-value of 7.25, which was observed to deviate from the parallel shift, the traces are quite different (fig. 7.14). At the start of the transition range the change to pH7.25 results in a near Nernstian shift, that gradually declines reaching 30 mV pH^{-1} near the depletion range. The pH-step towards pH6.87 exhibits a somewhat complementary characteristic with a lower sensitivity at the beginning of the transition region that increases towards the Nernstian limit and even exceeds it. The sensitivity profiles have an insufficient reproducibility that exceeds 5 mV pH^{-1}, although the reproducibility profiles for pH7.25 are well below 3 mV. These observations suggest that the interpolation method is not suitable for an absolute and unambiguous determination of pH-sensitivity from impedance-voltage profiles.

The origin of the deviation at pH7.25 is not obvious, even though it is reproducible and has also been observed in repeated measurements with different sensor chips. Possibly, the buffer system plays some part in this effect, as the phosphate buffer has an pK_a of 7.21, which is very close to the investigated pH-value. In the vicinity of the pK_a, the charging states of the anion change quickest, i.e. the protonation slope of the base is steepest. For the buffer solution with a pH-value of 7.63 the anion HPO_4^{2-} is dominant, for pH6.87 it is $H_2PO_4^-$ and

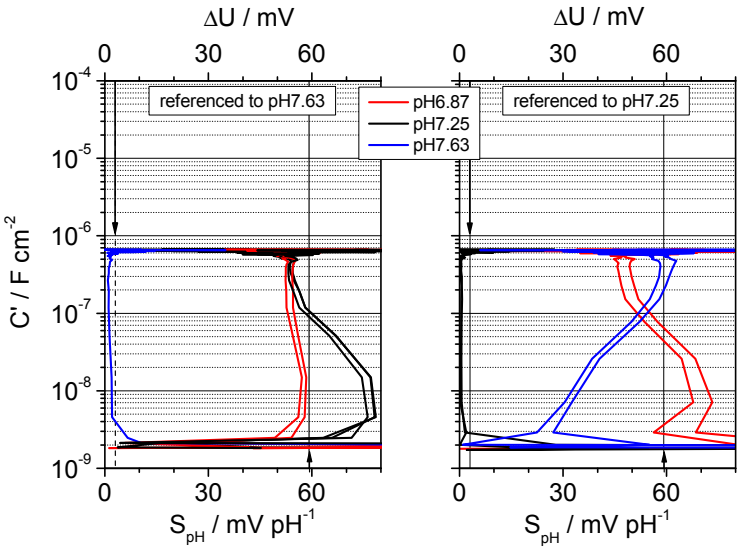

Figure 7.14: Comparison of the sensitivity profiles referenced to pH7.63 and pH7.25.

at pH7.25 their ratio is approximately one. Small influences, such as the DC leakage current, may shift this ratio and result in the observed deviations. Another possible explanation can be found in the point of zero charge pH_{pzc} of the metal oxide, which is assumed to be in the same region (cf. table 3.1). As the net surface charge changes its sign in the vicinity of the pH_{pzc}, solutions with such a pH-value might invoke uncommon effects. Despite this deviation, the overall shape of the sensitivity profile suggests that the change of pH-value only induces a voltage shift, while all other characteristics are maintained. This assumption is generally confirmed by the *parameter footprint*, which allows to extract quantitative information from the *voltage profile*.

From the *parameter footprint* (fig. 7.13), the pH-sensitivity is determined by the inflection point method and the integration method. Both analysis methods are based on the principles that have already been employed for the characterisation of drift effects: the determination of threshold voltages U_{th_C} and U_{th_G} via the inflection point and the estimation of sheet charge density N_s via integration. The only difference is that these parameters are now plotted versus the corresponding pH-value. In order to asses the impact of the measurement sequence, a rainbow color coding from red (first measurement) to blue (last measurement) is used. The pH-sensitivity is derived from these plots simply by linear approximation. It should be noted that these methods cannot derive complete pH-sensitivity profiles, but only overall sensitivity slopes. Nevertheless, they are suitable for the determination of pH-sensitivity and subsequent measurement of an unknown pH-value, as absolute and unambiguous values are obtained. The pH-sensitivities S_{pH}, derived by linear approximation (red lines), are summarised in table 7.3. In addition, the standard deviation SD and the coefficient of variation $c_v = SD/S_{pH}$ is given. The coefficient of variation is a

Table 7.3: Best case pH-sensitivity of U_{th_C}, U_{th_G} and N_s for an AlGaN-EIHS ($B_{10}^{30}C_2$).

parameter	sensitivity S_{pH} (pH^{-1})	standard deviation SD	rel. imprecision c_v (pH)
U_{th_C} (mV)	-56.5 ± 2.0	1.5	0.03
U_{th_G} (mV)	-51.8 ± 1.3	1.0	0.02
N_s (10^9 cm^{-2})	-220.0 ± 5.6	4.3	0.02

measure for the relative imprecision of the obtained pH-sensitivity and is given in pH-units. Effectively, it indicates how precise the pH-values can be determined with the derived parameters.

A reproducible and linear pH-sensitivity was obtained for U_{th_C} and U_{th_G} with values that are generally lower than the ideal Nernstian limit of $59.2\,\mathrm{mV\,pH}^{-1}$. The slope of U_{th_C} agrees well with the published values, which have been summarised in table 4.1. A slightly lower pH-sensitivity is obtained for U_{th_G}, but the relative imprecision of both parameters is very low. With values of 0.03pH or less, the requirements for clinical and industrial applications are satisfied. The difference between the sensitivities of U_{th_C} and U_{th_G} may be explained by the connection of G to the depletion of the outer 2DEG. It was assumed that the last portion of the conductance-depletion is determined by the pinch-off in the outer 2DEG. Therefore, it is likely that the overall pH-sensitivity of G is partly determined by the outer 2DEG. As the outer 2DEG is not influenced by the pH-value of the electrolyte solution, this sensitivity is reduced. In contrast, the pH-sensitivity of U_{th_C} is only dependent on the inner 2DEG, due to the discussed con-

nection of C to the area-depletion of the inner 2DEG. The impact of the 2DEG pinch-off on the pH-sensitivity of the AlGaN-EIHS is discussed in more detail in following section 7.2.2. For N_s a highly linear and reproducible slope is obtained. Its relative imprecision is as low as for the threshold voltages and thereby also satisfies the requirements of the RiLiBÄK. The pH-sensitivity $dN_s dpH^{-1}$ allows to estimate the pH-induced change of channel conductivity κ, and the drain current I_d in turn. For I_d it can be derived that:

$$I_d = \kappa \frac{HW}{L} U_{ds} = qn\mu \frac{HW}{L} U_{ds} = q\mu N_s \frac{W}{L} U_{ds}, \tag{7.1}$$

where W and L are the width and length of the gate area, μ is mobility of the electrons in the 2DEG and U_{ds} is the applied drain-source voltage. The product of the volume charge density n and the height of the 2DEG channel H equals N_s. In turn, the pH-sensitivity $dI_d dpH^{-1}$ of an ISFET with can be calculated by:

$$\frac{dI_d}{dpH} = q\mu \frac{dN_s}{dpH} \frac{W}{L} U_{ds}. \tag{7.2}$$

A value of $(194 \pm 5)\,\mu\mathrm{A\,pH^{-1}}$ is obtained for an ISFET with a $B_{10}^{30}C_2$ heterostructure, assuming a W/L-ratio of 10, an electron mobility $\mu = 1100\,\mathrm{cm^2/V\,sec}$ and $U_{ds} = 0.5\,\mathrm{V}$. This value is plausible, as it is in the same range as the sensitivities reported by Kittler [16] and Cimalla [17] for slightly different heterostructures. Both the zero bias capacitance and conductance are also plotted in the *parameter footprint*, but they exhibit no pronounced pH-sensitivity. Only a marginal trend towards lower values with increasing pH-value is found with slopes of $(-1.1 \pm 0.8)\,\mathrm{nF\,cm^{-2}\,pH^{-1}}$ and $(-2.1 \pm 0.9)\,\mu\mathrm{S\,pH^{-1}}$ for C_0' and G_0, respectively.

The data shown in this section is an example for high pH-sensitivity obtained with AlGaN-EIHS sensor chips. The very low imprecision indicates that the EIHS, the employed impedance-voltage profiles and the developed analysis methods are very suitable for pH-measurements. In the next section, worst case examples are presented and discussed, in order to identify the sources of diminished pH-sensitivity. In the course of this discussion, the advantages and limits of the employed methods for the determination of pH-sensitivity are evaluated.

7.2.2 Diminished pH-Sensitivity

The measurement series shown in this section were not recorded with the electrochemical measurement setup, as it is described in section 5.2.2, but with earlier prototypes. These setups were not yet fully optimised with regard to ambient influences, such as light or electromagnetic interference, and the design of the measurement cell. This is why the recorded impedance-voltage profiles exhibited differing depletion characteristics, ranging from insufficient to intensified depletion. Although these deviations are due to systematic errors induced by the preliminary measurement setups, they are very well suited to discuss the sources of reduced pH-sensitivity and the advantages and limits of the employed analysis methods.

Insufficient Depletion Characteristic

In figures 7.15 and 7.16 a pH-sensitivity measurement series is shown that does not exhibit a clear and typical depletion characteristic. In the *voltage profile* (fig. 7.15), no distinct pH-shift of the profiles is observed and C and G decrease by less than a decade, which signifies an insufficient depletion of the 2DEG. In the magnified phase angle profile, it is

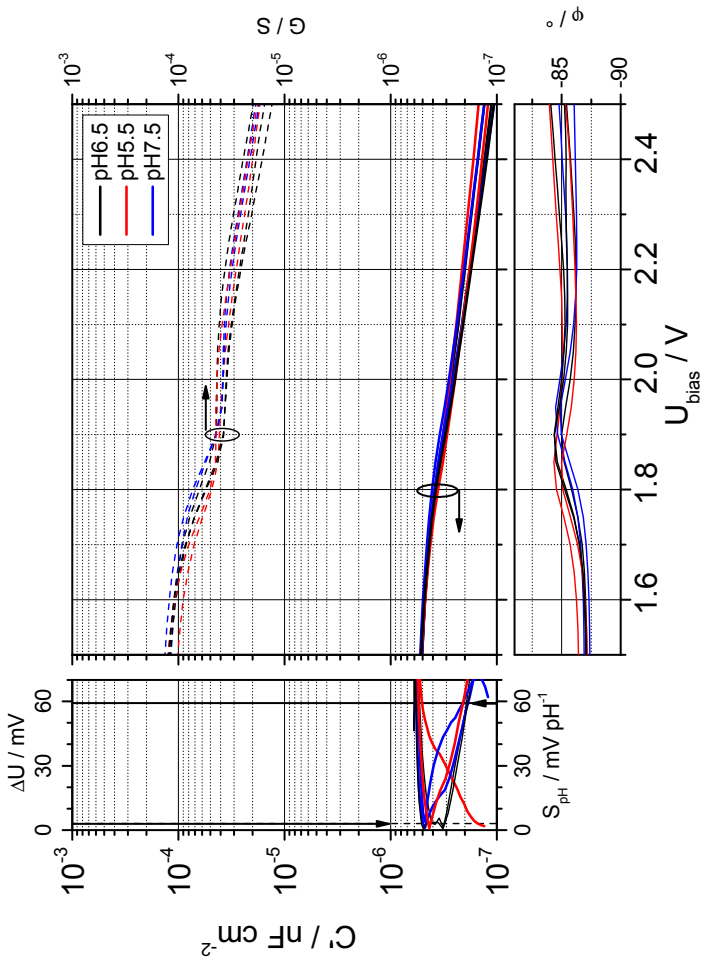

Figure 7.15: *Voltage profile* of a pH-sensitivity measurement series with an AlGaN-EIHS ($B_{10}^{30}C_2$) that exhibits no distinct depletion characteristic. Sensitivity profiles are referenced to pH6.5 (black).

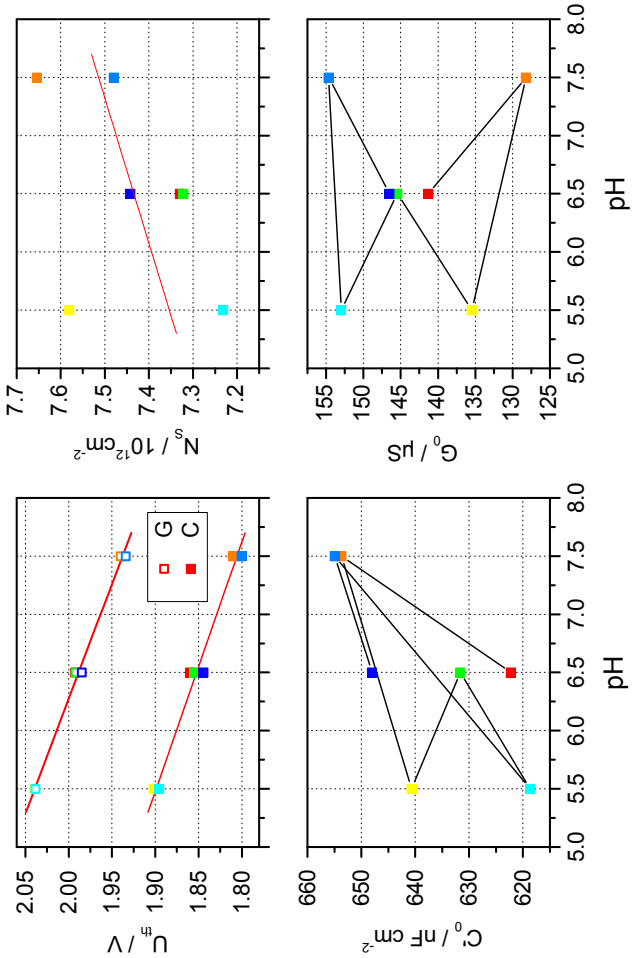

Figure 7.16: *Parameter footprint* of a pH-sensitivity measurement series with an AlGaN-EIHS ($B_{10}^{30}C_2$) that exhibits no distinct depletion characteristic. Solid lines depict linear approximations.

found that the phase angle ϕ is below $-84°$ for the entire investigated voltage range and that only a very shallow peak exists. The sensitivity profiles suggest that the investigated EIHS sensor chip has no pH-sensitivity. However, even from these highly distorted impedance-voltage profiles a pronounced linear pH-sensitivity can be derived from U_{th_C} and U_{th_G} using the inflection point method, as observed in the *parameter footprint* (fig. 7.16). The obtained values are summarised in table 7.4, alongside the pH-sensitivity derived from N_s using the integration method. For the slopes of U_{th_C} and U_{th_G}, reasonable standard deviations are obtained which can also been employed to correct the data for linear drift. Half the SD value multiplied with the measurement number n_{meas} (eqn. 7.3) was used to achieve a significant reduction of the approximation error and the standard deviation of S_{pH}. It was observed that this correction method is generally suitable to minimise the effects of linear drift. However, such drift was only encountered in few measurement series.

$$U_{th_{corr}} = U_{th} + n_{meas} \cdot \frac{SD}{2} \tag{7.3}$$

The reason for the insufficient depletion is likely to be a parasitic conductance parallel to the AlGaN/GaN heterostructure. Such a conductance bypasses the sensor structure and distorts the overall impedance characteristic. Evidence for this assumption is found in the absolute value of G_0 that has increased by a factor of 2, compared to the measurement series with high pH-sensitivity (fig. 7.13). Possible sources of this parasitic conductance are electrolyte solution leaking via the sealing ring or conducting properties of the residual photoresist contamination.

Table 7.4: pH-sensitivity of U_{th_C}, U_{th_G} and N_s for an AlGaN-EIHS ($B_{10}^{30}C_2$) without a distinct depletion characteristic.

parameter	sensitivity S_{pH} (pH^{-1})	standard deviation SD	rel. imprecision c_v (pH)
U_{th_C} (mV)	-48.7 ± 2.4	4.8	0.10
corrected	-46.7 ± 1.1	2.2	0.05
U_{th_G} (mV)	-50.8 ± 1.7	3.5	0.07
corrected	-50.8 ± 1.0	2.0	0.04
N_s (10^9 cm^{-2})	80.3 ± 74.4	148.8	1.85

The preceding discussion reveals that the obtained pH-sensitivity greatly depends on the analysis method. The pH-dependent changes of the surface potential are detected with the inflection point method, whereas both of the other analysis methods fail to do so. Neither the sensitivity profiles obtained by the interpolation method, nor N_s obtained by the integration method, give any indication that the pH-sensitivity still exists. In contrast, the pH-sensitivities derived from U_{th_C} and U_{th_G} are only slightly lower than the commonly obtained values and the relative imprecision is rather low, especially after the linear drift correction has been applied. This suggests that the inflection point method is very suitable for the determination of pH-sensitivity, even when the depletion of the 2DEG is inadequate.

Intensified Depletion Characteristic

In figures 7.17 and 7.18, a pH-sensitivity measurement series with an intensified depletion characteristic is shown. The only difference to the

commonly employed measurement setup (section 5.2.2) was the usage of FKM sealing ring with an increased thickness of 1 mm compared to 0.3 mm for the commonly applied PDMS sealing ring.

The capacitance and conductance profiles (fig. 7.17) show a pronounced depletion characteristic, but nearly no shift with pH-value is observed for both the capacitance and conductance. Compared to figure 7.12 the transition slope is much steeper, especially for the capacitance, and in the enhancement region the conductance is about a decade smaller. Additionally, the reproducibility has degraded. The lack of pH-induced shift for most part of the profiles is also reflected in the sensitivity profiles (referenced to pH7.5). They mostly run below $10\,\mathrm{mV\,pH^{-1}}$, except for the beginning of the transition range a small portion can be found with a maximum sensitivity of $40\,\mathrm{mV\,pH^{-1}}$. The moderate pH-sensitivity towards the end of the transition region for the change from pH7.5 to pH6.6 is not reproducible and clearly a drift artifact. A closer look at the beginning of the transition range with a linear capacitance scale (inset figure 7.17) reveals that a reproducible pH-shift is indeed present, but it is hidden by the logarithmic representation. In contrast, neither the conductance nor the phase profile exhibit a distinct dependence on pH-value even in this voltage range. The phase angle in the enhancement region is larger ($>-70°$) and the peak in the transition range is more pronounced with a maximum of approximately $-10°$ and a FWHM of about 0.4 V.

The intensified depletion characteristic severely reduces the portion of the capacitance profile that exhibits a distinct pH-sensitivity. The interpolation method is still capable to detect this range, although the sensitivity varies between 30 and $50\,\mathrm{mV\,pH^{-1}}$. Therefore, this analysis method is suitable to obtain qualitative information, but no accurate pH-measurement is possible. However, the inflection point method gen-

Table 7.5: pH-sensitivity of U_{th_C}, U_{th_G} and N_s for an AlGaN-EIHS ($B_{10}^{30}C_2$) with an intensified depletion characteristic.

parameter	sensitivity S_{pH} (pH^{-1})	standard deviation SD	rel. imprecision c_v (pH)
U_{th_C} (mV)	-1.8 ± 6.5	5.8	3.22
U_{th_G} (mV)	-8.2 ± 8.0	7.0	0.85
N_s (10^9 cm^{-2})	-96.5 ± 32.8	29.0	0.30

erally fails to extract a pH-sensitivity from the measured impedance profiles, although it was previously identified to be suitable for quantitative pH-measurements. The *parameter footprint*, shown in Fig. 7.18, reveals that only a rather uncertain trends of N_s is present. Most notably, the threshold voltages U_{th_C} and U_{th_G} no longer show any dependence on pH-value. The absolute values of U_{th_C} and U_{th_G} are generally smaller compared to the previous investigation, which signifies an early depletion of the 2DEG. In addition to that, G_0 has decreased by a factor of 10, compared to the values found in figure 7.13. The failure to extract the pH-sensitivity from the impedance profiles reveals the limit of the inflection point method, on the one hand, and the importance of 2DEG pinch-off location, on the other hand.

The location of the pinch-off is determined by the ratio between the sheet charge densities of the outer and the inner 2DEG N_{s_o}/N_{s_i}. The bottleneck characteristic of the outer 2DEG will become more pronounced for $N_{s_o}/N_{s_i} < 1$ and less significant for $N_{s_o}/N_{s_i} > 1$. The early and very steep depletion characteristic that is observed in figure 7.17 indicates that the pinch-off of the 2DEG is no longer domi-

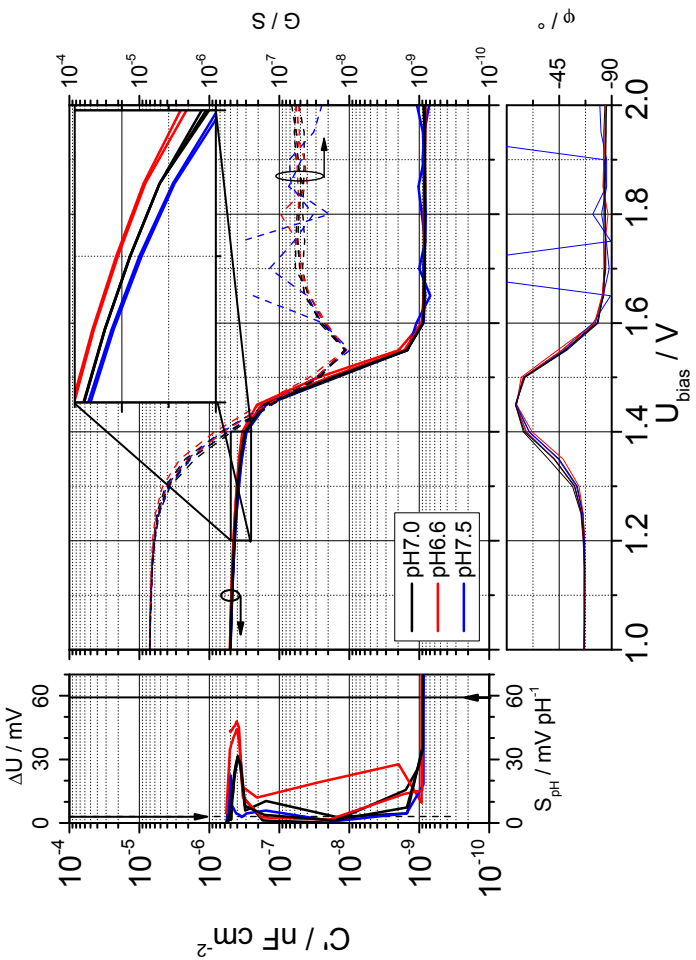

Figure 7.17: *Voltage profile* of a pH-sensitivity measurement series with an AlGaN-EIHS ($B_{10}^{30}C_2$) that exhibits an intensified depletion characteristic. Sensitivity profiles are referenced to pH7.5 (blue).

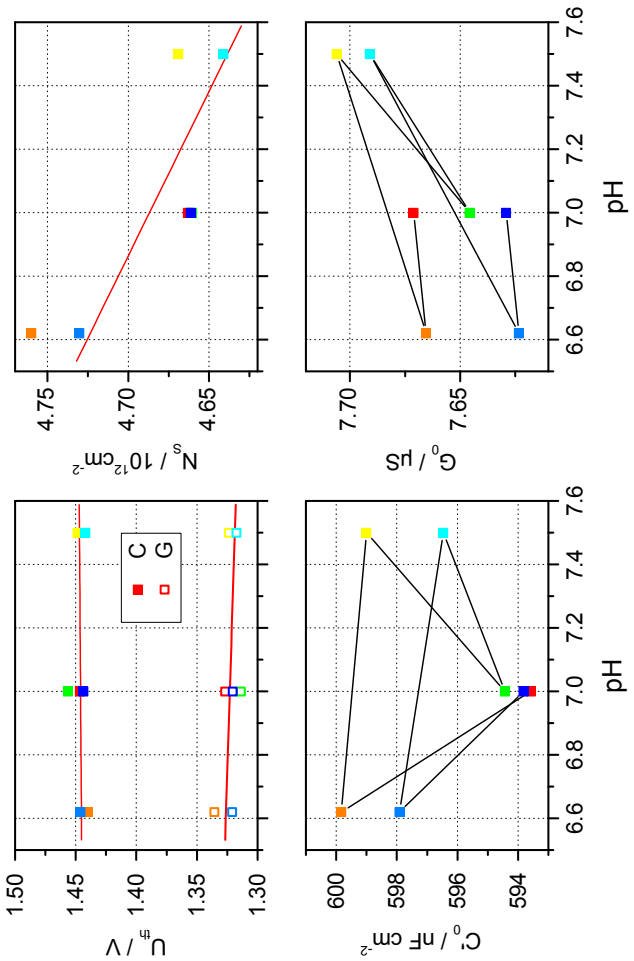

Figure 7.18: *Parameter footprint* of a pH-sensitivity measurement series with an AlGaN-EIHS ($B_{10}^{30}C_2$) that exhibits an intensified depletion characteristic. Solid lines depict linear approximations.

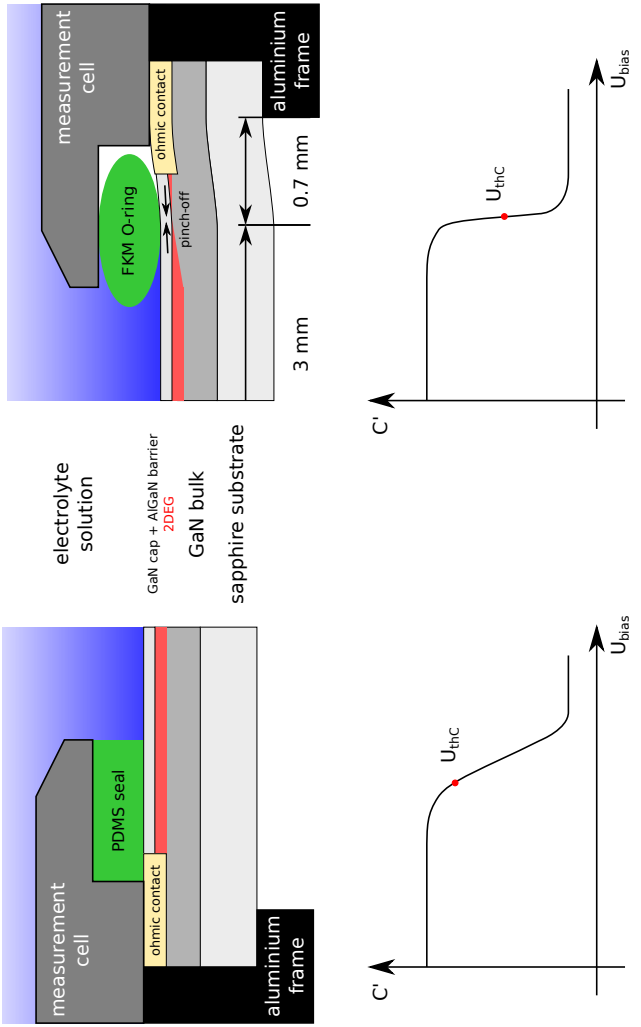

Figure 7.19: Schematic cross-section of an AlGaN-EIHS sensor chip in the electrochemical measurement cell with (a) a PDMS seal and (b) a FKM O-ring. The pressure-induced depletion of the outer 2DEG and its impact on U_{th_C} determined by the inflection point method are illustrated.

nated by the inner 2DEG. It can be assumed that the outer 2DEG has somehow been partially depleted and the ratio N_{s_o}/N_{s_i} is smaller than one. The low value of N_{s_o} is reflected in G_0, which is approximately a decade smaller than usual.

The origin of the partial depletion of N_{s_o} was found in the increased thickness of the sealing ring. In figure 7.19 a cross-section of the EIHS with the thin PDMS seal and the thick FKM O-ring is illustrated. As the measurement cell only has a shallow recess of 0.2 mm for the sealing ring, the 1 mm thick O-ring exerted a much higher force on the heterostructure when the aluminium frame with the sensor chip is fastened in the usual manner. This pressure results in a bending of the sensor chip, which is illustrated in the right-hand cross-section drawing. The distance between the bearing area of the sensor chip and the contact area of the O-ring is much smaller (~ 0.7 mm) than the diameter of the O-ring (3 mm). Therefore, the bending is largest between the O-ring and the bearing area. This concave bending induces compressive strain in the cap and barrier layer. As the heterostructure has piezoelectric properties, this strain will influence the electrical field in the AlGaN barrier layer by locally decreasing the magnitude of the polarisation P_{PE}. Subsequently, the polarisation induced charge $+\sigma_{P,AlGaN}$ at the GaN/AlGaN interface is reduced and the 2DEG is partially depleted. The magnitude of bending determines how strongly the 2DEG is depleted. In figure 7.9, the worst case scenario of complete depletion is depicted. For the thin PDMS sealing ring, no bending can be expected as it fits the recess in the measurement cell.

The early pinch-off at the outer 2DEG shows the limits of the inflection point method quite plainly. This is mainly due to the pronounced influence of the profile shape on the inflection point, as illustrated in the two graphs of figure 7.19. For a normal or shallow depletion, the

inflection point is found in the upper portion of the profile. A steep and sudden depletion, however, shifts the inflection point towards the lower portion of the profile. As the lower portion is always determined by the outer 2DEG, no pH-sensitivity is observed in this case. Despite the plain decrease of the measurable pH-sensitivity, it is assumed that the pH-dependent potential generation at the sensor surface is not affected. It is very unlikely that the protonation and deprotonation of the amphoteric metal oxide groups is influenced by the bending of the sensor chip.

Although this discussion reveals that the diminished pH-sensitivity is clearly a systematic error that is induced by a maladjusted measurement setup it also emphasises the importance of $N_{s_o}/N_{s_i} > 1$. The profiles shown in figure 7.17 are a worst-case example, but a reduced sheet charge density in the outer 2DEG was found to be the most important impact on the pH-sensitivity. As the outer 2DEG is also influenced by the passivation layer, the choice of a suitable material must be considered carefully. If the material leads to a partial depletion the range of the pH-sensitivity can be seriously restricted. Silicon nitride may be a suitable choice for the passivation layer, as it enhances the underlining 2DEG [215].

The slope of N_s shows that the integration method is slightly more robust with regard to the intensified depletion characteristic. As the integration is performed over the entire capacitance profile, the small pH-dependent region is accounted for and a mediocre pH-sensitivity can be derived (table 7.5). Nevertheless, the relative imprecision is too high for reproducible measurements.

7.2.3 Summary

The results and conclusions obtained from the characterisation of pH-sensitivity of the AlGaN-EIHS can be summarised as follows:

- Impedance-voltage profiling is a suitable measurement method for the determination of pH-sensitivity. Three methods for the analysis of the recorded profiles have been evaluated, which were shown to have a significant influence on the obtained results.

- The interpolation method is suitable for the qualitative characterisation of pH-sensitivity. The obtained sensitivity profiles allow to evaluate the entire capacitance range and identify portions with decreased sensitivity. However, the method is unsuitable for quantitative analysis, due to insufficient reproducibility. In addition, only relative information can be obtained and a pronounced dependence on the reference profile has been demonstrated.

- The inflection point method is very suitable for quantitative determination of pH-sensitivity, as the relative imprecision and reproducibility were found to be very good. It is the only method that is capable of extracting the pH-dependent voltage shifts from impedance profiles with insufficient depletion characteristics. Its only disadvantage is that it fails for the intensified depletion characteristic, as the inflection point strongly depends on the shape of the profile. Nevertheless, it is generally equal or superior to the other methods.

- The integration method is comparable to the inflection point method for typical impedance profiles and allows for quantitative pH-measurements. By its definition it accounts for the whole profile and can therefore qualitatively extract small pH-sensitive

regions encountered for the intensified depletion characteristic. No pH-sensitivity was derived for the insufficient depletion with this method.

- It was demonstrated that sheet charge density in the outer 2DEG influences the measurable pH-sensitivity of the EIHS. The sensitivity is reduced for a ratio $N_{s_o}/N_{s_i} < 1$, as the depletion of the pH-insensitive outer 2DEG dominates the overall impedance profiles. This effect is assumed to limit only the transducing mechanism of the heterostructure, but not the actual pH-dependent potential generation at the surface. Nevertheless, care must be taken to establish a ratio $N_{s_o}/N_{s_i} > 1$, e.g. by the choice of a suitable passivation layer.

In this section, the best and worst case pH-sensitivities obtained for an AlGaN-EIHS were shown. From the numerous measurement series ($n = 22$) that were recorded for this work a typical U_{th_C} pH-sensitivity of 48.1 mV pH^{-1} ($SD = 5.8$ mV pH^{-1}) was obtained for the EIHS with a $B_{10}^{30}C_2$ heterostructure in the dark. Although the sensitivity varies between the different series, the relative imprecision in a single series was always less than 0.1pH. Thus, it can be concluded that the EIHS is well suited for pH-measurements, when the actual pH-sensitivity is determined beforehand.

7.3 Cross-sensitivity to Ionic Strength

A cross-sensitivity to the ionic strength can be expected, based on the publications on ion-sensing with GaN bulk or AlGaN-ISFETs (section 4.4). In the theoretical description of the sensing mechanism, using

the site-dissociation model (section 3.3.1), the differential capacitance C_{dif} was introduced by van Hal et al. to account for this effect [70].

The influence of ionic strength on the AlGaN-EIHS was investigated using electrochemical impedance profiling. The principal buffer system was unchanged, but this time the pH-value was kept constant and the ionic strength was varied from 1 mM to 100 mM. Preliminary experiments with unbuffered electrolyte solutions, made from deionised water and different concentrations of KCl, showed that the pH-value of these unbuffered solutions is subject to large deviations between pH6 and pH8. In addition, very long equilibration times and insufficient reproducibility were observed for pH-measurements with a conventional glass electrode, especially at low ionic strengths. Continuous purging of the solutions with nitrogen did not improve the stability of the pH-value. Therefore, unbuffered solutions are not suitable for the determination of cross-sensitivity and were not used. In contrast, the pH-value of the employed buffered electrolyte solutions PB1, PB10 and PB100 was sufficiently stable (± 0.05 pH).

The *voltage profile* for different ionic strengths is given in figure 7.20. The shapes of the capacitance profiles are typical and only a slight voltage shift is seen for the lowest ionic strength. The voltage shift is also seen in the conductance profiles in addition to a large conductance shift in the enhancement range. On the logarithmic scale, it is approximately linear and covers a range of one order of magnitude between an ionic strength of 1 mM and 100 mM. The phase angle profile reflects the conductance shift in an increase of ϕ, but otherwise it exhibits a typical shape. The extent of the absolute voltage shift is seen in the reproducibility profiles (referenced to $I = 1$ mM), where both the medium and high ionic strength induce a shift of up to 30 mV and the reproducibility of 1 mM is about 5 mV. In the *parameter footprint* a distinct

Table 7.6: Cross-sensitivity of U_{th_C}, U_{th_G} and N_s to ionic strength for an AlGaN-EIHS ($B_{10}^{30}C_2$).

parameter	sensitivity (1–100) mM S_{pK} (pK^{-1})	standard deviation SD
U_{th_G} (mV)	58.4 ± 1.2	3.3
G_0 (µS)	$(-7.1 \pm 0.1)\,\mathrm{pK}^{-0.5}$	1.7
	sensitivity (1–10) mM	
U_{th_C} (mV)	22.7 ± 1.6	1.1
C_0' ($\mathrm{nF\,cm^{-2}}$)	-1.6 ± 0.3	0.8
N_s (10^9 $\mathrm{cm^{-2}}$)	79.9 ± 2.8	4.4

linear dependence can be found for U_{th_G} and G_0. It should be noted that on the x-axis a logarithmic scaling was used for U_{th}, N_s and C_0', which corresponds to $pK_I = -\log \frac{I}{mM}$ and G_0 is plotted versus $\sqrt{I}$. The zero bias capacitance C_0' only shows a very small, positive trend, whereas U_{th_C} and N_s are clearly non-linear with a relatively large slope towards 1 mM and virtually no change towards 100 mM. The slopes of the linear approximations are given in table 7.6.

In order to interpret the impact of the ionic strength on the impedance profiles, the conductance of the buffer solution has to be taken into account, as it directly depends on ionic strength. Previously, it was derived that the series conductance G_s of the full equivalent circuit is a lumped representation of all resistive elements outside the actual sensor heterostructure. The conductance of the electrolyte solution was expected to influence the value of G_s, especially at low ionic strengths. For the reduced equivalent circuit, an estimate of G_s can be derived from the value of G in the enhancement range. Therefore, an influence of the ionic strength on G_0 is expected and also observed in the *pa-*

rameter footprint. As a consequence, the linear dependence of G_0 on $\sqrt{I}$ may primarily be determined by the conductance of the electrolyte solution.

A similar proportionality to $\sqrt{I}$ can be derived from the Deybe-Hückel-Onsager theory for the molar conductivity λ_m [21]. Assuming that K_2HPO_4 and KH_2PO_4 dissociate completely in water they can be treated as strong electrolytes and λ_m is approximately proportional to $\sqrt{I}$:

$$\Lambda_m \propto \sqrt{I}. \tag{7.4}$$

However, the molar conductivity is defined as the conductivity κ_e divided by the electrolyte concentration c and it can be shown that G_0 does not reflect the Deybe-Hückel-Onsager theory. Assuming that G_0 is proportional to κ_e, one gets:

$$\Lambda_m = \frac{\kappa_e}{c} \propto \frac{G_0}{c} \propto \frac{\sqrt{I}}{c}, \tag{7.5}$$

which disagrees with the proportionality in equation 7.4.

Possibly, this deviation is due to the rather complex composition of the buffer solution. Although the potassium phosphate salts are strong electrolytes, the resulting weak acid H_3PO_4 is also a weak electrolyte. This implies that the cations K^+ as well as the different protonation states of H_3PO_4 determine the overall electrolyte conductance. An additional influence is the pH-value itself with the corresponding ions H_3O^+ and OH^-. This complex overall ionic composition may be responsible for the observed deviations.

Another possible explanation is connected to the thickness of the electric double layer that is expressed by the Debye length λ_D, which

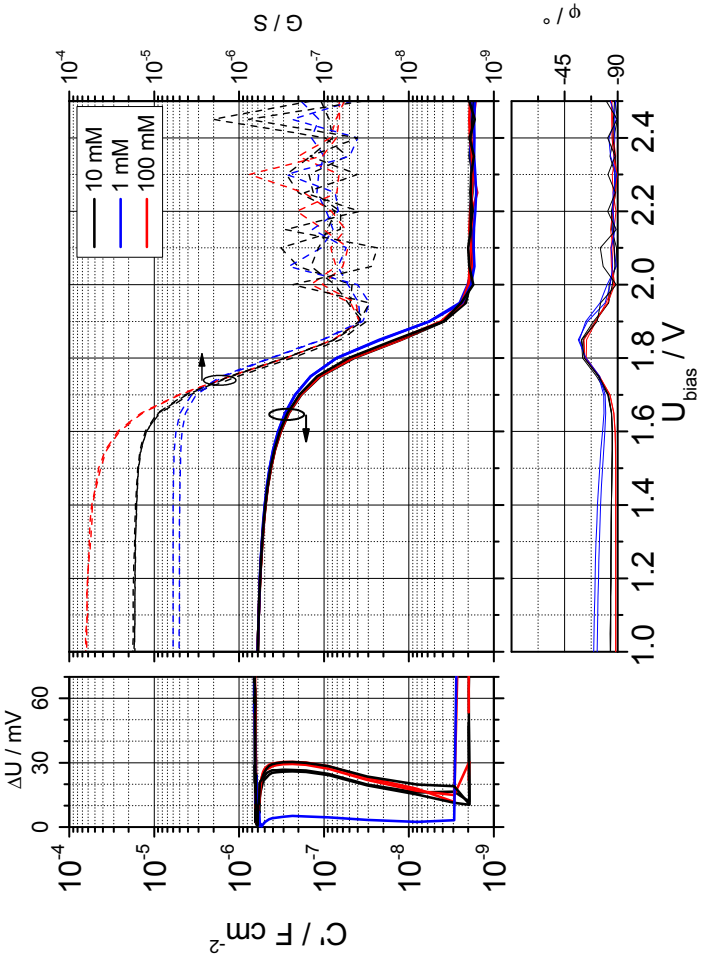

Figure 7.20: *Voltage profile* of an ionic strength measurement series with an AlGaN-EIHS ($B_{10}^{30}C_2$). Reproducibility profiles are referenced to 1 mM (blue).

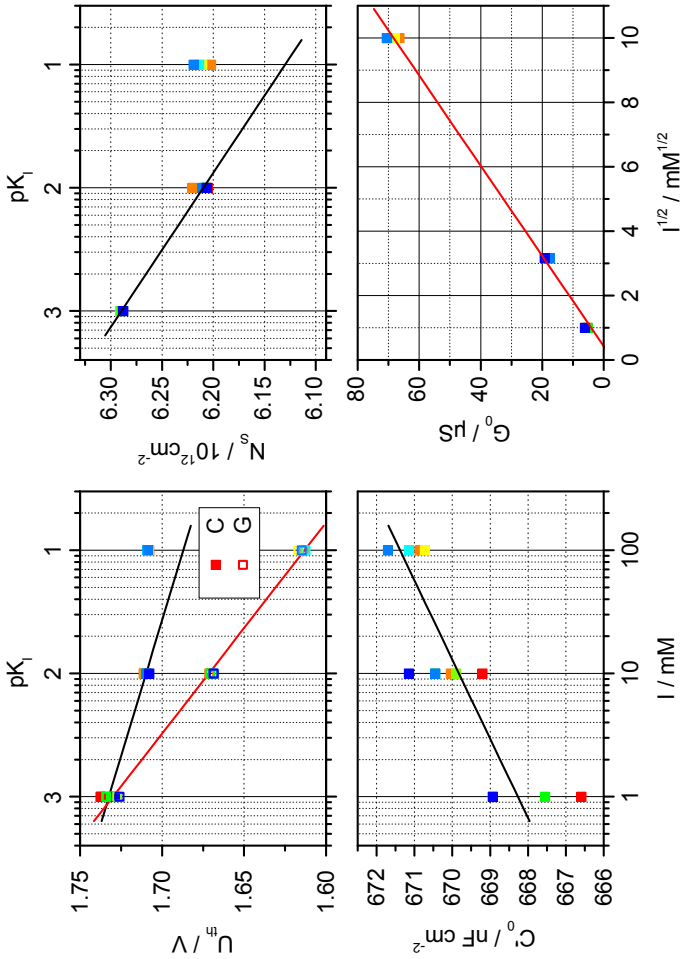

Figure 7.21: *Parameter footprint* of an ionic strength measurement series with an AlGaN-EIHS ($B_{10}^{30}C_2$). Solid lines depict linear approximations.

is inversely proportional to $\sqrt{I}$ (eqn. 2.9). Assuming that the increased concentration in the EDL results in a decreased ion mobility, κ_{EDL} may be treated as a constant. The conductance of the EDL can be then estimated as follows:

$$G_{EDL} = \kappa_{EDL} \frac{A}{\lambda_D} \approx \kappa_{EDL} \frac{A}{0.304\,\mathrm{nm/M}} \sqrt{I}. \tag{7.6}$$

This relation can explain the proportionality to $\sqrt{I}$, when the impact of G_{EDL} on G_0 is significant.

The conductance shift in the enhancement range is also primarily responsible for the linear shift that is found for U_{th_G}, as the conductance profile is relatively unchanged in the transition and depletion range. Similar to the shift of U_{th_C} for the intensified depletion characteristic (fig. 7.19), the shape of the conductance profile influences the value of U_{th_G}. At 100 mM the conductance in the enhancement range is high and the inflection point, and therefore U_{th_G}, is located at low bias voltage. With decreasing ionic strength, U_{th_G} shifts towards high values. It is interesting to note that the magnitude of the shift is very close to the Nernstian limit. This connection may just be a coincidence, but repeated measurement series, even with variations of the heterostructure, always yielded values of (53–59) $\mathrm{mV\,pK^{-1}}$. If there is indeed a connection to the Nernst equation (eqn. 2.7) it implies that some chemical reaction in the measurement chain is determined by the ionic strength of the electrolyte. These reactions might take place at the reference electrode or at the sensor surface. As the reference electrode is designed to deliver a constant potential by the exchange of chloride ions from the inner reference electrolyte with the Ag/AgCl electrode, only the diffusion potential at the ceramic diaphragm comes into consideration. However, such linear potentials are unlikely to be generated

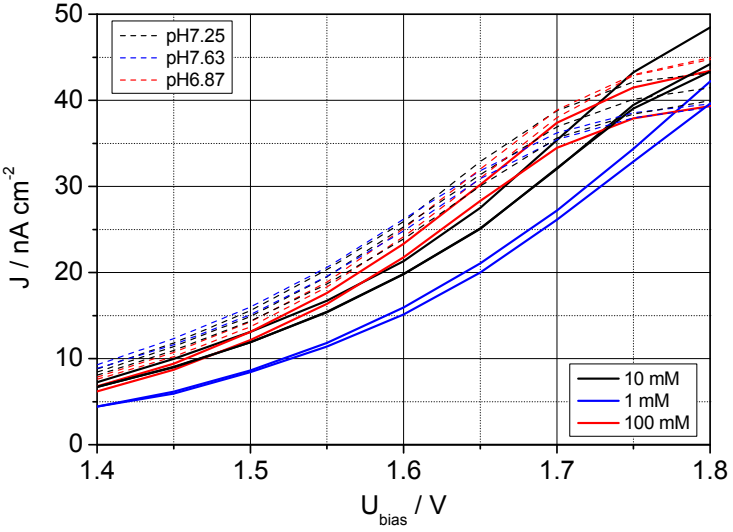

Figure 7.22: Comparison of DC current density profiles of pH-sensitivity (dashed lines) and ionic strength measurement series (solid lines) with an AlGaN-EIHS ($B_{10}^{30}C_2$).

by diffusion. Another possibility is the specific adsorption of anions at the sensor surface, which has been claimed in several publications (cf. section 4.4). An unblocked reaction of ions with the surface would result in a Nernstian shift, comparable to the reaction of chloride ions in the reference electrode. However, this adsorption would also lead to a change of surface charge and a voltage shift of the impedance profiles, which is only observed for the lowest ionic strength. The specific adsorption can therefore be ruled out. In conclusion, a connection of U_{th_G} to the Nernst equation cannot be confirmed.

The voltage shift of U_{th_C} at $I = 1\,\mathrm{mM}$ is unlikely to be induced by a specific sensitivity to ionic strength. Instead, the DC voltage drop in the electrolyte solution has to be considered. This voltage drop develops between the reference electrode and the sensor surface and it is proportional to the DC current and the electrolyte conductance. As observed in G_0 and discussed earlier, the conductance is determined by the ionic strength. Therefore, a decreasing ionic strength leads to an increased voltage drop in the solution. Unlike the voltage shift induced by varying the pH-value, the variation of electrolyte conductance should also be reflected in the DC current density profile. This assumption is confirmed by figure 7.22, where a shift of up to 50 mV is found for a decreasing ionic strength. A shift of similar magnitude is found in the reproducibility profiles (fig. 7.20). This similarity of AC and DC characteristic is evidence that the shift is induced by a simple resistive element, namely the conductance of the electrolyte. In case of the specific dependence on pH-value, which is overlaid in figure 7.22, only a very small shift is observed. This suggests that specific adsorption processes have a significant impact on the AC characteristics of the EIHS, but do not influence the DC characteristic.

The impact of the voltage drop can be minimised by the use of a three-electrode measurement setup. The additional counter electrode that draws the DC current would be placed at some distance to the EIHS. The reference electrode can then be placed very close to the EIHS and its potential is controlled by a potentiostat. This way the voltage drop via the electrolyte solution and possible overpotentials at the reference electrode are minimised. It might then be possible to obtain information on specific processes at the sensor surface that are connected to ionic strength.

In summary, the following results and conclusion have been obtained in the preceding discussion:

- No distinct cross-sensitivity towards ionic strength can be derived from the electrochemical impedance profiles of the AlGaN-EIHS in a two-electrode measurement setup.
- The proportionality $G_0 \propto \sqrt{I}$ and the similar voltage shifts in the sensor's AC and DC characteristics suggest that all changes of the impedance-voltage profiles observed for varying ionic strength can be attributed to the electrolyte conductance.
- With a three-electrode measurement setup the influence of the electrolyte conductance might be minimised.

8 Optimisation of Ambient Conditions and Heterostructure Layout

In this chapter, the optimisation of the illumination conditions in the measurement setup and the cap layer thickness and barrier layer Al-content of the heterostructure will be discussed. This optimisation is aimed at the reduction of the pronounced light sensitivity with the drawn-out PPC characteristic and the enhancement of the corrosion stability of the sensor surface. Continuous violet and red illumination was investigated as a means to minimise the influence of additional ambient illumination and to reduce the PPC drift duration, respectively. A pronounced photoelectrochemical corrosion process was discovered for continuous violet illumination.

The optimisation approach for the heterostructure is aimed at the reduction of the dislocation density at the surface and the reduction of the operating voltage, by increasing the GaN cap layer thickness and decreasing the Al-content in the AlGaN barrier layer. For each optimisation step, the corrosion drift and pH-sensitivity are characterised for comparison.

8.1 Continuous Violet Illumination

A continuous backside illumination of the AlGaN-based pH-ISFET was suggested by Kittler [16] to reduce the light sensitivity and, especially, the impact of the PPC. For a violet LED with a near band gap wavelength of $\lambda = 400\,\mathrm{nm}$, he observed the smallest influence of simultaneous ambient illumination (fig. 4.5). However, with regard to the publications on photoelectrochemical etching of III-nitrides (cf. section 4.3.3), an amplification of the corrosion drift can be expected.

8.1.1 Photoelectrochemical Corrosion with Violet Light

The actual impact of the photoelectrochemical corrosion is illustrated in figures 8.1 and 8.2. The *voltage profile* and *parameter footprint* are shown for an EIHS based on a $B_{10}^{30}C_2$ heterostructure. The impedance-voltage profiles were recorded in direct succession in the phosphate buffer solution PB6.88. For the continuous backside illumination, a violet LED, similar to that used in the thesis of Kittler [16], was chosen. As a first step, the obtained impedance-voltage profiles, DC current density profiles and SEM images of the corroded surface are shown and described. Subsequently, these results are discussed.

Most strikingly, the capacitance and conductance profiles are neither solely shifted nor skewed, but distorted and stretched into two separate transitions. The initial impedance profile (black) was recorded after more than 24 h in the dark. It exhibits typical shapes for the capacitance, conductance and phase angle profiles. When the illumination is turned on, the profiles (red) are shifted towards larger U_{bias} in less than a single measurement time period (15 min). Additionally,

the slopes of the capacitance and conductance become less steep and the value of C' in the depletion region is increased by a factor of three. The phase peak is smoothed out and a second peak starts to develop. In the course of the subsequent measurements (blue) a shift towards lower bias voltages is observed. The lower part of the capacitance and conductance profiles start to settle after 5 measurements, but the upper part continues to drift approximately linearly with the number of measurements. This two-fold behaviour is also very well seen in the reproducibility profile, where the shift with regard to the first profile upon illumination is nearly equidistant for the upper capacitance portion. For the lower capacitance portion, the reproducibility profile stays constant after 10 measurements. The phase profile is stretched out even further into two peaks. Especially the second, lower peak is smoothed out almost completely, becomes less defined and is reduced in height considerably.

In the corresponding *parameter footprint* (fig. 8.2), the corrosion is reflected by the pronounced negative drift of U_{th_C}, U_{th_G} and N_s, as well as the varying drifts of C'_0 and G_0. The slopes of the linear portions, given in table 8.1, show that the violet light induces large drifts in all investigated parameters. To confirm that the observed corrosion phenomenon is mainly dependent on the number of measurements, and independent of time, the measurement series was repeated with a pause of 45 min between each impedance profile. The slopes of the linear portions are also given in table 8.1. Compared to the measurements without a pause, only a small increase is found, which may be due to a light-induced corrosion process in the measurement pause.

The incident violet light also has a prominent influence on the leakage DC current, as illustrated in figure 8.3. Here, the DC current density J, which is recorded parallel to the impedance profile, is plotted versus

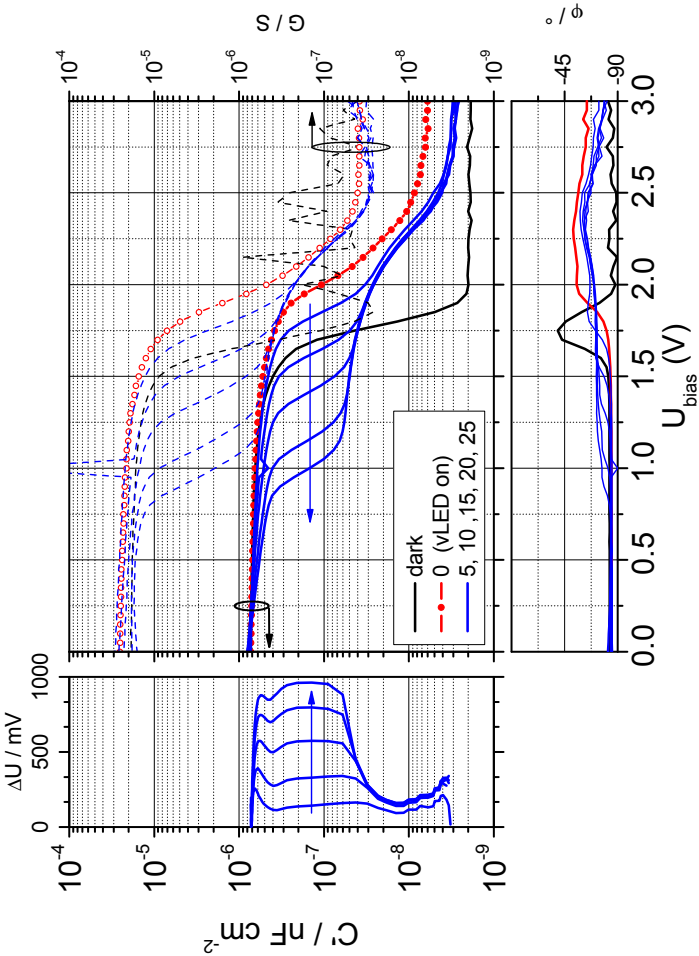

Figure 8.1: *Voltage profile* of an AlGaN-EIHS ($B_{10}^{30}C_2$) continuously illuminated with violet light. Reproducibility profiles are referenced to measurement count 0 (red circles).

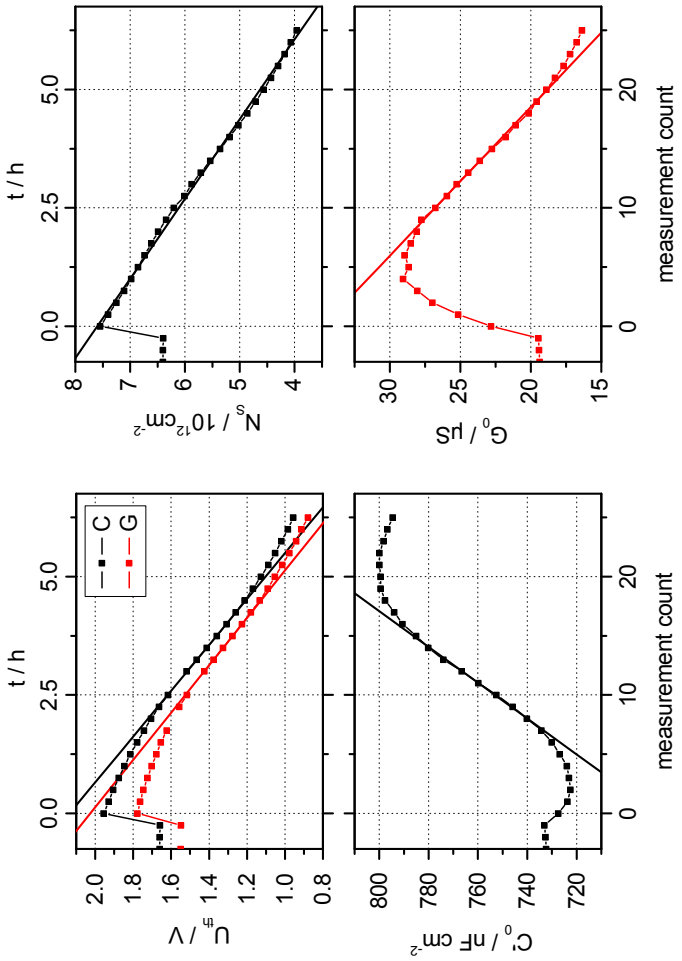

Figure 8.2: *Parameter footprint* of an AlGaN-EIHS ($B_{10}^{30}C_2$) continuously illuminated with violet light. Solid lines depict linear approximations.

Table 8.1: Drift slopes of U_{th_C}, U_{th_G}, N_s, C'_0 and G_0 for the photoelectrochemical corrosion of an AlGaN-EIHS ($B^{30}_{10}C_2$) with continuous violet light - measured in direct succession and with a measurement pause of 45 min.

parameter	drift (meas^{-1}) direct succession	drift (meas^{-1}) pause 45 min
U_{th_C} (mV)	−51.7	−52.3
U_{th_G} (mV)	−48.2	−50.6
N_s (10^9 cm^{-2})	−148.6	−173.0
C'_0 ($\text{nF}\,\text{cm}^{-2}$)	6.6	6.8
G_0 (µS)	−0.8	−1.5

U_{bias} for the same measurement counts as in the *voltage profile*. The initial dark current (black) has a magnitude of less than $10\,\text{nA}\,\text{cm}^{-2}$, which cannot be resolved in the shown graph. When the illumination is turned on, J increases by a factor of 200 within a single measurement and continues to increase for the subsequent measurements until a maximum value of $1.3\,\mu\text{A}\,\text{cm}^{-2}$ is reached in the depletion region. The general shape of the DC current density profile bears resemblance to the transfer characteristic of a transistor, with an approximately linear slope for small bias voltages and a nearly constant saturation region at higher voltages. It can be seen that U_{th_C} from the corresponding capacitance profiles, which is overlaid as vertical lines, closely matches the transition point between the linear and the saturation region.

The surface morphology after the photoelectrochemical corrosion was investigated using SEM. In figure 8.4, SEM images of the sensor surface are shown for an area that was covered by the sealing ring (fig. 8.4a), for an area that was subjected to the electrolyte solution (fig. 8.4b) and the transition between both areas (fig. 8.4c). The covered area

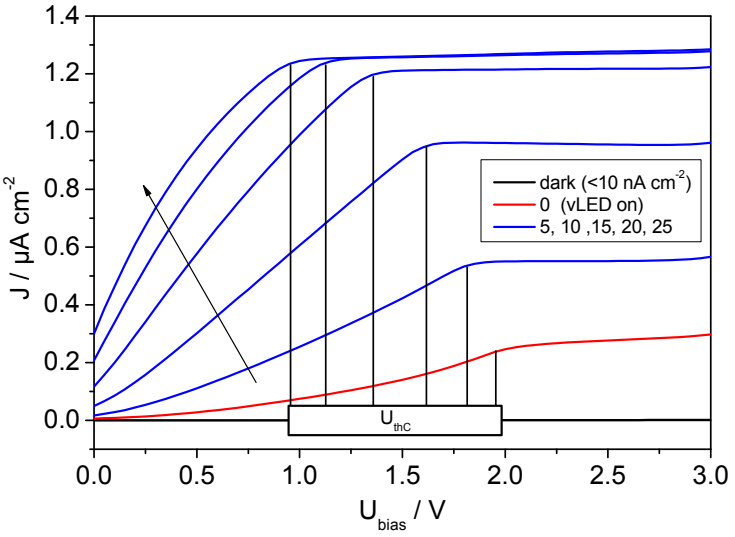

Figure 8.3: DC current density profiles of an EIHS sensor chip ($B_{10}^{30}C_2$) with continuous violet illumination. The vertical lines indicate the threshold voltage U_{th_C} obtained from the corresponding capacitance profiles.

mainly exhibits small pits with diameters of less than 10 nm, which are partially lined up in a way that hints at underlying grain boundaries. In addition to that, a few larger pits and trenches can be found with a width of up to 30 nm. For the corroded surface, the overall density of corrosion pits is approximately the same, but their size is increased to a typical diameter of (30–50) nm. This is also why more trench-like features can be found, which result from the merging of single holes. For the corroded surface the commonly observed surface charging artifacts were much less pronounced.

In the following paragraphs, the obtained results are discussed. The photoelectrochemical corrosion that is induced by violet light has a strong influence on the measured impedance profiles and the parameters that are derived from them. The connection of the upper and lower capacitance profile portion to the inner and outer 2DEG, respectively, is clearly seen in figure 8.1. The prominent distortion of the capacitance and conductance profiles into two depletion levels indicates that only certain parts of the sensor are influenced by the corrosion process. These levels can be assigned to the depletion of the inner and outer 2DEG channel. The inner 2DEG is influenced by the inner heterostructure, which is covered with electrolyte solution. In contrast, the outer 2DEG is covered by the sealing ring and is therefore not influenced by the electrolyte solution. As the corrosion process alters the inner heterostructure, mainly the sheet charge density of the inner 2DEG is decreased and the outer 2DEG is not influenced significantly. This characteristic is reflected very clearly in the capacitance and conductance profiles. The upper portion of the profiles drifts significantly, which corresponds to the depletion of the inner 2DEG. The lower portion settles to a fixed course, as the outer heterostructure is not corroded and the outer 2DEG is relatively unchanged. The parallel shift of the upper

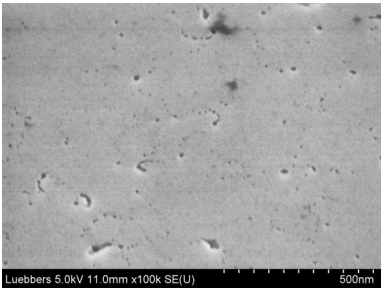

(a)

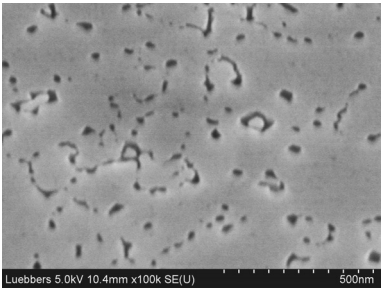

(b)

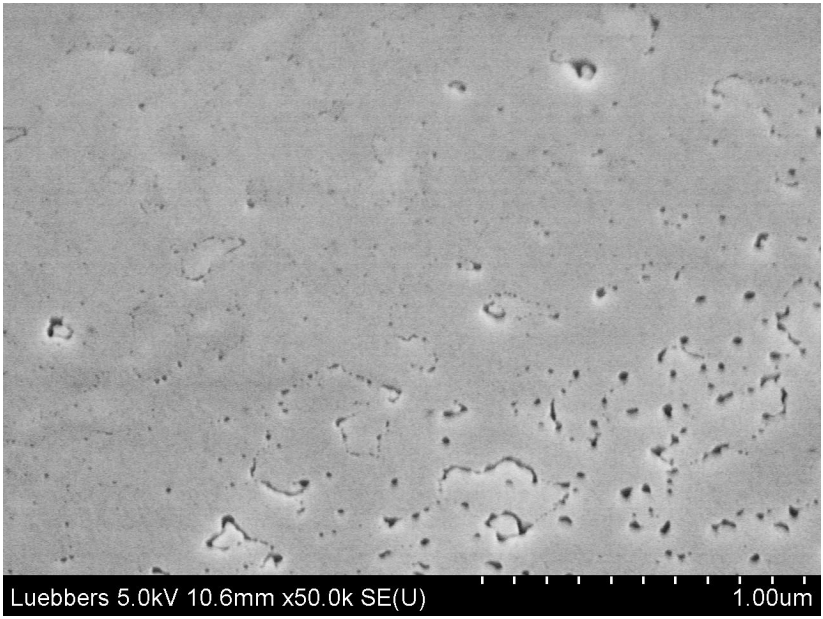

(c)

Figure 8.4: SEM images that show (a) uncorroded and (b) corroded areas as well as (c) the transition between both areas for an AlGaN-EIHS sensor chip ($B_{10}^{30}C_2$) after photoelectrochemical corrosion with violet light.

portion suggests that the corrosion is a linear and rather homogeneous process. The conductance profiles exhibit characteristics similar to the capacitance profiles. This includes the initial voltage shift and the general increase in the depletion region upon illumination as well as the distortion into two depletion characteristics. Minor differences include the smaller drift and faster settling of the lower portion of the profile and the drift in the enhancement region, which is seen more clearly in the *parameter footprint*.

The splitting of the single phase angle peak into two peaks is a clear indication of the corrosion process. As the peak signifies a depletion process, two peaks correspond to two 2DEG portions that are depleted. For an uncorroded sensor chip the depletion of the outer 2DEG is overlapped by the depletion of the inner 2DEG. In contrast, the corrosion of the inner heterostructure partially depletes the inner 2DEG and the upper depletion range is shifted to lower voltages, whereas the outer 2DEG seems to be relatively unaffected. This way the depletion ranges and their corresponding phase peaks become separated.

In general, the illustration of the measured data in the developed *voltage profile* layout is advantageous for the determination of the corrosion state of the sensor. The distortions of the capacitance and conductance profiles can clearly be seen in the reproducibility profiles and in the shape of the phase angle peak. The advantage of the phase angle peak, compared to the reproducibility profiles, is the immediate availability during the recording of the impedance spectra without further analysis. A single phase profile is sufficient to assess the corrosion state of the sensor chip. When two peaks are found, the sensor chip has been corroded to some extent. For the calculation of the reproducibility profiles, at least two capacitance profiles are needed and many more profiles if the corrosion process is very slow.

The *parameter footprint* is mainly useful to quantify the magnitude of the corrosion drift for practical measurement purposes, but some information on structural changes of the sensor chip can also be obtained. The sheet charge density and the threshold voltages reflect depletion of the 2DEG. However, U_{th_C} and U_{th_G} only comprise the depletion of the inner 2DEG, whereas N_s comprises both the inner and the outer 2DEG. In general, the drift magnitudes of N_s and U_{th} clearly show that the violet light is not a suitable illumination source. Compared to the pH-sensitivity that can be obtained with the AlGaN pH-sensors, the drift amounts to one pH-unit per measurement.

The linear decrease of N_s suggests that the influence of the corrosion process on the heterostructure might also be linear. However, the varying course of C_0' indicates that the structural changes of the cap and barrier layer are non-linear. The SEM images show that the dislocations in the heterostructure are the primary target of the corrosion process. The enlargement is clearly seen and a deepening of these structural defects can be assumed. The vertical etching component leads to a thinning of the cap and barrier layer and the capacitance at these locations will be increased due to the smaller insulator thickness. As the corroded and uncorroded parts of the heterostructure are in parallel, the measured overall capacitance increases. The lateral etching component amplifies this drift by increasing the corroded portion of the surface. However, the preceding considerations are only valid as long as the 2DEG below the corroded dislocations is sufficiently conductive. As the thinning of the barrier and cap layer also depletes the underlying 2DEG portion, it will be depleted completely when the dislocation is etched to a certain depth. At this point the effective surface area, which is the portion of the surface with an underlying 2DEG back electrode, is decreased and the capacitance decreases. This increase and decrease

is clearly seen in the course of C_0'. The initial decrease that is observed when the illumination is switched on is more difficult to interpret. Possibly, the light- and bias-induced positive charge at the surface leads to an oxidation of the surface and effectively to an increase of the topmost metal oxide layer. This would increase the overall thickness of the heterostructure and decrease its capacitance, before the vertical etching of the dislocations becomes dominant. However, this explanation is rather speculative.

The course of G_0 bears resemblance to C_0', with the exception of opposite drift directions. The origin of the initial increase of G_0 is unknown. However, it can be ruled out that it originates from the previously discussed electrolyte leakage of the reference electrode. The observed drift for the photoelectrochemical corrosion is much faster than the drift that was induced by the leakage of reference electrolyte. The subsequent linear decrease can be explained by the ongoing depletion of the 2DEG below the corroding dislocations, as G_0 also comprises the conductance of the inner and the outer 2DEG. When the inner 2DEG is depleted locally the conductance of the inner 2DEG is decreased. When it falls below a critical value it will begin to dominate the overall conductance, which is reflected in G_0. The reason for the slower decrease of G_0 towards the end of the measurement series might be due to an accumulation of electrolyte ions in the corrosion pits, which result in regions of increased conductivity. Effectively, part of the insulating heterostructure would have been replaced by conducting electrolyte regions.

This assumption is confirmed by the continuous and pronounced increase of the DC current density. It indicates that the DC conductance of the formerly insulating cap and barrier layer increases, most likely by the local thinning of these layers and the accumulation of electrolyte

ions in the corrosion pits. The dislocations are also the weakest link of the heterostructure in terms of electrical resistance, as they are more reactive and run through the entire structure. Thereby, they are the preferred path for the leakage current. In turn, this local increase of current flow accelerates the corrosion, leading to larger dislocations and the process is amplified. The DC current density profiles consist of a linear and a constant range. The linear increase at low bias voltages signifies an ohmic behaviour as long as the inner 2DEG is not depleted. The pinch-off of the 2DEG can be clearly seen in the saturation of J, which coincides with U_{th_C}. From this connection it can be inferred that the inflection method is indeed very suitable for the determination of the threshold voltage.

For the explanation of the current saturation, and the loss of the ohmic behaviour, the similarity to the transfer characteristic of a field effect transistor can again be invoked. When the channel of a FET is pinched-off at the edge of the gate towards the drain contact the drain current saturates, as the electrons are subject to ballistic transport through the generated depletion region. Increasing the gate-source voltage broadens the depletion region and accelerates the charge carriers in such a way that the resulting drain current is nearly constant. For the EIHS, as well as the MIHS, the same mechanism is responsible for the saturation of the DC leakage current. This is due to the fact that the bias voltage is applied between an inner Schottky contact and an outer ohmic contact, instead of a bulk contact. The 2DEG is depleted laterally, instead of vertically, once the inner 2DEG is depleted. This depletion of the outer 2DEG generates a depletion region in a lateral direction, which forces the leakage current to saturate analogously to the drain current of a FET. Figuratively speaking, the E/MIHS, resembles the drain half of a FET. However, for the uncorroded EIHS this effect

is difficult to seen, as only a very small leakage current is flowing. As the corrosion dramatically increase the leakage current, the saturation characteristic is easily seen then.

The pronounced contrast of the corrosion pits in the SEM images suggests a vertical corrosion process. It can be assumed that the photoelectrochemical corrosion is an anisotropic etching process with a larger vertical component. This assumption was confirmed by the observation that the lateral size of the corrosion pit is not increased, even when the electrical properties of the heterostructure have degraded completely, i.e. the inner 2DEG no longer exists. The actual depth of the pits cannot be determined e.g. by AFM as their diameter is still too small, even after the corrosion process. Due to the triangular shape of the AFM tip, the bottom of the pits is not reached. The observation that the charging artifacts are greatly reduced for the corroded sensor areas confirms that the cap and barrier layers are no longer insulating. The charge that is introduced by the electron beam of the SEM can flow via the remaining 2DEG channel towards the ohmic contacts.

From the comparison of this dislocation corrosion to the published results for the etching with KOH (section 4.3.3), in general, and the AFM image shown in figure 4.8, in particular, the following differences are observed: Most obviously, the diameters of the corroded dislocations are much smaller and do not display the typical hexagonal shape of the KOH etch pits. This difference confirms that the vertical component dominates for the photoelectrochemical corrosion, as the hexagonal shape is an indicator for dominant lateral etching. Additionally, the density of the corroded dislocations is much higher (on the order of $1 \times 10^{10}\,\mathrm{cm}^{-2}$). As the dislocation density is comparable to the value obtained after the removal of the photoresist (cf. section 7.1.1), it can be concluded that the corrosion process does not increase the dislocation

density. As a consequence, only the fabrication process with the high temperature annealing step seems to be responsible for the increase of the dislocation density compared to the as-grown wafer.

Compared to the purely electrochemical corrosion that was discussed earlier, the photoelectrochemical corrosion with violet light is much more pronounced and severely influences the sensor's electrical characteristics. However, as the principle impact on the *voltage profile* and *parameter footprint* is similar for the electrochemical corrosion it can be assumed that the additional violet light primarily amplifies the process, which is otherwise similar.

8.1.2 Characterisation of Light- and pH-Sensitivity of the Corroded Sensor in the Dark

Although the severe photoelectrochemical corrosion prevents the use of continuous violet illumination to reduce the influence of ambient light, the corroded EIHS sensor chip can be characterised in the dark with regard to its PPC characteristic and pH-sensitivity. These investigations are employed to refine the model of the inner and outer 2DEG depletion. In addition, it will be shown that the light sensitivity of the inner 2DEG is significantly reduced and it is verified that the pH-sensitivity is conveyed by specific adsorption.

Light Sensitivity and PPC

In figure 8.5, the *voltage profile* of a standard PPC decay measurement series is shown for a corroded EIHS sensor chip with a $B_{10}^{30}C_2$ heterostructure. After the chip had been darkened for more than 12 h, the violet LED was switched on for two measurements ($\sim$ 30 min).

Afterwards, the decay characteristic was measured for a duration of approximately 10 h.

The initial dark characteristic clearly indicates that the sensor chip is severely corroded, as the typical two-fold depletion characteristic can be found in the capacitance and conductance profiles and the phase angle exhibits a widely stretched double peak. When the violet illumination is switched on, the lower depletion is shifted by a significant amount towards higher U_{bias}. For the upper depletion, no pronounced shift is observed. Only a slight shift towards lower U_{bias} is observed in the capacitance profile and a very small positive shift is found in the conductance profile. When the illumination is switched off, the typical drawn-out PPC decay characteristic is observed for the lower depletion and after 10 h it matches the initial dark course. In contrast, the upper depletion is nearly unchanged when the illumination is switched off. A small shift towards lower U_{bias} is found in both the capacitance and conductance profiles after 10 h. The reproducibility profiles, referenced to the initial dark profile, illustrate that the shift of the upper depletion (50 mV) is much smaller than the shift of the lower depletion (500 mV). The constant offset of the upper depletion is almost unchanged when the illumination is switched off. In contrast, the lower depletion slowly drifts back and after 10 h an offset of (5–10) mV to the initial dark profile is obtained. These results underline that the two depletion ranges have to assigned to different portions of the 2DEG channel. On the one hand, the typical PPC decay characteristic of the lower depletion suggests that the corresponding 2DEG portion has not been degraded by the corrosion process. Therefore, it has to be assigned to the part of the heterostructure that is covered by the sealing ring and the underlying outer 2DEG. On the other hand, the very low light sensitivity of the upper depletion is fundamentally different from the typical PPC

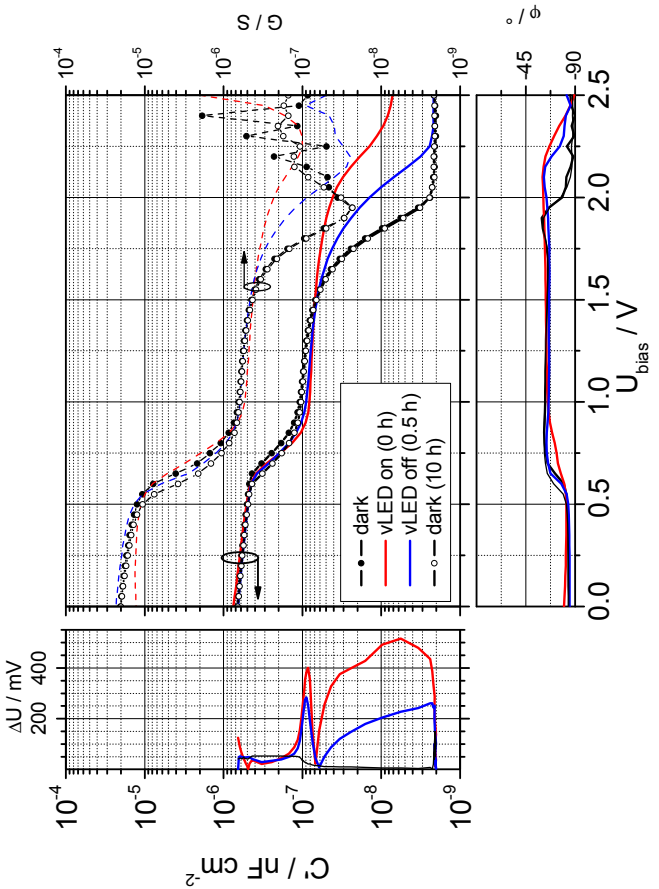

Figure 8.5: *Voltage profile* of a corroded AlGaN-EIHS ($B_{10}^{30}C_2$) after prolonged darkening (black circles), with violet illumination (red), after switching off the illumination (blue) and after 10 h without illumination (black open circles). Reproducibility profiles are referenced to initial dark profile (black circles).

decay characteristic and therefore has to be assigned to the corroded, inner heterostructure and the inner 2DEG.

This difference also raises the question why no PPC characteristic is observed for the upper depletion and whether this effect might be exploited for the construction of light-insensitive AlGaN-based pH-sensors. Apparently, there is a connection between the corrosion state of the heterostructure and the light sensitivity. Neither the switch-on, nor the switch-off of the illumination has a significant impact on the upper portion of the capacitance profiles. Two conclusions can be drawn from this observation: Firstly, the density of corresponding trap states has been reduced and secondly, that these states are not located in the GaN bulk, but in the AlGaN barrier, GaN cap or at the sensor surface. If the trap states were mainly located in the GaN bulk, they would not be affected to this extent by the corrosion process.

The reason for the reduction of traps states during corrosion may be found in the oxidation of the sensor surface. The oxidation of Ga is one step of the overall corrosion or etching process, as discussed in section 4.3. During this step, the surface states are affected and it is possible that they are either removed or compensated. For InN, it has been reported that anodic oxidation reverts the band bending at the surface, by a compensation of surface accumulation charge [216]. Possibly, a similar effect is present for GaN and the net density of surface states is reduced after oxidation. The connection between specific surface states and the PPC, as reported by Horn et al. [134], implies that this reduction of surface states would also account for the diminished light-sensitivity.

Another explanation for the reduced light sensitivity may be found in the Si-doping below the GaN/AlGaN interface. It is employed to reduce the relative influence of ambient illumination [16] by increasing

Table 8.2: Drift slopes of U_{th_C}, U_{th_G}, N_s, C_0' and G_0 for the electrochemical corrosion of a corroded AlGaN-EIHS ($B_{10}^{30}C_2$) in the dark.

parameter	drift (meas^{-1})
U_{th_C} (mV)	-0.2
U_{th_G} (mV)	-0.6
N_s (10^9 cm^{-2})	-1.5
C_0' ($\text{nF}\,\text{cm}^{-2}$)	-0.1
G_0 (µS)	-0.03

the 2DEG sheet charge density. As long as the 2DEG channel exists, all charge carriers from the Si-doping can be assumed to contribute to N_s. However, in case the 2DEG channel is depleted completely or destroyed by the corrosion process, the doping region might act as an alternative, "fall-back" channel. For this channel the 2DEG-specific light-sensitivity and the PPC characteristic would no longer be observed. Nevertheless, with a doping concentration of $2 \times 10^{17}\,\text{cm}^{-3}$ and a thickness of 45 nm, its sheet charge density is only on the order of $1 \times 10^{12}\,\text{cm}^{-2}$, whereas a value of about $3 \times 10^{12}\,\text{cm}^{-2}$ is obtained from the capacitance profiles. Thus, it is unlikely that the Si-doping primarily accounts for the diminished light-sensitivity, although it may contribute to some extent.

The application of the reduced light-sensitivity for the construction of light-insensitive AlGaN-based sensor chips might be possible. However, several limiting aspects have to be considered. For one, the advanced state of the surface corrosion makes the sensor more susceptible to further electrochemical corrosion. This can be seen from the drift values of the corroded sensor in the dark that are summarised in table 8.2.

Compared to the drift slopes of an uncorroded sensor (table 7.2), an increase by a factor of two to three is found. In addition, the drift slope was found to increase with ongoing usage. Effectively, this implies that the lifetime of the sensor chip is limited by the deliberate deterioration of the sensor structure. Presumably, this slightly amplified and ongoing corrosion process will also degrade the sensitivity and reproducibility of the sensor. To clarify this aspect, the pH-sensitivity of the corroded sensor is investigated in the next section.

pH-Sensitivity

In figure 8.6, the impedance-voltage profiles of the corroded AlGaN-EIHS are shown for the standard pH-sensitivity measurement series. The pH-sensitivities obtained from the *parameter footprint* are summarised in table 8.3. In the sensitivity profiles, it can be seen that only the upper portions of the capacitance profiles shift with pH-value. No significant pH-sensitivity is observed for the lower portion. This two-fold behaviour is another verification of the model of inner and outer 2DEG, as the outer 2DEG is not exposed to electrolyte solution and thus not influenced by the pH-value. This behaviour is also an important indicator for the nature of the sensing mechanism. If the pH-value influences the entire measurement chain by the addition of a pH-dependent voltage fraction, the profiles would shift as a whole, i.e. the upper as well as the lower portion. As this is not the case, the sensing mechanism cannot be explained by the simple addition of a pH-dependent potential. In fact, the results show that the pH-value only influences the inner 2DEG, which can be achieved selectively by specific adsorption of charges at the surface. Thereby, the surface states of the heterostructure are modified, which in turn leads to a direct

Table 8.3: pH-sensitivity of U_{th_C}, U_{th_G} and N_s for a corroded AlGaN-EIHS ($B_{10}^{30}C_2$).

parameter	sensitivity S_{pH} (pH^{-1})	standard deviation SD	rel. imprecision c_v (pH)
U_{th_C} (mV)	-44.5 ± 3.8	2.9	0.07
U_{th_G} (mV)	-51.3 ± 4.3	3.2	0.06
N_s (10^9 cm^{-2})	-182.8 ± 8.1	6.2	0.03

manipulation of the electric field in the insulator and a pH-dependent depletion of only the inner 2DEG. The shift of surface potential can therefore be seen as a result of the modified electrical field, due to the specifically adsorbed charge. This confirms the central assumption of the site-dissociation model.

In a way, the depletion characteristic of the corroded sensor is the opposite of the pressure-induced intensified depletion discussed in section 7.2.2. The corrosion of the heterostructure depletes the inner 2DEG, resulting in a ratio $N_{s_o}/N_{s_i} > 1$. In this case, the pH-sensitivity can be determined very well by each of the three analysis methods (interpolation, inflection point and integration). Additionally, the outer 2DEG bottleneck is separated from the pH-sensitive depletion of the inner 2DEG. This wide separation may also be beneficial for the electrical characteristic of HEMT structures with regard to the impact of current collapse, for example.

With regard to the construction of a light-insensitive AlGaN-based pH-sensor, it can be found that the pH-sensitivity still exists and that it has a reasonable reproducibility. The values for the threshold voltages

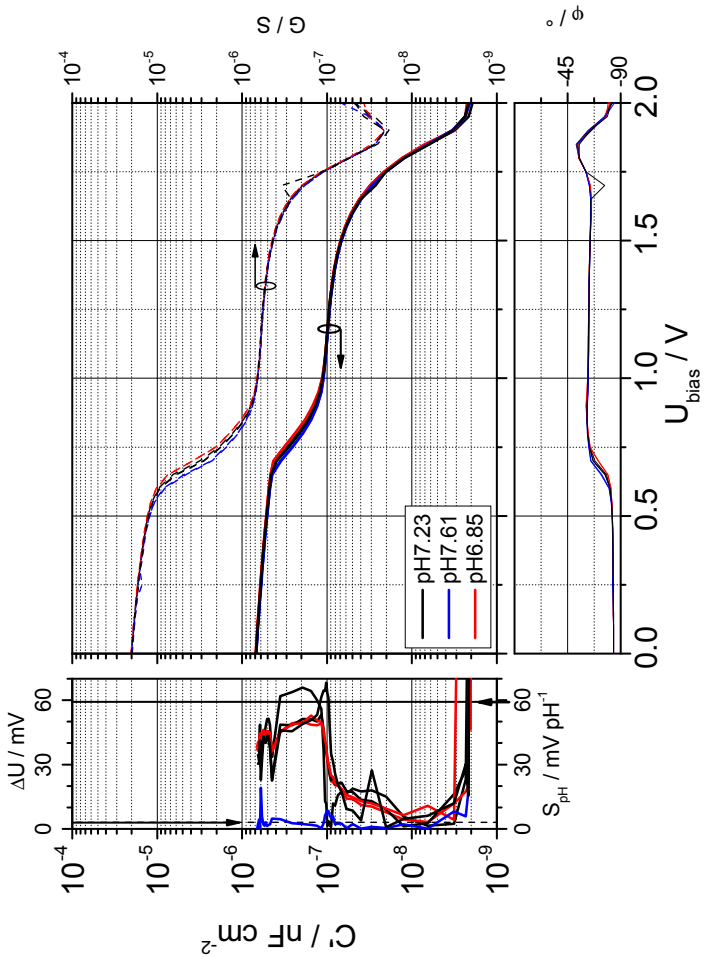

Figure 8.6: *Voltage profile* of a pH-sensitivity measurement series with a corroded AlGaN-EIHS ($B_{10}^{30}C_2$). Sensitivity profiles are referenced to pH7.63 (blue).

are within the typical range that was given in section 7.2.3. Nevertheless, only the relative imprecision of N_s is acceptable for very accurate and precise measurements.

8.1.3 Summary

In summary, the following results and conclusions were obtained from the investigations on the continuous violet illumination of the AlGaN-EIHS:

- In general, the violet light is unsuitable for continuous illumination, as it leads to a pronounced photoelectrochemical corrosion of the sensor surface even in neutral buffer solutions. It was confirmed that the corrosion drift primarily depends on the number of measurements and is independent of time. The typical drift slope per measurement is equivalent to a change of one pH-unit.

- In SEM images, the corrosion pits exhibited a diameter of (30–50) nm. A primarily vertical corrosion process was assumed, as the bottom of the corrosion pits could not be discerned and the lateral dimension did not increase with ongoing corrosion. A corrosion pit density of $1 \times 10^{10}\,\mathrm{cm}^{-2}$ was found.

- The corrosion process results in a splitting of the capacitance and conductance profiles into two depletion ranges, which were assigned to the inner and outer 2DEG. The double peak found in the phase angle profile is a good indicator for the corrosion state of the sensor.

- The characterisation of the corroded EIHS sensor verified that the upper and lower depletion portion of the capacitance profile

have to be assigned to the inner and outer 2DEG, respectively. The lower portion (outer 2DEG) exhibited the typical PPC characteristic, but no pH-sensitivity. For the upper portion (inner 2DEG), the light-sensitivity was greatly reduced, whereas a typical pH-sensitivity is still present.

- The reason for the reduced light-sensitivity of the inner 2DEG was suggested to be the compensation of surface states by the oxidation sub-step of the corrosion process. For the construction of light-insensitive AlGaN-based pH-sensors this behaviour might be exploited, with certain limitations.

8.2 Continuous Red Illumination

As the photoelectrochemical corrosion induced by violet illumination leads to a large signal drift and the destruction of the sensor chip within a few measurements, an alternative illumination is needed. A wavelength of 630 nm was chosen based on the results obtained by Kittler [16], which show that the relative change of the ISFET channel current upon darkening is smaller at this wavelength compared to (550–600) nm (fig. 4.5). The constant illumination is assumed to limit the drawn-out recombination characteristic of the PPC to a level above the 2DEG sheet carrier density in the dark. In section 8.2.2 it will be discussed whether a stable sensor signal is obtained earlier, compared to no illumination. Additionally, the pH-sensitivity under continuous red illumination is investigated. However, the impact of the red light on the corrosion process needs to be characterised beforehand, to verify that the light-induced corrosion drift is sufficiently low. This investigation is presented and discussed in the following section.

8.2.1 Photoelectrochemical Corrosion with Red Light

The *voltage profile* and *parameter footprint* of the measurement series with continuous red LED illumination is given in figures 8.7 and 8.8. Close to 1000 single impedance profiles were recorded and analysed, corresponding to a total measurement duration of nearly 100 h. As this measurement series had been performed on a different impedance analyser and the voltage range was reduced to (0–2) V, the time for a single profile was approximately 7 min. The DC current-voltage profile could not been recorded simultaneously. Nevertheless, this measurement series was chosen as it shows the prominent features of the photoelectrochemical corrosion with red light very well.

In the *voltage profile* (fig. 8.7) the initial dark voltage profiles (black) are given for comparison. The capacitance and conductance profiles have the typical enhancement and depletion features and the phase profile shows a single, symmetric peak. When the red LED is switched on, the profiles (red) shift parallel by 0.75 V towards higher bias voltages. From the capacitance and conductance profiles no skewing of the slope can be derived. The phase angle profile, however, shows a small decrease of the peak height ($-55°$ to $-57°$) and a slight broadening of the peak. Subsequent measurements up to a measurement count of 400 exhibit a small, parallel shift of all profiles back to lower bias voltages. The initially parallel shift is also reflected in the corresponding reproducibility profile. All reproducibility profiles have been calculated versus the initial profile under red light (red). With increasing measurement count the shift of the lowest part of the capacitance and conductance profiles comes to a halt and only the middle and upper parts drift continuously. The reproducibility profiles confirm this twofold behaviour of the capacitance profiles. In the phase angle pro-

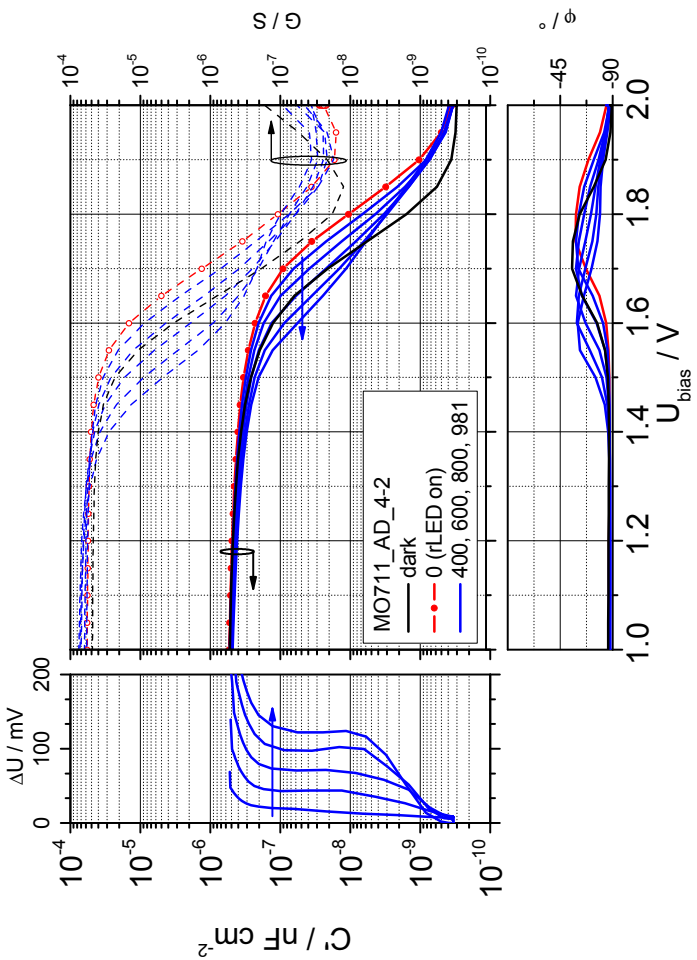

Figure 8.7: *Voltage profile* of a long-term measurement series with an AlGaN-EIHS ($B^{30}_{10}C_2$) continuously illuminated with red light. Reproducibility profiles are referenced to measurement count 0 (red circles).

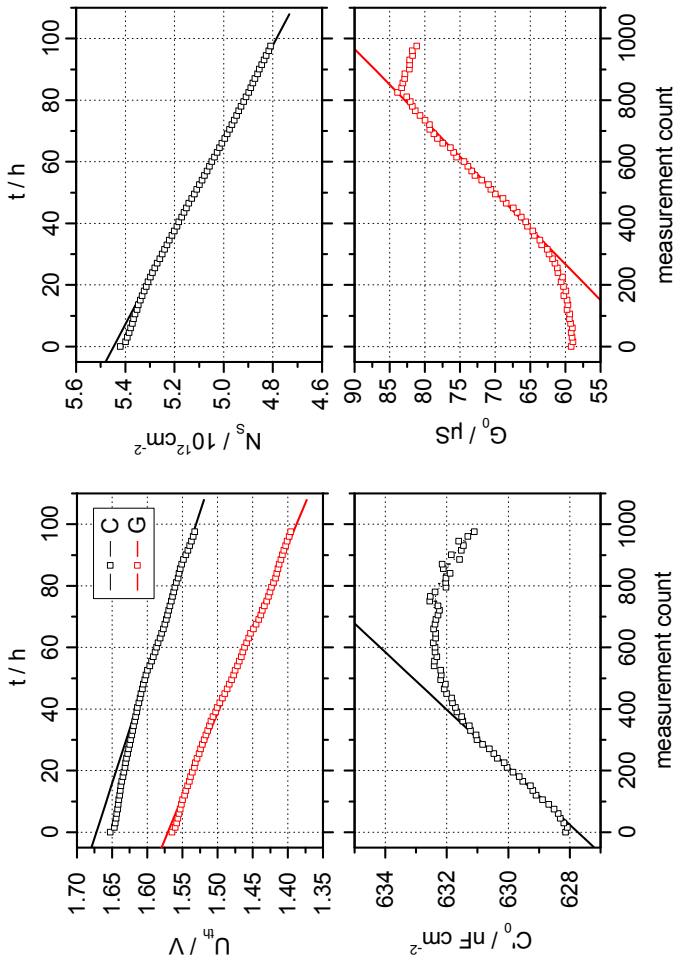

Figure 8.8: *Parameter footprint* of a long-term measurement series with an AlGaN-EIHS ($B_{10}^{30}C_2$) continuously illuminated with red light. Solid lines depict linear approximations.

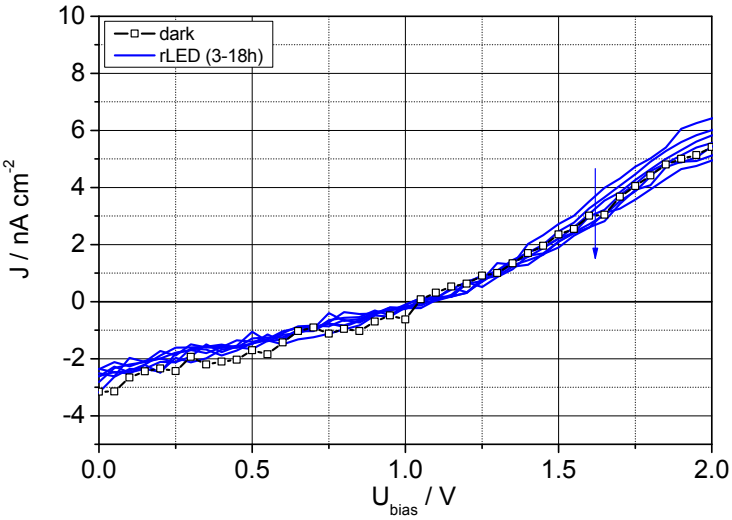

Figure 8.9: DC current density profiles of an EIHS sensor chip ($B_{10}^{30}C_2$) after prolonged darkening (black open circles) and with continuous red illumination (blue).

Table 8.4: Drift slopes of U_{th_C}, U_{th_G}, N_s, C_0' and G_0 for the photoelectrochemical corrosion of an AlGaN-EIHS ($B_{10}^{30}C_2$) with continuous red illumination.

parameter	drift (meas^{-1})
U_{th_C} (mV)	-0.14
U_{th_G} (mV)	-0.18
N_s (10^9 cm^{-2})	-0.66
C_0' ($\text{nF}\,\text{cm}^{-2}$)	0.01
G_0 (µS)	0.04

file, the peak shifts during the first 400 measurements and is split into two phase peaks afterwards. The primary peak is fixed at its initial location, but its height decreases by nearly 70% and the defined shape is lost. In contrast, the new secondary peak is shifted similarly to the profiles of the other parameters and it approximately maintains its height. Over the course of the last 600 measurements its height is reduced by less than 10%.

The *parameter footprint* (fig. 8.8) shows linear drift portions in all four parameters. Their approximated slopes are given in table 8.4. The threshold voltages and the sheet carrier concentration exhibit an overall linear decrease with a slightly lower slope for the first 200 measurements. The zero bias capacitance C_0' has a very small linear slope for the initial 400 measurements that increases the capacitance by less than 1%. After a plateau phase of approximately 200 measurements, C_0' decreases again with a marginal slope of $-0.005\,\text{nF}\,\text{cm}^{-2}\,\text{meas}^{-1}$. The principal behaviour of G_0 is similar to C_0', although the position of linear portion is shifted towards higher measurement count and the change of drift direction happens more abrupt. In separately recorded

current-voltage profiles (fig. 8.9) only a very small increase is observed when the illumination is switched on, which decreases subsequently with a very small slope.

The photoelectrochemical corrosion induced by red light is very small judging by the magnitude of the drift that is observed. From the comparison of table 8.4 and 7.2, it can be seen that the red light amplifies the drift by a factor of less than two. As the values of the dark drift already are within the resolution limit of the measurement equipment, this increase is either negligible or can be treated as a indication of a marginal trend. Effectively, the corrosion with incident red light is equal to the purely electrochemical corrosion. Nevertheless, the differences to the photoelectrochemical corrosion with violet light are discussed to gain insight into the general corrosion process and the factors that influence the stability of the AlGaN pH-sensor.

Despite the huge difference in the drift rates (cf. table 8.1), the corrosion with red light shows similar drift characteristics to the corrosion with violet light, albeit on a much larger time scale. For instance, the capacitance and conductance profiles exhibit a comparable two-fold drift behaviour. Their upper portion is shifted, whereas this is not observed for the lower portion, and the reproducibility profiles confirm that the upper portion is shifted parallel. However, for red light the upper portion is considerably larger compared to violet light and the lower portion is reduced to the very end of the transition range (cf. fig. 8.1). This difference also leads to the distinct change of the phase angle profiles. To explain this difference the surface morphology after corrosion needs to be considered.

High resolution SEM images of the corroded surface were taken after the measurement series (fig. 8.10). These images reveal broad and shallow corrosion pits and trenches. A pit density of $1 \times 10^{10}\,\mathrm{cm}^{-2}$ can be estimated. The recording of the images was hindered by pronounced charging artifacts, especially at very high resolutions.

The SEM images of the corroded surface after red illumination differ significantly from those after violet illumination. In contrast to the deep corrosion pits, much broader pits can found. Their depth is much smaller, as the bottom portion is clearly seen. This indicates that the vertical component of the corrosion process is minimised under these condition and only the lateral component remains. In order to determine the depth of the corrosion pits, AFM topography profiles of the surface were taken. A typical profile and the corresponding portion of the topography image are shown in figure 8.11. In contrast to the narrow corrosion pits after violet illumination, the broader pits and trenches after red illumination are clearly visible in the AFM topography image. Nevertheless, the true depth of these features cannot be derived from these measurements, as no two adjacent measurement point can be found at the bottom of the pits. This suggests that the lateral resolution of the AFM is insufficient for the high aspect ratio of the corrosion pits. Nevertheless, a minimum depth of more than 2 nm can be assumed. This rules out that only the GaN cap layer is attacked by the corrosion process.

The surface morphology after the corrosion process with red illumination can be explained as follows. In general, the current paths in the semiconductor dictate the spatial corrosion characteristic, as the corrosion is determined by the faradaic current at the semiconductor-electrolyte interface. For the electrochemical corrosion with no or only a marginal photoinduced component, the charges flow via the 2DEG

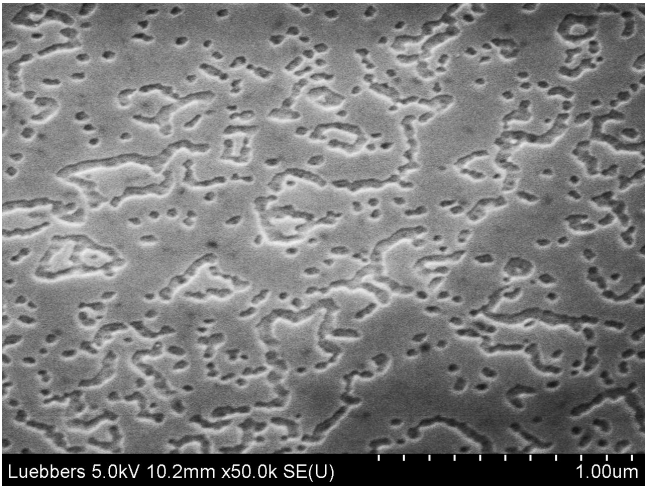

(a)

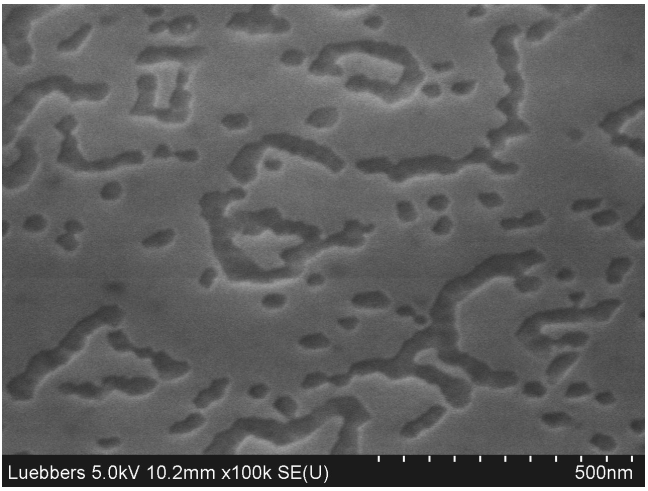

(b)

Figure 8.10: SEM images of an AlGaN-EIHS sensor chip ($B_{10}^{30}C_2$) after photoelectrochemical corrosion with red light.

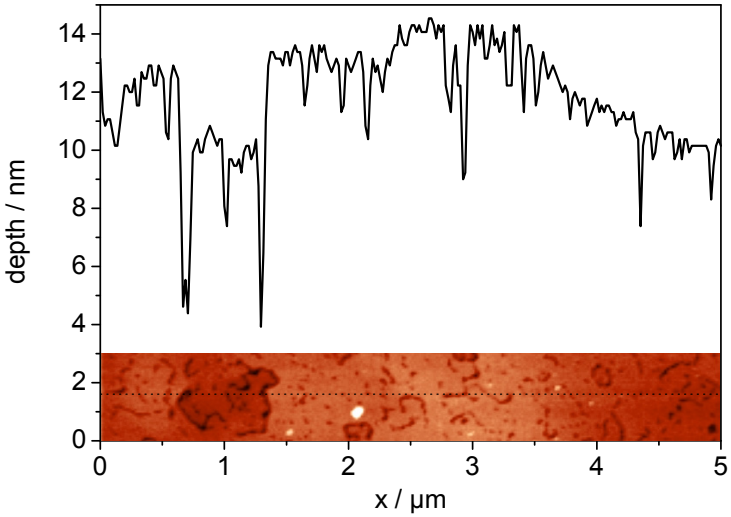

Figure 8.11: AFM Depth profile obtained after the photoelectrochemical corrosion with red light. The location of the profile is marked by the dashed line in the corresponding portion of the topography image.

and the dislocations towards the surface. For an uncorroded surface this is equivalent to a current flow that is mainly vertical to the heterostructure. Therefore a vertical corrosion of the dislocations occurs. However, when the vertical corrosion of the dislocations depletes the 2DEG down to a critical level, the preferred current paths in the vicinity of the dislocation are no longer vertical, but lateral towards the closest portion of sufficiently conducting 2DEG. This leads to a reduction of the vertical corrosion component and to an increase of the lateral component. The charging artifacts during SEM analysis and the low values of the DC current density confirm that the barrier layer is not removed completely in the corrosion pits. The vertical corrosion is therefore stopped or at least greatly reduced when the underlying 2DEG is depleted. This implies that the depth of the corrosion pits is smaller than the total insulator thickness of 12 nm.

The different surface morphology for the photoelectrochemical corrosion with violet light, is most likely due to the photoinduced generation of charge carriers. These are generated throughout the heterostructure, including the GaN bulk, and subsequently accumulated at the surface of the semiconductor. This accumulation is clearly seen in the very high leakage currents and their ongoing increase. Thereby, photoinduced charge carriers are always available for the corrosion process, even when the pits have penetrated the barrier layer and destroyed the corresponding part of the 2DEG channel. The vertical corrosion component is therefore always present under violet illumination.

Keeping the changes of surface morphology in mind, the impact of the corrosion process on the phase angle profile can be interpreted as follows. In previous consideration, the peak height was assigned to a pinch-off location of the 2DEG channel. A high peak was assigned to a pinch-off at the outer 2DEG. However, this interpretation is only valid

for a single peak. As the corrosion process results in a splitting of the phase angle peak, each peak already corresponds to either the inner or the outer 2DEG. Therefore, the interpretation of the peak height must be extended. A phase angle larger than $-45°$ signifies a dominant resistive characteristic, as ϕ is determined by the ratio of the capacitive and resistive portion of the investigated sample. For the AlGaN-EIHS, a dominant resistive characteristic corresponds to the pronounced decrease of the 2DEG conductance. If this conductance depletion happens earlier and faster than the general area depletion of the 2DEG the height of the phase angle is increased. This is the case when the 2DEG channel is pinched-off at some critical location, even though most part of the 2DEG is still enhanced with charge carriers. For the uncorroded EIHS sensor chip this critical location is the transition between the inner and the outer 2DEG. Therefore, the connection between an increased peak height and the pinch-off at the outer 2DEG is valid. For the corroded EIHS sensor chip, however, the corrosion pits become critical pinch-off locations, due to the partial depletion of the underlying 2DEG portions. Due to the homogenous distribution of dislocation pits and corresponding pinch-off locations, the conductance depletion is much more pronounced and a high phase angle peak is found for the inner 2DEG. In contrast, the peak height of the outer 2DEG is reduced, as its influence on the conductance depletion becomes marginal.

For the photoelectrochemical corrosion with violet light, an opposite behaviour is observed. The phase angle peak assigned to the inner 2DEG decreases with ongoing corrosion. This indicates that the corrosion pits have thinned the barrier to a certain level and the underlying 2DEG is depleted completely. Subsequently, the dominance of the conductance depletion decreases for the inner 2DEG and the peak height is

reduced. The high phase angle peak for the outer 2DEG signifies that the conductance depletion is primarily determined here. In summary, the phase angle peak height can be taken as an qualitative indicator for the dominance of the 2DEG conductance depletion.

A prominent influence of the illumination wavelength is also found for the DC current density. The violet light induces a large photocurrent, whereas no increase of J can be found upon incident red light. This difference can be an indicator for the spatial location of the excited defects. Photoinduced electron-hole pairs that are generated in the AlGaN barrier are separated by internal electrical field and the electrons and holes accumulate in the 2DEG and at the semiconductor-electrolyte interface, respectively. The positive charge at the surface results in a faradaic compensation current from the electrolyte and an overall increase of J. However, if electron-hole pairs are generated in the GaN bulk layer the polarisation field will draw the holes towards the substrate and the electrons into the 2DEG. The charging state of the surface is not influenced and therefore the J is unchanged. Applying these considerations to the measured DC current density profiles (fig. 8.3 and 8.9), they imply that the photon energy of the red light (2.0 eV) does not generate charges in the AlGaN barrier layer, in contrast to the violet light with its higher photon energy (3.1 eV). Regarding the corresponding defects, the defects in the AlGaN layer seem to be located more than 2.0 eV below the conduction band. The observation that the red light does induce an increase of N_s, but not of J, implies that its energy is sufficient to generate charge carriers in the GaN bulk. Another possible factor is the large difference in the thickness of the AlGaN barrier layer and the GaN bulk. Assuming that the only difference between the red and violet light is the amount of photoinduced charge, the total amount of charge that is induced by

the red light in the very thin AlGaN layer might not be sufficient to increase J, but in the thick GaN bulk sufficient charge is generated that results in an increase of N_s.

8.2.2 Characterisation of Light- and pH-Sensitivity

As the corrosion drift was confirmed to be very low, the continuous red illumination of the sensor chip can now be analysed with regard to its actual purpose - the improvement of the PPC characteristic. Subsequently, it is investigated whether the pH-sensitivity is influenced by the continuous red illumination.

Light-Sensitivity and PPC

A common fluorescent desk lamp was used for ambient illumination from the front side, passing through the transparent PC cover plate and the sample solution. Continuous backside illumination is performed using a red LED, which mounted into the measurement setup (cf. fig. 5.4). The ambient illumination does not directly influence the outer 2DEG, as it is covered by the sealing ring and the measurement cell. However, an indirect influence from stray light that is reflected at the back of the unpolished sapphire substrate is probable.

The *parameter footprint* shown in figure 8.12 demonstrates the different decay characteristics when the ambient frontside illumination is switched off. The black traces reflect the decay without continuous illumination and the red traces reflect the decay with continuous red backside illumination. A typical PPC characteristic is obtained when switching to no illumination, with a drawn-out decay of U_{thC}, U_{thG} and N_s. Both C_0' and G_0 are not affected. For the constant illumination with red light pronounced differences are observed. The initial decay

of U_{th_C}, U_{th_G} and N_s is approximately equal, but it settles earlier and at a higher level compared no illumination. For U_{th_C} and U_{th_G} a short constant plateau is found around (2–3) h and N_s increases slightly in this time frame. After 5 h all three parameters pass over into a linear decrease. A rather pronounced initial drift is found for C_0' and G_0. Both parameter settle to a small linear drift after 5 h. The magnitude of C_0' under red light is similar to no illumination, whereas G_0 is slightly higher.

In figure 8.13 the derivatives of U_{th_C} and N_s are plotted versus time after switching off the ambient illumination, to determine the slope of the drift versus time. For both parameters the drift slope decreases significantly faster with constant red illumination. Especially within the first two hours this decrease is very pronounced, leading to a very small drift of U_{th_C} and even a positive drift of N_s (indicated by the black triangles). Up to a measurement time of 6 h the magnitude increase again, settling at $2\,\mathrm{mV\,h^{-1}}$ for U_{th_C} and at about $6 \times 10^9\,\mathrm{cm^{-2}\,h^{-1}}$ for C_0'. After more than 8 h, the drift magnitude with and without backside illumination are approximately equal. However, it can be noted that the noise level is slightly higher when the red LED is used.

The initial drift of C_0' and G_0 may be linked to differences in the outer and inner 2DEG. The inner 2DEG is influenced by the ambient and the continuous red illumination, whereas the outer 2DEG is only influenced by the latter. When the ambient illumination is switched off, compensation effects between the different sheet carrier densities in inner and outer 2DEG (N_{s_i} and N_{s_o}) may induce the observed drift. The different values of N_{s_i} and N_{s_o} were also found to be reflected in the height of the phase angle peak (not shown). It is increased during ambient illumination, indicating that G depletes earlier than C, and decreases when switching to no or red illumination. This demonstrates

that not only pressure applied to the outer 2DEG (cf. section 7.2.2) or the passiviation layer can result in a ratio $N_{s_o}/N_{s_i} < 1$, but also selective enhancement of the inner 2DEG by illumination. Therefore care must also be taken when establishing the illumination conditions of the sensor device. This includes that the passivation layer has to be sufficiently transparent in the case of front side illumination. In general, back side illumination is preferable as both portions of the 2DEG will be influenced to the same extent.

The desired impact of the continuous red illumination is confirmed by figure 8.13. The drift slope becomes stable within the first 3 h compared to 8 h without continuous illumination. Although the initial decrease is unchanged, the recombination of the charge carriers that were photo-induced by the ambient illumination is limited effectively. Thus, the red illumination is favourable when the light-drift duration needs to be minimised, for example when the sensor device is exchanged and subjected to ambient illumination repeatedly. This light source was also chosen to establish a light barrier directly through the sensor chip for the detection of air bubbles in the micro blood-pH analyser, as described in section 9.2. The trade-off is a slightly increased noise level compared to no illumination. This increase can be expected, as the continuous illumination is a disturbance of the equilibrium within the semiconductor and at the semiconductor-electrolyte interface, in addition to the applied bias voltage. As a consequence, a less stable quasi-equilibrium and an increased noise level are obtained, even when the illumination conditions are kept constant.

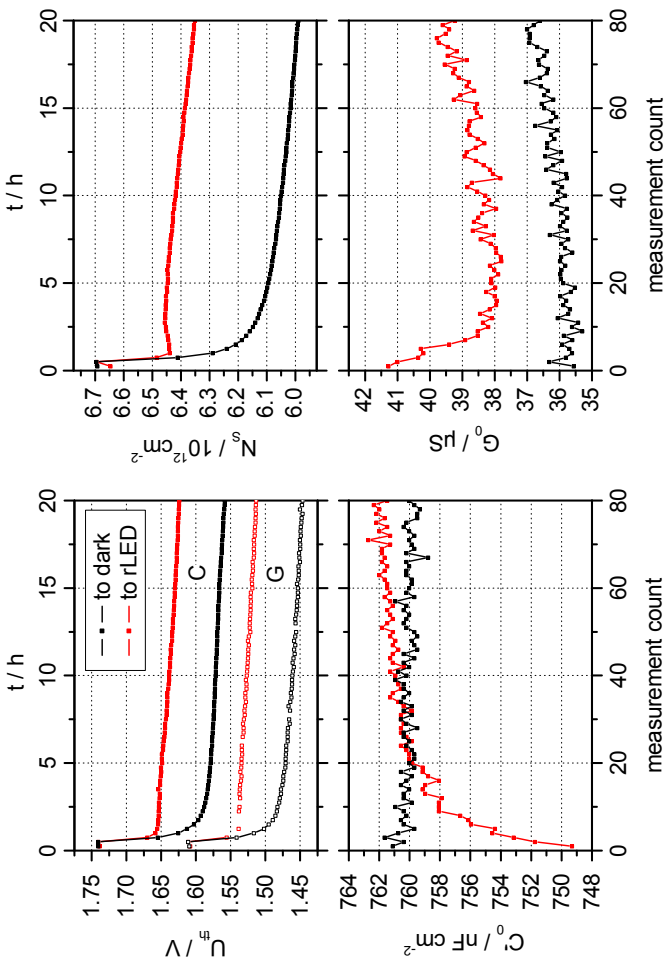

Figure 8.12: *Parameter footprint* of an AlGaN-EIHS ($B_{10}^{30}C_2$) after switching off the ambient illumination, without continuous illumination (black) and with continuous red illumination (red).

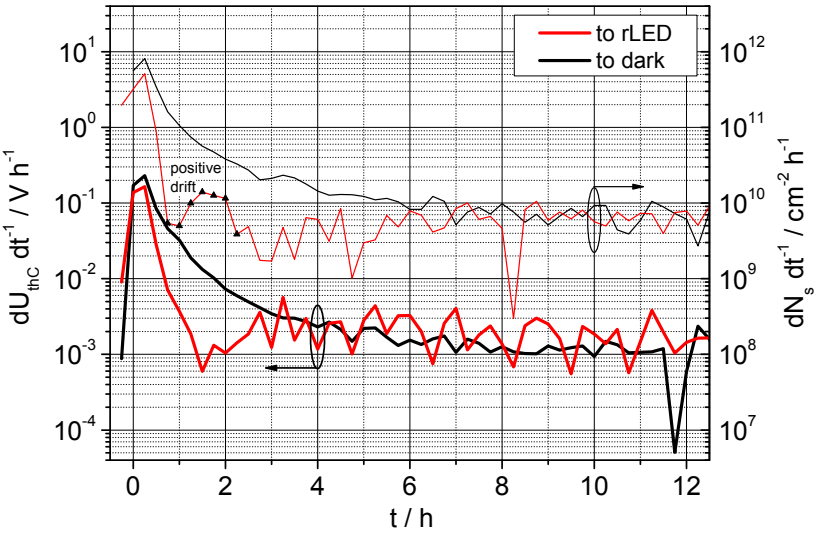

Figure 8.13: Plot of the derivatives of U_{th_C} and N_s versus time after switching off the ambient illumination, without continuous illumination (black) and with continuous red illumination (red).

Table 8.5: pH-sensitivity of U_{th_C}, U_{th_G} and N_s for an AlGaN-EIHS ($B_{10}^{30}C_2$) with continuous red illumination.

parameter	sensitivity S_{pH} (pH^{-1})	deviation deviation SD	rel. imprecision c_v (pH)
U_{th_C} (mV)	-50.7 ± 3.6	2.8	0.06
U_{th_G} (mV)	-47.9 ± 5.2	3.2	0.07
N_s (10^9 cm^{-2})	-202.2 ± 3.2	2.5	0.01

pH-sensitivity

The pH-sensitivity under continuous red illumination was determined using the standard measurement cycle at 10 Hz. The pH-sensitivities of U_{th_C}, U_{th_G} and N_s are given in the table 8.5. Compared to the ideal results obtained without illumination (table 7.3) the slopes are slightly lower and a larger uncertainty is found.

From repeated determination of pH-sensitivity under continuous red illumination it can be verified that the mean pH-sensitivity and the standard deviation is effectively equal to no illumination. Figure 8.14 depicts the pH-sensitivities (U_{th_C}) obtained over the course of this work versus the illumination conditions and the type of sealing ring. It can clearly be observed that the type of sealing ring has the biggest impact on the pH-sensitivity, due to the pressure-induced depletion of the outer 2DEG. In contrast, no significant difference is found for the different illumination conditions. The mean pH-sensitivities were determined to be 48.1 mV pH^{-1} ($SD = 5.8$ mV pH^{-1}) and 49.6 mV pH^{-1} ($SD = 4.1$ mV pH^{-1}) for no illumination and continuous red illumination, respectively.

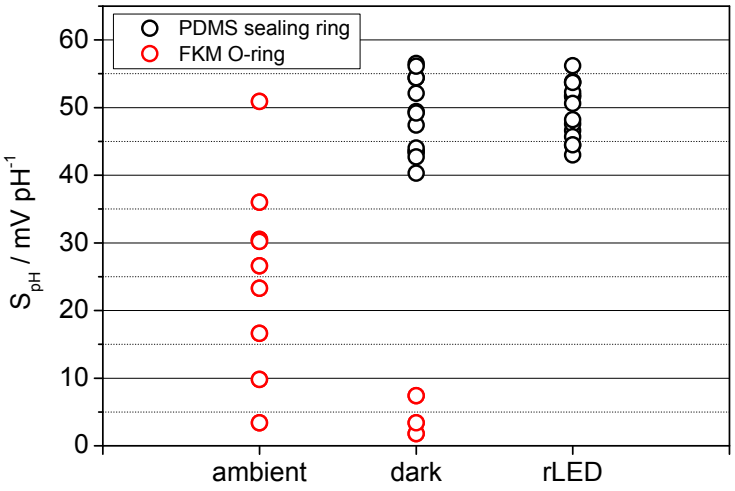

Figure 8.14: Comparison of pH-sensitivity (U_{th_C}) with regard to the employed sealing ring and illumination conditions.

8.2.3 Summary

The results and conclusions obtained for the continuous illumination with red light can be summarised as follows:

- The photoelectrochemical corrosion with red light is very low. Compared to the electrochemical corrosion without illumination, it is only marginally higher. In contrast to violet light, no appreciable photocurrent is induced.

- The surface morphology after long-term corrosion with red light revealed that the lateral corrosion component prevails and relatively shallow pits can be found. It was suggested that the vertical component is reduced by the depletion of the 2DEG below the corrosion pits. The depth of the corrosion pits was estimated to be larger than the GaN cap layer, but smaller than the total insulator thickness.

- In general, the height of the phase angle peak is a qualitative indicator for the dominance of the 2DEG conductance depletion. This interpretation can also be applied separately to the depletion of the inner and outer 2DEG.

- The continuous illumination with a red LED ($\lambda = 630\,\mathrm{nm}$) reduces the PPC decay duration to 3 h. After this time a constant drift level of $2\,\mathrm{mV\,h^{-1}}$ for U_{th_C} and $6 \times 10^9\,\mathrm{cm^{-2}\,h^{-1}}$ for N_s are obtained. An increased noise level was found, compared to no illumination.

- The pH-sensitivity under continuous red illumination typically amounted to about $50\,\mathrm{mV\,pH^{-1}}$. It is practically equal to the sensitivity obtained without illumination.

The continuous red illumination is used as a standard condition for subsequent characterisations, mainly because the targeted application needs to include an optical air bubble detection to optimise the filling procedure for very small sample volumes. For practical purposes the shorter stabilisation duration is beneficial. Especially when several different sensor chips need to be characterised, the setup time is greatly reduced. This commonly outweighs the small disadvantage of higher noise. However, if it is possible to shield the sensor chip from any illumination and a stabilisation duration of more than 12 h is acceptable, the completely darkened configuration should be favoured.

8.3 Increased cap layer thickness

The increase of the cap layer thickness was the first step that was taken for the optimisation of the AlGaN/GaN heterostructure. This way the chemical stability of the sensor chip is increased, as GaN is more stable than AlGaN. Another advantage is that the crystal quality of the GaN cap layer is enhanced and that a closed, homogeneous layer can be achieved. It is assumed that the commonly employed thin cap layer (2 nm) does not form a closed layer and that a non-stoichiometric $Al_xGa_yO_zN$ layer is present at the surface. With a cap layer thickness of 10 nm the fraction of residual aluminium at the surface is reduced and the surface oxide will primarily contain gallium.

The properties of an EIHS sensor chip with a 10 nm $Al_{0.3}Ga_{0.7}N$ barrier and a 10 nm GaN cap layer (abbreviated: $B_{10}^{30}C_{10}$) have been characterised with regard to photoelectrochemical corrosion and pH-sensitivity using electrochemical impedance-voltage profiling. The standard measurement cycle with continuous red illumination is employed for the pH-sensitivity and the photoelectrochemical corrosion is mea-

Table 8.6: Drift slopes of U_{th_C}, U_{th_G}, N_s, C_0' and G_0 for the photoelectrochemical corrosion with violet illumination of an AlGaN-EIHS with increased cap layer thickness ($B_{10}^{30}C_{10}$).

parameter	drift (meas^{-1})
U_{th_C} (mV)	−8.1
U_{th_G} (mV)	−5.1
N_s (10^9 cm^{-2})	−12.2
C_0' (nF cm^{-2})	2.4
G_0 (µS)	−0.3

sured under violet illumination. All results are compared to the $B_{10}^{30}C_2$ heterostructure under the same conditions.

8.3.1 Photoelectrochemical Corrosion

The chemical stability of the sensor chip is the primary property that is assumed to be enhanced by the increased cap layer thickness. In principle, the obtained capacitance and conductance profiles (not shown) are very similar to the profiles of the $B_{10}^{30}C_2$ heterostructure. They revealed the previously discussed corrosion behaviour, including the development of a two-fold depletion in the capacitance and conductance profiles and the splitting of the phase angle peak. The drift slopes derived for U_{th_C}, U_{th_G}, N_s, C_0' and G_0 are given in table 8.6. They reveal a decrease of more than 80% for the threshold voltages and of more than 90% for N_s. The corrosion drift of C_0' and G_0 is reduced by 70%. The DC current density profiles exhibit the same large photocurrent that was previously observed for the 2 nm cap layer.

In figure 8.15, SEM images of the corroded surface of the $B_{10}^{30}C_{10}$ heterostructure are shown. A significant reduction of the dislocation

density to a value of about $2.5 \times 10^9\,\mathrm{cm}^{-2}$ is found. The corrosion pits have a diameter of (30–50) nm and exhibit a large contrast. The bottom of the pits cannot be determined and no pronounced charging artifacts were observed during the recording of the images.

The pronounced reduction of the drift of all investigated parameter suggests that the chemical stability of the surface is indeed enhanced, compared to the 2 nm cap layer. Qualitatively, the corrosion mechanism is still the same, but the magnitude is much smaller. This decrease is mainly due to the reduced density of the dislocations, which are the primary target of the corrosion process. From the SEM images, it can be verified that the dislocation density has decreased by about 80%, compared to the $B_{10}^{30}C_2$ heterostructure. This suggests that the dislocation density is directly proportional to the drift slopes, as their relative reduction is approximately equal. The narrow and deep shape of the dislocation pits confirms that the vertical corrosion component also dominates for the 10 nm cap layer.

The reduced dislocation density might be explained by the reduction of relaxation processes in the barrier layer. Effectively, the AlGaN barrier may clamped by the GaN bulk and cap layer and the thicker cap layer inhibits the relaxation of the barrier layer. This would result in fewer dislocations, assuming that the relaxation of the barrier layer is responsible for the increased dislocation density after the fabrication process.

8.3.2 Characterisation of pH-Sensitivity

In the pH-sensitivity measurement series under red illumination, the shape of the capacitance and conductance profiles (not shown) exhibited no distinct differences to the $B_{10}^{30}C_2$ heterostructure. Only a lower

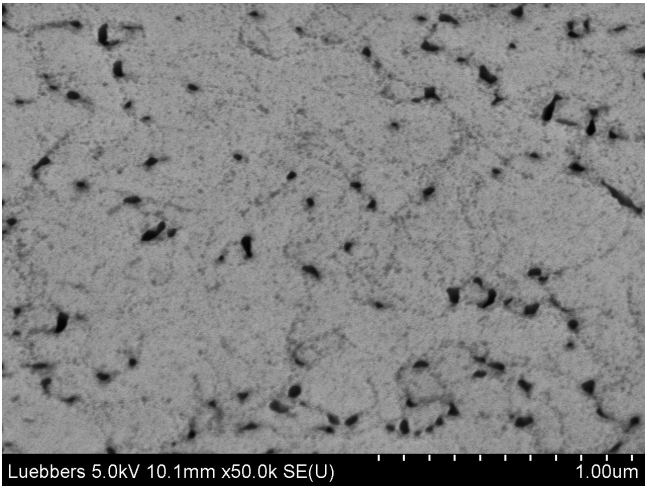

(a)

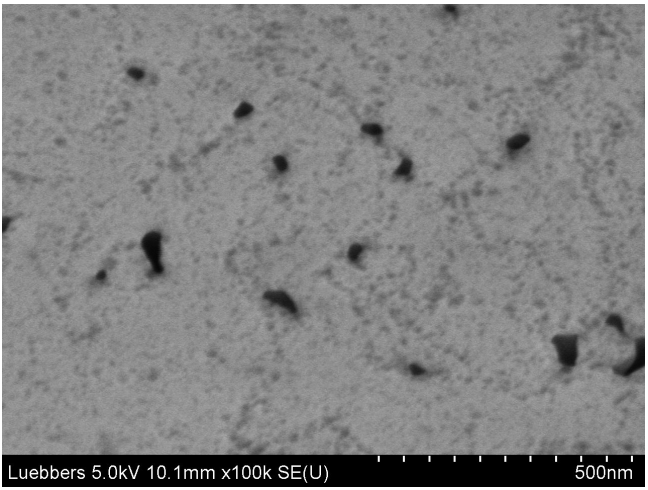

(b)

Figure 8.15: SEM images of an AlGaN-EIHS sensor chip with increased cap layer thickness ($B_{10}^{30}C_{10}$) after photoelectrochemical corrosion with violet light.

capacitance in the enhancement range and a slightly smaller transition slope is found. From the sensitivity profiles a high, nearly ideal sensitivity of $(58 \pm 2)\,\mathrm{mV\,pH^{-1}}$ is derived, which is relatively constant for the whole capacitance range. The absolute values of U_{th_C}, U_{th_G}, N_s, C_0' and G_0 were found to be decreased to a certain extent for the increased cap layer thickness. While U_{th_C} and U_{th_G} are only decreased by 100 mV, the sheet charge density N_s and the zero bias capacitance C_0' are reduced by one third. The magnitude of G_0 is only slightly lower.

The increased cap layer thickness primarly increases the distance between the sensor surface and the 2DEG, which is reflected by the lower value of C_0'. Using equation 5.6 a total insulator thickness of approximately 18 nm is calculated, assuming that the cap and barrier layer exhibit equal dielectric properties. The deviation to the targeted thickness of 20 nm may be due to differences between the cap and barrier layer properties or the opposing electrical fields in the layers, both of which are not taken into account by the simple thickness calculation. Another possible explanation is that the thickness of the cap layer has not reached 10 nm during the growth procedure, as no in-situ monitoring of the actual thickness is possible. The determination of the layer thickness after growth with high-resolution x-ray diffraction fails for the $B_{10}^{30}C_{10}$ heterostructure, due to the similar material properties and thicknesses of the cap and barrier layers.

The small decrease of the absolute value of U_{th_C} shows that the surface potential is not influenced to a great extent by the increase of the cap layer thickness. Photoreflectance measurements on GaN/AlGaN/GaN heterostructures published by Buchheim [119] reveal the same behaviour. For a variation of GaN cap layer thickness between 1 and 5 nm only a small, but not significant, increase of the surface potential was

Table 8.7: pH-sensitivity of U_{th_C}, U_{th_G} and N_s for an AlGaN-EIHS with an increased cap layer thickness ($B_{10}^{30}C_{10}$).

parameter	sensitivity S_{pH} (pH^{-1})	deviation deviation SD	rel. imprecision c_v (pH)
U_{th_C} (mV)	-54.1 ± 3.5	2.7	0.05
U_{th_G} (mV)	-52.5 ± 4.4	4.0	0.08
N_s (10^9 cm^{-2})	-158.8 ± 2.9	2.9	0.02

found. This increase corresponds to a slightly lower threshold voltage, as observed for U_{th_C}. The combined decrease of C_0' and U_{th_C} result in the observed decrease of N_s. The relative decrease of N_s (-66%) is approximately the sum of the relative changes of C_0' (-63%) and U_{th_C} (-5%). This is expected as N_s is estimated by integration of $C'(U_{bias})$ (eqn. 5.5). The slightly lower value of G_0 is not significant, especially when considering the multitude of influences on this parameter. Nevertheless, a reduced sheet charge density will inevitably lead to a decrease of the 2DEG conductance, which affects G_0.

The pH-sensitivities extracted from the linear slopes of U_{th_C}, U_{th_G} and N_s are given in table 8.7. The sensitivity of U_{th_C} and U_{th_G} are comparable to the mean pH-sensitivity obtained for the $B_{10}^{30}C_2$. In contrast, the pH-sensitivity of N_s is reduced to about $150 \times 10^9\,\mathrm{cm}^{-2}\,\mathrm{pH}^{-1}$, which is a significant reduction compared to the EIHS with a 2 nm cap layer. The significant decrease of the pH-sensitivity of N_s is linked to the increase of the total insulator thickness. This was verified by impedance-voltage profiles of a heterostructure with a 20 nm $Al_{0.3}Ga_{0.7}N$ barrier and no cap layer (abbreviated: $B_{20}^{30}C_0$), which has the same dis-

tance between the 2DEG and the surface. For this $B_{20}^{30}C_0$ heterostructure, a comparable sensitivity of $146 \times 10^9\,\mathrm{cm}^{-2}\,\mathrm{pH}^{-1}$ was found. This suggests that field effect between the surface potential and the 2DEG sheet charge density is attenuated by the increased total insulator thickness. The decreased sensitivity of N_s is also confirmed by simulation result shown in figure 8.16. The simulation was performed using BIOnextnano^3 [217], employing the model given in figure 4.12 with a AlGaN barrier thickness of 10 nm and GaN cap layer thicknesses of 2 and 10 nm. The pH-sensitivity of the N_s was calculated and the simulated slopes of N_s were shifted onto the measured values at pH7.25. It was found that the simulated absolute values were significantly higher compared to the measured ones. Presumably, this deviation is due to the limitations of the simulation model, especially its only one-dimensional approach. Nevertheless, the slopes of the simulated and measured sensitivities agree very well, demonstrating that the reduced slope of N_s can indeed be explained by the previous consideration.

From the pH-sensitivity $dN_s dpH^{-1}$, the drain current pH-sensitivity $dI_d dpH^{-1}$ can be estimated for an ISFET fabricated from the same heterostructure, using equation 7.2. A value of $(140 \pm 3)\,\mu\mathrm{A}\,\mathrm{pH}^{-1}$ is obtained for $U_{ds} = 0.5\,\mathrm{V}$ and $W/L = 10$. In section 9.4, it will be investigated whether this value compares well to the measured pH-sensitivity of ISFET sensors.

8.3.3 Summary

Summarising, the following results and conclusions were obtained for the increase of GaN cap layer thickness to 10 nm:

- The stability of the sensor surface to photoelectrochemical corrosion with violet light is increased. The corresponding drift of

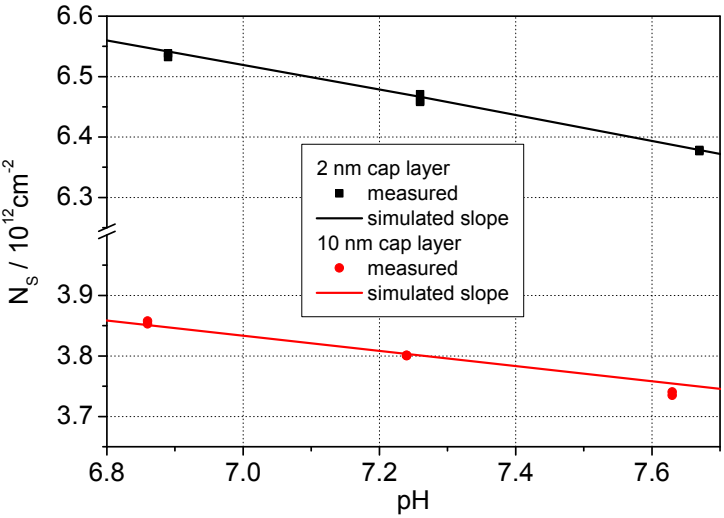

Figure 8.16: Comparison of the measured and simulated pH-sensitivity of the sheet carrier concentration N_s for a $GaN/Al_{0.3}Ga_{0.7}N/GaN$ heterostructure with 2 nm and 10 nm cap layer thickness.

the investigated parameters is reduced by (70–90) %, due to a decrease of the dislocation density by 80%. The proportionality of corrosion drift and dislocation density verifies that the corrosion process is mainly determined by the structural quality of the cap and barrier layer.

- The decreased dislocation density is assumed to be due to the clamping of the AlGaN barrier and the resulting reduction of relaxation processes.

- The pH-sensitivity of the surface potential, which is reflected in U_{th_C} and U_{th_G}, is not affected by the increased cap layer thickness.

- Due to a decreased field effect, the pH-sensitivity of N_s is reduced. The corresponding drain current pH-sensitivity of an ISFET based on the $B_{10}^{30}C_{10}$ has been calculated

In conclusion, the increase of the cap layer thickness was found to be an advantageous optimisation step to increase the corrosion resistance of the AlGaN-EIHS. Except for the slight decrease of the field effect, all other electrical properties are comparable to the $B_{10}^{30}C_2$ heterostructure. The total insulator thickness is still very small (20 nm) compared to Si-based ISFET devices (>100 nm) and the excellent sensitivity to changes of the surface potential is retained. Therefore, the $B_{10}^{30}C_{10}$ structure has been adopted as the new standard heterostructure, not only for the measurement of pH-value, but also for other applications. In this context, an increased yield and reliability of sensor devices with this heterostructure layout was observed.

8.4 Reduced Al-content in the Barrier Layer

From the preceding investigation of the increased cap layer thickness it becomes clear that the structural defects at the sensor surface are the weakest link with regard to corrosion resistance. Another likely source for an increased dislocation density in the heterostructure is the tensile stress in the AlGaN barrier, which is proportional to the Al-content. It was suggested that the high temperature annealing step amplifies the mechanical stress in the layers, in general, and the tensile stress in the barrier, in particular. The reduction of the Al-content to 20% was investigated as a measure to avoid this degradation of layer quality and the corresponding increase of dislocation density. The trade-off for the strain relaxation is the reduction of N_s and a possible loss of carrier confinement in the 2DEG [110]. However, the decrease of N_s will also lead to a decrease of the threshold voltages, which is favourable for less electrochemical corrosion. In addition, less electrostatic stress will have to be applied to the passivation layer of an ISFET sensor and to living cells, when used as a biosensor.

The reduction of the Al-content is performed in addition to the previously described optimisation steps: the 10 nm $Al_{0.2}Ga_{0.8}N$ barrier layer is followed by a 10 nm cap layer (abbreviated: $B_{10}^{20}C_{10}$) and the fabricated sensor chip is kept under continuous red illumination for the measurement of pH-sensitivity. Due to the lower threshold voltage the applied bias range could be reduced to (0–1.5) V resulting in a measurement duration of 10 min for a single impedance profile.

8.4.1 Photoelectrochemical Corrosion

The drift slopes that are summarised in table 8.8 clearly reveal that the photoelectrochemical corrosion is nearly stopped for the $B_{10}^{20}C_{10}$

Table 8.8: Drift slopes of U_{th_C}, U_{th_G}, N_s, C'_0 and G_0 for the photoelectrochemical corrosion with violet illumination of an AlGaN-EIHS with reduced barrier layer Al-content and increased cap layer thickness ($B^{20}_{10}C_{10}$).

parameter	drift (meas^{-1}) up to 150 meas	drift (meas^{-1}) after more than 200 meas
U_{th_C} (mV)	0.5	−1.0
U_{th_G} (mV)	−0.05	0.1
N_s (10^9 cm^{-2})	1.0	1.3
C'_0 ($\text{nF}\,\text{cm}^{-2}$)	0.5	0.8
G_0 (µS)	0.1	−0.1

heterostructure. During the first 150 measurements with continuous violet illumination the drift is very low and the signal stability is only determined by the measurement noise level. The drift is positive for U_{th_C} and G_0 and negative for U_{th_G}. For subsequent measurements, the direction is inverted for these parameters. In contrast, the drift of N_s and C'_0 is positive throughout the entire measurement series. After more than 200 measurements, the slopes are increased, but still amount to only less than 2% of the corrosion drift that was found for the $B^{30}_{10}C_2$.

For the DC current density, the photo-induced increase is very small for the first 100 measurements. The maximum current density amounts to $100\,\text{nA}\,\text{cm}^{-2}$. After 200 measurements an increase to $200\,\text{nA}\,\text{cm}^{-2}$ is observed and in the subsequent 100 measurement the current density increases to $1.2\,\mu\text{A}\,\text{cm}^{-2}$. SEM images taken after the photoelectrochemical corrosion process show that very few, but relatively large, corrosion pits can be found. Diameters of up to 100 nm are found and a density of $1 \times 10^9\,\text{cm}^{-2}$ can be estimated.

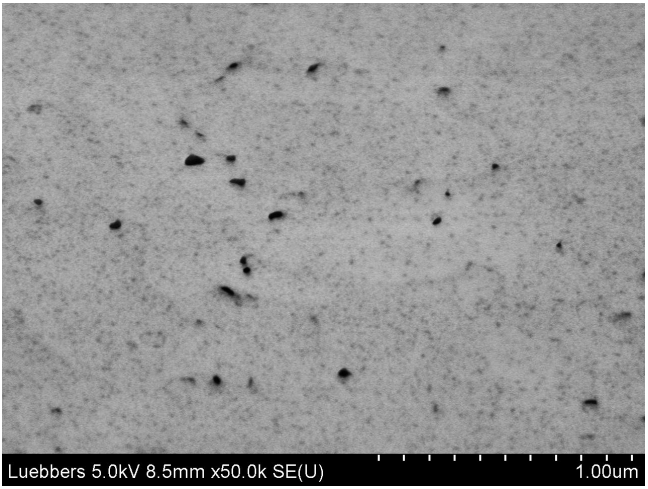

(a)

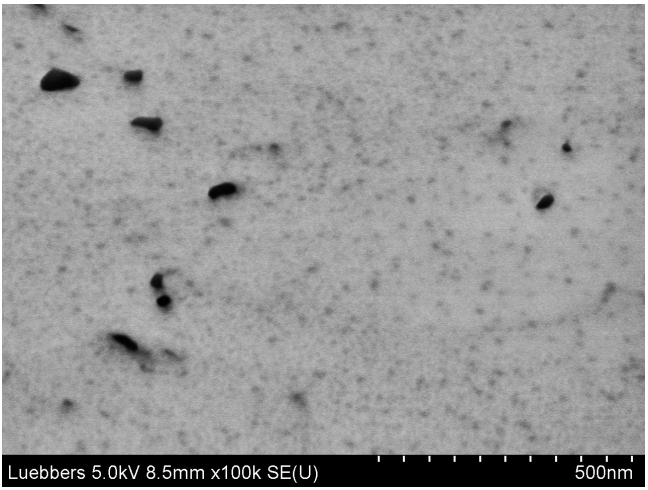

(b)

Figure 8.17: SEM images of an AlGaN-EIHS sensor chip with reduced barrier layer Al-content and increased cap layer thickness ($B_{10}^{20}C_{10}$) after photoelectrochemical corrosion with violet light.

The drift slopes reveal that the photoelectrochemical corrosion under violet illumination is nearly stopped for the $B_{10}^{20}C_{10}$ heterostructure. This enhancement of chemical stability is mainly assigned to two factors: the reduction of the dislocation density and the lower applied bias voltage. The reason for the first factor can be attributed to the reduction of tensile strain in the barrier layer. It is assumed that the smaller lattice mismatch of $Al_{0.2}Ga_{0.8}N$ to GaN is responsible for this reduction and that the relaxation of the barrier layer is less pronounced. The lower applied bias voltage, however, also needs to be taken into account, as it contributes to the electrical field strength in barrier. Thereby, the field strength does not reach the magnitude that is present for higher Al-content, where both the piezoelectric polarisation and the bias voltage are higher. The SEM images clearly show that the corrosion pit density is much lower, but also that the pits are larger. Their increased size allows for relatively high DC currents, even though their density is decreased and the bias voltage is lower. Eventually, the DC current density reaches the same magnitude that was found for the $B_{10}^{30}C_2$ heterostructure, but only after a very long measurement duration.

8.4.2 Characterisation of pH-Sensitivity

In the pH-sensitivity measurement series, capacitance and conductance profiles are found that are qualitatively similar to the $B_{10}^{30}C_{10}$ heterostructure, except for a large voltage shift of 1 V towards lower bias voltages values when the Al-content is reduced to 20%. The transition range in the capacitance profile is slightly steeper and the phase peak is increased accordingly. The sensitivity profiles yield a pH-sensitivity of $(52 \pm 2)\,\mathrm{mV\,pH^{-1}}$ with a marginally better reproducibility. The absolute values of U_{th_C} and N_s are reduced to 33% compared to an Al-

Table 8.9: pH-sensitivity of U_{th_C}, U_{th_G} and N_s for an AlGaN-EIHS with reduced barrier layer Al-content and increased cap layer thickness ($B_{10}^{20}C_{10}$).

parameter	sensitivity S_{pH} (pH^{-1})	deviation deviation SD	rel. imprecision c_v (pH)
U_{th_C} (mV)	-52.4 ± 2.3	1.8	0.03
U_{th_G} (mV)	-46.3 ± 2.5	1.9	0.04
N_s (10^9 cm^{-2})	-122.8 ± 10.3	8.8	0.07

content of 30%, whereas C_0' and G_0 are nearly unchanged. The pH-sensitivities (table 8.9) of U_{th_C} and U_{th_G} are comparable to the $B_{10}^{30}C_{10}$ heterostructure. For N_s, the decrease is more pronounced and amounts to 25%.

The values obtained for U_{th_C} and U_{th_G} confirm that the Al-content in the barrier does not influence the pH-sensitivity of the surface potential. This can be expected, as the thick GaN cap layer guarantees that the surface oxide is independent of the composition of the AlGaN barrier layer. The decreased pH-sensitivity of N_s shows that Al-content does influence the field effect. The reason for this impact is the lower electric field strength in the barrier layer. This decrease of electric field strength with decreasing Al-content has also been verified by photoreflectance measurement [119]. The reduced value for the pH-sensitivity of N_s, along with the rather large standard deviation, result in an increase of the relative imprecision compared to the values that are commonly obtained for N_s. In contrast, the relative imprecisions of

the threshold voltages are low and therefore suitable for quantitative pH-measurements.

8.4.3 Summary

In summary, the combination of an increased cap layer thickness and a decreased Al-content in the barrier layer led to the following results and conclusions:

- An excellent resistance to photoelectrochemical corrosion with violet light was found. Even for a long-term measurement series of 48 h the corrosion drift is very low. It is therefore safe to assume that electrochemical corrosion without illumination or with red illumination does not take place.

- The dislocation density of the $B_{10}^{20}C_{10}$ heterostructure was found to be reduced to $1 \times 10^9\,\mathrm{cm}^{-2}$. This reduction can be attributed to less tensile strain in the barrier layer, as a result of the reduced Al-content.

- The observed threshold voltage of less than 1 V allows for operation of the sensor chip at small bias voltages or even zero bias. This feature is beneficial for low electrostatic stress of the passiviation layer on ISFET devices or for the application to measurement of living cell systems.

- For the pH-sensitivity of U_{th_C} and U_{th_G}, no influence of the reduced Al-content was observed and typical values of about $50\,\mathrm{mV\,pH}^{-1}$ have been obtained. The pH-sensitivity of N_s is decreased, as the field effect is influenced by the Al-content in the barrier layer.

Although further investigations with respect to the reliability and yield for this heterostructure layout are pending, the $B_{10}^{20}C_{10}$ layout is advantageous with regard to corrosion resistance and operating voltage. However, it also needs to be investigated whether the rather low sheet charge density in the 2DEG will also result in an increased noise level. As only a few measurement series have been performed with this heterostructure, no mean pH-sensitivity with statistical significance can be given. Nevertheless, no large deviation from the previously obtained mean values is expected.

9 Measurement of pH-Value and Development of a Micro-Blood-pH Analyser

In this chapter the measurement of pH-value with AlGaN-based pH-sensors is discussed and the realisation of a micro-blood-pH analyser is described. The results from the characterisation and optimisation of the AlGaN heterostructure are applied to allow for sufficiently accurate and precise measurements which fulfil the requirements for medical and industrial applications in general. Foetal blood sampling was chosen as a specific application to demonstrate the potential of AlGaN-based pH-sensors. This application example is particularly challenging due to very small sample volumes, fast coagulation and demanding accuracy and precision requirements.

In order to tackle the first challenge, a microfluidic setup was developed that allows for sample volumes of 10 µl. A prerequisite for this miniaturisation is that the areas of both the pH-sensor and the reference electrode are reduced to less than $1\,\mathrm{mm}^2$. The realised micro-blood-pH measurement setup is described in section 9.2. To account for the faster coagulation the layout of the fluidic channel was optimised to facilitate cleaning with a rinsing solution and the measurement duration was minimised by the use of an AlGaN-based pH-ISFET. Both

the AlGaN-based EIHS and ISFET are characterised to determine the accuracy and precision that can be achieved for the measurement of pH-value. As a first step, pH-measurements were performed using impedance-voltage profiling of the AlGaN-EIHS in the electrochemical characterisation setup. The results of these measurements are given in section 9.3, followed by the measurement of umbilical cord blood pH-value with the EIHS in the micro-blood-pH analysis setup using a micro reference electrode. The results of several measurement series in the micro-blood-pH analyser setup with an AlGaN-based ISFET are presented in section 9.4. A simple statistical analysis is performed to verify that the requirements of the RiLiBÄK are satisfied for the measurement of pH-value in 10 µl of umbilical cord blood.

Before the results of the measurements are presented and discussed, a short overview of the relevance and technique of foetal blood sampling is given and the commonly applied blood gas analysers are discussed.

9.1 Foetal Blood Sampling

The standard electronic foetal monitoring technique is the non-invasive CTG, which records the foetal heart beat and uterine contractions. An abnormal heart rate during labour may indicate a compromised oxygen supply (hypoxia) of the foetus, which can lead to foetal suffocation (asphyxia). FBS is employed to enhance the specificity towards foetal asphyxia, as the blood pH-value reflects the state of the foetal oxygen metabolism. In the first stage of hypoxia the pCO_2 increases, leading to a decrease of the blood pH-value. The second, and more critical, stage of hypoxia is characterised by a change to an anaerobic metabolism that produces lactic acid. At this stage the pH-value decreases more rapidly indicating a pathological acidosis, which can result in brain

damage or can even be fatal for the foetus. A pH-value below 7.25 is a sign for a starting acidosis and when the pH-value drops below 7.20 the immediate instrumental delivery of the foetus, e.g. by Cesarean section, is necessary [218].

The sampling technique for FBS has not been modified since the 1960s [5]. The cervix needs to be sufficiently dilated to allow access to the scalp of the foetus and a small incision is made. The blood is collected with a capillary and transferred to a suitable analysis system. In order to prevent the blood sample from clogging, the capillary is coated with an anti-coagulant, e.g. heparin. Although FBS is an established method, its implementation is rather challenging, especially in the generally stressful situation in the delivery room. The fast coagulation of foetal blood and the restricted sampling area result in very small sample volumes that can be below the minimum volume (35 µl) accepted by commercial blood gas analysers. These systems commonly employ glass or membrane pH-electrodes with comparatively large sensing areas, on the order of $4\,\mathrm{mm}^2$. In 2010 smaller POCT systems (e.g. Radiometer ABL90 Flex) based on micro-arrays of polymer-coated electrodes have been introduced, which have the potential for further miniaturisation. Another possibility is the use of optodes that are read-out optically and require no reference electrode. Thereby, the sample only needs to cover the optode and very low volumes may be realised. Blood gas analysers based on this technique have been commercialised by OPTI Medical Systems. Nevertheless, both approaches have not been optimised for low volumes and currently the minimum sample volume of the corresponding systems is still rather large (about 60 µl). On an interesting historical side note, the measurement setup employed by Saling for the very first FBS investigations in 1961 was already capable of measuring the pH-value in blood sample volumes of 25 µl [219].

However, this value has never been achieved by commercial blood gas analysis systems. This suggests that the commercial development has made no headway in the last 50 years, with regard to very small sample volumes.

9.2 Description of the Developed Micro-Blood-pH Analyser

The primary requirement for the micro-blood-pH analyser is the reduction of the sample volume in comparison to the commercially available blood gas analysers. The targeted volume of less than 10 µl is achieved by employing a capillary channel with an inner diameter of 1 mm and by placing a miniaturised reference electrode close to the AlGaN pH-sensor. To be able to integrate the pH-sensor and the reference electrode into the fluidic setup, their dimensions have to be reduced to less than the inner diameter of the channel. The AlGaN-ISFET is very well suited for this purpose as sensing areas down to 50x50 µm^2 can be fabricated. However, the miniaturisation of the reference electrode is much more challenging, which is why a commercially available micro reference electrode (LF1, Harvard Apparatus) with an outer diameter of 1 mm was selected. The dead volume of the fluidic channels is reduced further by placing the inlet for the sample as close to the sensor as possible. This way the cleaning of the system is simplified and the risk of sample residues and contamination is reduced. Another important requirement was to reproduce the simple operation procedures and sample handling of the commercial blood gas analyser with the setup.

In figure 9.1 the basic layout of the fluidic channel is illustrated. The channel is angled towards the interface with the sensor, where it is cut

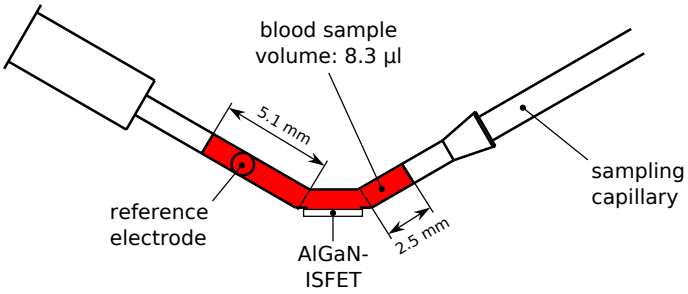

Figure 9.1: Schematic drawing illustrating the dimensions of the fluidic channel for sample volumes of less than 10 µl

open over a length of 2.5 mm and a width of slightly less than 1 mm. The opening for the reference electrode is located in the side of the channel's ascending portion. With a reserve of approximately 2 mm channel length on each side, a sample of less than 10 µl covers both the sensor and the electrode. The sample capillary is introduced into the setup at the right hand side and sealed via a silicone seal (Sylgard 184, Dow Corning), with a conic inner diameter. This way sample capillaries with outer diameters from 1 to 2 mm can be sealed by simple insertion. The gasket for the sensor is also cast from Sylgard 184, with inner dimensions equal to the channel's sensor opening, outer dimensions of 2x4 mm and a thickness of 300 µm. The reference electrode is sealed using a squeezed O-ring.

An exploded assembly drawing of the complete measurement cell is shown in figure 9.2. The fluidic module is the central element of the setup as it includes the fluidic channel with its interfaces for the sensor and the reference electrode, as well as an optical detection system for gas bubbles in the sample fluid. For this purpose the transparency of the sensor is utilised to create a simple photoelectric barrier directly

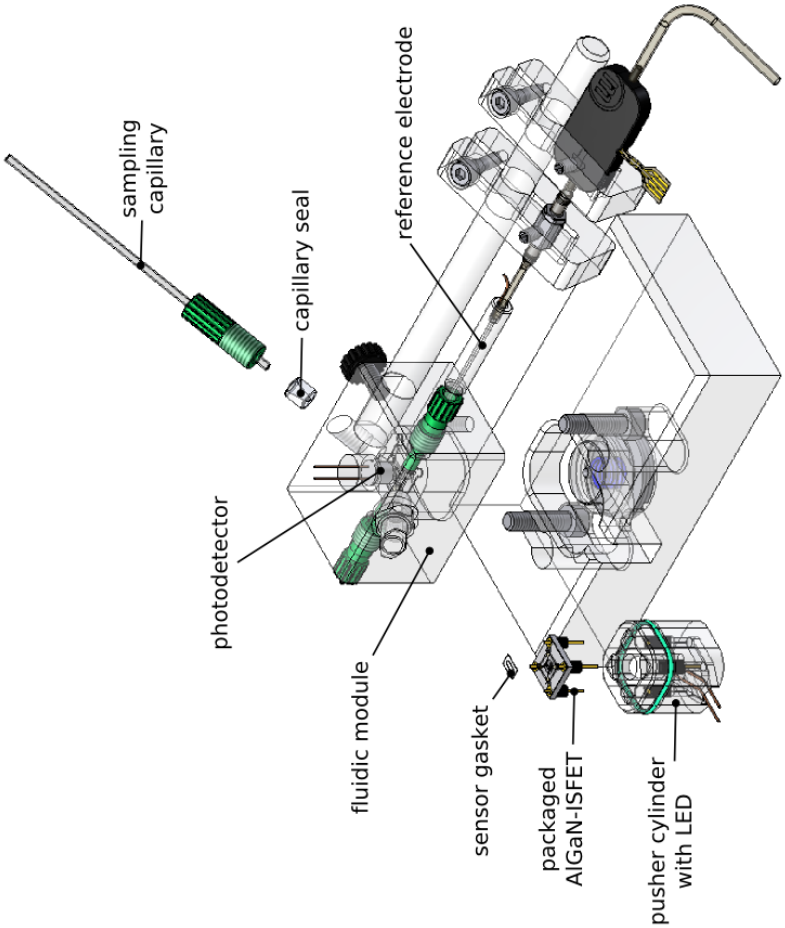

Figure 9.2: Exploded assembly drawing of the micro-blood-pH measurement cell.

through the sensor with an opposing photodetector. Thereby, the dimensions of the fluidic channel do not have to be enlarged and the small footprint of the fluidic module is preserved. A red LED and a Si PIN photodiode (BPX 65, Osram), operated in photovoltaic mode, were used for the photoelectric barrier.

The AlGaN sensor itself is fixed to a conductor board and the electrical contact is made using conductive silver lacquer. This simple sensor module is plugged into a pusher cylinder that is wired to the measurement instrumentation and also holds the LED for the illumination of the sensor. The cylinder with the sensor module is pressed onto the PDMS gasket and the fluidic channel. To ensure an even contact pressure the force of a prestressed spring is transferred centrally to the cylinder using a small ball joint. In order to shield the measurement cell from ambient illumination and electromagnetic interference, it is wrapped in aluminium foil, which is grounded at the measurement instrumentation.

The actuation of the fluids is performed with a two-channel peristaltic pump (REGLO Digital, Ismatec), which is controlled via an RS232 interface. A flow selection valve with four inlets (080T412-62, Bio-Chem Valve) is employed to switch between two calibration fluids, a cleaning solution and air. A schematic illustration of the fluidic circuitry is given in figure 9.3. The outlet of the measurement cell is connected to the valve, which supplies the calibration and cleaning fluids. At the inlet either the sample capillary can introduced or a tube leading to the waste container can be connected. The connecting tubes outlet-to-valve and inlet-to-waste are fixed to the pump in opposite directions. For the calibration and cleaning procedures the waste tube needs to be connected to the inlet and the fluids are forced into the cell at the outlet and aspirated from it at the inlet. For the aspiration of

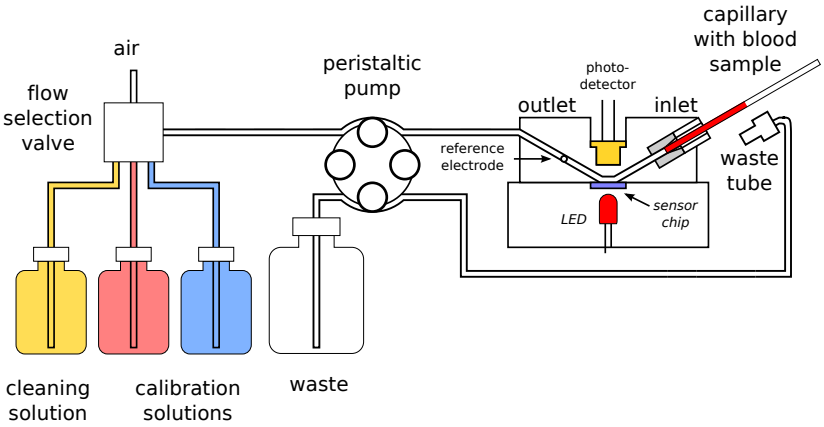

Figure 9.3: Schematic drawing of the fluidic circuitry of the micro-blood-pH measurement setup.

blood from the sample capillary, the waste tube is removed and only the outlet-to-valve tube is utilised. In figure 9.4, the realisation of the complete micro-blood-pH analyser setup is shown.

Electrical measurements were carried out with the impedance analyser, in the case of the EIHS sensor, or with source-meter units for the ISFET sensor. A LabVIEW (impedance analyser and EIHS) or Agilent VEE (source-meter unit and ISFET) program controls both the pump and the valve as well as the measurement instrumentation. The main elements of both programs are: cleaning, calibration and sample pH-measurement.

The cleaning of the measurement cell is a critical step as the carry-over from samples has to be avoided. Blood is a very complex biological fluid that contains a multitude of proteins and the coagulation mechanism can form blood clots. The application to foetal blood aggravates the problem of blood clots as the coagulation is faster. Thus, residues

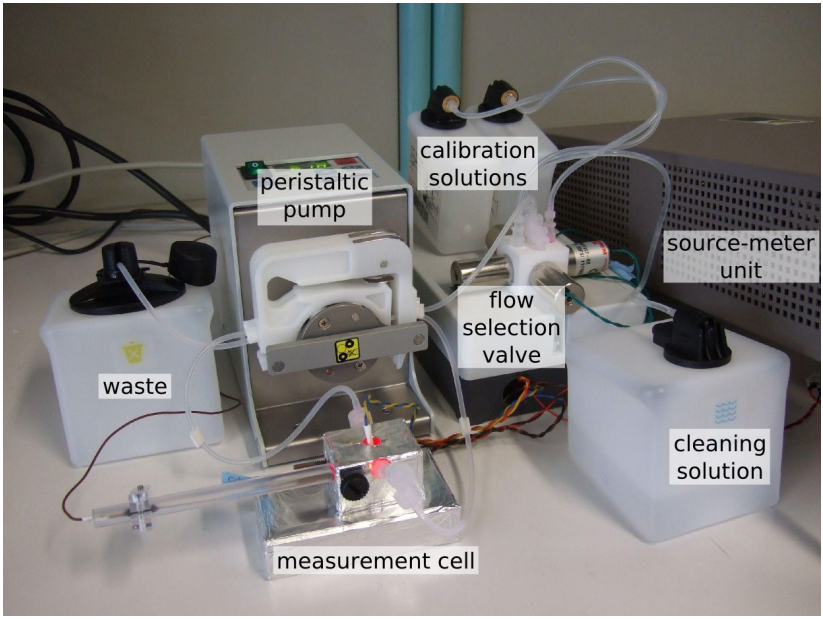

Figure 9.4: Realised micro-blood-pH analyser setup.

from the blood are likely to form and to adhere to the fluidic channel and the sensor. In addition to that, the small dimensions of the channel make it susceptible to clots or trapped air bubbles and make it difficult to clean. The cleaning procedure has two important aspects: a chemical component (composition of the cleaning fluid) and a physical component supporting the procedure. As investigations on the composition of the cleaning fluid are beyond the scope of this work, a standard cleaning solution for commercial blood gas analysers was chosen. A light physical component is introduced by intermittent air bubbles, resulting in a segmented flow of cleaning fluid. During one cleaning cycle the length of the segments is varied from smaller (30 µl) to larger ones (90 µl) with a large, continuous segment at the end of the cycle. The pump speed is also varied between high (125 µl/s) to low fluid velocities (25 µl/s). The sample fluid is aspirated with a velocity of 7 µl/s only as far as necessary, i.e. until the reference electrode is covered. Cleaning the channel from the opposite direction ensures that no sample residues or other contamination are carried into the setup. The waste tube ensures that the fluids are diverted into the waste container.

The calibration procedure can be performed as a one- or two-point calibration (see section 2.2). The two-point procedure is needed to obtain the pH-sensitivity of the sensor. The measurement cell is filled from the outlet side with each calibration solution and the electrochemical measurement is started. Between the calibration solutions a slightly shorter cleaning step is performed. The analysis of the calibration data using equation 2.21 yields the offset and the slope of the pH-sensitivity S_{pH}. For the application of equation 2.21, the emfs E_{s1} and E_{s2} have to be replaced by the corresponding quantities from the electrochemical measurement, i.e. U_{th_C} for the EIHS sensor and I_d for the ISFET. The one-point calibration can only be applied if the pH-sensitivity has

been determined beforehand. It is an appropriate method to check and recalibrate for a constant offset of the system, assuming that the sensitivity slope is unchanged.

After the calibration of the system, the pH-value of a sample fluid can be analysed. The capillary is inserted into the conic seal at the inlet of measurement cell and the sample is aspirated slowly into the fluidic channel (fig. 9.5a). Using the signal of the photoelectric barrier, trapped air bubbles can be detected and the fill level of the channel can be calculated. A distinct signal change ($\pm 5\,\mathrm{mV}$) was observed with a simple multimeter upon filling the channel with fluid, when the photodetector was operated in photovoltaic mode. The electrochemical measurement is started when the sensor and the reference electrode are covered without intermediate air bubbles (fig. 9.5b). From the known pH-sensitivity the pH-value is calculated using equation 2.20. Afterwards, the measurement the channel is cleaned immediately to minimise the formations of sample protein residues and blood clots.

Umbilical cord blood was used as a substitute for foetal scalp blood, as typically no excess blood samples are obtained from foetal blood sampling that could be used for testing. Additionally, it is not possible to conserve the very small blood samples for shipping. However, the properties of the blood from the umbilical cord are very similar to the foetal scalp blood. The samples were supplied in a Monovette (Sarstedt), with added lithium-heparin as an anticoagulant, by the Placenta Lab at the Jena University Hospital. The samples were taken within an hour after birth, stored at (4–8) °C and shipped within one day. It was observed that the pH-value had decreased by (0.2–0.3) pH during shipping to values around (7.2–7.0) pH. For validation and comparison a commercial blood gas analyser (ABL5, Radiometer) was available.

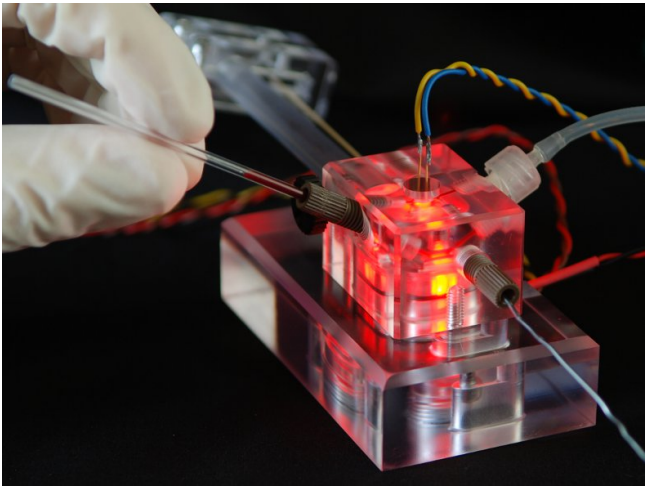

(a)

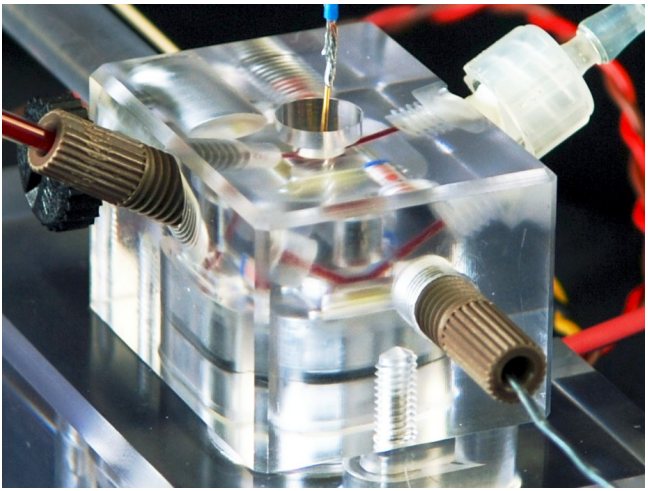

(b)

Figure 9.5: Filling the micro-blood-pH analyser with umbilical cord blood (a) and close-up of the filled fluidic channel (b). For illustration purposes, the aluminium foil was removed and the LED switched off in (b).

9.3 Measurement of pH-Value with EIHS

The measurement of pH-value with the EIHS was investigated simultaneously to the characterisation and optimisation experiments. A brief summary of these investigations is given in this section, to illustrate the suitability of the EIHS for accurate pH-measurements. The analysed samples include simple phosphate buffer solutions, commercially available calibration and QC solutions and umbilical cord blood. The electrochemical characterisation setup with sample volumes of 10 ml was used for the first investigations with phosphate buffer solutions, whereas all other investigations were carried out in the micro-blood-pH analyser setup with 10 µl samples.

For the first investigation concerning the accuracy of pH-measurements with impedance-voltage profiles, an EIHS sensor chip based on a $B^{30}_{10}C_2$ heterostructure was employed in the electrochemical characterisation setup without illumination. Simple phosphate buffer solutions (PB7.0 and PB7.5) were used to obtain the calibration curve and test solutions were derived from PB7.5 by addition of HCl. The two-point calibration was performed by measuring complete impedance profiles ($U_{bias} = (2\text{–}0)\,\mathrm{V}$) of PB7.0 and PB7.5 multiple times in an alternating sequence. A pH-sensitivity of $(52.1 \pm 0.7)\,\mathrm{mV\,pH^{-1}}$ ($SD = 0.4\,\mathrm{mV}$) was obtained. The obtained results are shown in figure 9.6. Here, the threshold voltage U_{th_C} is plotted versus the "true" pH-value, as determined with a glass electrode and a standard pH-meter. The error bars indicate a deviation of ±0.03pH. It is clearly seen that the pH-value of the sample solutions can be measured with an accuracy better than ±0.03pH, even without the discussed optimisation steps. The "true" pH-value is always about 0.02 pH-units higher than the pH-value that is calculated from calibration slope (eqn. 3.6). A linear correction of

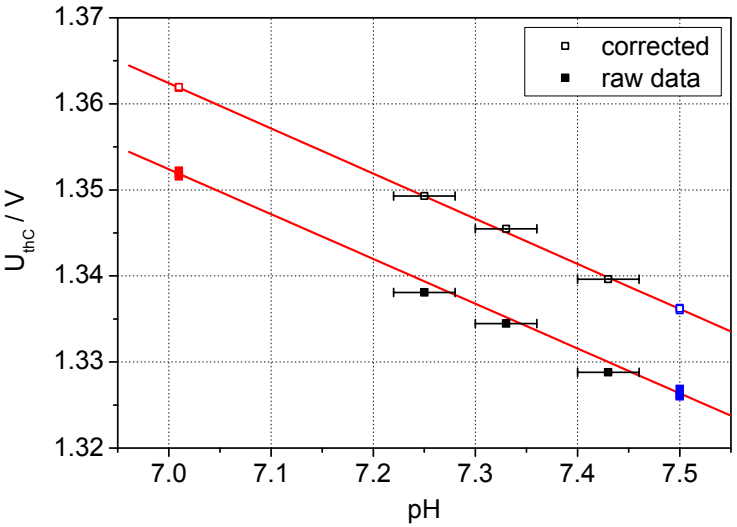

Figure 9.6: Plot of U_{th_C} versus pH-value showing the two-point calibration with phosphate buffer solutions (red and blue) and the measurement of phosphate buffer solutions with differing pH-value (black).

the measured U_{th_C} can be applied (eqn. 7.3) with a correction value of $0.2\,\mathrm{mV\,meas^{-1}}$. This greatly reduces the uncertainty of the calibration slope yielding $(52.1 \pm 0.2)\,\mathrm{mV\,pH^{-1}}$, $SD = 0.1\,\mathrm{mV}$. The measured sample pH-values then match the "true" value within ±0.01pH.

These results demonstrate that with controlled ambient conditions accurate measurement of pH-value is possible. Constant illumination conditions and electromagnetic shielding are especially important. Neither an optimisation of the semiconductor heterostructure nor a special treatment of its surface is necessary to achieve this accuracy. However, the linear drift indicates that the sensor is susceptible to electrochemical corrosion and a linear drift correction may not always be possible. In addition, the recording of complete impedance profiles is very time consuming and the duration to achieve a stable sensor signal after illumination was shown to be at least 12 h.

In a next step, the preliminary micro-blood-pH analyser setup was used to achieve a reduction of sample volume down to 10 µl. A continuous red illumination of the sensor chip was applied to enable the detection of air bubbles and to reduce the light stabilisation time. The employed sensor chip was not optimised and still based on a $B^{30}_{10}C_2$ heterostructure. To speed up the measurement duration from 15 min to 2 min, the impedance-voltage profiles were only recorded in a small range (U_{bias} = (1.75–1.50) V, 50 mV steps). The filling and cleaning was performed manually, using syringes, since the setup had not yet been fully automated. Despite the use of a non-optimised sensor chip and the manual filling, the suitability for the measurement of foetal blood pH-value is clearly demonstrated in figure 9.7. The calibration was performed using the modified standard phosphate buffer solutions (MPB6.81 and MPB7.36). A slope of $(48.5 \pm 0.8)\,\mathrm{mV\,pH^{-1}}$ ($SD = 0.6\,\mathrm{mV}$) was obtained for the pH-sensitivity after a linear drift

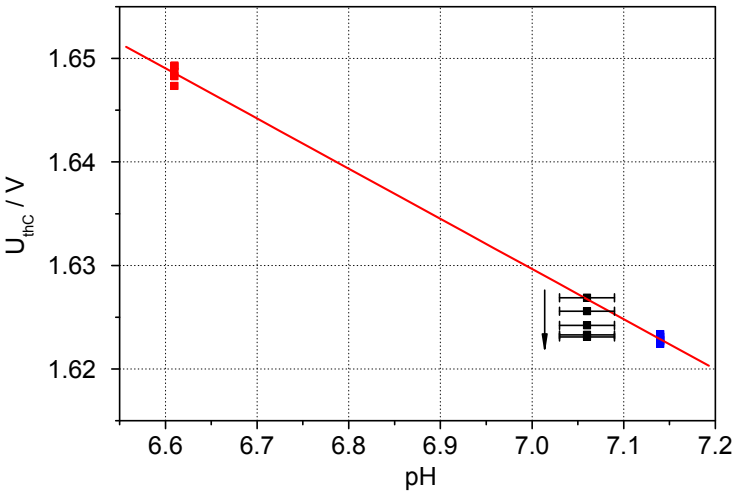

Figure 9.7: Plot of U_{th_C} versus pH-value showing the two-point calibration with modified phosphate buffer solutions (red and blue) and the measurement of umbilical cord blood pH-value (black).

correction of $0.4\,\mathrm{mV\,meas^{-1}}$. The error bars signify a deviation of ± 0.03pH. The umbilical cord blood was filled into the measurement channel and measured multiple times. It is found that the measured and the "true" pH-value match very well for the first measurement and also the second measurement is within ± 0.03pH. However, in the subsequent measurements a drift towards lower threshold voltages is observed and the deviation exceeds ± 0.06pH. Two effects can be responsible for this behaviour. Firstly, biochemical reactions in the very small sample volume can lead to pH-value shifts, especially when the sample is subjected to air. An alteration of the sample is very probable, as the total measurement duration was rather long (10 min). Secondly, the surface potential at the AlGaN-EIHS and the diffusion potential at the reference electrode might be affected by the prolonged contact with blood. The observed increase of the DC current density by a factor of five upon exposure to blood, argues for some form of corrosive attack of the sensor surface. Therefore, the contact time with the blood sample and the measurement duration should be minimised.

In conclusion, this measurement series shows that the umbilical cord blood pH-value can be measured in the micro-blood-pH analyser setup with good accuracy. The reduction of sample volume, the continuous red illumination and the minimisation of the recorded voltage range do not impair this accuracy. However, the measurement duration has to be reduced to minimise drift and possible biochemical corrosion of the sensor chip.

A first characterisation of the complete micro-blood-pH analyser setup with the implemented automation of the measurement and the fluidic system was also performed with an EIHS sensor chip ($B_{10}^{30}C_2$). Commercially available calibration (S1545 and S1555) solutions were used for the two-point calibration yielding a slope of $(40.5 \pm 0.9)\,\mathrm{mV\,pH^{-1}}$

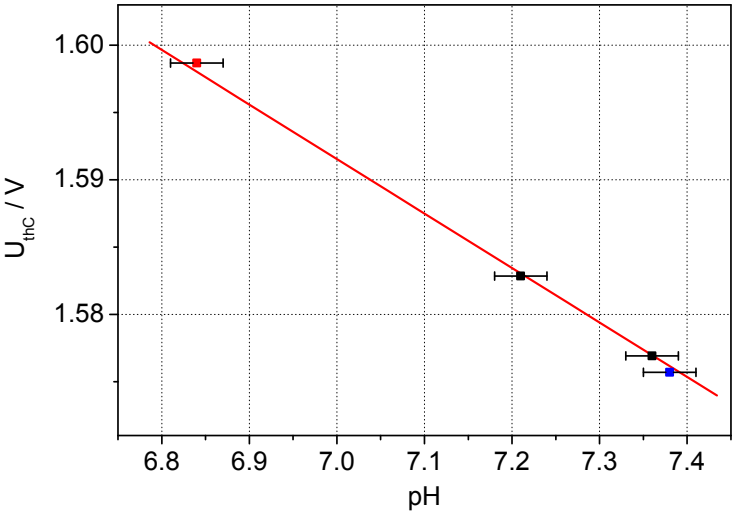

Figure 9.8: Plot of U_{th_C} versus pH-value showing the calibration slope obtained with commercial buffer solutions (red line). The pH-values of the calibration solutions are rechecked (red and blue squares) and commercial quality control solutions are measured (black squares).

($SD = 0.5\,\mathrm{mV}$). The "true" pH-value of the calibration and QC solutions were taken from the data sheets. In between each measurement, a cleaning cycle with rinsing solution (S4930) was performed. The impedance-voltage profiles were recorded for the voltage range of (1.650–1.525) V with steps of 25 mV. In figure 9.8 the calibration slope is shown as a red line. The pH-values of both calibration solutions were rechecked (red and blue squares) and ISETROL Level 1 and 2 QC solutions (black squares) were measured. For all measurements an excellent accuracy of ± 0.01pH was obtained without the need for drift correction. A possible explanation for these results can be found in the calibration and QC solutions that are specifically adjusted to the investigated pH-range and the composition of the samples as well as the QC solutions. Especially in terms of pH-value stability and buffer capacity the calibration and the QC solutions are superior to the simple self-made buffer solutions. Thus, one of the limits on the accuracy of the developed micro-blood-pH analyser can be found in the electrolyte solutions rather than the AlGaN-EIHS sensor chip itself. In general, these results reveal that commercial solutions can be used for calibration and cleaning of the analysis system, even if they have not been developed and optimised for pH-ISFETs. The accurate measurements of the QC solutions indicate that single measurements with the micro-blood-pH analyser already satisfy the requirements of the RiLiBÄK. The measurement chain as a whole, especially the AlGaN pH-sensor and the reference electrode, is suitable for the purpose of pH-value measurements in the microlitre range. It needs to be stated, however, that the presented data only represents the best results that were obtained with the EIHS. The reproducibility was not satisfactory. However, in the next section it is shown that the reproducibility can be enhanced when AlGaN-based pH-ISFET are employed.

9.4 Measurement of pH-Value with ISFETs

The most important advantage of the ISFET structure is that it combines the sensing and transducing elements into one sensor device (cf. chapter 3.3). This way a high input impedance, via capacitive coupling over the insulator, and a low output impedance, via the conducting channel, are realised and simple measurement instrumentation can be employed. In addition, the amplification of the input signal can be adjusted by the gate width to length ratio (W/L). The application of the AlGaN-based pH-ISFET in the micro-blood-pH analyser makes shorter analysis times possible and reduces the complexity of the required instrumentation. No sophisticated impedance analyser is needed and a simple measurement of the drain current with an SMU or a suitable circuit, such as a source follower, can be used. For the micro-blood-pH analyser, the constant voltage method was applied, in which the gate-source and the drain-source voltages, U_{gs} and U_{ds}, are fixed and the gate and drain current, I_g and I_d, are measured. The gate source voltage is the analogous to the bias voltage of the EIHS, except for an inverted sign ($U_{gs} = -U_{bias}$). It should be noted that the gate of the ISFET consists of the electrolyte solution and the reference electrode. Thereby, the gate current is the leakage current via the passivation layer in addition to the leakage current via the heterostructure. As the passiviation layer is still the weakest link in the insulation towards the electrolyte solution, I_g does not necessarily correspond to the DC leakage current of the EIHS.

The layout of the ISFET sensor chips was optimised to fit the opening of the fluidic channel. Two ISFET structures, an Au conductive path and an Au electrode pad are integrated on an area of 1x2.5 mm^2. The gate width is 500 µm and the gate length is 50 µm ($W/L = 10$) for

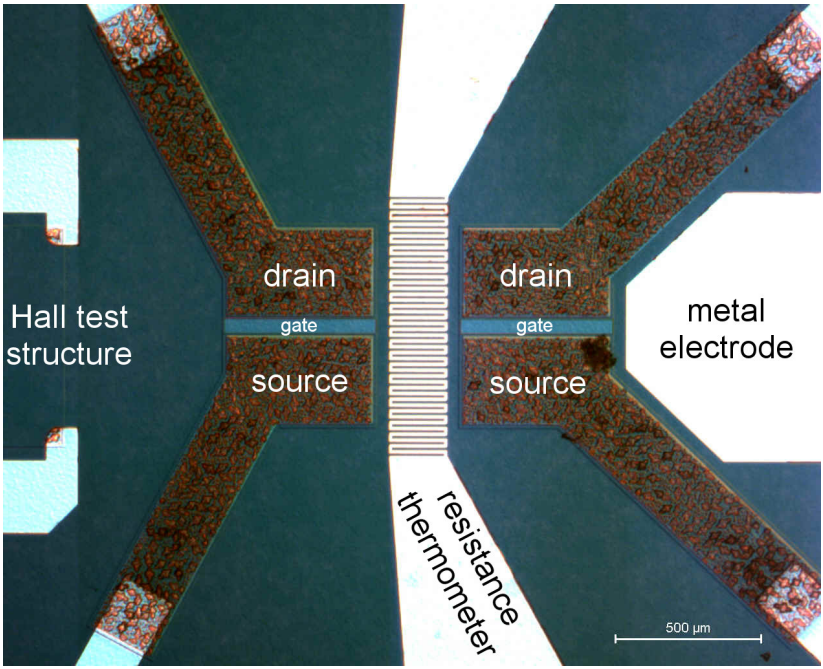

Figure 9.9: Microscopic image of the pH-sensor chip with two ISFETs, a resistance thermometer, a metal electrode and part of a Hall test structure.

both ISFETs (fig. 9.9). This allows for redundant measurements and a possible enhancement of measurement accuracy. The Au conductive path is planned to be used as a resistance thermometer and the Au pad as a secondary reference or counter electrode in addition to the reference electrode. A $B_{10}^{30}C_{10}$ heterostructure was employed for the sensor chips.

The voltages U_{gs} and U_{ds} are applied using a two-channel SMU (2602A, Keithley) that also measures the currents I_g and I_d. The

two-point calibration cycles are performed multiple times to check the stability of the measured pH-sensitivity. Several different umbilical cord blood samples were measured in both the commercial blood gas analyser, to determine their "true" pH-value, and in the micro-blood-pH analyser. In figure 9.10, the pH-sensitivity of the pH-ISFET (blue triangles), the "true" pH-value (red open circles) and the measured pH-value (black squares), with an error bar of ±0.03pH, are plotted versus the number of measurements. The single points reflect the sequence of measurements. The red line is a guide to the eye, projecting the "true" pH-value onto the number of measurements. Two measurement series of different samples measured with different sensor chips at operating voltages of $U_{ds} = 0.5\,\mathrm{V}$ and $U_{gs} = -0.5\,\mathrm{V}$ or $-0.75\,\mathrm{V}$ are shown. This way the reproducibility of the results can be demonstrated, even if several measurement conditions are changed.

For the chip A3+3 a mean pH-sensitivity of $(-132.7 \pm 1.7)\,\mu\mathrm{A\,pH^{-1}}$ ($SD = 4.5\,\mu\mathrm{A\,pH^{-1}}$) was obtained at $U_{gs} = -0.5\,\mathrm{V}$ and chip A1+3 yielded $(-104.3 \pm 2.9)\,\mu\mathrm{A\,pH^{-1}}$ ($SD = 5.9\,\mu\mathrm{A\,pH^{-1}}$) at $U_{gs} = -0.75\,\mathrm{V}$. It can be seen that the measured pH-value is always inside the required maximum deviation interval of ±0.03pH for both measurement series. The pH-sensitivity of $(140 \pm 3)\,\mu\mathrm{A\,pH^{-1}}$ that was calculated in section 8.3 from the pH-sensitivity of N_s is slightly higher than the measured values. In addition, it is observed that the measured pH-sensitivity decreases for more negative U_{gs}. This deviation can be explained by the influence of U_{gs}, which results in an initial depletion of the 2DEG. In contrast to the commonly employed integration up to 0 V, the integration of $C'(U_{bias})$ in equation 5.5 has to be performed up to $U_{bias} = -U_{gs}$, to account for this depletion. In doing so, $N_s(U_{gs})$ is obtained and the pH-sensitivity can be derived from these values. A slight decrease of pH-sensitivity was observed for $N_s(-0.5\,\mathrm{V})$

and $N_s(-0.75\,\mathrm{V})$, compared to $N_s(0\,\mathrm{V})$. However, a value of about $140\,\mathrm{cm}^{-2}\,\mathrm{pH}^{-1}$ was found for both negative U_{gs}, which corresponds to a drain current pH-sensitivity of approximately $120\,\mu\mathrm{A}\,\mathrm{pH}^{-1}$. Although the difference of the measured values is still rather large, this value is a good estimate. The significant difference that is found for the measured pH-sensitivities at different U_{gs} may well be due to the distribution of electrical properties between the single sensor chip and not an impact of the applied U_{gs}. Despite the difference in pH-sensitivity, figure 9.10 shows that an excellent agreement between the measured and the "true" pH-value exists.

Statistical analysis of small measurement series is performed to calculate the measured mean pH-value $\overline{pH}$ and to estimate relative inaccuracy and imprecision as well as the coefficient of the root mean square deviation (RMSD) with regard to the "true" pH-value pH_0. The relative inaccuracy δ_r is calculated using:

$$\delta_r = \frac{\delta}{pH_0} = \frac{\overline{pH} - pH_0}{pH_0}. \tag{9.1}$$

The coefficient of variation c_v is taken as a measure for the relative imprecision and calculated from the estimated standard deviation divided by the mean value:

$$c_v = \frac{SD}{\overline{pH}} = \frac{\sqrt{\frac{\sum_{i=1}^{n}(pH_i - \overline{pH})^2}{n-1}}}{\overline{pH}}, \tag{9.2}$$

where pH_i is the i-th measured pH-value and n the number of measurements.

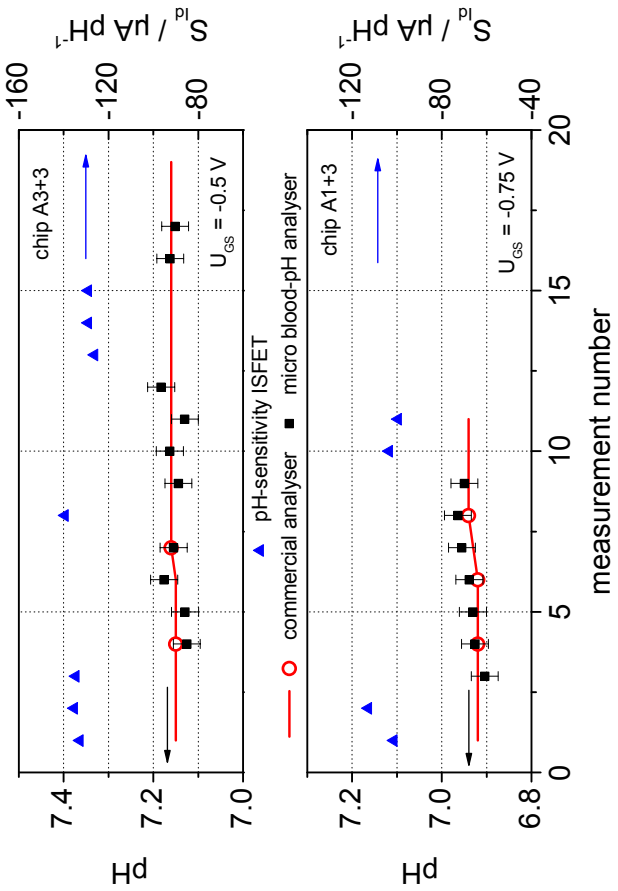

Figure 9.10: Plot of the pH-value of umbilical cord blood obtained with the micro-blood-pH analyser in 10 µl (black squares) compared to a commercial blood gas analyser in 100 µl (red open circles). The error bars indicate a deviation of ±0.03pH. The plotted pH-sensitivities S_{Id} of the AlGaN-ISFET (blue triangles) indicate at which point a two-point calibration was performed.

The coefficient of the RMSD c_{RMSD} includes both SD and δ. It was introduced into the RiLiBÄK in 2010 as a combined measure of instrument performance [10]. It is calculated using:

$$c_{RMSD} = \frac{\sqrt{\frac{n-1}{n}SD^2 + \delta^2}}{pH_0} = \frac{\sqrt{\frac{\sum_{i=1}^{n}(pH_i - pH_0)^2}{n}}}{pH_0}. \tag{9.3}$$

In table 9.1 these statistical parameters are calculated for three measurement series, including the two series shown in figure 9.10. To fulfil the requirements of the RiLiBÄK, δ_r must not exceed 0.8% and c_v and c_{RMSD} have to be less than 0.4% for the measurement of blood pH-value in the range from pH6.75 to pH7.80. The table reveals that all three measurement series fulfil these requirements referenced to the "true" pH-value measured with the commercial blood gas analyser. It can be seen that the measurements with the micro-blood-pH analyser tend to be more accurate (low value of δ_r) than precise (high value of c_v). This implies that some form of measurement noise limits the precision of the measurement chain.

The origin of this noise may be small potential fluctuations in the measurement chain. This primarily includes the surface potential of the AlGaN-ISFET and the reference electrode potential. Possibly, longer equilibration times are needed before the actual electrochemical measurement is started, in order to achieve a preconditioning of the ISFET and the reference electrode. It may also be useful to keep the ISFET and the reference electrode exposed to a baseline solution that ensures stable potentials when no measurement is performed. However, this continuous exposure can degrade the insulating properties of the passivation layer.

Table 9.1: Statistical analysis of the measurement of umbilical blood pH-value with the micro-blood-pH analyser in a sample volume of 10 µl.

	series 1	series 2	series 3
"true" pH-value - pH_0	7.15	6.93	7.14
measured mean pH-value - $\overline{pH}$	7.15	6.94	7.14
number of measurements - n	10	7	5
rel. incorrectness - δ_r	0.03%	0.13%	0.04%
rel. imprecision - c_v	0.28%	0.29%	0.36%
rel. RMSD - c_{RMSD}	0.08%	0.32%	0.09%

9.5 Summary

In summary, the following results and conclusions were obtained in the preceding investigation on pH-measurement with AlGaN-based pH-sensors and for the development of a micro-blood-pH analyser:

- A micro-blood-pH analyser setup was developed and successfully realised for the pH-measurement of foetal blood samples. The reduction of the sample volume to 10 µl was performed and no adverse influence on the measurement accuracy was discovered.
- For EIHS sensors based on a $B_{10}^{30}C_2$ heterostructure, a linear correction needs to be applied in most cases to account for electrochemical corrosion drift. The measurement accuracy can be achieved for a variety of sample solutions, ranging from simple phosphate buffer solutions to umbilical cord blood. For specially adjusted calibration and QC systems, an accuracy of close to ±0.01pH can be obtained. The prolonged measurement of umbilical cord blood revealed that the initially accurate measurement

is subject to drift, due to biochemical reaction in the blood and at its interface with the sensor or the reference electrode. Therefore, the measurement duration needs to be minimised.

- For an ISFET sensor with an optimised $B_{10}^{30}C_{10}$ heterostructure, no linear correction of the measured values is necessary. Statistical analysis of three measurement series with at least five single measurements each revealed that the requirements of the RiLiBÄK can be fulfilled. A relative incorrectness of 0.1% or less and a relative imprecision of about 0.3% were calculated for these series.

- In general, accurate measurement of pH-value can be performed with both the EIHS and the ISFET sensor. It was found that controlled ambient conditions, especially illumination and electromagnetic shielding, are the most important prerequisites for these measurements.

It was demonstrated that a micro-blood-pH analyser for foetal blood samples with a volume of 10 µl can successfully be realised using AlGaN-based pH-ISFETs. The performance of the developed analyser was confirmed to fulfil the demanding requirements of the RiLiBÄK for several measurement series. Clinical test runs in the placenta lab at Jena University Hospital are underway, in order to evaluate the suitability of the system for daily use.

10 Conclusions and Outlook

In this thesis the impedance characterisation of AlGaN-based pH-sensors was presented and optimisation approaches for the accurate and precise measurement of pH-value were evaluated. In order to gain insight into the fundamental electrical and sensory properties of these pH-sensors, the commonly employed AlGaN-based ion-sensitive field-effect transistor (ISFET) was reduced to its basic sensing and transducing structure - the AlGaN/GaN eletrolyte-insulator-heterostructure (EIHS). Based on the results of the characterisation and optimisation, a micro blood-pH analyser for foetal blood sampling was developed and successfully realised.

From the fundamental impedance characterisation of AlGaN-based capacitor heterostructures with a metal (MIHS) and an electrolyte solution contact (EIHS), the following results were obtained:

- A full and a reduced equivalent circuit were derived from impedance spectroscopy. The full equivalent circuit is very suitable to describe the impedance characteristic of both the MIHS and the EIHS in a large frequency and bias voltage range. The broad distribution of trap time constants in AlGaN/GaN heterostructures was successfully modelled with constant phase elements. Although these equivalent elements are seldom employed in semiconductor physics, it was verified that they are a suitable for a phenomenological description.

- It was found that the AlGaN/GaN heterostructure cannot be described by the commonly employed one-dimensional model, as the 2DEG exhibits a two-dimensional depletion geometry. This depletion geometry is due to the absence of a bulk contact in the AlGaN/GaN heterostructure. The vertical component dominates for as long as the 2DEG is sufficiently conducting, whereas a lateral component dominates when part of the 2DEG channel is depleted. Due to this two-fold behaviour, the 2DEG conductance and the 2DEG area are influenced differently.

- For the application of impedance-voltage profiling, a reduced equivalent circuit $C+R$ was derived to calculate equivalent capacitance and conductance profiles. A method for the unambiguous estimation of threshold voltage was developed based on the inflection point of the capacitance profiles.

- No pronounced difference was observed between the impedance characteristic of the MIHS and the EIHS, with the exception of the resistance of the reference electrode and the electrolyte solution. Information on the semiconductor-electrolyte interface and the electrical double layer could not be obtained.

- It was demonstrated that high resolution SEM images can be employed to determine the dislocation density of AlGaN/GaN heterostructures.

Employing the derived reduced equivalent circuit, it was possible to characterise the drift behaviour, pH- and cross-sensitivity of the AlGaN-EIHS using impedance-voltage profiling. These investigations yielded the following results:

- Three main drift effects were identified: an initial drift due to photoresist contamination, the well-known PPC characteristic upon darkening and a slow electrochemical corrosion drift. The contamination drift was eliminated by an appropriate cleaning protocol, whereas for the minimisation of the latter two drift effects specific optimisation steps were necessary.

- It was shown that impedance-voltage profiling is very suitable for the determination of pH-sensitivity. From the evaluation of three different analysis methods, the inflection point method was found to be the most suitable to obtain quantitative results with a good reproducibility, even from slightly distorted profiles.

- A mean pH-sensitivity of $48.1\,\mathrm{mV\,pH^{-1}}$ ($SD = 5.8\,\mathrm{mV\,pH^{-1}}$) was determined from more than 20 measurement series. The relative imprecision was always lower than 0.1pH.

- The measurable pH-sensitivity was found to be influenced by the 2DEG depletion characteristic of the AlGaN-EIHS. The measurable pH-sensitivity is reduced, when the depletion characteristic is intensified due to a reduced sheet charge density in the outer 2DEG (N_{s_o}) compared to the inner 2DEG (N_{s_i}). In this case, the sensor characteristic is mainly determined by the outer 2DEG, which is independent of pH-value.

- No specific cross-sensitivity to the ionic strength of the electrolyte solutions was discovered. Instead, it was verified that equivalent conductance profiles partly reflect the conductance of the electrolyte solution.

In order to minimise the impact of the PPC characteristic and to enhance the corrosion resistance, the illumination conditions and the layout of the AlGaN/GaN-heterostructure were optimised with the following results:

- The continuous illumination with violet light ($\lambda = 400\,\mathrm{nm}$) was found to be unsuitable for reducing the influence of ambient illumination, as it led to pronounced photoelectrochemical corrosion. It was observed that the corrosion process attacks dislocations at the sensor surface and has a dominant vertical component. Nevertheless, the characterisation of the corroded EIHS sensor was useful in order to refine the model that was developed for the AlGaN/GaN heterostructure.

- The continuous illumination with red light ($\lambda = 630\,\mathrm{nm}$) did not increase the corrosion drift compared to no illumination. From long-term measurements it was derived that the very slow corrosion process is mainly lateral. The PPC decay duration was successfully limited to (2–3) h as a result of continuous illumination. No significant change of the mean pH-sensitivity was discovered with continuous red illumination ($49.6\,\mathrm{mV\,pH^{-1}}$ ($SD = 4.1\,\mathrm{mV\,pH^{-1}}$)).

- A reduction of corrosion drift by about 80% was achieved by increasing the GaN cap layer thickness of the heterostructure to 10 nm. The observation that the relative decrease of dislocation density was comparable confirmed that the corrosion process is almost exclusively determined by the dislocation density. The pH-sensitivities of the threshold voltages were found to be unchanged, whereas the sensitivity of N_s was lower due to a reduction of the field effect.

- An additional reduction of the Al-content in the AlGaN barrier layer to 20% reduced the corrosion drift to almost negligible values, even with continuous violet illumination. The dislocation density was determined to be significantly lower. The pH-sensitivity of N_s was reduced further, in contrast to the sensitivity of the threshold voltages.

In general, the results obtained from the characterisation and optimisation of the AlGaN-EIHS demonstrate that electrochemical impedance spectroscopy and impedance-voltage profiling are very suitable to determine structural, electrical and sensory properties of AlGaN-based pH-sensors. These results greatly contributed to achieving accurate and precise pH-measurement with both EIHS and ISFET sensors. For the development of a micro-blood-pH analyser this accuracy and precision were the primary requirement. The following results were obtained:

- A micro blood-pH analyser with AlGaN-based pH-sensors was developed and successfully realised for pH-measurements in foetal blood samples with a volume of 10 µl.

- Even with the non-optimised EIHS sensor, a high measurement accuracy was achieved for a variety of sample solutions, ranging from simple phosphate buffer solutions to umbilical cord blood. It was found that the control of ambient conditions is the most important prerequisite for accurate and precise pH-measurements. The analysis of the pH-sensitivity using the developed inflection point method, also contributed to be measurement accuracy and precision. However, a linear drift correction was necessary to account for electrochemical corrosion.

- For the ISFET sensor based on an optimised heterostructure, no drift correction was necessary to obtain a high accuracy. The simple measurement instrumentation and measurement methods for the ISFET resulted in a much shorter measurement duration, compared to the EIHS. This is why the ISFET was employed in the micro-blood-pH analyser.

- The performance of the micro-blood-pH analyser was evaluated by basic statistical analysis. A relative incorrectness of 0.1% or less and a relative imprecision of around 0.3% was calculated for measurement series of umbilical cord blood. With these values the analyser satisfies the requirements of the guideline of the German Medical Association (RiLiBÄK). In order to evaluate the practical benefit of this analyser, initial clinical tests are underway.

It can be summarised that the results obtained in this thesis demonstrate for the first time that AlGaN-based pH-sensors are very suitable for the accurate and precise measurement of pH-value. Thereby, special application fields of medical engineering are opened up that are covered inadequately by common pH-sensors. The high accuracy and precision was achieved by appropriate optimisation of the AlGaN/GaN heterostructure and by controlled ambient conditions.

For further improvement of the AlGaN-based pH-sensors several further research avenues can be conceived, as given in the following:

- A crucial aspect is the minimisation of measurement noise. It can be assumed that a significant noise level is present, as the pH-measurements were found to be very accurate, but only reasonably precise. Possible optimisation approaches include the evaluation of different reference electrodes, the use of an additional, grounded quasi-reference electrode and the continuous preconditioning of the sensor surface and the reference electrode by a baseline electrolyte solution.

- The reduced light-sensitivity of the corroded EIHS sensor may be exploited for the construction of a light-insensitive sensor. However, in order to achieve this, comprehensive investigations on the responsible mechanism are needed and the disadvantages of the deliberate deterioration have to be evaluated.

- In order to obtain more information on the semiconductor-electrolyte interface using impedance spectroscopy, the measurement setup has to be modified. Most importantly, a reference electrode with a low impedance, on the order of 1 kΩ or less, has to be used. With an additional counter electrode, a three electrode configuration can be realised to minimise the potential drop in the electrolyte solution. Thereby, the actual influence of the ionic strength on the EDL may be measurable.

- Although the pH-ISFETs fabricated for this work yielded good results, there is still a large potential for optimisation. In this context, the presented characterisation and optimisation of the heterostructure are only the first steps that give insight into the

depletion characteristic of the 2DEG and enhance the corrosion stability. However, for the ISFET another lateral dimension is introduced with the W/L ratio of the gate area and the measurement instrumentation is fundamentally different. Systematic investigations are needed to verify that the results obtained for the EIHS can be directly applied to the ISFET.

Additionally, the results obtained in this thesis also suggest further research work beyond the optimisation of AlGaN-based pH-sensors:

- Especially the two-dimensional depletion geometry of the 2DEG can be assumed to have a profound impact on the properties of all devices that are based on AlGaN/GaN heterostructures, including AlGaN-HEMT devices. With regard to the parasitic effect of current collapse, this depletion geometry needs to be considered and the ratio of N_{s_o}/N_{s_i} should be investigated in more detail. In this context, the influence of the passivation layer and the illumination conditions on N_{s_o} and N_{s_i} have to be considered.

- It was shown that the CPE is very suitable for the phenomenological description of trap states with a broad distribution of time constants. It is therefore likely that the CPE can also be applied to other semiconductor devices or material systems. Thereby, the modelling in semiconductor physics could benefit from an equivalent element that was introduced in electrochemistry.

References

[1] M. Dole. pH and Detergency. *American Dyestuff Reporter*, 30:231–238, 1941.

[2] F. Haber and Z. Klemensiewicz. Über elektrische Phasengrenzkräfte. *Zeitschrift für Physikalische Chemie*, 67:385–431, 1909.

[3] P. Bergveld. Development of an ion-sensitive solid-state device for neurophysiological measurements. *IEEE Transactions on Biomedical Engineering*, 17:70–71, 1970.

[4] P. Bergveld. Thirty years of ISFETOLOGY:What happened in the past 30 years and what may happen in the next 30 years. *Sensors and Actuators B: Chemical*, 88(1):1–20, 2003.

[5] E. Saling. Neues Vorgehen zur Untersuchung des Kindes unter der Geburt. *Archives of Gynecology and Obstetrics*, 197(1):108–122, 1962-03-01.

[6] S. Schmidt, B. Misselwitz, and W. Künzel. Optimiert die Fetalblutanalyse die Qualität der geburtshilflichen Versorgung? *Geburtshilfe und Frauenheilkunde*, 65(04):368,373, 2005.

[7] Bundesgeschäftsstelle Qualitätssicherung gGmbH. BQS-Bundesauswertung 2007 Geburtshilfe, 2008.

[8] Statistisches Bundesamt Deutschland. Krankenhausstatistik 2009, 2010.

[9] L. Seyfarth. Market potential of a simple and compact analysis system for foetal blood sampling: personal communication.

[10] Bundesärztekammer. Bekanntmachungen: Richtlinie der Bundesärztekammer zur Qualitätssicherung laboratoriumsmedizinischer Untersuchungen. *Deutsches Ärzteblatt*, 105:341–355, 2008.

[11] G. Steinhoff, M. Hermann, W. J. Schaff, L. F. Eastman, M. Stutzmann, and M. Eickhoff. pH response of GaN surfaces and its application for pH-sensitive field-effect transistors. *Applied Physics Letters*, 83(1):177–179, 2003.

[12] G. Steinhoff, O. Purrucker, M. Tanaka, M. Stutzmann, and M. Eickhoff. $Al_xGa_{1-x}N$ - A new material system for biosensors. *Advanced Functional Materials*, 13:841, 2003.

[13] S. J. Pearton, B. S. Kang, S. Kim, F. Ren, B. P. Gila, C.R. Abernathy, J. Lin, and Chu S. N. G. GaN-based diodes and transistors for chemical, gas, biological and pressure sensing. *Journal of Physics: Condensed Matter*, 16(29):R961, 2004.

[14] I. Cimalla, F. Will, K. Tonisch, M. Niebelschutz, V. Cimalla, V. Lebedev, G. Kittler, M. Himmerlich, S. Krischok, J. A. Schaefer, M. Gebinoga, A. Schober, T. Friedrich, and O. Ambacher. Impact of Device Technology Processes on the Surface Properties and Biocompatibility of Group III Nitride Based Sensors. *Materialwissenschaft und Werkstofftechnik*, 37:919–923, 2006.

[15] I. Cimalla, B. Lübbers, V. Cimalla, M. Gebinoga, A. Schober, and O. Ambacher. Group III-nitride based sensors - Advances

towards a new generation of biosensors. In C. Ho-Young, editor, *Advanced Semiconductor Materials and Devices Research: III-Nitrides and SiC*, pages 341–374. Transworld Research Network, Kerala, India, 2010.

[16] G. Kittler. *GaN-basierte pH-Sensoren: Empfindlichkeit, Drift und Passivierungsrechnologien*. PhD thesis, Technische Universität Ilmenau, Ilmenau, 2007.

[17] I. Cimalla. *AlGaN/GaN sensors for direct monitoring of fluids and bioreactions*. PhD thesis, Ilmenau, 2010.

[18] B. S. Kang, H. T. Wang, F. Ren, M. Hlad, B. P. Gila, C.R. Abernathy, S. J. Pearton, C. Li, Z. N. Low, J. Lin, J. W. Johnson, P. Rajagopal, J. C. Roberts, E. L. Piner, and K. J. Linthicum. Role of Gate Oxide in AlGaN/GaN High-Electron-Mobility Transistor pH Sensors. *Journal of Electronic Materials*, 37(5):550–553, 2008.

[19] M. Kittler. Reproducibility of pH-measurements with AlGaN-based pH-ISFETs: personal communication.

[20] W. J. Moore, D. O. Hummel, G. Trafara, and K. Holland-Moritz. *Physikalische Chemie*, volume 4., durchges. und verb. Aufl. de Gruyter, Berlin, 1986.

[21] P. W. Atkins, C. A. Trapp, and M. Zillgitt. *Physikalische Chemie*. VCH, Weinheim [u.a.], 4., vollst. überarb edition, 2006.

[22] W. M. Siu and R. S. C. Cobbold. Basic properties of the electrolyte-SiO_2-Si system: Physical and theoretical aspects. *IEEE Transactions on Electron Devices*, 26(11):1805–1815, 1979.

[23] L. J. Bousse, N. F. de Rooij, and P. Bergveld. The influence of counter-ion adsorption on the ψ_0/pH characteristics of insulator surfaces. *Surface Science*, 135(1-3):479–496, 1983.

[24] K. Schwabe. *pH-Messtechnik: Mit 60 Tabellen*. Steinkopff, Dresden, 4 edition, 1976.

[25] H. Galster. *pH-Messung: Grundlagen, Methoden, Anwendungen, Geräte*. VCH, Weinheim, 1990.

[26] S. Arrhenius. Über die Dissoziation der im Wasser gelösten Stoffe. *Zeitschrift für Physikalische Chemie*, 1:631–648, 1887.

[27] J. N. Brønstedt. Einige Bemerkungen über den Begriff der Säuren und Basen. *Recueil des Travaux Chimiques des Pays-Bas*, 42:718–728, 1923.

[28] T.M Lowry. The uniqueness of hydrogen. *J. Soc. Chem. Ind.*, 42:43–47, 1923.

[29] L. Michealis. *Die Wasserstoffionenkonzentration: Ihre Bedeutung für die Biologie und die Methoden ihrer Messung*, volume 1 of *Monographien aus dem Gesamtgebiet der Physiologie der Pflanzen und Tiere*. Verlag von Julius Springer, Berlin, 1914.

[30] J. W. Baker. *Katalyse in Lösungen*, volume 2 of *Handbuch der Katalyse*. Springer, Wien, 1940.

[31] L. Kratz. *Die Glaselektrode und ihre Anwendungen: Mit 20 Tabellen*. Steinkopff, Frankfurt/Main, 1950.

[32] S. P. L. Sørensen. Enzymstudien II. Mitteilung: Über die Messung und die Bedeutung der Wasserstoffionenkonzentration bei

enzymatischen Prozessen. *Biochemische Zeitung*, 21:131–199, 1909.

[33] B. Lübbers and A. Schober. Comparing the ISFET to the Glass Electrode: Advantages, Challenges and Similarities. *Chemia Analityczna*, 54:1121–1148, 2009.

[34] J. I. Peterson, S. R. Goldstein, R. V. Fitzgerald, and D. K. Buckhold. Fiber optic pH probe for physiological use. *Analytical Chemistry*, 52(6):864–869, 1980.

[35] S. Arrhenius. *Zeitschrift für Physikalische Chemie*, 4:226, 1889.

[36] W. Salessky. Über Indikatoren der Azidimetrie und Alkalimetrie. *Zeitschrif für Elektrochemie*, 10:204–208, 1904.

[37] E. Biilmann. Sur l'hydrogenation des Quinhydrones. *Ann. Chim.*, 15:109–157, 1921.

[38] D. A. MacInnes and M. Dole. The behaviour of glass electrodes of different compositions. *Journal of the American Chemical Society*, 52(1):29–36, 1930.

[39] B. Emmerich. Die Emailelektrode, eine neue Lösung zur pH-Messung im Betrieb. *Regelungstechnische Praxis*, 20:313–317, 1978.

[40] H. Kaden, H. Jahn, and M. Berthold. Study of the glass/polypyrrole interface in an all-solid-state pH sensor: Proceedings of the Annual Meeting of International Society of Electrochemistry. *Solid State Ionics*, 169(1-4):129–133, 2004.

[41] T. Eriksson and G. Johansson. Determination of the concentration of strong acids with a permaplex membrane electrode in

the presence of hydrofluoric acid and various cations. *Analytica Chimica Acta*, 63(2):445–453, 1973.

[42] P. Schulthess, Y. Shijo, H. V. Pham, E. Pretsch, D. Ammann, and W. Simon. A hydrogen ion-selective liquid-membrane electrode based on tri-n-dodecylamine as neutral carrier. *Analytica Chimica Acta*, 131:111–116, 1981.

[43] A. Uhl and W. Kestranek. *Monatschrift Chemie*, 44:29, 1923.

[44] F. C. Thompson and F. Brudevold. A Micro-Antimony Electrode Designed for Intraoral pH Measurements in Man and Small Experimental Animals. *Journal of Dental Research*, 33(6):849–853, 1954.

[45] D. N. Mehta and S. K. Kulkarni Jatkar. *Journal of the Indian Institute of Sciene*, 18A:75, 1935.

[46] H. Brintzinger and B. Rost. Die Bestimmung der Wasserstoff-Ionen-Konzentration mit Wolfram- und Molybdänelektroden. *Fresenius' Journal of Analytical Chemistry*, 120(5):161–165, 1940.

[47] P. Shuk, K. V. Ramanujachary, and M. Greenblatt. Molybdenum oxide bronzes as pH sensors. *Electrochimica Acta*, 41(13):2055–2058, 1996/8.

[48] W. T. Grubb and L. H. King. Palladium-palladium oxide pH electrodes. *Analytical Chemistry*, 52(2):270–273, 1980.

[49] W. Vonau, U. Enseleit, F. Gerlach, and S. Herrmann. Conceptions, materials, processing technologies and fields of application

for miniaturized electrochemical sensors with planar membranes. *Electrochimica Acta*, 49(22-23):3745–3750, 2004.

[50] A. Fog and R. P. Buck. Electronic semiconducting oxides as pH sensors. *Sensors and Actuators*, 5(2):137–146, 1984.

[51] P. Bergveld. Development, Operation, and Application of the Ion-Sensitive Field-Effect Transistor as a Tool for Electrophysiology. *IEEE Transactions on Biomedical Engineering*, BME-19(5):342–351, 1972.

[52] T. Matsuo and K. D. Wise. An Integrated Field-Effect Electrode for Biopotential Recording. *IEEE Transactions on Biomedical Engineering*, 21(6):485–487, 1974.

[53] H. Abe, M. Esashi, and T. Matsuo. ISFET's using inorganic gate thin films. *IEEE Transactions on Electron Devices*, 26(12):1939–1944, 1979.

[54] T. Matsuo and M. Esashi. Methods of ISFET fabrication. *Sensors and Actuators*, 1:77–96, 1981.

[55] J. Janata. Historical review. Twenty years of ion-selective field-effect transistors. *The Analyst*, 119:2275–2278, 1994.

[56] S. J. Pearton, J. C. Zolper, R. J. Shul, and F. Ren. GaN: Processing, defects, and devices. *Journal of Applied Physics*, 86(1):1–78, 1999.

[57] M. Eickhoff, J. Schalwig, G. Steinhoff, O. Weidemann, L. Görgens, R. Neuberger, M. Hermann, B. Baur, G. Müller, O. Ambacher, and M. Stutzmann. Electronics and sensors based on

pyroelectric AlGaN/GaN heterostructures - Part B: Sensor applications. *physica status solidi (c)*, 0:1908–1918, 2003.

[58] F. G. K. Baucke. Glass Electrodes: Why and How They Function. *Berichte der Bunsengesellschaft: physical chemistry, chemical physics*, 100:1466–1474, 1996.

[59] R. G. Bates. *Determination of pH. Theory and practice*. Wiley, New York, 2 edition, 1973.

[60] S. I. Sokolov and A. H. Passinski. Über Glaselektroden. *Zeitschrift für Physikalische Chemie*, A 160:366–377, 1932.

[61] W. M. Baumann and W. Simon. Säure-Base-Titrationen in flüssigem Ammoniak. *Fresenius' Journal of Analytical Chemistry*, 216(2):273–278, 1966.

[62] A. Disteche. pH Measurements with a Glass Electrode Withstanding 1500 kg/cm^{-2} Hydrostatic Pressure. *Review of Scientific Instruments*, 30(6):474–478, 1959.

[63] J. Bausells, J. Carrabina, A. Errachid, and A. Merlos. Ion-sensitive field-effect transistors fabricated in a commercial CMOS technology. *Sensors and Actuators B: Chemical*, 57(1-3):56–62, 1999.

[64] D. E. Yates, S. Levine, and T. W. Healy. Site-binding model of the electrical double layer at the oxide/water interface. *Journal of the Chemical Society, Faraday Transactions 1*, 70:1807–1818, 1974.

[65] T. W. Healy and L. R. White. Ionizable surface group models of aqueous interfaces. *Advances in Colloid and Interface Science*, 9(4):303–345, 1978.

[66] L. J. Bousse. *The chemical sensitivity of electrolyte, insulator, silicon structures fundamental of ISFET operation*. PhD thesis, Technische Hogeschool Twente, Enschede, 1982.

[67] M. Kosmulski. *Chemical properties of material surfaces*, volume 102 of *Surfactant science series*. Marcel Dekker, New York, 2001.

[68] L. J. Bousse, N. F. de Rooij, and P. Bergveld. Operation of chemically sensitive field-effect sensors as a function of the insulator-electrolyte interface. *IEEE Transactions on Electron Devices*, 30(10):1263–1270, 1983.

[69] C. D. Fung, P. W. Cheung, and W. H. Ko. A generalized theory of an electrolyte-insulator-semiconductor field-effect transistor. *IEEE Transactions on Electron Devices*, 33(1):8–18, 1986.

[70] R.E.G. van Hal, J.C.T. Eijkel, and P. Bergveld. A novel description of ISFET sensitivity with the buffer capacity and double-layer capacitance as key parameters. *Sensors and Actuators B: Chemical*, 24(1-3):201–205, 1995.

[71] R.E.G. van Hal, J.C.T. Eijkel, and P. Bergveld. A general model to describe the electrostatic potential at electrolyte oxide interfaces. *Advances in Colloid and Interface Science*, 69(1-3):31–62, 1996.

[72] D. L. Harame, L. J. Bousse, J. D. Shott, and J. D. Meindl. Ion-sensing devices with silicon nitride and borosilicate glass insulators. *IEEE Transactions on Electron Devices*, 34(8):1700–1707, 1987.

[73] C.G. Armistead, A.J. Tyler, F.H. Hambleton, S.A. Mitchell, and J. A. Hockey. Surface hydroxylation of silica. *Journal of Physical Chemistry*, 73(11):3947–3953, 1969.

[74] J.B. Peri. Infrared and Gravimetric Study of the Surface Hydration of gamma-Alumina. *Journal of Physical Chemistry*, 69(1):211–219, 1965.

[75] L. J. Bousse, S. Mostarshed, B. H. van der Schoot, N. F. de Rooij, P. Gimmel, and W. Göpel. Zeta potential measurements of Ta_2O_5 and SiO_2 thin films. *Journal of Colloid and Interface Science*, 147(1):22–32, 1991.

[76] B.I. Lobov, L.A. Rubina, I.G. Vinogradova, and I.F. Marvin. Acid-base properties of aluminium, indium, gallium solid oxides. *Zhurnal Neorganicheskoi Khimii*, 34:2495–2498, 1989.

[77] E.A. Necheav. *Kolloidnyi Zhurnal*, 42:371–373, 1980.

[78] M. Kosmulski. Pristine Points of Zero Charge of Gallium and Indium Oxides. *Journal of Colloid and Interface Science*, 238(1):225–227, 2001.

[79] M. Bayer, C. Uhl, and P. Vogl. Theoretical study of electrolyte gate AlGaN/GaN field effect transistors. *Journal of Applied Physics*, 97(3):033703, 2005.

[80] P. Bergveld. The operation of an ISFET as an electronic device. *Sensors and Actuators*, 1:17–29, 1981.

[81] M. Klein. Time effects of ion-sensitive field-effect transistors. *Sensors and Actuators*, 17(1-2):203–208, 1989.

[82] W. Oelßner, J. Zosel, F. Berthold, and H. Kaden. Investigation of the dynamic response behaviour of ISFET pH sensors by means of laser Doppler velocimetry (LDV): Eurosensors VIII. *Sensors and Actuators B: Chemical*, 27(1-3):345–348, 1995.

[83] T. Matsuo and H. Nakajima. Characteristics of reference electrodes using a polymer gate ISFET. *Sensors and Actuators*, 5(4):293–305, 1984.

[84] A. van den Berg, A. Grisel, H. H van den Vlekkert, and N. F. de Rooij. A micro-volume open liquid-junction reference electrode for pH-ISFETs. *Sensors and Actuators B: Chemical*, 1(1-6):425–432, 1990.

[85] W. Oelßner, J. Zosel, U. Guth, T. Pechstein, W. Babel, J. G. Connery, C. Demuth, M. G. Gansey, and J. B. Verburg. Encapsulation of ISFET sensor chips: Piet Bergveld Special Issue. *Sensors and Actuators B: Chemical*, 105(1):104–117, 2005.

[86] H. S. Wolff. The radio pill. *New Scientist*, 12:419, 1961.

[87] P. Bergveld. The development and application of FET-based biosensors. *Biosensors*, 2(1):15–33, 1986.

[88] A. Sibbald, A. K. Covington, and R. F. Carter. Simultaneous online measurement of blood K^+, Ca^{2+}, Na^+, and pH with a four-function ChemFET integrated-circuit sensor. *Clinical Chemistry*, 30(1):135–137, 1984.

[89] P. Arquint, M. Koudelka-Hep, B. H. van der Schoot, P. D. van der Wal, and N. F. de Rooij. Micromachined analyzers on a silicon chip. *Clinical Chemistry*, 40(9):1805–1809, 1994.

[90] S. Shoji and M. Esashi. Micro flow cell for blood gas analysis realizing very small sample volume. *Sensors and Actuators B: Chemical*, 8(2):205–208, 1992/5.

[91] W. Olthuis, B. H. van der Schoot, F. Chavez, and P. Bergveld. A dipstick sensor for coulometric acid-base titrations. *Sensors and Actuators*, 17(1-2):279–283, 1989.

[92] K. Izutsu, T. Nakamura, and S. Hiraoka. Use of pH-Sensitive ISFETs as Sensors for pH in Nonaqueous Solutions and for Proton Solvation. *Chemistry Letters*, 22(11):1843–1846, 1993.

[93] K. Domansky, J. Janata, M. Josowicz, and D. Petelenz. Present state of fabrication of chemically sensitive field effect transistors—Plenary lecture. *The Analyst*, 118:335–340, 1993.

[94] C. Westcott. *pH measurements*. Acad. Press, New York, N.Y., 1978.

[95] I-Yu Huang, R.-S. Huang, and L.-H. Lo. Improvement of integrated Ag/AgCl thin-film electrodes by KCl-gel coating for ISFET applications. *Sensors and Actuators B: Chemical*, 94(1):53–64, 2003.

[96] A. Simonis. *Untersuchungen zur Entwicklung einer feldeffekt-basierten Biosensoranordnung mit integriertem Referenzsystem*. PhD thesis, Rheinisch-Westfälischen Technischen Hochschule Aachen, Aachen, 2006.

[97] A.W.J. Cranny and J.K. Atkinson. Thick film silver-silver chloride reference electrodes. *Measurement Science and Technology*, 9(9):1557–1565, 1998.

[98] H. Suzuki, A. Hiratsuka, S. Sasaki, and I. Karube. Problems associated with the thin-film Ag/AgCl reference electrode and a novel structure with improved durability. *Sensors and Actuators B: Chemical*, 46(2):104–113, 1998/2/15.

[99] H. Nakajima, M. Esashi, and T. Matsuo. The Cation Concentration Response of Polymer Gate ISFET. *Journal of The Electrochemical Society*, 129(1):141–143, 1982.

[100] J. M. Chovelon, J. J. Fombon, P. Clechet, N. Jaffrezic-Renault, C. Martelet, A. Nyamsi, and Y. Cros. Sensitization of dielectric surfaces by chemical grafting: application to pH ISFETs and REFETs. *Sensors and Actuators B: Chemical*, 8(3):221–225, 1992.

[101] H. H van den Vlekkert, N. F. de Rooij, A. van den Berg, and A. Grisel. Multi-ion sensing system based on glass-encapsulated pH-ISFETs and a pseudo-REFET. *Sensors and Actuators B: Chemical*, 1(1-6):395–400, 1990/1.

[102] B. Gil, editor. *Group III nitride semiconductor compounds: Physics and applications*. Clarendon Press, Oxford, 6 edition, 1998.

[103] H. P. Maruska and J. J. Tietjen. The preperation and properties of vapor-deposited single-crystal-line GaN. *Applied Physics Letters*, 15(10):327–329, 1969.

[104] S. Nakamura, T. Mukai, and M. Senoh. Candela-class high-brightness InGaN/AlGaN double-heterostructure blue-light-emitting diodes. *Applied Physics Letters*, 64(13):1687–1689, 1994.

[105] B. Monemar. Fundamental energy gap of GaN from photoluminescence excitation spectra. *Physical Review B*, 10(2):676, 1974.

[106] S. Yoshida, S. Misawa, and S. Gonda. Properties of $Al_xGa_{1-x}N$ films prepared by reactive molecular beam epitaxy. *Journal of Applied Physics*, 53(10):6844–6848, 1982.

[107] J. Wu, W. Walukiewicz, K. M. Yu, J. W. Ager III, E. E. Haller, Hai Lu, W. J. Schaff, Y. Saito, and Y. Nanishi. Unusual properties of the fundamental band gap of InN. *Applied Physics Letters*, 80(21):3967–3969, 2002.

[108] T.-H. Young and C.-R. Chen. Assessment of GaN chips for culturing cerebellar granule neurons. *Biomaterials*, 27(18):3361–3367, 2006.

[109] I. Cimalla, F. Will, K. Tonisch, M. Niebelschutz, V. Cimalla, V. Lebedev, G. Kittler, M. Himmerlich, S. Krischok, J. A. Schaefer, M. Gebinoga, A. Schober, T. Friedrich, and O. Ambacher. AlGaN/GaN biosensor–effect of device processing steps on the surface properties and biocompatibility. *Sensors and Actuators B: Chemical*, 123(2):740–748, 2007.

[110] O. Ambacher, J. Smart, J. R. Shealy, N. G. Weimann, K. Chu, M. Murphy, W. J. Schaff, L. F. Eastman, R. Dimitrov, L. Wittmer, M. Stutzmann, W. Rieger, and J. Hilsenbeck. Two-dimensional electron gases induced by spontaneous and piezoelectric polarization charges in N- and Ga-face AlGaN/GaN heterostructures. *Journal of Applied Physics*, 85(6):3222–3233, 1999.

[111] H. Okano, Y. Takahashi, T. Tanaka, K. Shibata, and S. Nakano. Preparation of c-Axis Oriented AlN Thin Films by Low-

Temperature Reactive Sputtering. *Japanese Journal of Applied Physics*, 31(Part 1, No. 10):3446, 1992.

[112] S.C. Jain, M. Willander, J. Narayan, and R. van Overstraeten. III–nitrides: Growth, characterization, and properties. *Journal of Applied Physics*, 87(3):965–1006, 2000.

[113] S. Nakamura, M. Senoh, S.-I. Nagahama, N. Iwasa, T. Yamada, T. Matsushita, H. Kiyoku, and Y. Sugimoto. InGaN-Based Multi-Quantum-Well-Structure Laser Diodes. *Japanese Journal of Applied Physics*, 35(Part 2, No. 1B):L74, 1996.

[114] C. Rivera, J. L. Pau, F. B. Naranjo, and E. Munoz. Novel photodetectors based on InGaN/GaN multiple quantum wells. *physica status solidi (a)*, 201:2658–2662, 2004.

[115] O. Ambacher. Growth and applications of Group III-nitrides. *Journal of Physics D: Applied Physics*, 31(20):2653–2710, 1998.

[116] N. Friedrich. High-Power Transistors Surf GaN Wave : http://www.mwrf.com/article/articleid/13001/13001.html (05.07.2010).

[117] C. Deger, E. Born, H. Angerer, O. Ambacher, M. Stutzmann, J. Hornsteiner, E. Riha, and G. Fischerauer. Sound velocity of $Al_xGa_{1-x}N$ thin films obtained by surface acoustic-wave measurements. *Applied Physics Letters*, 72(19):2400–2402, 1998.

[118] B.P. Luther, S.D. Wolter, and S.E. Mohney. High temperature Pt Schottky diode gas sensors on n-type GaN. *Sensors and Actuators B: Chemical*, 56(1-2):164–168, 1999.

[119] C. Buchheim. *Dielektrische Funktion und elektrooptische Eigenschaften von (Al,Ga)N/GaN-Heterostrukturen*. PhD thesis, Technische Universität Ilmenau, Ilmenau, 2010.

[120] J. P. Ibbetson, P. T. Fini, K. D. Ness, S. P. DenBaars, J. S. Speck, and U. K. Mishra. Polarization effects, surface states, and the source of electrons in AlGaN/GaN heterostructure field effect transistors. *Applied Physics Letters*, 77(2):250–252, 2000.

[121] K. Kohler, S. Muller, R. Aidam, P. Waltereit, W. Pletschen, L. Kirste, H. P. Menner, W. Bronner, A. Leuther, R. Quay, M. Mikulla, O. Ambacher, R. Granzner, F. Schwierz, C. Buchheim, and R. Goldhahn. Influence of the surface potential on electrical properties of $Al_xGa_{1-x}N$/GaN heterostructures with different Al-content: Effect of growth method. *Journal of Applied Physics*, 107(5):053711–5, 2010.

[122] J. Chen. Measurement of threading dislocation densities in GaN by wet chemical etching. *Semiconductor Science and Technology*, 21(9):1229, 2006.

[123] S. D. Lester, F. A. Ponce, M. G. Craford, and D. A. Steigerwald. High dislocation densities in high efficiency GaN-based light-emitting diodes. *Applied Physics Letters*, 66(10):1249–1251, 1995.

[124] P. Visconti, K. M. Jones, M. A. Reshchikov, R. Cingolani, H. Morkoc, and R. J. Molnar. Dislocation density in GaN determined by photoelectrochemical and hot-wet etching. *Applied Physics Letters*, 77(22):3532–3534, 2000/11/27.

[125] D. V. Lang, R. A. Logan, and M. Jaros. Trapping characteristics and a donor-complex (DX) model for the persistent-photoconductivity trapping center in Te-doped $Al_xGa_{1-x}As$. *Physical Review B*, 19(2):1015, 1979.

[126] H. M. Chen, Y. F. Chen, M. C. Lee, and M. S. Feng. Persistent photoconductivity in n-type GaN. *Journal of Applied Physics*, 82(2):899–901, 1997.

[127] J. Z. Li, J. Y. Lin, H. X. Jiang, M. A. Khan, and Q. Chen. Persistent photoconductivity in a two-dimensional electron gas system formed by an AlGaN/GaN heterostructure. *Journal of Applied Physics*, 82(3):1227–1230, 1997.

[128] G. Beadie, W. S. Rabinovich, A. E. Wickenden, D. D. Koleske, S.C. Binari, and J. A. JR. Freitas. Persistent photoconductivity in n-type GaN. *Applied Physics Letters*, 71(8):1092–1094, 1997.

[129] M. T. Hirsch, J. A. Wolk, W. Walukiewicz, and E. E. Haller. Persistent photoconductivity in n-type GaN. *Applied Physics Letters*, 71(8):1098–1100, 1997/08/25.

[130] C. Johnson, J. Y. Lin, H. X. Jiang, M. A. Khan, and C. J. Sun. Metastability and persistent photoconductivity in Mg-doped p-type GaN. *Applied Physics Letters*, 68(13):1808–1810, 1996/03/25.

[131] C. V. Reddy, K. Balakrishnan, H. Okumura, and S. Yoshida. The origin of persistent photoconductivity and its relationship with yellow luminescence in molecular beam epitaxy grown undoped GaN. *Applied Physics Letters*, 73(2):244–246, 1998/07/13.

[132] X. Z. Dang, C. D. Wang, E. T. Yu, K. S. Boutros, and J. M. Redwing. Persistent photoconductivity and defect levels in n-type AlGaN/GaN heterostructures. *Applied Physics Letters*, 72(21):2745–2747, 1998.

[133] C. H. Qiu and J. I. Pankove. Deep levels and persistent photoconductivity in GaN thin films. *Applied Physics Letters*, 70(15):1983–1985, 1997/04/14.

[134] A. Horn, O. Katz, G. Bahir, and J. Salzman. Surface states and persistent photocurrent in a GaN heterostructure field effect transistor. *Semiconductor Science and Technology*, 21(7):933, 2006.

[135] M. D. McCluskey, N. M. Johnson, C. G. van de Walle, D. P. Bour, M. Kneissl, and W. Walukiewicz. Metastability of Oxygen Donors in AlGaN. *Physical Review Letters*, 80(18):4008, 1998/05/04.

[136] O. Seifert. *Persistente Photoleitfähigkeit in dünnen GaN- und AlGaN-Schichten* . PhD thesis, Universität Oldenburg, Oldenburg, 1999.

[137] T. Ning, C. Osburn, and H. Yu. Effect of electron trapping on IGFET characteristics. *Journal of Electronic Materials*, 6(2):65–76, 1977.

[138] A. Kastalsky and R. A. Kiehl. On the low-temperature degradation of (AlGa)As/GaAs modulation-doped field-effect transistors. *IEEE Transactions on Electron Devices*, 33(3):414–423, 1986.

[139] S.C. Binari, W. Kruppa, H. B. Dietrich, G. Kelner, A. E. Wickenden, and J. A. JR. Freitas. Fabrication and characterization of

GaN FETs: Proceedings of the Topical Workshop on Heterostructure of Microlectronics. *Solid-State Electronics*, 41(10):1549–1554, 1997.

[140] P. B. Klein, J. A. JR. Freitas, S.C. Binari, and A. E. Wickenden. Observation of deep traps responsible for current collapse in GaN metal–semiconductor field-effect transistors. *Applied Physics Letters*, 75(25):4016–4018, 1999.

[141] S.C. Binari, K. Ikossi, J. A. Roussos, W. Kruppa, P. Doewon, H. B. Dietrich, D. D. Koleske, A. E. Wickenden, and R. L. Henry. Trapping effects and microwave power performance in AlGaN/GaN HEMTs. *IEEE Transactions on Electron Devices*, 48(3):465–471, 2001.

[142] I. Daumiller, D. Theron, C. Gaquiere, A. Vescan, R. Dietrich, A. Wieszt, H. Leier, R. Vetury, U. K. Mishra, I. P. Smorchkova, S. Keller, C. Nguyen, and E. Kohn. Current instabilities in GaN-based devices. *Electron Device Letters, IEEE*, 22(2):62–64, 2001.

[143] R. Vetury, N. Q. Zhang, S. Keller, and U. K. Mishra. The impact of surface states on the DC and RF characteristics of AlGaN/GaN HFETs. *IEEE Transactions on Electron Devices*, 48(3):560–566, 2001.

[144] G. Verzellesi, R. Pierobon, F. Rampazzo, G. Meneghesso, A. Chini, U. K. Mishra, C. Canali, and E. Zanoni. Experimental/numerical investigation on current collapse in AlGaN/GaN HEMT's. *Electron Devices Meeting, 2002. IEDM '02. Digest. International*, pages 689–692, 2002.

[145] G. Koley, V. Tilak, L. F. Eastman, and M. G. Spencer. Slow transients observed in AlGaN/GaN HFETs: effects of SiNx passivation and UV illumination. *IEEE Transactions on Electron Devices*, 50(4):886–893, 2003.

[146] Y. Ando, A. Wakejima, Y. Okamoto, T. Nakayama, K. Ota, K. Yamanoguchi, Y. Murase, K. Kasahara, K. Matsunaga, T. Inoue, and H. Miyamoto. Novel AlGaN/GaN dual-field-plate FET with high gain, increased linearity and stability. In *IEDM Technical Digest*, pages 576–579, 2005.

[147] K. Horio. Analysis of field-plate effects on buffer-related lag phenomena and current collapse in GaN MESFETs and AlGaN/GaN HEMTs. *Semiconductor Science and Technology*, 24(8):085022, 2009.

[148] S. K. Hong, B. J. Kim, H. S. Park, Y. Park, S. Y. Yoon, and T. I. Kim. Evaluation of nanopipes in MOCVD grown (0 0 0 1) GaN/Al_2O_3 by wet chemical etching. *Journal of Crystal Growth*, 191(1-2):275–278, 1998/1/7.

[149] M. S. Minsky, M. White, and E. L. Hu. Room-temperature photoenhanced wet etching of GaN. *Applied Physics Letters*, 68(11):1531–1533, 1996/03/11.

[150] C. Youtsey, I. Adesida, and G. Bulman. Highly anisotropic photoenhanced wet etching of n-type GaN. *Applied Physics Letters*, 71(15):2151–2153, 1997/10/13.

[151] L. H Peng, C. W Chuang, J. K Ho, C. N Huang, and C. Y Chen. Deep ultraviolet enhanced wet chemical etching of gallium nitride. *Applied Physics Letters*, 72(8):939–941, 1998.

[152] C. Youtsey, I. Adesida, L. T. Romano, and G. Bulman. Smooth n-type GaN surfaces by photoenhanced wet etching. *Applied Physics Letters*, 72(5):560–562, 1998/02/02.

[153] Bo Yang and Patrick Fay. Bias-enhanced lateral photoelectrochemical etching of GaN for the fabrication of undercut micromachined system structures. *Journal of Vacuum Science & Technology B*, 24(3):1337–1340, 2006/05/00.

[154] J. W. Seo, C. S. Oh, J. W. Yang, G. M. Yang, K. Y. Lim, C. J. Yoon, and H. J. Lee. Allowable Substrate Bias for the Etching of n-GaN in Photo-Enhanced Electrochemical Etching. *physica status solidi (a)*, 188(1):403–406, 2001.

[155] J. W. Seo, C. S. Oh, H. S. Jeong, J. W. Yang, K. Y. Lim, C. J. Yoon, and H. J. Lee. Bias-assisted photoelectrochemical oxidation of n-GaN in H_2O. *Applied Physics Letters*, 81(6):1029–1031, 2002.

[156] E. Alptekin, H. Yu, E. Ozbay, and O. Aktas. Low Damage Etching of GaN Surfaces via Bias-Assisted Photoenhanced Electrochemical Oxidation in Deionized Water. *Journal of Electronic Materials*, 36(6):629–633, 2007.

[157] R. Neuberger, G. Müller, O. Ambacher, and M. Stutzmann. Ion-Induced Modulation of Channel Currents in AlGaN/GaN High-Electron-Mobility Transistors. *physica status solidi (a)*, 183:R10, 2001.

[158] R. Neuberger, G. Müller, M. Eickhoff, O. Ambacher, and M. Stutzmann. Observation of ion-induced changes in the channel current of high electron mobility AlGaN/GaN transistors

(HEMT). *Materials Science and Engineering: B*, 93(1-3):143–146, 2002.

[159] R. Neuberger, G. Müller, O. Ambacher, and M. Stutzmann. High-Electron-Mobility AlGaN/GaN Transistors (HEMTs) for Fluid Monitoring Applications. *physica status solidi (a)*, 185:85–89, 2001.

[160] R. Mehandru, B. Luo, B. S. Kang, J. Kim, F. Ren, S. J. Pearton, C.-C. Pan, G.-T. Chen, and J.-I. Chyi. AlGaN/GaN HEMT based liquid sensors. *Solid-State Electronics*, 48(2):351–353, 2004.

[161] T. Kokawa, T. Sato, H. Hasegawa, and T. Hashizume. Liquid-phase sensors using open-gate AlGaN/GaN high electron mobility transistor structure. *Journal of Vacuum Science & Technology B*, 24(4):1972–1976, 2006.

[162] B. S. Kang, G. Louche, R. S. Duran, Y. Gnanou, S. J. Pearton, and F. Ren. Gateless AlGaN/GaN HEMT response to block co-polymers. *Solid-State Electronics*, 48(5):851–854, 2004.

[163] K. Prabhakaran, T.G. Andersson, and K. Nozawa. Nature of native oxide on GaN surface and its reaction with Al. *Applied Physics Letters*, 69(21):3212–3214, 1996.

[164] N.J. Watkins, G.W. Wicks, and Y. Gao. Oxidation study of GaN using x-ray photoemission spectroscopy. *Applied Physics Letters*, 75(17):2602–2604, 1999.

[165] S. Kocha, M. W. Peterson, D. J. Arent, J. M. Redwing, M. A. Tischler, and J. A. Turner. Electrochemical Investigation of the Gallium Nitride-Aqueous Electrolyte Interface. *Journal of The Electrochemical Society*, 142(12):L238–L240, 1995.

[166] B. Lübbers, G. Kittler, P. Ort, S. Linkohr, D. Wegener, B. Baur, M. Gebinoga, F. Weise, M. Eickhoff, S. Maroldt, A. Schober, and O. Ambacher. A novel GaN-based multiparameter sensor system for biochemical analysis. *physica status solidi (c)*, 6:2361–2363, 2008.

[167] J.-L. Chiang, Y.-C. Chen, and J. C. Chou. Simulation and Experimental Study of the pH-Sensing Property for AlN Thin Films. *Japanese Journal of Applied Physics*, 40(Part 1, No. 10):5900, 2001.

[168] Y. Alifragis, A. Georgakilas, G. Konstantinidis, E. Iliopoulos, A. Kostopoulos, and N. A. Chaniotakis. Response to anions of AlGaN/GaN high-electron-mobility transistors. *Applied Physics Letters*, 87(25):253507, 2005.

[169] K. H. T. Ba, M. A. Mastro, J. K. Hite, C. R. [JR.] Eddy, and T. Ito. Nitrogen-polar gallium nitride substrates as solid-state pH-selective potentiometric sensors. *Applied Physics Letters*, 95(14):142501–142503, 2009.

[170] M. Hofstetter, J. Howgate, I. D. Sharp, M. Funk, M. Stutzmann, H. G. Paretzke, and S. Thalhammer. Real-time x-ray response of biocompatible solution gate AlGaN/GaN high electron mobility transistor devices. *Applied Physics Letters*, 96(9):092110–092113, 2010.

[171] T. Hashizume, S.-Y. Ootomo, R. Nakasaki, S. Oyama, and M. Kihara. X-ray photoelectron spectroscopy characterization of AlGaN surfaces exposed to air and treated in NH_4OH solution. *Applied Physics Letters*, 76(20):2880–2882, 2000.

[172] D. R. Lide. *CRC handbook of chemistry and physics: A ready-reference book of chemical and physical data*. CRC Press, Boca Raton, 84th ed edition, 2003.

[173] B. S. Kang, R. Mehandru, S. Kim, F. Ren, R.C. Fitch, J.K. Gillespie, N. Moser, G. Jessen, T. Jenkins, R. Dettmer, D. Via, A. Crespo, B. P. Gila, C.R. Abernathy, and S. J. Pearton. Hydrogen-induced reversible changes in drain current in Sc_2O_3/AlGaN/GaN high electron mobility transistors. *Applied Physics Letters*, 84(23):4635–4637, 2004.

[174] N. A. Chaniotakis, Y. Alifragis, G. Konstantinidis, and A. Georgakilas. Gallium Nitride-Based Potentiometric Anion Sensor. *Analytical Chemistry*, 76(18):5552–5556, 2004.

[175] Y. Alifragis, G. Konstantinidis, A. Georgakilas, and N. A. Chaniotakis. Anion Selective Potentiometric Sensor Based on Gallium Nitride Crystalline Membrane. *Electroanalysis*, 17:527–531, 2005.

[176] N. A. Chaniotakis, Y. Alifragis, A. Georgakilas, and G. Konstantinidis. GaN-based anion selective sensor: Probing the origin of the induced electrochemical potential. *Applied Physics Letters*, 86(16):164103–3, 2005.

[177] A. Costales, A. K. Kandalam, A. Martin Pendas, M. A. Blanco, J. M. Recio, and R. Pandey. First Principles Study of Polyatomic Clusters of AlN, GaN, and InN. 2. Chemical Bonding. *Journal of Physical Chemistry B*, 104(18):4368–4374, 2000.

[178] V.M. Bermudez. Study of oxygen chemisorption on the GaN(0001)-(1 x 1) surface. *Journal of Applied Physics*, 80(2):1190–1200, 1996.

[179] M. Eickhoff, R. Neuberger, G. Steinhoff, O. Ambacher, G. Müller, and M. Stutzmann. Wetting behaviour of GaN surfaces with Ga- or N-face polarity. *physica status solidi (b)*, 228:519, 2001.

[180] S.D. Wolter, B.P. Luther, D.L. Waltemyer, C. Onneby, S.E. Mohney, and R. J. Molnar. X-ray photoelectron spectroscopy and x-ray diffraction study of the thermal oxide on gallium nitride. *Applied Physics Letters*, 70(16):2156–2158, 1997.

[181] L. Smith, S.W. King, R.J. Nemanich, and R. Davis. Cleaning of GaN surfaces. *Journal of Electronic Materials*, 25(5):805–810, 1996.

[182] I. G. R. Gutz. CurTiPot : http://www2.iq.usp.br/docente/gutz/curtipot_.html (05.07.2010).

[183] B. S. Kang, F. Ren, M. C. Kang, C. Lofton, W. Tan, S. J. Pearton, A. Dabiran, A. Osinsky, and P. P. Chow. Detection of halide ions with AlGaN/GaN high electron mobility transistors. *Applied Physics Letters*, 86(17):173502, 2005.

[184] R. Dimitrova, L. Catalan, D. Alexandrov, and A. Chen. Evaluation of GaN and $In_{0.2}Ga_{0.8}N$ semiconductors as potentiometric anion selective electrodes. *Electroanalysis*, 19(17):1799–1806, 2007.

[185] C. Buchheim, G. Kittler, V. Cimalla, V. Lebedev, M. Fischer, S. Krischok, V. Yanev, M. Himmerlich, G. Ecke, J. A. Schaefer, and O. Ambacher. Tuning of Surface Properties of AlGaN/GaN Sensors for Nanodroplets and Picodroplets. *Sensors Journal, IEEE*, 6(4):881–886, 2006.

[186] Y. Alifragis, A. Volosirakis, N. A. Chaniotakis, G. Konstantinidis, A. Adikimenakis, and A. Georgakilas. Potassium selective chemically modified field effect transistors based on AlGaN/GaN two-dimensional electron gas heterostructures. *Biosensors and Bioelectronics*, 22(12):2796–2801, 2007.

[187] Y. Alifragis, A. Volosirakis, N. A. Chaniotakis, G. Konstantinidis, E. Iliopoulos, and A. Georgakilas. AlGaN/GaN high electron mobility transistor sensor sensitive to ammonium ions. *physica status solidi (a)*, 204:2059, 2007.

[188] V.M. Bermudez. Functionalizing the GaN(0 0 0 1)-(1x1) surface I. The chemisorption of aniline. *Surface Science*, 499(2-3):109–123, 2002.

[189] V.M. Bermudez. Functionalizing the GaN(0 0 0 1)-(1x1) surface II. Chemisorption of 3-pyrroline. *Surface Science*, 499(2-3):124–134, 2002.

[190] B. S. Kang, F. Ren, L. Wang, C. Lofton, W. W. Tan, S. J. Pearton, A. Dabiran, A. Osinsky, and P. P. Chow. Electrical detection of immobilized proteins with ungated AlGaN/GaN high-electron-mobility Transistors. *Applied Physics Letters*, 87(2):023508, 2005.

[191] B. Baur, J. Howgate, H.-G. von Ribbeck, Y. Gawlina, V. Bandalo, G. Steinhoff, M. Stutzmann, and M. Eickhoff. Catalytic activity of enzymes immobilized on AlGaN/GaN solution gate field-effect transistors. *Applied Physics Letters*, 89(18):183901–183903, 2006.

[192] B. S. Simpkins, K. M. Mccoy, L. J. Whitman, and P. E. Pehrsson. Fabrication and characterization of DNA-functionalized GaN nanowires. *Nanotechnology*, 18(35):355301, 2007.

[193] B. S. Kang, H.T. Wang, T.P. Lele, Y. Tseng, F. Ren, S. J. Pearton, J. W. Johnson, P. Rajagopal, J. C. Roberts, E. L. Piner, and K. J. Linthicum. Prostate specific antigen detection using AlGaN/GaN high electron mobility transistors. *Applied Physics Letters*, 91(11):112106, 2007.

[194] B. S. Kang, S. J. Pearton, J. J. Chen, F. Ren, J. W. Johnson, R. J. Therrien, P. Rajagopal, J. C. Roberts, E. L. Piner, and K. J. Linthicum. Electrical detection of deoxyribonucleic acid hybridization with AlGaN/GaN high electron mobility transistors. *Applied Physics Letters*, 89(12):122102, 2006.

[195] M. Gebinoga, I. Cimalla, L. Silveira, M. Klett, V. Lebedev, F. Niebelschuetz, O. Ambacher, and A. Schober. Response of nerve cell to inhibitor recorded by aluminium-gallium-nitride FET. In M.-I Baraton, editor, *Sensors for environment, health and security*, pages 311–318. Springer, Dordrecht, 2008.

[196] C. R. Miskys, M. K. Kelly, O. Ambacher, and M. Stutzmann. Freestanding GaN-substrates and devices. *physica status solidi (c)*, 0(6):1627–1650, 2003.

[197] K. Tonisch. *AlGaN/GaN-Schichtsysteme für piezoelektrisch angeregte Resonatoren*. PhD thesis, Technische Universität Ilmenau, Ilmenau, 2009.

[198] F. Niebelschuetz. *Mikrostrukturierungstechniken zur Herstellung von MEMS aus Halbleitern großer Bandlücke*. PhD thesis, Technische Universität Ilmenau, Ilmenau, 2010.

[199] DIN Deutsches Institut für Normung e. V. pH measurement - Reference buffer solutions for the calibration of pH measuring equipment, 2000.

[200] A. H. Maas. pH determination in body fluids using a cell with an isotonic sodium chloride bridge. *Journal of Applied Physiology*, 30(2):248–250, 1971.

[201] K. S. Cole and R. H. Cole. Dispersion and Absorption in Dielectrics I. Alternating Current Characteristics. *Journal of Chemical Physics*, 9(4):341–351, 1941.

[202] E. Barsoukov and J. R. Macdonald. *Impedance spectroscopy: Theory, experiment, and applications*. Wiley-Interscience, Hoboken, NJ, 2. ed. edition, 2005.

[203] D. K. Schroder. *Semiconductor material and device characterization*. Wiley-Interscience [u.a.], Hoboken, NJ, 3. ed. edition, 2006.

[204] E. H. Nicollian and J. R. Brews. *MOS (Metal oxide semiconductor) physics and technology*. A Wiley-interscience publication. Wiley, New York, NY, 1982.

[205] M. E. Levinshtein, S. L. Rumyantsev, and M. S. Shur, editors. *Properties of advanced semiconductor materials: GaN, AlN, InN, BN, SiC, SiGe*. Wiley, New York, 2001.

[206] E. J. Miller, X. Z. Dang, H. H. Wieder, P. M. Asbeck, E. T. Yu, G. J. Sullivan, and J. M. Redwing. Trap characterization by gate-drain conductance and capacitance dispersion studies of an AlGaN/GaN heterostructure field-effect transistor. *Journal of Applied Physics*, 87(11):8070–8073, 2000.

[207] E. Kohn, I. Daumiller, P. Schmid, N. X. Nguyen, and C. N. Nguyen. Large signal frequency dispersion of AlGaN/GaN heterostructure field effect transistors: Electronics Letters. *Electronics Letters*, 35(12):1022–1024, 1999.

[208] J. R. Shealy and R. J. Brown. Frequency dispersion in capacitance-voltage characteristics of AlGaN/GaN heterostructures. *Applied Physics Letters*, 92(3):032101–032103, 2008.

[209] S. Kochowski and K. Nitsch. Description of the frequency behaviour of metal-SiO_2-GaAs structure characteristics by electrical equivalent circuit with constant phase element. *Thin Solid Films*, 415(1-2):133–137, 2002.

[210] S. Kochowski, K. Nitsch, B. Paszkiewicz, R. Paszkiewicz, and M. Szydlowski. Studies of GaAs metal-insulator-semiconductor structures by the admittance spectroscopy method: Proceedings of the 3rd International Workshop on Semiconductor Surface Passivation. *Applied Surface Science*, 235(3):389–394, 2004.

[211] G. J. Brug, A. L. G. van den Eeden, M. Sluyters-Rehbach, and J. H. Sluyters. The analysis of electrode impedances complicated by the presence of a constant phase element. *Journal of Electroanalytical Chemistry*, 176(1-2):275–295, 1984.

[212] L. J. Bousse and P. Bergveld. On the impedance of the silicon dioxide/electrolyte interface. *Journal of Electroanalytical Chemistry*, 152(1-2):25–39, 1983.

[213] T. Wolff, M. Rapp, and T. Rotter. Electrochemical CV-profiling of GaN. *physica status solidi (c)*, 1(10):2491–2494, 2004.

[214] T. Wolff, M. Rapp, and T. Rotter. Electrochemical Etching and CV-Profiling of GaN. *physica status solidi (a)*, 201(9):2067–2075, 2004.

[215] J. R. Shealy, T. R. Prunty, E. M. Chumbes, and B. K. Ridley. Growth and passivation of AlGaN/GaN heterostructures. *Journal of Crystal Growth*, 250(1-2):7–13, 2003/3.

[216] A. Denisenko, C. Pietzka, A. Chuvilin, U. Kaiser, H. Lu, W. J. Schaff, and E. Kohn. Depletion of surface accumulation charge in InN by anodic oxidation. *Journal of Applied Physics*, 105(3):033702–7, 2009.

[217] S. Birner. BIO-nextnano^3 : http://www.nextnano.de/ (05.07.2010).

[218] E. Saling. *Das Kind im Bereich der Geburtshilfe*. Georg Thieme Verlag, Stuttgart, 1966.

[219] O. S. Andersen, K. Engel, K. Jørgensen, and P. Astrup. A Micro Method for Determination of pH, Carbon Dioxide Tension, Base Excess and Standard Bicarbonate in Capillary Blood. *Scandinavian Journal of Clinical & Laboratory Investigation*, 12(2):172–176, 1960.